Investigation of Coupled Processes and Impact of High Temperature Limits in Argillite Rock

Fuel Cycle Research & Development

Prepared for

U.S. Department of Energy
Used Fuel Disposition Campaign

Liange Zheng
Jonny Rutqvist
Kunhwi Kim
Jim Houseworth

Lawrence Berkeley National Laboratory

July 2015

FCRD-UFD-2015-000362

Revision 2
12/20/2012

APPENDIX E

FCT DOCUMENT COVER SHEET [1]

Name/Title of Deliverable/Milestone/Revision No.	Investigation of Coupled Processes and Impact of High Temperature Limits in Argillite Rock
Work Package Title and Number	DR Argillite Disposal R&D – LBNL - FT-15LB080603
Work Package WBS Number	1.02.08.06
Responsible Work Package Manager	Jim Houseworth (Signature on File) (Name/Signature)

Date Submitted 7/31/2015

Quality Rigor Level for Deliverable/Milestone[2]	☒ QRL-3	☐ QRL-2	☐ QRL-1 ☐ Nuclear Data	☐ Lab/Participant QA Program (no additional FCT QA requirements)

This deliverable was prepared in accordance with Lawrence Berkeley National Laboratory
(Participant/National Laboratory Name)

QA program which meets the requirements of
☒ DOE Order 414.1 ☐ NQA-1-2000 ☐ Other

This Deliverable was subjected to:

☒ Technical Review ☐ Peer Review

Technical Review (TR)

Review Documentation Provided

☐ Signed TR Report or,
☐ Signed TR Concurrence Sheet or,
☒ Signature of TR Reviewer(s) below

Peer Review (PR)

Review Documentation Provided

☐ Signed PR Report or,
☐ Signed PR Concurrence Sheet or,
☐ Signature of PR Reviewer(s) below

Name and Signature of Reviewers

Peter Persoff (Signature on file)

NOTE 1: *Appendix E should be filled out and submitted with the deliverable. Or, if the PICS:NE system permits, completely enter all applicable information in the PICS:NE Deliverable Form. The requirement is to ensure that all applicable information is entered either in the PICS:NE system or by using the FCT Document Cover Sheet.*

NOTE 2: *In some cases there may be a milestone where an item is being fabricated, maintenance is being performed on a facility, or a document is being issued through a formal document control process where it specifically calls out a formal review of the document. In these cases, documentation (e.g., inspection report, maintenance request, work planning package documentation or the documented review of the issued document through the document control process) of the completion of the activity along with the Document Cover Sheet is sufficient to demonstrate achieving the milestone. If QRL 1, 2, or 3 is not assigned, then the Lab/Participant QA Program (no additional FCT QA requirements box must be checked, and the work is understood to be performed, and any deliverable developed, in conformance with the respective National Laboratory/Participant, DOE- or NNSA-approved QA Program..*

This page is intentionally blank.

CONTENTS

1. INTRODUCTION 1

2. INVESTIGATION OF THE IMPACTS OF HIGH TEMPERATURE LIMITS WITH THMC MODELING 3
2.1 Introduction 3
2.2 Model Development 4
2.3 Model Results 12
2.4 Conclusions 46
References 49

3. DEVELOPING THMC MODELS FOR FEBEX-DP 52
3.1 Introduction 52
3.2 A Brief Description of FEBEX Experiments 52
3.3 Model Development 58
3.4 Model Results 65
3.5 Summary and Future Work 92
References 94

4. THM MODELING: FE HEATER TEST AND DECOVALEX 97
4.1 Modeling Approach 98
4.2 Mont Terri HE-E Experiment (DECOVALEX) 102
4.3 Horonobe EBS Experiment (DECOVALEX) 109
4.4 FE Experiment at the Mont Terri Site (Mont Terri Project) 118
4.5 Status of THM Modeling of Heater Experiments and Plans 126
References 128

5. DISCRETE FRACTURE NETWORK (DFN) APPROACH FOR THM DAMAGE MODELING IN ARGILLACEOUS ROCK 130
5.1 RBSN for Mechanical Damage Modeling of Geomaterials 131
5.2 Hydro-Mechanical Modeling Using TOUGH-RBSN 136
5.3 Fluid-Driven Fracture Simulations 140
5.4 Development of Dynamic Simulation Code 145
5.5 Conclusions 153
5.6 Future Work 153
References 155

6. SUMMARY 157

7. ACKNOWLEDGMENT 161

FIGURES

Figure 2-1. The coupling scheme for TOUGHREACT-FLAC3D. 5

Figure 2-2. Domain for the test example of a bentonite back-filled horizontal emplacement drift at 500 m (Rutqvist et al., 2014). Modeling monitoring points: A: inside the bentonite near the canister, B: inside the bentonite and near the EBS-NS interface, C: inside the clay rock formation and near the EBS-NS interface, D: inside the clay rock formation at a distance of 10 m from the canister. "High T": 200 ºC; "Low T": 100ºC. 6

Figure 2-3. Swelling pressure versus mass fraction of smectite for various bentonites. ▲, FEBEX bentonite (ENRESA, 2000); ●, Montigel bentonite (Bucher and Muller-Vonmoos, 1989); □, Kunigel VI bentonite (JNC, 1999); ○, Kunigel bentonite (Komine and Ogata, 1996), ♦ are data for reference material from Czech, Danish, Friedland, Milos Deponit CA-N, Kutch (Indian) and Wyoming MX-80 (Karnland et al., 2006). 9

Figure 2-4. Temperature evolution at points A, B, C, and D. 14

Figure 2-5. The temporal evolution of water saturation at points A, B, C, and D. 15

Figure 2-6. The temporal evolution of pore pressure at points A, B, C, and D. 16

Figure 2-7. The temporal evolution of smectite volume fraction at points A, B, C, and D. 18

Figure 2-8. The temporal evolution of illite volume fraction at points A, B, C, and D. 19

Figure 2-9. The temporal evolution of smectite volume fraction at points A and B, with X-axis plotted in linear scale. 19

Figure 2-10. The temporal evolution of K-feldspar volume fraction at points A and B, with X-axis plotted in linear scale. 20

Figure 2-11. The temporal evolution of quartz volume fraction at points A, B, C, and D. 20

Figure 2-12. The temporal evolution of K-feldspar volume fraction at points A, B, C, and D for the "high T" base run and a sensitivity run with K-feldspar dissolution rate two orders of magnitude higher. 23

Figure 2-13. The temporal evolution of smectite volume fraction at points A, B, C, and D for the "high T" base run and a sensitivity run with K-feldspar dissolution rate two orders of magnitude higher. 24

Figure 2-14. The temporal evolution of smectite volume fraction at points A, B, C, and D for the "high T" base run and a sensitivity run with K-feldspar dissolution rate two orders of magnitude higher. 25

Figure 2-15. The temporal evolution of calcite volume fraction at points A, B for the case with Ca-smectite and Na-smectite in Kunigel-VI bentonite. 26

Figure 2-16. The temporal evolution of smectite volume fraction at points A, B for the case with Ca-smectite and Na-smectite in Kunigel-VI bentonite. 26

Figure 2-17. The temporal evolution of illite volume fraction at points A, B for the case with Ca-smectite and Na-smectite in Kunigel-VI bentonite. 27

Figure 2-18. Simulation results of mean total stress, pore pressure, and thermal stress at point A for the "low T" and "high T" scenario, respectively. 28

Figure 2-19. Simulation results of mean total stress, pore pressure, and thermal stress at point B for the "low T" and "high T" scenario, respectively. 29

Figure 2-20. Simulation results of swelling stress at point A for the "low T" and "high T" scenarios, respectively. 29

Figure 2-21. Simulation results of swelling stress at point B for the "low T" and "high T" scenarios, respectively. 30

Figure 2-22. Simulation results of mean total stress, pore pressure, and thermal stress at point C for the "low T" and "high T" scenario, respectively. 31

Figure 2-23. Simulation results of mean total stress, pore pressure, and thermal stress at point D for the "low T" and "high T" scenario, respectively. 31

Figure 2-24. Simulation results of mean total stress at point C for the "high T" scenarios in three cases: the 'high T, base case" in which the effect ion concentration and smectite change on stress are considered; the "high T, no Sc" case in which the contribution of smectite change to stress is neglected and the "high T, no C, no Sc" case in which both the contribution of smectite change and ion concentration to stress are neglected. 32

Figure 2-25. Simulation results of mean total stress at point D for the "high T" scenarios in three cases: the 'high T, base case" in which the effect ion concentration and smectite change on stress are considered; the "high T, no Sc" case in which the contribution of smectite change to stress is neglected and the "high T, no C, no Sc" case in which both the contribution of smectite change and ion concentration to stress are neglected. 32

Figure 2-26. The temporal evolution of smectite volume fraction at points A, B, C, and D for Kunigel and FEBEX bentonite. 35

Figure 2-27. The temporal evolution of illite volume fraction at points A, B, C, and D for Kunigel and FEBEX bentonite. 36

Figure 2-28. The temporal evolution of K-feldspar volume fraction at points A, B, C, and D in the base case with Kunigel bentonite and a sensitivity case with FEBEX bentonite. 37

Figure 2-29. The temporal evolution of quartz volume fraction at points A, B, C, and D in the base case with Kunigel bentonite and a sensitivity case with FEBEX bentonite. 38

Figure 2-30. The temporal evolution of calcite volume fraction at points A and B for the case with Ca-smectite and Na-smectite in FEBEX bentonite..... 39

Figure 2-31. The temporal evolution of Ca-smectite/Na-smectite volume fraction for 200 years at points A and B for the case with Ca-smectite and Na-smectite in FEBEX bentonite. 39

Figure 2-32. The temporal evolution of illite volume fraction at points A and B for the case with Ca-smectite and Na-smectite in FEBEX bentonite..... 39

Figure 2-33. The temporal evolution of illite volume fraction at points A, B for the case with Ca-smectite and Na-smectite in FEBEX bentonite. 40

Figure 2-34. Simulation results of mean total stress, pore pressure, swelling stress, and thermal stress at point A in the sensitivity case with FEBEX bentonite for the "low T" and "high T" scenarios, respectively. 41

Figure 2-35. Simulation results of mean total stress, pore pressure, swelling stress, and thermal stress at point B in the sensitivity case with FEBEX bentonite for the "low T" and "high T" scenarios, respectively. 41

Figure 2-36. Simulation results of mean total stress at point A for Kunigel-VI and FEBEX bentonite for the “low T” and “high T” scenarios, respectively. 42

Figure 2-37. Simulation results of mean total stress at point B for Kunigel-VI and FEBEX bentonite for the “low T” and “high T” scenarios, respectively. 42

Figure 2-38. Simulation results of swelling stress at point A for the FEBEX bentonite for the “low T” and “high T” scenarios, respectively, focusing on the stress range from 4.5 to 5 MPa. 44

Figure 2-39. Simulation results of swelling stress at point A for the FEBEX bentonite for the “low T” and “high T” scenarios, respectively, focusing on the stress range from 4.5 to 5 MPa. 45

Figure 2-40. Simulation results of swelling stress at point B for the FEBEX bentonite for the “low T” and “high T” scenarios, respectively, focusing on the stress range from 4.5 to 5 MPa. 45

Figure 2-41. Simulation results of swelling stress at point B for the FEBEX bentonite for the “low T” and “high T” scenarios, respectively, focusing on the stress range from 4.5 to 5 MPa. 46

Figure 3-1. The operational stages of FEBEX *in situ* test (Vomvoris, personal communication). 53

Figure 3-2. Schematic design of the heating and hydration laboratory experiment in the cell CT23 (ENRESA, 2006a). 54

Figure 3-3. Schematic design of mock-up test (Martín et al., 2006). 55

Figure 3-4. The initial configuration of FEBEX in situ test at the Grimsel underground laboratory (Switzerland) (ENRESA, 2000). 56

Figure 3-5. The moisture content (gravimetric water content) at section 15(Vomvoris, personal communication). 57

Figure 3-6. Layout of the sampling sections during the dismantling of heater 1 in 2002. In blue color are the common sections for THG and THM analyses (Fernandez and Rivas, 2003) 57

Figure 3-7. *In situ* test configuration following dismantling of heater 1 (Huertas et al., 2005). 58

Figure 3-8. Mesh used for the model, not to the scale. 60

Figure 3-9. Measured temperature by sensors located at radial distance of 0.48 m in sections E2 and F2 and model results from the base TH model. 66

Figure 3-10. Measured temperature by sensors located at radial distance of 0.8 m in sections E2 and F2and model results from the base TH model. 67

Figure 3-11. Measured temperature by sensors located at radial distance of 1.05 m in sections E2 and F2 and model results from the base TH model. 67

Figure 3-12. Measured temperature by sensors located at radial distance of 1.09 m in sections E2 and F2 and model results from the base TH model. 68

Figure 3-13. Measured relative humidity by sensors located at radial distance of 0.52 m in sections E2 and E1 and model results from the base TH model. 69

Figure 3-14. Measured relative humidity by sensors located at radial distance of ~0.8 m in sections E1, E2, F1 and F2 and model results from the base TH model 69

Figure 3-15. Measured relative humidity by sensors located at radial distance of ~1.05 m in section F2 and model results from the base TH model. 70

Figure 3-16. Measured relative humidity by sensors located at radial distance of ~1.1 m in sections E1, E2 and F1 and model results from the base TH model 70

Figure 3-17. Measured relative humidity by sensors located at radial distance of 0.52 m and model results from the base model and two sensitivity runs with different permeability for granite. 71

Figure 3-18. Measured relative humidity by sensors located at radial distance of 0.8 m and model results from the base model and two sensitivity runs with different permeability for granite. 72

Figure 3-19. Measured temperature by sensors located at radial distance of ~1.05 m and model results from the base model and two sensitivity runs with different permeability for granite. 72

Figure 3-20. Measured relative humidity by sensors located at radial distance of 1.1 m and model results from the base model and two sensitivity runs with different permeability for granite. 73

Figure 3-21. Saturated hydraulic conductivity as a function of dry density (ENRESA, 2000) 74

Figure 3-22. Measured relative humidities by sensors located at radial distance of 0.52 m and model results from the base model and two sensitivity runs with different permeability for bentonite. 74

Figure 3-23. Measured relative humidities by sensors located at radial distance of 0.8 m and model results from the base model and two sensitivity runs with different permeability for bentonite. 75

Figure 3-24. Measured relative humidities by sensors located at radial distance of 1.1 m and model results from the base model and two sensitivity runs with different permeability for bentonite. 75

Figure 3-25. Schematic design of the permeation test (Samper et al., 2008b). 77

Figure 3-26. Measured cumulative water flux data and Darcy flow model, marked “Darcy” in the figure and Non-Darcian flow model, marked as “ND” in the figure with different A values while keeping B equal to -0.78. 78

Figure 3-27. Measured cumulative water flux data and Darcy flow model, marked “Darcy” in the figure and Non-Darcian flow model, marked as “ND” in the figure with different B values while keeping A equal to 2×10^{-13}. 78

Figure 3-28. Measured relative humidities by sensors located at radial distance of 0.52 m and model results from the base model and the Non-Darcian flow model. 79

Figure 3-29. Measured relative humidities by sensors located at radial distance of 0.8 m and model results from the base model and the Non-Darcian flow model. 80

Figure 3-30. Measured relative humidities by sensors located at radial distance of 1.1 m and model results from the base model and the Non-Darcian flow model. 80

Figure 3-31. Measured temperature by sensors located at radial distance of 0.48 m and model results from the base model and the Non-Darcian flow model. 81

Figure 3-32. Measured temperature by sensors located at radial distance of 1.1 m and model results from the base model and the Non-Darcian flow model. 81

Figure 3-33. The positions where samples were taken for geochemical analyses at section 29 after the dismantling of heater 1 in 2002 (Zheng et al., 2011). 83

Figure 3-34. The concentration profile of chloride at 1930 days (Zheng et al., 2011) and model results from the base model. 84

Figure 3-35. The concentration profile of sodium at 1930 days (Zheng et al., 2011) and model results from the base model and sensitivity run that does not consider any chemical reaction. 85

Figure 3-36. The concentration profile of calcium at 1930 days (Zheng et al., 2011) and model results from the base model and sensitivity run that does not consider any chemical reaction. 85

Figure 3-37. The concentration profile of magnesium at 1930 days (Zheng et al., 2011) and model results from the base model and sensitivity run that does not consider any chemical reaction. 86

Figure 3-38. The concentration profile of potassium at 1930 days (Zheng et al., 2011) and model results from the base model and sensitivity run that does not consider any chemical reaction. 86

Figure 3-39. Computed profile of volume fraction change of smectite at the 1930 days (after the dismantling of heater 1) and at 6698 days (July 1, 2015). 87

Figure 3-40. Computed profile of volume fraction change of dolomite at the 1930 days (after the dismantling of heater 1) and at 6698 days (July 1, 2015). 87

Figure 3-41. Computed profile of volume fraction change of calcite at the 1930 days (after the dismantling of heater 1) and at 6698 days (July 1, 2015). 88

Figure 3-42. Computed profile of volume fraction change of illite at the 1930 days (after the dismantling of heater 1) and at 6698 days (July 1, 2015). 88

Figure 3-43. The profile of pH at 1930 days (Zheng et al., 2011) and model results from the base model. 89

Figure 3-44. The concentration profile of bicarbonate at 1930 days (Zheng et al., 2011) and model results from the base model. 89

Figure 3-45. The concentration profile of sulfate at 1930 days (Zheng et al., 2011) and model results from the base model. 90

Figure 3-46. The concentration profile of chloride at 1930 days (Zheng et al., 2011) and model results from the base model and two sensitivity runs with different permeability for granite. 91

Figure 3-47. The concentration profile of chloride at 1930 days (Zheng et al., 2011) and model results from the base model and two sensitivity runs with different chloride initial concentrations. 91

Figure 4-1. Schematic of linking of TOUGH2 and FLAC3D in a coupled TOUGH-FLAC simulation. 99

Figure 4-2. Numerical procedure of a linked TOUGH2 and FLAC3D simulation. 99

Figure 4-3. BBM constitutive model showing the yield surface in q-p-s space. 100

Figure 4-4. (a) Pore size distribution and (b) schematic representation of the two structural levels considered in the dual structure model. Clay particles are represented by the gray lines. 102

Figure 4-5. Schematic setup of HE-E experiment at Mont Terri and photo of micro-tunnel (Garritte, 2012). 103
Figure 4-6. TOUGH-FLAC 3-D model of the Mont Terri HE-E experiment. 104
Figure 4-7. Vertical cross-section through the model grid. 105
Figure 4-8. Steps for modeling the Mont Terri HE-E experiment. 106
Figure 4-9. Calculated evolution of (a) liquid saturation and (b) temperature. 107
Figure 4-10. Calculated evolution of (a) liquid saturation relative humidity and (b) temperature at monitoring points in the granular bentonite (above heater) and bentonite blocks (below heater). 108
Figure 4-11. Comparison of predicted (dashed lines) and measured (solid lines) evolutions of (a) liquid saturation relative humidity and (b) temperature. 108
Figure 4-12. Comparison of predicted (dashed lines) and measured (solid lines) evolutions of pore pressure in Opalinus Clay at a point located 3.54 m from the tunnel wall. 109
Figure 4-13. Layout of the Horonobe URL in Hokkaido, Japan. 110
Figure 4-14. General description of the EBS experiment at the Horonobe URL Project in Japan. 111
Figure 4-15. Early time monitored fluid pressure in the test pit and temperature evolution at the heater surface that will help to define boundary conditions in the interpretive modeling of the Horonobe EBS experiment. 112
Figure 4-16. TOUGH-FLAC 3-D numerical grid of the Horonobe EBS experiment. 114
Figure 4-17. TOUGH-FLAC simulation results of temperature in the buffer and rock. 116
Figure 4-18. TOUGH-FLAC simulation results of liquid saturation in the buffer, sand layer and rock. 117
Figure 4-19. TOUGH-FLAC simulation results of extensometer displacements in the rock. 117
Figure 4-20. Comparison of simulated temperature profiles at 10 and 365 days among the DECOVALEX modeling teams. 117
Figure 4-21. Comparison of simulated saturation profiles at 10 and 365 days among the DECOVALEX modeling teams. 118
Figure 4-22. Images from the construction and installation of heaters, bentonite buffer and plugs from NAGRA daily reports by Herwig Müller, NAGRA. 119
Figure 4-23. Plan view of experiment setup and borehole layout. 120
Figure 4-24. View of FE tunnel face from the FE niche showing beddings dipping 45° (Vietor, 2012). 122
Figure 4-25. TOUGH-FLAC 3-D numerical grid of the FE experiment. 123
Figure 4-26. Capillary curves for Bentonite and Opalinus clays. 124
Figure 4-27. Model prediction of (a, b) temperature and (c, d) liquid saturation for staged power in first emplaced heater. The results in (a) and (b) and (c) and (d) are the same but using different range on the time axis to highlight the early time behavior (a) and (c) of the first 100 days and longer term response (b) and (d) up to 1000 days. Solid lines refer to evolution at the heater that is turned on, whereas dashed lines refers to evolution at heater that are turned off. 125

Figure 5-1. Discretization process: a) nodal point generation; b) Delaunay tessellation; and c) Voronoi tessellation. 132

Figure 5-2. Typical RBSN element *ij*: a) within a Voronoi grid; b) isolated from the network; and c) a zero-size spring set located at centroid *C* of Voronoi cell boundary area A_{ij}. 133

Figure 5-3. Stress tensor at a Voronoi cell node: a) components of spring force local coordinates; b) a set of nodal forces satisfying the equilibrium; and c) complete stress tensor at Voronoi cell node (Adapted from Yip et al., 2005). 135

Figure 5-4. Mohr-Coulomb fracture surface with tension cut-off. 136

Figure 5-5. Flow diagram of the coupling procedure between TOUGH2 and RBSN (adapted from Asahina et al., 2014). 138

Figure 5-6. Fracture mapping and discretization within an unstructured Voronoi grid. 139

Figure 5-7. Adjustment of nodal connections for flow modeling with discrete fractures: a) original matrix nodes and connections; and b) insertion of fracture nodes and connections. 140

Figure 5-8. Hydraulic fracturing simulation of a single fracture: a) 2-D model set up; and b) comparison between the numerical model and the analytical approximation in terms of fracture aperture profiles 141

Figure 5-9. Modeling of discrete fracture networks: a) geometric topology of fracture networks; and mapping of the fracture pattern onto unstructured Voronoi grids with different mesh density: approximately b) 5000 and c) 10000 Voronoi cells, respectively. 141

Figure 5-10. Simulation results at a final stage of hydraulic fracturing: a) deformed shape; and b) fracture propagation paths overlaid on the pre-existing fracture network. 142

Figure 5-11. Pressure distributions captured at: a) at the point of fracture initiation; b) at the early stage; c) at the latter stage; and d) at the final stage of fracture propagation 143

Figure 5-12. Evolutions of injected fluid pressure for different compressibility coefficients of the borehole region. 144

Figure 5-13. Abnormal break-up of the domain due to numerical instability: a) final time step as a meaningful result; and b) abrupt fracture generation at the next time step. 145

Figure 5-14. Free-body diagram of a Voronoi cell: a) with external nodal forces; and b) with internal spring forces. 146

Figure 5-15. Conceptual drawing of mass-spring system. 148

Figure 5-16. Propagation of a disturbance in the mass-spring system: a) no damping except for mass 1; and b) damping for masses 11 through 20 and mass 1. 151

Figure 5-17**.** Comparison of damping with no damping of masses 11 through 20. Black lines for damped case, red lines for undamped case (except mass 1 which is damped in both cases). 152

TABLES

Table 2-1. Mineral volume fraction (dimensionless, ratio of the volume for a mineral to the total volume of medium) of the Kunigel-VI bentonite (Ochs et al., 2004), FEBEX bentonite (ENRESA, 2000; Fernández et al., 2004; Ramírez et al., 2002) and Opalinus Clay (Bossart 2011; Lauber et al., 2000). 10

Table 2-2. Pore-water composition (mol/kg water, except pH) of Kunigel-VI bentonite (Sonnenthal et al., 2008), FEBEX bentonite (Fernández et al., 2001) and Opalinus Clay (Fernández et al., 2007). 10

Table 2-3. Thermal and hydrodynamic parameters. 11

Table 2-4. Kinetic properties for minerals considered in the model (Xu et al., 2006)..... 12

Table 2-5. The geochemically induced swelling stress for Kunigel and FEBEX bentonite at points A and B for "high T" scenario. Stress reduction by ion concentration is the difference between the swelling stress obtained with "σ=f(Sl)" and "σ=f(Sl,C)", and the stress reduction by smectite dissolution is the difference between the swelling stress obtained with "σ=f(Sl,C)" and "σ=f(Sl,C,Ms)" (see Figure 2-26), where the relative amount (%) use the results from "σ=f(Sl)" as the basis. 44

Table 3-1. Thermal and hydrodynamic parameters. 61

Table 3-2. Mass fraction of minerals for FEBEX bentonite from different publications (%) 62

Table 3-3. Mineral volume fraction (dimensionless, ratio of the volume for a mineral to the total volume of medium) FEBEX bentonite (ENRESA, 2000; Fernández et al., 2004; Ramírez et al., 2002) and granite (Zheng et al., 2011). 62

Table 3-4. Pore-water composition (mol/kg water except for pH) of FEBEX bentonite (Fernández et al., 2001) and granite (Zheng et al., 2011)..... 63

Table 3-5. Aqueous complexes and their dissociation constants 63

Table 3-6. Surface protonation reactions on montmorillonite (Bradbury and Baeyens, 2005) 64

Table 3-7. Cation exchange reactions on montmorillonite and illite (Bradbury and Baeyens, 2005) 64

Table 3-8. Equilibrium constants for mineral precipitation/dissolution 64

Table 3-9. Kinetic properties for minerals considered in the model (Xu et al., 2006)..... 65

Table 4-1. Parameters used in the modeling of the Mont Terri HE-E experiment. 105

Table 4-2. Details on the sequence of construction and installation of the Horonobe EBS experiment 111

Table 4-3. DECOVALEX research teams and numerical simulators in modeling Horonobe EBS experiment 113

Table 4-4. Material parameters for modeling Horonobe EBS experiment. 115

Table 4-5. Parameters for the Opalinus and Bentonite clay used in the modeling of the FE experiment. 124

ACRONYMS

BBM	Barcelona Basic Model
BExM	Barcelona Expansive Model
DFN	Discrete Fracture Network
DMS	Document Management System
DOE	Department of Energy
DRZ	Disturbed Rock Zone
EBS	Engineered Barrier System
EBS-NS	Engineered Barrier System-Natural System
EDZ	Excavation Damaged Zone
FE	Full-Scale Emplacement Experiment
FEBEX	Full-Scale Engineered Barrier Experiment
FEBEX-DP	Full-Scale Engineered Barrier Experiment-Dismantling Project
FEPs	Features, Events and Processes
HLW	High-Level Radioactive Waste
HPLC	High Pressure Liquid Chromatograph
JAEA	Japan Atomic Energy Agency
LBNL	Lawrence Berkeley National Laboratory
NBS	Natural Barrier System
PWR	Pressurized Water Reactor
R&D	Research and Development
RBSN	Rigid Body Spring Network
TH	Thermal and Hydrogeological
THC	Thermo-Hydro-Chemical
THMC	Thermal-Hydrological-Mechanical-Chemical
TPHM	Two-Parts Hooke's Model
UFD	Used Fuel Disposition
UFDC	Used Fuel Disposition Campaign

1. INTRODUCTION

Shale and clay-rich geological formations have been considered as potential host rock for geological disposal of high-level radioactive waste throughout the world, because of their low permeability, low diffusion coefficient, high retention capacity for radionuclides, and capability to self-seal fractures. The low permeability of clay and shale rock are well-known in the hydrogeology community where these rock types represent aquitards that severely limit groundwater movement, and in petroleum geology, where they act as caprocks limiting the rise of buoyant petroleum fluids. While fractures can occur, clay and shale often demonstrate the tendency to self-seal fractures, which reduces the effects of fractures on bulk permeability. Other favorable characteristics of clay/shale rock are the strong sorptive behavior for many radionuclides, reducing conditions because of the lack of oxygen transport from the surface, and chemical buffering of introduced materials.

A large body of information concerning the behavior of clay/shale geologic environments using bentonite backfill/buffers for nuclear waste disposal has been developed through the repository programs with underground research laboratories in Switzerland, France, Belgium, and Japan. In this report, we document modeling of tests conducted at Switzerland's Mont Terri underground rock laboratory and the Horonobe underground research laboratory in Japan.

The focus of research within the UFD Campaign is on repository-induced interactions that may affect the key safety characteristics of an argillaceous rock. These include thermal-hydrological-mechanical-chemical (THMC) process interactions that occur as a result of repository construction and waste emplacement. Some of the key questions addressed in this report include the development of fracturing in the excavation damaged zone (EDZ) and THMC effects on the near-field argillaceous rock and buffer minerals and petrophysical characteristics, particularly the impacts of induced temperature rise caused by waste heat.

Within the Natural Barrier System (NBS) group of the Used Fuel Disposition (UFD) Campaign at the Department of Energy's (DOE) Office of Nuclear Energy, LBNL's research activities have focused on understanding and modeling EDZ evolution and the associated coupled processes, and impacts of high temperature on parameters and processes relevant to performance of a clay repository to establish the technical base for the maximum allowable temperature. This report documents results from some of these activities. These activities address key Features, Events and Processes (FEPs), which have been ranked in importance from medium to high, as listed in Table 7 of the *Used Fuel Disposition Campaign Disposal Research and Development Roadmap* (FCR&D-USED-2011-000065 REV0) (Nutt, 2011). Specifically, they address FEP 2.2.01, Excavation Disturbed Zone, for clay/shale, by investigating how coupled processes affect EDZ evolution; FEP 2.2.05, Flow and Transport Pathways; and FEP 2.2.08, Hydrologic Processes, and FEP 2.2.07, Mechanical Processes and FEP 2.2.09, Chemical Process—Transport, by studying near-field coupled THMC processes in clay/shale repositories. The activities documented in this report also address a number of research topics identified in *Research & Development (R&D) Plan for Used Fuel Disposition Campaign (UFDC) Natural System Evaluation and Tool Development* (Wang, 2011), including Topics S3, Disposal system modeling – Natural system; P1, Development of discrete fracture network (DFN) model; P14, Technical basis for thermal loading limits; and P15 Modeling of disturbed rock zone (DRZ) evolution (clay repository).

This report documents the following research activities:

- Chapter 2 presents the development and application of thermal-hydrological-mechanical-chemical (THMC) modeling capabilities to assess engineering-barrier-system (EBS) responses to different temperatures and pressures, and to evaluate impacts of the interaction between EBS and host rocks. Model results are presented that help to understand the impact of high temperatures on the properties and behavior of clay.
- Chapter 3 presents a pre-test modeling exercise for the FEBEX-DP dismantling experiment. This has been done using THMC predictive modeling of the FEBEX EBS response after almost two decades of heating, prior to the actual dismantling.
- Chapter 4 presents THM modeling for the FE heater tests at Mont Terri, Switzerland. THM modeling of the FE Heater test was performed using TOUGH-FLAC simulator. The Full-Scale Emplacement Experiment (FE) at the Mont Terri site, Switzerland is one of the largest and longest-duration heater tests worldwide. The analyses have been used to calibrate clay properties by modeling lab tests and through model-result comparisons with other teams. THM modeling is also presented for the HE-E heater test at Mont Terri and the Horonobe EBS experiment as part of the DECOVALEX tasks for this year. Modeling of the Mont Terri HE-E Experiment and the EBS Horonobe experiment are compared with results from international modeling teams.
- Chapter 5 presents the development of a THM fracture damage model for investigating coupled processes in the EDZ. Simulations of fracturing for a laboratory experiment on hydraulic fracturing are presented. Issues concerning the effects of boundary conditions and computational efficiency are identified along with the potential resolution of these issues through the development of a dynamic discrete fracture damage model.
- Chapter 6 summarizes the main research accomplishments for FY 2015 and proposes future work activities.

This report is milestone M3FT-15LB0806032, and it incorporates milestones M3FT-15LB0806042, and M3FT-15LB0806052; the latter two milestones were planned as input to M3FT-15LB0806032.

2. INVESTIGATION OF THE IMPACTS OF HIGH TEMPERATURE LIMITS WITH THMC MODELING

2.1 Introduction

Radioactive waste from spent fuel emanates a significant amount of thermal energy due to decay processes, which causes temperature increases in the surrounding environment particularly in the early stages of waste emplacement. The temperature to which the EBS (engineered barrier system) and natural rock can be exposed is one of the most important design variables for a geological repository, because it determines waste package spacing, distance between disposal galleries, and therefore the overall size (and cost) of repository for a given amount of heat-emanating waste (Horseman and McEwen, 1996). This is especially important for a clay repository, because argillaceous rocks have relatively small heat conductivity. All disposal concepts throughout the world, despite their differences in design concepts, unanimously impose a temperature limit of about 100 ^{o}C (Hicks et al., 2009). Chemical alteration and the subsequent changes in mechanical properties are among the determining factors. A high temperature could result in chemical alteration of buffer and backfill materials (bentonite) within the EBS through illitization and cementation, which compromise the function of these EBS components by reducing their plasticity and capability to swell when wetting (Pusch and Karnland, 1996; Pusch et al., 2010; Wersin et al., 2007). The swelling capability of clay minerals within the bentonite is important for sealing gaps between bentonite blocks, between bentonite and other EBS components, and between the EBS and the surrounding host rock. Chemical alteration may also occur in the near-field host rock, which could reduce the clay capability for self-sealing within the excavation damaged zone (EDZ). Because the permeability of clay rock is low, a high temperature may induce significant pore pressure build-up (through pore water expansion and vaporization) in the near field, which could generate adverse mechanical deformation (such as fracturing), damaging the integrity of the host rock (Horseman and McEwen, 1996).

Regarding the concern of chemical alteration and the associated mechanical changes, Wersin et al. (2007), after reviewing a number of data sets, concluded that the criterion of 100^{o}C for the maximum temperature within the bentonite buffer is overly conservative. Their conclusion was based on their findings that no significant changes in bentonite hydraulic properties occur at temperatures of up to 120^{o}C under wet conditions and that bentonite is chemically stable to much higher temperature under dry conditions. The impact of a high temperature on bentonite and clay host rock behavior, and the consequences on repository performance, are largely open questions for a clay repository system. While various studies shed light on certain aspects of this question, there is no study that integrates the relevant THMC processes and considers the interaction between EBS and host rock.

Since FY13, in UFDC, LBNL has used coupled THMC modeling to evaluate the chemical alteration and mechanical changes in EBS bentonite and the NS (natural system) clay formation under various scenarios, attempting to provide necessary information for decisions on temperature limits. In the FY13 report (Liu et al., 2013), after an extensive review of the THMC alteration of EBS and argillite under various temperature conditions, fully coupled THMC simulations were developed for a nuclear waste repository in a clay formation with a bentonite-backfilled EBS. Two scenarios were simulated for comparison: a case in which the temperature in the bentonite near the waste canister can reach about 200^{o}C and a case in which the

temperature in the bentonite near the waste canister peaks at about 100°C. In these simulations, it was assumed that the EBS bentonite was Kunigel-VI bentonite (Ochs et al., 2004) and that the host rock properties were representative of Opalinus Clay (Bossart 2011; Lauber et al., 2000). Simulations showed that the decrease in smectite volume fraction in bentonite ranges from 0.004 to a maximum of 0.085, or up to about 27% of the initial volume fraction of smectite for the 200 °C scenario in 1,000 years. This decrease in smectite volume fraction led to a reduction in swelling stress ranging from 16-27%, subject to a great deal of variation depending on smectite volume fraction and swelling pressure under different chemical conditions. In FY14, we continued to analyze more scenarios based on Kunigel-VI bentonite, including sensitivity analyses to key mechanical-chemical coupling parameters. In addition, THMC models were developed for FEBEX (ENRESA, 2000) bentonite, which differs from Kunigel-VI bentonite in terms of the content of smectite and swelling pressure. By comparing the model results for Kunigel-VI and FEBEX bentonite, we found out the illitization is enhanced at high temperature for both bentonites. However, the magnitude of illitization varies a great deal and has to be evaluated case by case. During FY15, we continued to improve our modeling capability and refine the model so that we can better understand coupled processes in bentonite and a clay formation. One of the major achievements is the implementation of a time-step management scheme in the TOUGHREACT-FLAC3D simulator, which reduces simulation time and enables us to extend the simulations from 1,000 years to 100,000 years. The simulator was also modified to include chemical-mechanical coupling for a clay formation. We also performed an evaluation of Ca-smectite illitization (in FY13 and FY14, we evaluated Na-smectite illitization), which sheds light on the potential for calcite to interfere with smectite illitization.

2.2 Model Development

Because the model used in this report is similar to that in previous years (Liu et al., 2013; Zheng et al., 2014), we briefly describe each element of the THMC model here, focusing on the updates in FY15. Additional details on the THMC model are presented in Liu et al.(2013).

2.2.1 Simulator

The numerical simulations are conducted with TOUGHREACT-FLAC3D, which sequentially couples the multiphase fluid flow and reactive transport simulator, TOUGHREACT (Xu et al., 2011), with the finite-difference geomechanical code FLAC3D (Itasca, 2009). The coupling of TOUGHREACT and FLAC3D was initially developed in Zheng et al. (2011) to provide the necessary numerical framework for modeling fully coupled THMC processes. It included a linear elastic swelling model (Zheng et al., 2012; Rutqvist et al., 2013) to account for swelling as a result of changes in saturation and pore-water composition and the abundance of swelling clay (Liu et al., 2013; Zheng et al., 2014). The major improvement in TOUGHREACT-FLAC3D is the implementation of a time-step management scheme to reduce the simulation time. Figure 2-1 shows the coupling scheme of TOUGHREACT-FLAC3D. In each time step, TOUGHREACT calculates the primary variables for THC processes including temperature (T), liquid pressure (P_l) or gas pressure (P_g), water saturation (S_l), ion concentrations of pore water (C_i) and concentration of exchangeable cations and/or abundance of swelling clay minerals (X_i). These primary variables are then passed to FLAC3D via a coupling module to conduct stress and strain analysis (see Figure 2-1). The coupling between THC processes (provided by TOUGHREACT) and the mechanical part (FLAC3D) is carried out at every time step. The FLAC3D stress and

strain analysis consumes a large portion of the total computation time. For example, in the base case for FEBEX bentonite described below, a THC run took about 4.5 hours but the THMC runs (which calls FLAC3D at every time step) took about 4 days. The length of time step is constrained by the chemical calculation to accommodate small changes in the concentrations. However, such small changes in chemical conditions lead to very minimal changes in stress and it is unnecessary to update the stress every time step. Therefore, a time step management scheme was implemented in TOUGHREACT-FLAC3D. A subroutine was inserted in TOUGHREACT to check the change of primary variables from the previous time step and decide if the change is large enough to warrant an update in stress/strain based on the predetermined criteria. The choice of criteria is arbitrary. We tested several values and a criterion of 2% reduces computation time significantly and the calculated stress is very close (within 0.1% difference) to that obtained by updating stress/strain every time step.

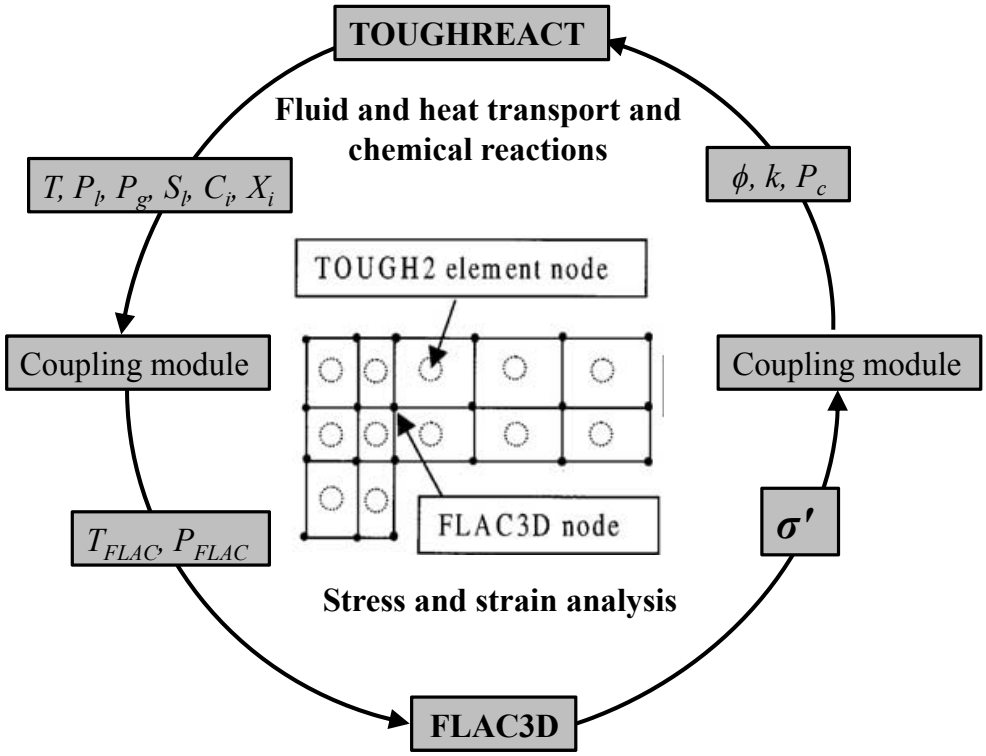

Figure 2-1. The coupling scheme for TOUGHREACT-FLAC3D.

2.2.2 Modeling scenario

The model scenario is still the same as in Liu et al. (2013) and Zheng et al., (2014). The model is applied to a hypothetical bentonite-backfilled nuclear waste repository in clay rock, a repository example that involves a horizontal nuclear waste emplacement tunnel at 500 m depth (Figure 2-2) (Rutqvist et al., 2013). The Z-axis is set as vertical, while the horizontal Y- and X-axes are aligned parallel and perpendicular to the emplacement tunnel, respectively (Figure 2-2) in this 2-D model. Note that while the canister is modeled as a heat source with mechanical properties of

steel, the THC changes in the canister and their interactions with EBS bentonite are not considered here for the sake of simplicity.

An initial stress field is imposed by the self-weight of the rock mass. Zero normal displacements are prescribed on the lateral boundaries of the model. Zero stress is applied to the top and vertical displacements are prevented at the bottom. An open boundary is applied to the liquid pressure at top and bottom and initially the model domain is in a hydrostatic state. The initial temperature at the top is about 11 ^{o}C, with a thermal gradient of 27 ^{o}C/km, the initial temperature at the bottom is 38 ^{o}C. The model simulation was conducted in a nonisothermal mode with a time-dependent heat power input (Rutqvist et al., 2014). The power curve in Figure 2-2 was adopted from representative heating data from the U.S. DOE's Used Fuel Disposition campaign for pressurized water reactor (PWR) used fuel. This heat load is then scaled in the 2-D model to represent an equivalent line load, which depends on the assumed spacing between individual waste packages along an emplacement tunnel. The heat load for the "low-T" case corresponds to an initial thermal power of 3144 W for a 4-PWR-element waste package after aging for 60 years, a 50-m spacing between emplacement tunnels, and 3-m spacing between the 5-m long packages. The heat load for the "high T" case represents similar waste package and spacing, except with only 20 years of aging. Initially the EBS bentonite has a water saturation of 65% and the clay formation is fully saturated. From time zero, the EBS bentonite undergoes simultaneously re-saturation, heating, chemical alteration, and stress changes.

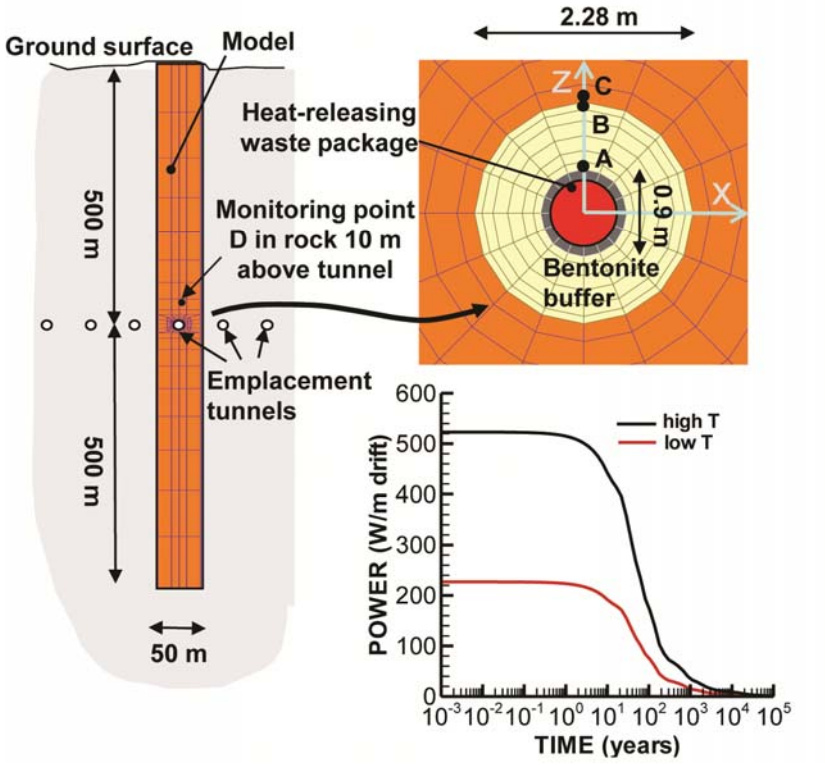

Figure 2-2. Domain for the test example of a bentonite back-filled horizontal emplacement drift at 500 m (Rutqvist et al., 2014). Modeling monitoring points: A: inside the bentonite near the canister, B: inside the bentonite and near the EBS-NS interface, C: inside the clay rock formation

and near the EBS-NS interface, D: inside the clay rock formation at a distance of 10 m from the canister. “High T”: 200 ºC; “Low T”: 100ºC.

2.2.3 Mechanical Model

Details of mechanical model implemented in the TOUGHREACT-FLAC3D are given in Rutqvist et al., (2014). Here we briefly describe the mechanical models for the EBS bentonite and clay formation. For nonisothermal behavior of unsaturated soils, we may partition the total incremental strain into elastic (ε^e), plastic(ε^p), suction(ε^s), thermal strains (ε^T)and chemical strains(ε^c):

$$d\varepsilon = d\varepsilon^e + d\varepsilon^p + d\varepsilon^s + d\varepsilon^T + d\varepsilon^c \tag{2-1}$$

where the suction strain represents the strain associated with changes in suction and chemical strain represents the strains associated with change in chemical conditions, including changes in ion concentration and abundance of swelling clays. Each of these types of strain, except chemical strain, is described in Rutqvist et al., (2014).

Similar to thermally induced strains, chemical strains are purely volumetric:

$$d\varepsilon^c = -A_n^* \, dC + A_{sc}^* dMs \tag{2-2}$$

where A_n^* is a constant that linearly relates ion concentration (C) variation and the corresponding strain change. A_{sc}^* is a constant that relates the change in mass fraction of swelling clay, m_s, to change in strain.

A linear elastic swelling model essentially defines the suction stress as a function of water saturation:

$$d\varepsilon^s = \beta_{sw} dSl \tag{2-3}$$

where Sl is the water saturation and β_{sw} is a moisture swelling coefficient.

Under mechanically constrained conditions and considering the linear relationship between swelling stress and suction strain, $d\sigma_s = 3Kd\varepsilon^s$, we have a swelling stress that is linearly proportional to the saturation:

$$d\sigma_s = 3K\beta_{sw} dSl \tag{2-4}$$

where K is the bulk modulus. Equation (2-4) is what was used for EBS bentonite in Rutqvist et al. (2011). In this report, β_{sw} is 0.048, calibrated based using the swelling pressure of 1 MPa for

Kunigel-VI bentonite (Börgesson et al. 2001) under the condition that bentonite is saturated with dilute solution (e.g. deionized water), and K is 20 MPa (Rutqvist et al., 2011).

To consider the swelling due to both moisture and chemical changes, we include the stress due to a change of ion concentration in the pore water and abundance of swelling clay:

$$d\sigma_s = 3K(d\varepsilon^s + d\varepsilon^c) = 3K(\beta_{sw}dSl + A_n^* dC + A_{sc}^* dMs) = 3K\beta_{sw}dSl + A_n dC + A_{sc}dMs \quad (2\text{-}5)$$

where $A_n = 3KA_n^*$ is a constant that linearly relates ion concentration (C) variation and the corresponding swelling stress change. $A_{sc} = 3KA_{sc}^*$ is a constant that relates the change in mass fraction of swelling clay, *Ms*, to change in swelling stress.

A_n is typically calculated from swelling pressures measured using a different solution (e.g. deionized water versus 1 M NaCl solution) to saturate the bentonite. Laredj et al. (2010) proposed the following expression for A_n:

$$A_n = \frac{(5.312\ln C - 23.596)}{\sqrt{C}} - \frac{7.252\times10^{-4}}{C^2} \quad (2\text{-}6)$$

An empirical value for A_{sc} is derived through a linear regression of swelling pressure versus smectite mass fractions as shown in Figure 2-3, and A_{sc} is the slope of the linear correlation. However, probably because these bentonite materials differ not only in the mass fraction of smectite but also in other properties, these data points are fairly scattered. This makes it impossible to establish a unique linear regression between swelling pressure change and mass fraction change of smectite. Therefore, we chose a linear correlation line that crosses the measured swelling pressure for Kunigel VI bentonite and used the slope of this line as the value of A_{sc} which is 2.5×10^6 Pa. For FEBEX bentonite we used the slope of line that crosses the measured swelling pressure of FEBEX bentonite as the value of A_{sc} which is 6.5×10^6 Pa.

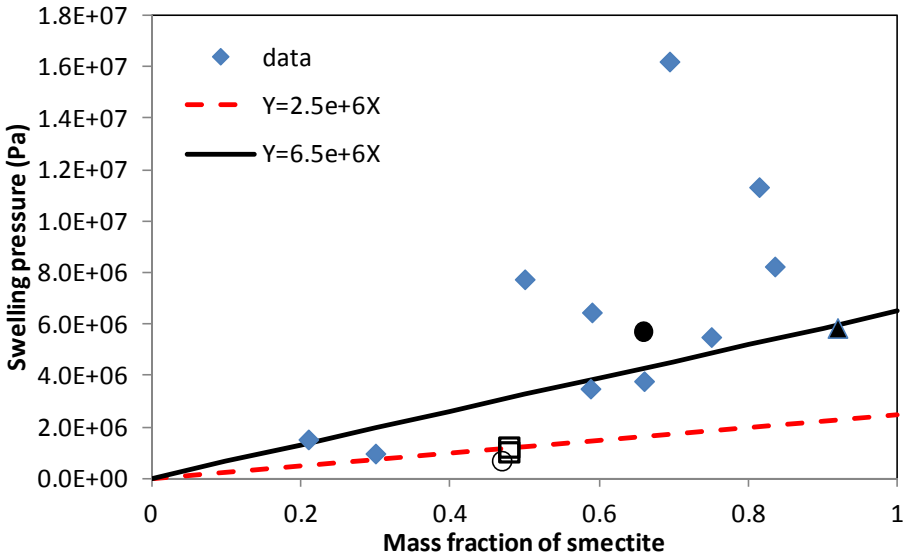

Figure 2-3. Swelling pressure versus mass fraction of smectite for various bentonites. ▲, FEBEX bentonite (ENRESA, 2000); ●, Montigel bentonite (Bucher and Muller-Vonmoos, 1989); □, Kunigel VI bentonite (JNC, 1999); ○, Kunigel bentonite (Komine and Ogata, 1996), ♦ are data for reference material from Czech, Danish, Friedland, Milos Deponit CA-N, Kutch (Indian) and Wyoming MX-80 (Karnland et al., 2006).

More sophisticated and realistic mechanical models are available in the literature and have been successfully used for bentonite and clay formations, such as the state surface approach (e.g. Nguyen et al., 2005) and the dual structure Barcelona Expansive Clay model (Alonso et al.,1999; Sánchez et al., 2005). In this report, we use a rather simple elastic model because it allows us to incorporate the contribution from the chemical components and parameters and the model can be relatively easily calibrated as discussed above.

For clay formations, we extend the elastic model used in Rutqvist et al., (2014) to consider the chemical strain as in Equation (2-2). The parameters, A_n and A_{sc} , are same as those used for bentonite, with an assumption that compact bentonite and clay rock behave similarly in terms of the effect of chemical change on strain. However, the validity of this assumption needs to be confirmed with more data.

2.2.4 Chemical Model

In these generic cases, it is assumed that that the host rock properties are representative of Opalinus Clay (Bossart 2011; Lauber et al., 2000). Two cases are used for the EBS backfill: one is Kunigel-VI bentonite (Ochs et al., 2004) and the other is FEBEX bentonite (ENRESA, 2000). The mineral compositions of the bentonite and clay formation are listed in Table 2-1. The pore-water compositions of the Kunigel-VI bentonite (Sonnenthal et al., 2008), FEBEX bentonite (Fernández et al., 2001) and the clay formation (Fernández et al., 2007) are listed in Table 2-2. Table 2-3 lists the thermal and hydrodynamic parameters used in the model. The majority of these parameters are taken from Sonnenthal et al. (2008) for Kunigel-VI bentonite and from Thury (2002) for the EBS bentonite and the NS clay formation. Permeability for the clay formation is from Soler (2001) and bentonite permeability is from JNC (1999).

FEBEX and Kunigel-VI bentonite also have distinct hydrological and thermal parameters, with the most relevant ones being thermal conductivity and permeability. However, in this report, we use the same thermal conductivity and permeability for both bentonites. These parameters are actually fairly similar for the two types of bentonite — thermal conductivity for saturated Kunigel-VI bentonite is 1.5W/m-^{o}C (see Table 2-2) and that for FEBEX bentonite is 1.3 W/m ^{o}C (ENRESA, 2000); permeability for Kunigel-VI bentonite is 2E-21 m^2 and that for FEBEX ranges from 1E-21 to 3.75E-21 m^2 (ENRESA, 2000; Zheng et al., 2011; Chen et al. 2009). Moreover, by using the same values of thermal conductivity and permeability for both bentonites, we can isolate the effect of variations in chemical and CM coupling parameters on the stress changes.

Table 2-1. Mineral volume fraction (dimensionless, ratio of the volume for a mineral to the total volume of medium) of the Kunigel-VI bentonite (Ochs et al., 2004), FEBEX bentonite (ENRESA, 2000; Fernández et al., 2004; Ramírez et al., 2002) and Opalinus Clay (Bossart 2011; Lauber et al., 2000).

Mineral	**EBS Bentonite: Kunigel-VI**	**EBS Bentonite: FEBEX**	**Clay formation: Opalinus Clay**
Calcite	0.016	0.0065	0.093
Dolomite	0.018	0.0	0.050
Illite	0.000	0.0	0.273
Kaolinite	0.000	0.0	0.186
Smectite	0.314	0.6	0.035
Chlorite	0.000	0.0	0.076
Quartz	0.228	0.026	0.111
K-Feldspar	0.029	0.0065	0.015
Siderite	0.000	0.0	0.020
Ankerite	0.000	0.0	0.045

Table 2-2. Pore-water composition (mol/kg water, except pH) of Kunigel-VI bentonite (Sonnenthal et al., 2008), FEBEX bentonite (Fernández et al., 2001) and Opalinus Clay (Fernández et al., 2007).

	EBS Bentonite: Kunigel-VI	**EBS Bentonite: FEBEX**	**Clay formation: Opalinus Clay**
pH	8.40	7.72	7.40
Cl	1.50E-05	1.60E-01	3.32E-01
SO_4^{-2}	1.10E-04	3.20E-02	1.86E-02
HCO_3^-	3.49E-03	4.1E-04	5.18E-03
Ca^{+2}	1.37E-04	2.2E-02	2.26E-02
Mg^{+2}	1.77E-05	2.3E-02	2.09E-02
Na^+	3.60E-03	1.3E-01	2.76E-01
K^+	6.14E-05	1.7E-03	2.16E-03
Fe^{+2}	2.06E-08	2.06E-08	3.46E-06
$SiO_2(aq)$	3.38E-04	1.1E-04	1.10E-04
AlO_2^-	1.91E-09	1.91E-09	3.89E-08

Table 2-3. Thermal and hydrodynamic parameters.

Parameter	**Clay formation : Opalinus Clay**	**EBS Bentonite**
Grain density [kg/m^3]	2700	2700
Porosity ϕ	0.162	0.33
Saturated permeability [m^2]	2.0×10^{-20}	2.0×10^{-21}
Relative permeability, k_{rl}	$m = 0.6$, $S_{rl} = 0.01$	$K_{rl} = S^3$
Van Genuchten α [1/Pa]	6.8×10^{-7}	3.3×10^{-8}
Van Genuchten m	0.6	0.3
Compressibility, β [1/Pa]	3.2×10^{-9}	5.0×10^{-8}
Thermal expansion coeff., [1/^{o}C]	1.0×10^{-5}	1.5×10^{-4}
Dry specific heat, [J/kg-^{o}C]	860	800
Thermal conductivity [W/m-^{o}C] dry/wet	1.48/1.7[$]	1.1/1.5
Tortuosity for vapor phase	$\phi^{1/3} S_g^{10/3}$	$\phi^{1/3} S_g^{10/3}$
Bulk modulus, (GPa)	4.17	0.02
Shear modulus, (GPa)	1.92	0.0067

From http://www.mont-terri.ch/internet/mont-terri/en/home/geology/key_characteristics.html

Mineral dissolution/precipitation is kinetically controlled. The kinetic law for mineral dissolution/precipitation is given in Xu et al. (2011):

$$r = kA\left|\left(1-(\frac{\mathrm{K}}{\mathrm{Q}})^{\theta}\right)\right|^{\eta} \tag{2-7}$$

where r is the kinetic rate, k is the temperature-dependent rate constant (mol/m^2-s), A is the reactive surface area per kg water, K is the equilibrium constant for the mineral–water reaction (written for the destruction of one mole of mineral), and Q is the reaction quotient. Here, for simplicity, the exponents θ and η are assumed equal to 1.

The kinetic rate constants can usually be summed for three mechanisms (Lasaga et al., 1994):

$$k = k_{25}^{nu}\exp\left[\frac{-E_a^{nu}}{R}\left(\frac{1}{T}-\frac{1}{298.15}\right)\right] + k_{25}^{H}\exp\left[\frac{-E_a^{H}}{R}\left(\frac{1}{T}-\frac{1}{298.15}\right)\right]a_H^{n_H} + k_{25}^{OH}\exp\left[\frac{-E_a^{OH}}{R}\left(\frac{1}{T}-\frac{1}{298.15}\right)\right]a_{OH}^{n_{OH}} \tag{2-8}$$

where superscripts *nu*, *H* and *OH* indicate neutral, acid, and alkaline mechanisms, respectively, E is the activation energy, k_{25} is the rate constant at 25 °C, R is the gas constant, T is the absolute temperature, α is the activity of the species, and n is a power term (constant). It should be noted that reaction rates depend on the reactive surface area A in Equation (2-7), which is a function of

the product of the specific surface area and the volume fraction of each mineral. Therefore, the calibrated values of specific surface area and volume fraction should be viewed as arbitrary and non-unique (co-linearly varying) values, the product of which is relevant but not each value separately.

The kinetic rates and surface areas for the minerals considered in the model were taken mostly from Xu et al. (2006) (Table 2-4). However, the illitization rate (the rate of illite precipitation and smectite dissolution) was calibrated (Liu et al., 2013) based on the measured illite percentage in an illite/smectite (I/S) mixed layer from Kinnekulle bentonite, Sweden (Pusch and Madsen, 1995). The thermodynamic data were taken from the Data0.dat.YMPv4.0, an EQ3/6 (Wolery, 1993) database qualified by the U.S. Department of Energy for the Yucca Mountain project.

Table 2-4. Kinetic properties for minerals considered in the model (Xu et al., 2006).

Mineral	A (cm^2/g)	Parameters for Kinetic Rate Law							
		Neutral Mechanism		Acid Mechanism			Base Mechanism		
		k_{25} ($mol/m^2/s$)	E_a (kJ/mol)	k_{25} ($mol/m^2/s$)	E_a (kJ/mol)	$n(H^+)$	k_{25} ($mol/m^2/s$)	E_a (kJ/mol)	$n(H^+)$
Quartz	9.8	1.023×10^{-14}	87.7						
K-feldspar	9.8	3.89×10^{-13}	38	8.71×10^{-11}	51.7	0.5	6.31×10^{-12}	94.1	-0.823
Kaolinite	151.6	6.91×10^{-14}	22.2	4.89×10^{-12}	65.9	0.777	8.91×10^{-18}	17.9	-0.472
Illite	1.18×10^4 (1)	1.66×10^{-13}	105 (2)						
Chlorite	9.8	3.02×10^{-13}	88	7.76×10^{-12}	88	0.5			
Calcite	3.5	1.63×10^{-7}	23.5						
Dolomite	12.9	2.52×10^{-12}	62.76	2.34×10^{-7}	43.54	1			
Ankerite	9.8	1.26×10^{-9}	62.76	6.46×10^{-4}	36.1	0.5			
Smectite	1.18×10^4 (1)	1.66×10^{-13}	105 (2)						

(1) calibrated based on the field illitization data (Liu et al., 2013)
(2) from Pusch and Madsen (1995)

2.3 Model Results

In Liu et al. (2013) and Zheng et al. (2014), the model results for first 1000 years, expressed as the evolution of temperature, pore pressure, water saturation, concentration and stress, were discussed in detail and a sensitivity analyses to key chemical and mechanical parameters were conducted to understand the coupling processes. The simulations were only conducted for a period of 1,000 years because the older version of TOUGHRACT-FLAC3D was not fast enough for longer simulation time periods and because it is assumed that coupled process effects are most pronounced in the first 1,000 years. One of the general observations based on these simulations is that illitization is enhanced at higher temperature, although the amount of illitization depends on chemical and hydrological conditions and varies a great deal. These results lead to questions about illitization at longer times (i.e., 100,000 years). For example, does illitization continue at the same rate or does it stabilize at long times and how does illitization effect stress at long times? In this report, we have been able to address these questions with the

improved version of TOUGHRACT-FLAC3D, which can carry out simulations to 100,000 years.

2.3.1 Cases for Kunigel-VI Bentonite

In the generic cases we used to study the effect of high temperature on the THMC evolution in bentonite and clay formation, two bentonites have been simulated: Kunigel-VI and FEBEX bentonite. In this section, model results for Kunigel-VI bentonite are presented. We first briefly discuss the changes in temperature, water saturation and the volume fraction of smectite because their changes essentially determine the evolution of stress; then the changes in stress are discussed.

2.3.1.1 THC Evolution

The evolution of heat release from decaying waste is shown in Figure 2-2. The heat release rates have been adjusted to make two cases for comparison: a "high T" case, in which the temperature near the canister can reach 200 °C; and a "low T" case, in which the temperature near the canister peaks at about 100 °C. In this report, the temporal evolution at the four monitoring points (shown in Figure 2-2) is used to present thermal, hydrological, chemical and mechanical results: point A is inside the bentonite near the canister, point B is inside the bentonite near the EBS-NS interface, point C is inside the clay formation near the EBS-NS interface, and point D is inside the clay formation at a distance of 10 m from the canister. The temperature evolution at the four monitoring points A, B, C, and D is shown in Figure 2-4. After 100,000 years, as expected from the heat release function shown in Figure 2-2, the temperature drops to about 27 ^{o}C. The clay formation near the EBS-NS interface goes through desaturation (Figure 2-5), which interestingly lasts much longer for the "low T" case than the "high T" case. Desaturation in the clay formation occurs because the host rock is not able to replenish water as fast as it is being imbibed by the EBS bentonite. For the "high T" case, the hydration of bentonite is slower because the high temperature leads to stronger outward vapor flow and higher pore pressure in the EBS bentonite, which gives the host rock more time to replenish the water lost to EBS bentonite and the outward vapor flow hydrates the outer portion of the bentonite. As a result, the clay formation saturation near the EBS-NS interface does not decrease as much for the "high T" case as for the "low T" case. Pore pressure increases as a result of re-saturation and heating. The "high T" case exhibits much higher pore pressure than the "low T", with a difference of about 5 MPa after 1,000 years (Figure 2-6), but by the end of 100,000 years, the difference is fairly small.

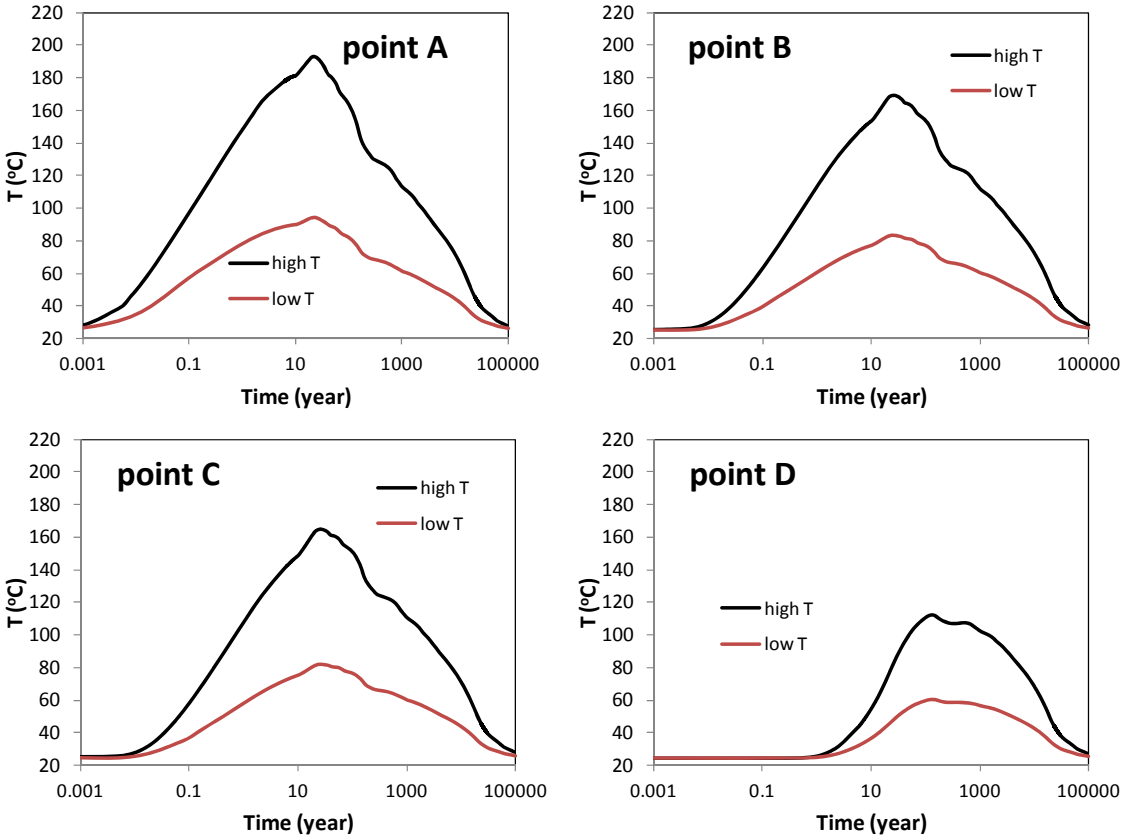

Figure 2-4. Temperature evolution at points A, B, C, and D.

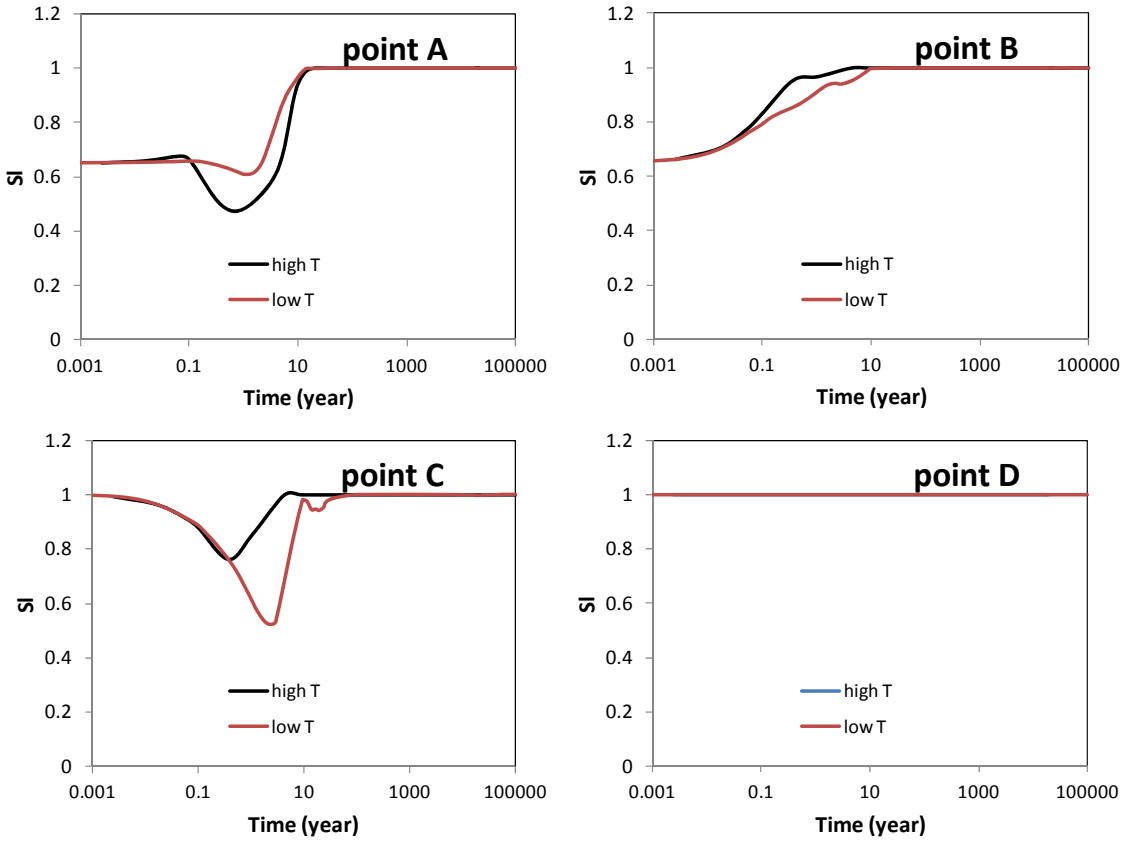

Figure 2-5. The temporal evolution of water saturation at points A, B, C, and D.

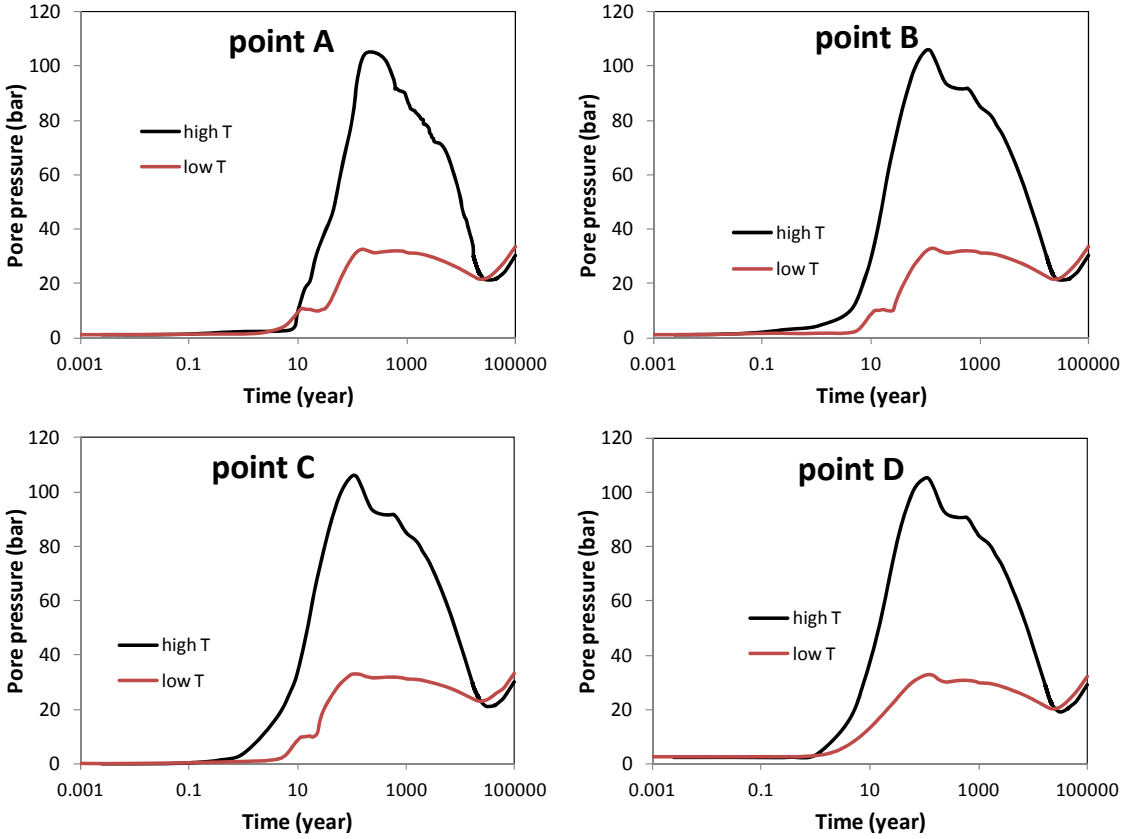

Figure 2-6. The temporal evolution of pore pressure at points A, B, C, and D.

In the base case, illitization is modeled as the dissolution of Na-smectite and precipitation of illite. The overall reaction can be written as:

$$\text{Na-smectite} + 0.52H^{+} + 0.63AlO_2^{-} + 0.6K \Leftrightarrow \text{illite} + 0.26H_2O + 0.08Mg^{+2} + 0.33Na^{+} + 0.5SiO_2(aq) \quad (2\text{-}9)$$

Other chemical parameters in the base case, such as reaction rate for Na-smectite and illite, K-feldspar, water compositions in bentonite and the clay formation, are presented in Section 2.2.4. As revealed from Liu et al., (2013) and Zheng et al., (2014), many factors can affect the chemical reactions such as the initial water-mineral disequilibrium in bentonite (since the water used for making bentonite blocks is not necessarily in equilibrium with the mineral phase in bentonite, and it takes time to reach that equilibrium), as well as the thermal and hydrological disturbances in response to emplacement.

Smectite volume fraction changes at points A through D are shown in Figures 2-7 (log time scale) and 2-9 (linear time scale); illite volume fraction changes are shown in Figures 2-8 (log time scale). Figures 2-7 and 2-8 show that illitization does occur in the EBS bentonite. In addition to temperature effects, illitization is affected by the initial disequilibrium between the pore-water solution and mineral phases. Initially, the pore water in the bentonite buffer is

oversaturated with respect to illite and undersaturated with respect to smectite. In addition, the pore water in the clay formation contains a much higher concentration of K and Al, and thus provides a source of Al and K for the EBS bentonite alteration through diffusion and advection. Note that the increase in Al and K concentrations in bentonite is caused not only by diffusion and advection, but also by the dissolution of other minerals, such as K-feldspar. In fact, as shown in Liu et al., (2013), the dissolution of K-feldspar is the major source of K for illitization, especially in the area that is away from the EBS-NS interface, such as point A. The pore water in the clay formation also has a higher concentration of Mg and Na, which inhibits illitization. But it seems that the factors in favor of illitization outpace those against illitization. After 1,000 years (the simulation time of previous models in Liu et al. (2013)) the smectite volume fraction in the bentonite decreases by 0.035 (or 11%) for the 'high T" case and 0.006 (or 2%) for the "low T" case, which corresponds to an illite volume fraction increase of similar magnitude. Smectite volume fraction changes are similar at point A and B. However, after 2,000 years, illitization exhibits distinct behavior at points A and B for the "high T' case. At point A, illitization is stagnant, which is more clearly illustrated in Figure 2-9 where time is plotted on a linear scale. This is mainly caused by the drop of temperature, which significantly slowed down the dissolution of K-feldspar (Figure 2-10) and subsequently the supply of K. The reduced temperature also significantly decreases the reaction rate of smectite and illite. Conversely, at point B, the illitization continues at fairly fast rate due to the interaction with clay formation. Although the dissolution rate of K-feldspar at point B is significantly reduced (which limits the supply of K), bentonite near the EBS-NS interface receives K from the clay formation. This source of K is depleted before 2,000 years by illitization in the clay formation. However, illitization ceases in the clay formation after 2,000 years such that K is free to move into the bentonite . After 100,000 years, for the "high T" case, at point A, smectite volume fraction decreases by about 0.05, equivalent to 17% of the initial amount of smectite, while at point B, smectite volume fraction decreases by about 0.19, close to 60% of the initial amount of smectite. The difference between the illitization at points A and B shows that without interaction with host rock, the thermal-induced chemical alteration in the EBS bentonite stabilizes after 2,000 years (e.g. results at point A), but the interaction with host rock may lead to dramatic changes in EBS bentonite as illustrated by the model results at point B. For the "low T", smectite volume fraction decreases about 0.03 (10% of initial amount) at points A and B after 100,000 years, which is substantially lower than that for "high T' case, especially at point B.

In Figures 2-7 and 2-8, model results are also shown for a simulation ("no heat") that assumes there is no heat release from waste package. This simulation illustrates the chemical alteration in EBS bentonite is caused mostly by the interaction between EBS bentonite and the clay formation. Even though there is no temperature increase, Kunigel-VI bentonite tends to undergo slight illitization which results in a decrease of smectite volume fraction of 0.02 (5% of the initial amount) in 100,000 years. In the "no heat" simulation, the model result at point D represents the chemical evolution for undisturbed temperature conditions — which shows a slow illitization in the clay formation, with a decrease of smectite volume fraction about 0.005 in 100,000 years.

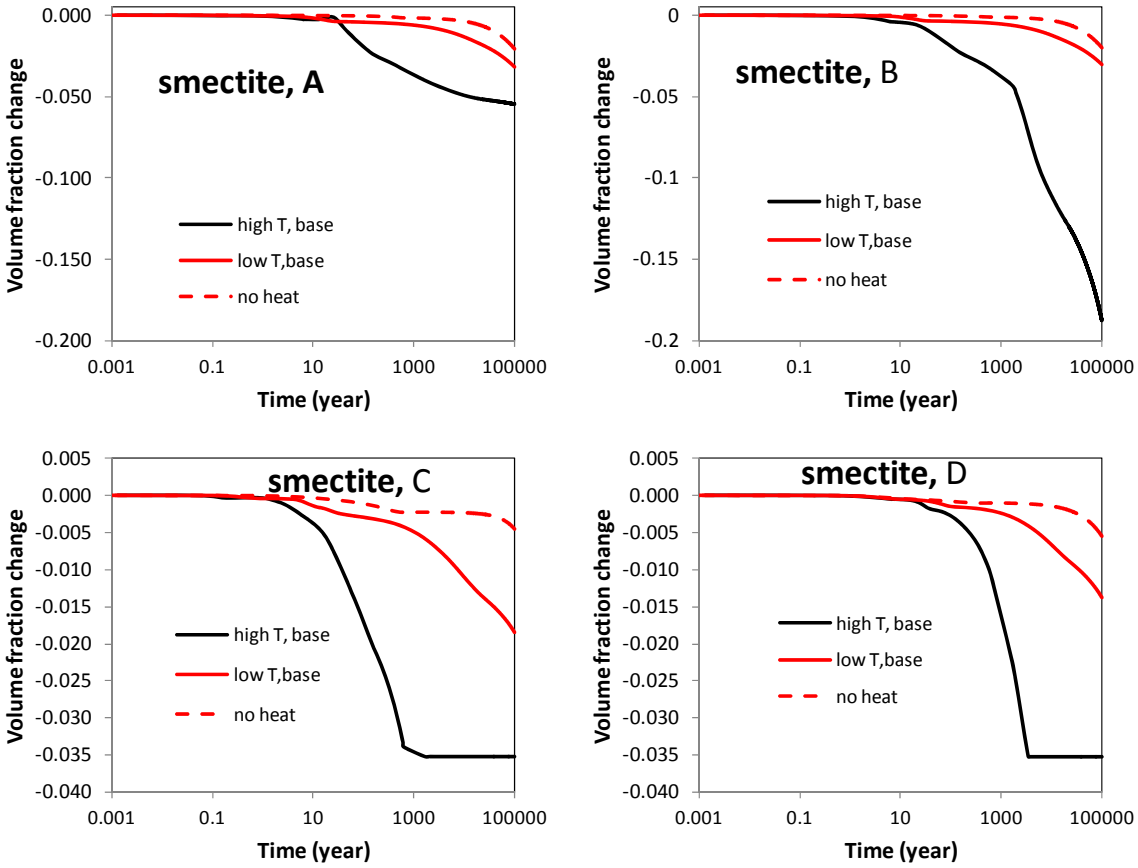

Figure 2-7. The temporal evolution of smectite volume fraction at points A, B, C, and D.

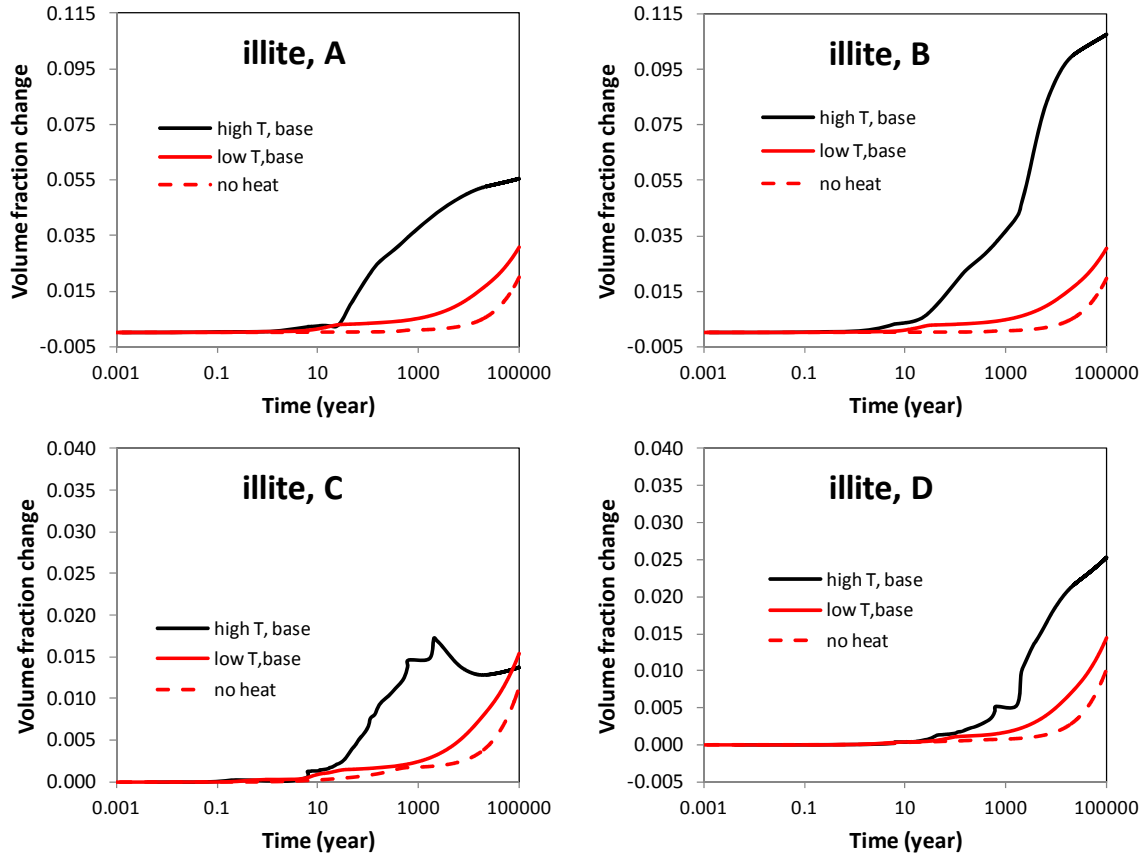

Figure 2-8. The temporal evolution of illite volume fraction at points A, B, C, and D.

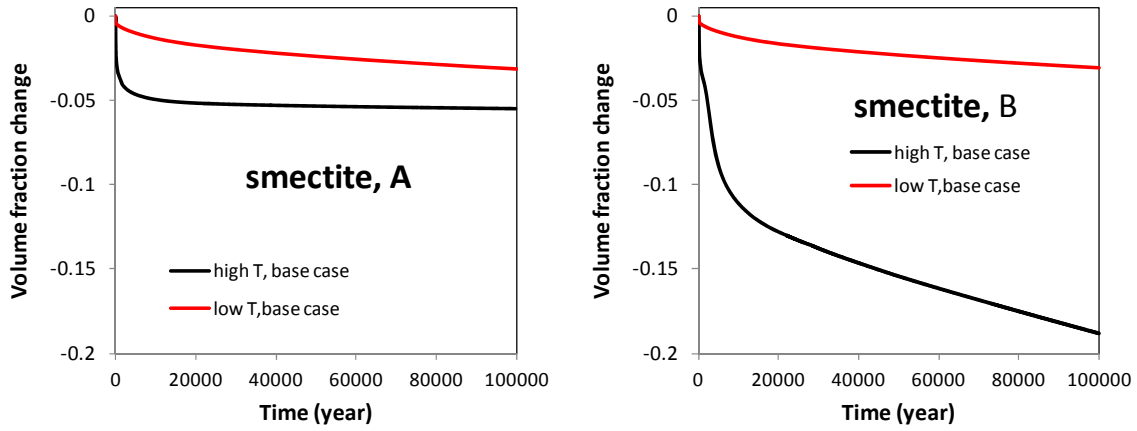

Figure 2-9. The temporal evolution of smectite volume fraction at points A and B, with X-axis plotted in linear scale.

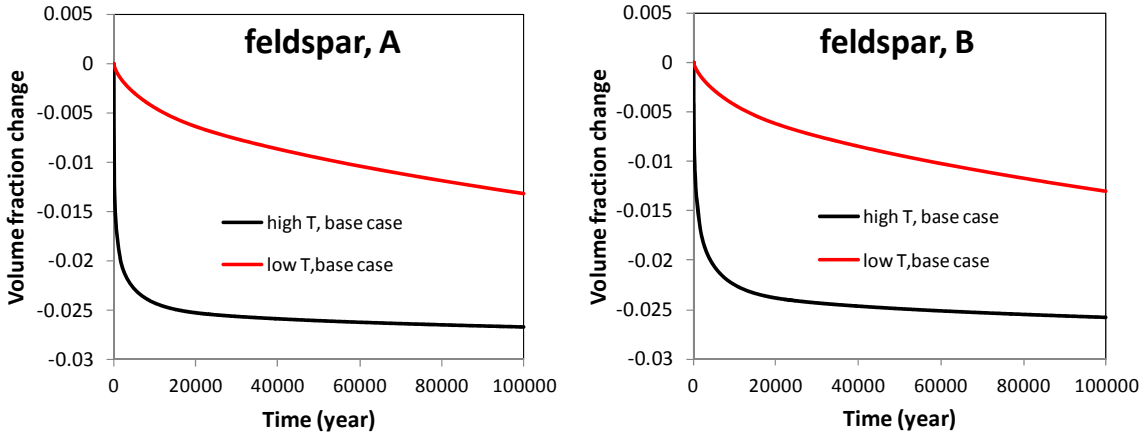

Figure 2-10. The temporal evolution of K-feldspar volume fraction at points A and B, with X-axis plotted in linear scale.

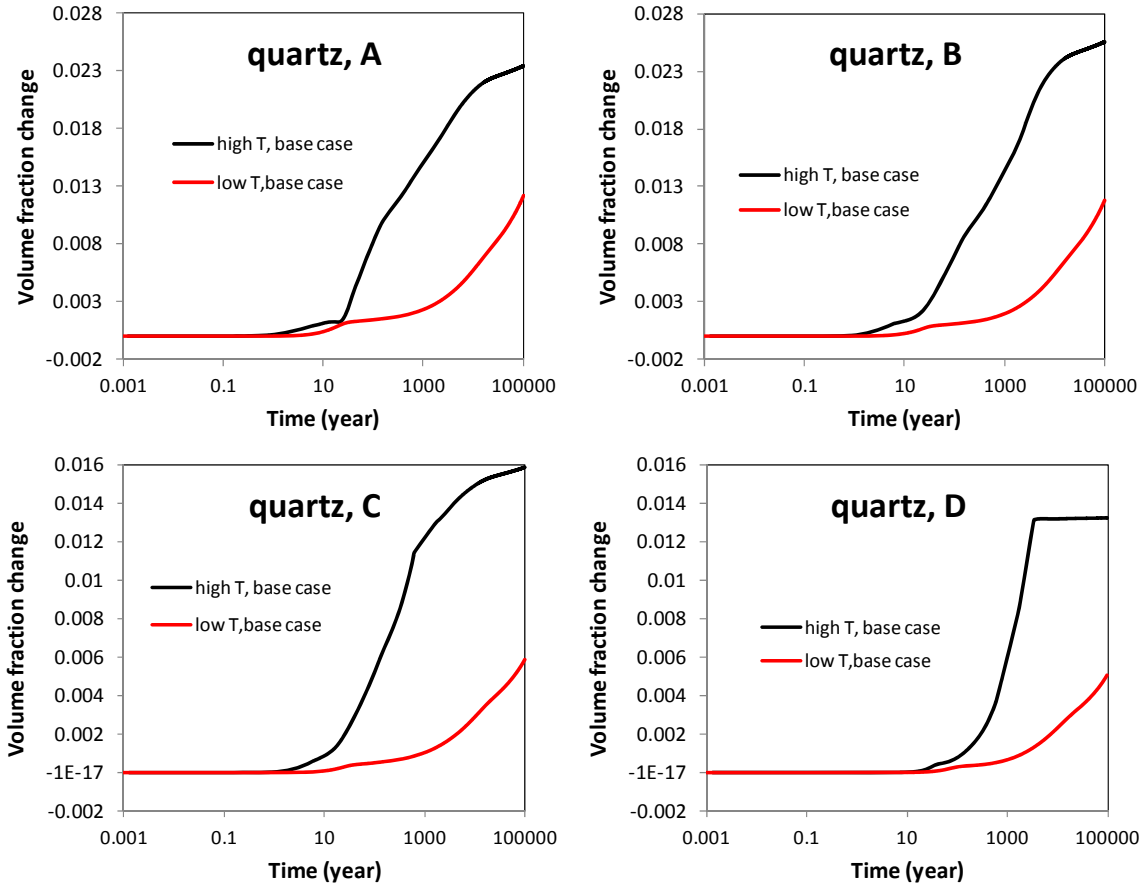

Figure 2-11. The temporal evolution of quartz volume fraction at points A, B, C, and D.

As a by-product of illitization, a moderate amount of quartz is formed after 100,000 years, as shown in Figure 2-11, which may cause the cementation of bentonite and make the bentonite more brittle. However, cementation of bentonite by silicate minerals is not considered in the mechanical-chemical coupling in the model and the model is therefore unable to quantify the

change of mechanical properties by cementation. In the near future, the effect of cementation on mechanical properties will be conceptualized and implemented in TOUGHREACT-FLAC3D.

Results from the base case (Figures 2-7 through 2-11) confirm that the clay host rock undergoes a small degree of illitization similar to observations in geological systems (e.g. Wersin et al., 2007; Pusch and Madsen, 1995).This is illustrated by the smectite dissolution at points C and D in Figure 2-7 and illite precipitation at points C and D in Figure 2-8. Results at point D represent the chemical alteration in the clay formation induced only by the long term heating. The volume fraction of smectite in the clay formation, which initially is 0.035, is depleted after 3,500 years for the "high T" case and decreases by 0.0135 (about 40% of initial amount) for the "low T" case. As a comparison, the "no heat" simulation shows that clay formation undergoes a decrease in smectite volume fraction of 0.005 (14% of the initial amount) for undisturbed temperature conditions. At point C near the EBS-NS interface, because the clay formation undergoes interaction with bentonite and experiences higher temperature, illitization is faster in comparison with that at point D. For the "high T" case, in only 650 years, the volume fraction of smectite decreases by 0.034 (about 97% of initial amount) and then in about 1,500 years, all smectite is transformed to illite; for the "low T" case, the volume fraction of smectite decreases about 0.017 (50% of the initial amount) in 100,000 years. As mentioned above, the quick depletion of smectite or the cessation of illitization in the clay formation near the EBS-NS interface has significant impact on the illitization in bentonite.

One of the key findings from Liu et al. (2013) is the critical role that K-feldspar plays on illitization in terms of supplying K, especially in the area far from the NS-EBS interface. Given the uncertainty associated with the reaction rate of K-feldspar, a sensitivity run with a K-feldspar dissolution rate two orders of magnitude higher than that in the base case was conducted in Liu et al. (2013) and model results showed that much more smectite dissolves in 1,000 years if the K-feldspar dissolution rate is higher. However, a question remains whether K-feldspar dissolution rate is still critical if the ultimate concern is the illitization after 100,000 years or even longer.

This year, a simulation with higher K-feldspar dissolution rate was conducted for 100,000 years and model results are given in Figures 2-12 through 2-14. Initially there is 2.9 vol% K-feldspar in the bentonite and increasing the dissolution rate of K-feldspar leads to a quick depletion of K-feldspar, as shown by the plateau of the volume fraction change after about 100 years in Figure 2-12. At point A, the volume fraction changes for K-feldspar (Figure 2-12), smectite (Figure 2-13) and illite (Figure 2-14) follow the same trend, which reveal the importance of K-feldspar dissolution on the illitization. The amount of K-feldspar dissolution determines the amount of smectite dissolution. Furthermore, the dissolution rate of K-feldspar determines the dissolution rate of smectite and the precipitation rate of illite. This is because the geochemical conditions in bentonite at point A are less affected by the host rock, so that the reactions can simply be described as the following reaction in a closed system:

$$\text{Na-smectite} + 0.52H^{+} + \text{K-feldspar} \Leftrightarrow \text{illite} + 0.26H_2O + 0.08Mg^{+2} + 0.33Na^{+} + 3.5SiO_2(aq) + 0.4K + 0.37AlO_2^{-} \quad (2\text{-}10)$$

Equation (2-10) clearly shows the interference of K-feldspar on illitization (dissolution of smectite and precipitation of illite). As shown in Table 2-4, the dissolution rate of smectite and precipitation rate of illite is on the order of 10^{-11} mol/m_2/s, but the dissolution rate of K-feldspar is around 10^{-13} mol/m_2/s. Because illitization involves in the current scenarios three minerals: illite, smectite and K-feldspar, the overall reaction rate of illitization depends on the slowest reacting mineral, as a result, the dissolution rate of K-feldspar becomes of the bottle neck of illitization. This is why at point A, the volume fraction change of smectite follows that of K-feldspar. However, at point B after K-feldspar runs out at around 100 years, smectite continues dissolving and illite continues forming because of the interaction between bentonite and the clay formation.

In the clay formation (see results at points C and D in Figures 2-12 through 2-14), the dissolution of K-feldspar and smectite and the precipitation of illite proceed concurrently because of the controlling of feldspar dissolution on the overall reactions of illitization (see Equation (2-10)). The clay formation at point C undergoes more interaction with bentonite, whereas at point D, the clay formation is much less affected by the interaction with bentonite. However, results at points C and D exhibit a similar trend, although the reactions occur at an earlier time at C than at D because temperature increases earlier at C than at D. This indicates that interaction between EBS bentonite and clay formation has much stronger effect on bentonite than the clay formation.

At the end of 100,000 years, both the base case and the sensitivity case with higher K-feldspar dissolution rate lead to similar quantities of smectite dissolution and illite precipitation, despite the difference at intermediate times. Therefore, if the ultimate concern is the quantity of illitization at 100,000 years (or even longer), it seems that the quantity of K-feldspar is more important that its dissolution rate.

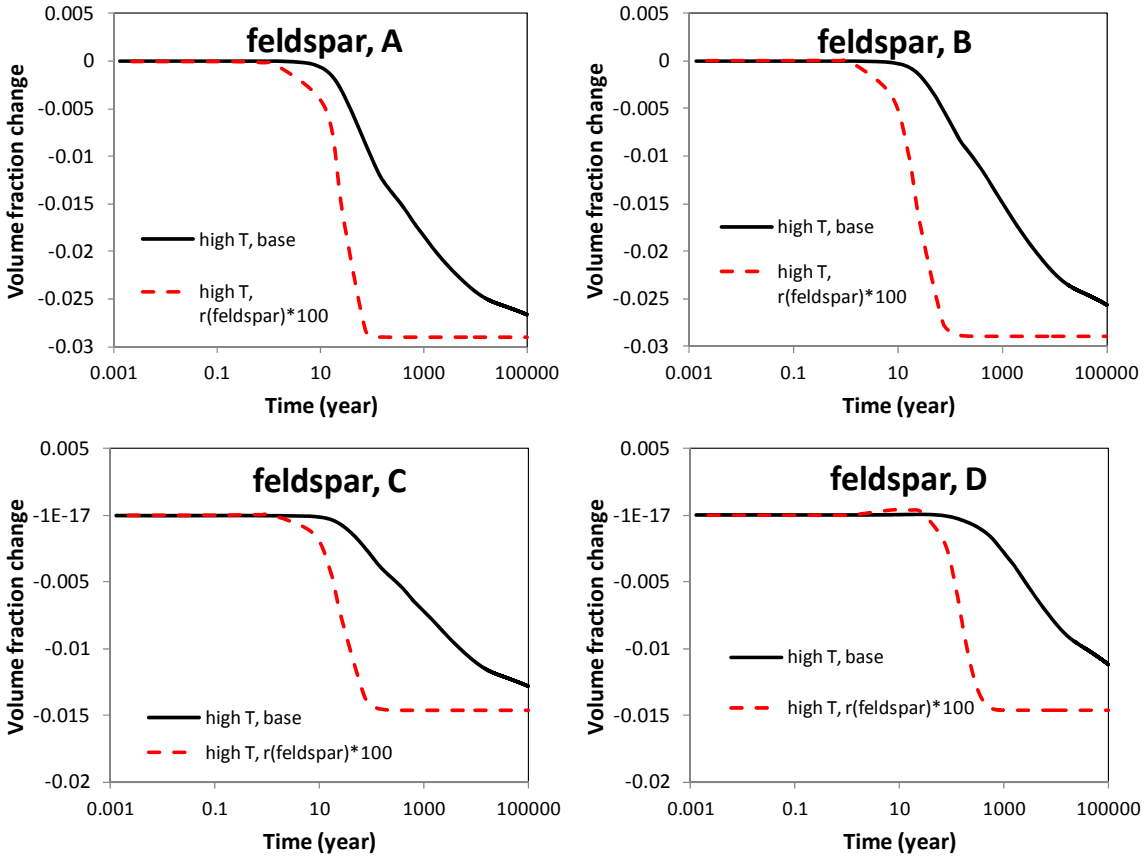

Figure 2-12. The temporal evolution of K-feldspar volume fraction at points A, B, C, and D for the "high T" base run and a sensitivity run with K-feldspar dissolution rate two orders of magnitude higher.

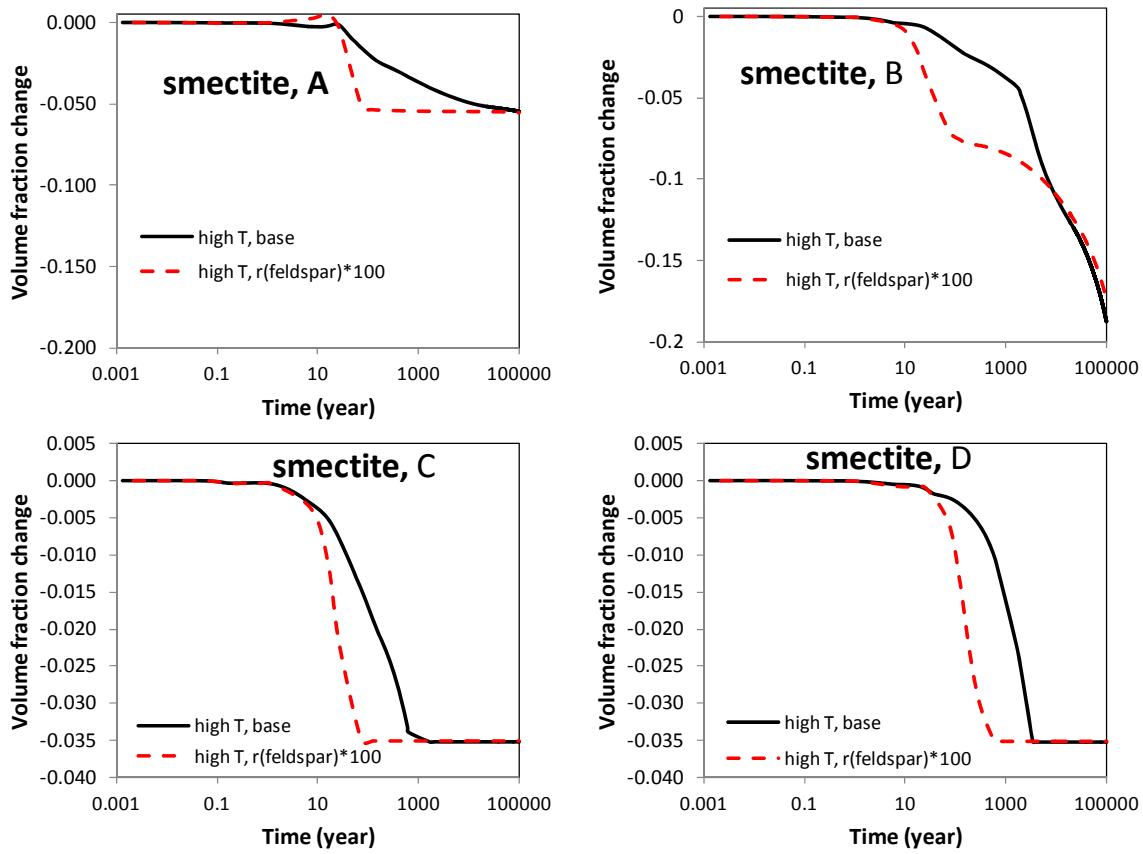

Figure 2-13. The temporal evolution of smectite volume fraction at points A, B, C, and D for the "high T" base run and a sensitivity run with K-feldspar dissolution rate two orders of magnitude higher.

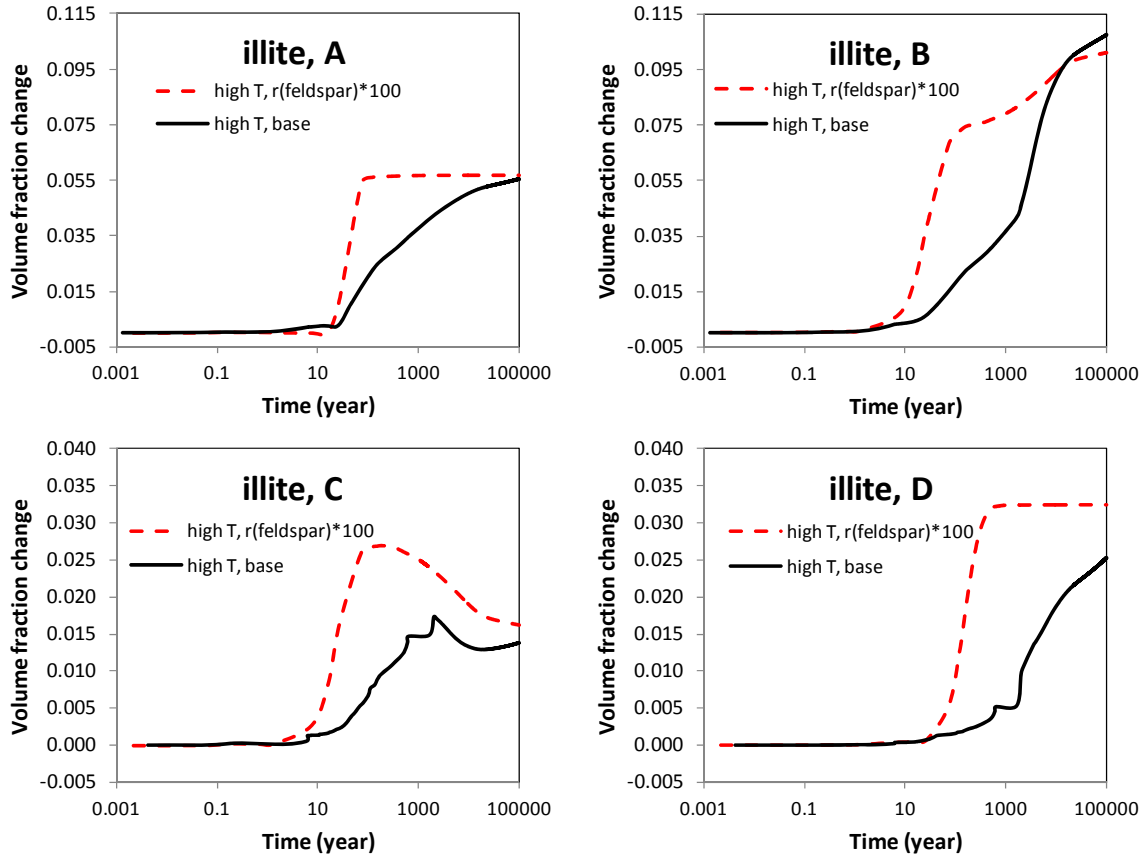

Figure 2-14. The temporal evolution of smectite volume fraction at points A, B, C, and D for the "high T" base run and a sensitivity run with K-feldspar dissolution rate two orders of magnitude higher.

Na-smectite and Ca-smectite are two representative smectites, with Na being the dominant interlayer cations for Na-smectite and Ca being the dominant interlayer cation for Ca-smectite. In the base cases for Kunigel-VI bentonite, illitization is modeled as the dissolution of Na-smectite and precipitation of illite, as shown in Equation (2-9). In the base case, we also observed that calcite dissolves and Ca^{+2} concentration increases. In the base case, because Na-smectite is considered in the model, the dissolution of calcite has no direct interaction with illitization. However, if Ca-smectite rather than Na-smectite were present in the mineral assemblage, calcite dissolution might affect the illitization. To evaluate this scenario, we create a hypothetical case in which Ca-smectite rather than Na-smectite is included in the model and overall reaction of illitization can be written as:

$$\text{Ca-smectite} + 0.52H^{+} + 0.63AlO_2^{-} + 0.6K \Leftrightarrow \text{illite} + 0.26H_2O + 0.08Mg^{+2} + 0.17Ca^{+2} + 0.5SiO_2(aq) \quad (2\text{-}11)$$

The log K for the above reactions is just slightly different from that for Equation (2-9) (the transformation from Na-smectite to illite).

Model results for calcite, smectite and illite are shown in Figures 2-15 through 2-17. Examination of these model results leads to the following observations:

- In general, switching Na-smectite to Ca-smectite does not have significant impact in terms of illitization.
- If Ca-smectite is present in the bentonite, the dissolution of calcite delays the start of smectite dissolution because higher Ca^{+2} concentration caused by the dissolution of calcite inhibit illitization.
- Eventually Ca-smectite leads to only slightly less illitization (less dissolution of smectite and less precipitation of illite) for both "high T" and "low T" cases. The reason is that the quantity of calcite that dissolves is quite small.

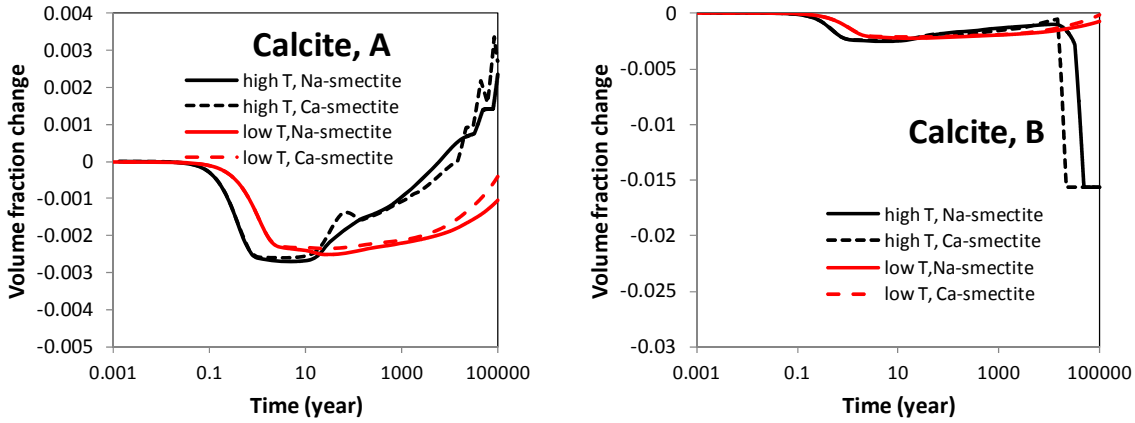

Figure 2-15. The temporal evolution of calcite volume fraction at points A, B for the case with Ca-smectite and Na-smectite in Kunigel-VI bentonite.

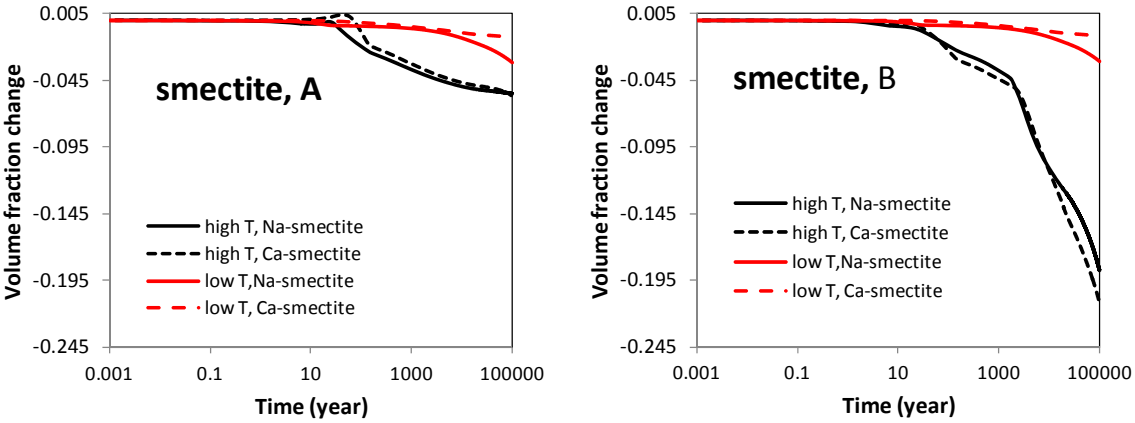

Figure 2-16. The temporal evolution of smectite volume fraction at points A, B for the case with Ca-smectite and Na-smectite in Kunigel-VI bentonite.

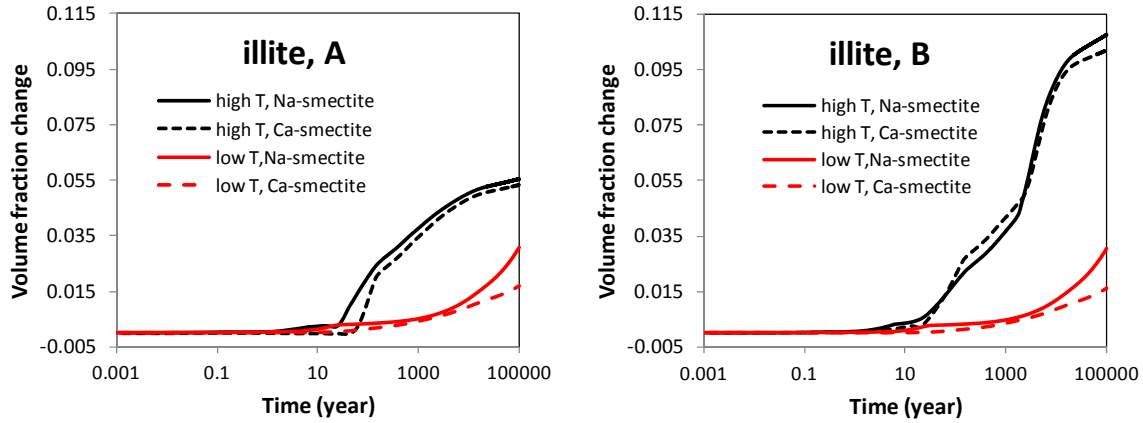

Figure 2-17. The temporal evolution of illite volume fraction at points A, B for the case with Ca-smectite and Na-smectite in Kunigel-VI bentonite.

2.3.1.2 Stress Evolution

The mechanical-chemical coupling implemented in the current model allows us to evaluate how the chemical changes described in Section 2.3.1.1 may affect the mechanical behavior of the EBS bentonite in terms of swelling and total stress. We limit our analysis to the effects of ion concentration and illitization on swelling and do not include other potential effects of chemical changes on mechanics, such as changes in mechanical properties due to cementation.

Figures 2-18 and 2-19 show the stress changes at point A and B for both "low T" and "high T" cases. Several processes combine to drive the peak stress in bentonite up to about 5 MPa for the "low T" case and 13 MPa for the "high T" case, both at around 100 years. Reasons for the stress increase include the increase in pore pressure due to hydration and thermal pressurization (a processes caused by the difference in thermal expansion of the fluid and solid host rock), bentonite swelling, and thermal expansion. Clearly the stronger thermal pressurization in the "high T" case leads to much higher stress in the bentonite than the "low T" case. For both the "high T" and "low T" cases, the major contribution to total stress within the buffer is pore pressure, with smaller contributions from swelling and thermal stresses. After 100 years, the stress gradually goes down and stabilizes somewhat after 30,000 years. By the end of 100,000 years, the difference between the "high T" and "low T" cases is minimal.

The constitutive relationship described by Equation (2-5) provides an opportunity to evaluate the effect of chemical changes on swelling stress. The mechanical results presented in this section are based on the chemical results in the previous section. In order to isolate the contributions of ion concentration changes versus smectite changes on swelling stress changes, we present three sets of calculated swelling stress. In the first set, denoted in Figures 2-19 and 2-20 as "σ=f(Sl,C,Ms)", the swelling stress is calculated according to Equation (2-5) as a function of liquid saturation changes (Sl), ion concentration (C) changes, and smectite (Ms) changes. In the second set, denoted as "σ=f(Sl,C)", the contribution from smectite changes in Equation (2-5) is disregarded, and the swelling stress is only a function of liquid saturation and ion concentration. In the third set, denoted as "σ=f(Sl)", all chemical effects are neglected, and the swelling stress is only a function of liquid saturation changes.

At early time (< 20 years), the fact that results for "σ=f(Sl,C,Ms)" and "σ=f(Sl,C)" cases are indistinguishable (Figures 2-20 and 2-21) indicates that smectite changes have not yet contributed to the stress change because the volume fraction of smectite changes significantly only after about 20 years (see Figure 2-7). Ion concentration changes start to affect stress at early times (< 20 years) and maintain such effects afterwards. Initially bentonite near the canister undergoes desaturation and therefore negative swelling stress (see Figure 2-5 for changes at point A). At point A, for the "low T' case, the ion concentration increase leads to a drop in swelling stress of about 0.11 MPa and the dissolution of smectite reduces the swelling stress a little further by about 0.06 MPa after 100,000 years. For the "high T" case, ion concentration changes cause about a 0.08 MPa decrease in swelling stress and the loss of smectite due to dissolution results in about a 0.09 MPa reduction of swelling stress after 100,000 years, (see Figure 2-20). In general, the chemical changes in bentonite have a fairly moderate effect on swelling stress, with about 17% swelling stress reduction being due to chemical change for the "low T" and "high T" cases at point A (Figure 2-20). In terms of the effect of ion concentration change on swelling stress, bentonite near the EBS-NS interface (point B) behaves similarly to bentonite near the canister. After 100,000 years, the ion concentration increase leads to a drop in swelling stress of about 0.1 MPa in both "low T' and "high T" case. In terms of the effect of smectite dissolution on the reduction in swelling stress, bentonite near the EBS-NS (point B) interface behaves similarly to those near the canister (point A) for the "low T" case, but not for the "high T" case. The chemical changes in bentonite lead to about 54% swelling stress reduction " high T" case (see Figure 2-21), which is much higher than the 17% swelling stress reduction at point B for the "low T" case. This is caused by more dissolution of smectite in bentonite near EBS-NS interface (see Figure 2-7 at point B) for the "high T" case. In terms of the total stress, the decrease of swelling stress accounts for about a 3-10% reduction of the total stress after 100,000 years.

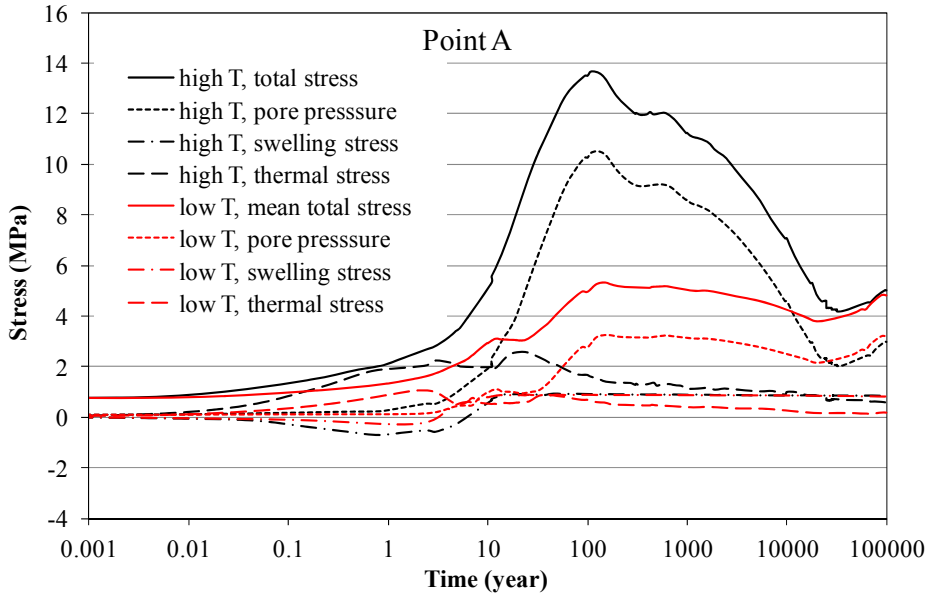

Figure 2-18. Simulation results of mean total stress, pore pressure, and thermal stress at point A for the "low T" and "high T" scenario, respectively.

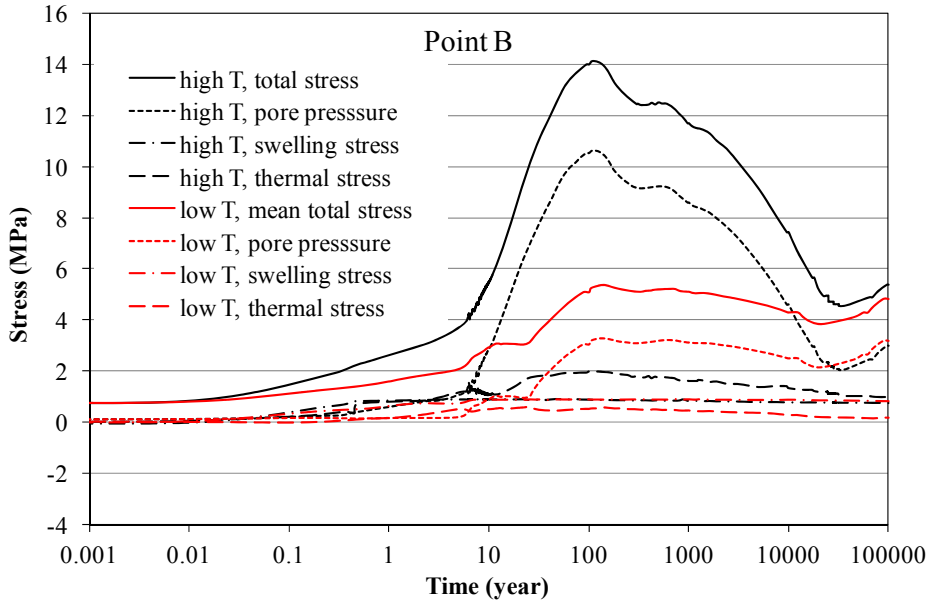

Figure 2-19. Simulation results of mean total stress, pore pressure, and thermal stress at point B for the "low T" and "high T" scenario, respectively.

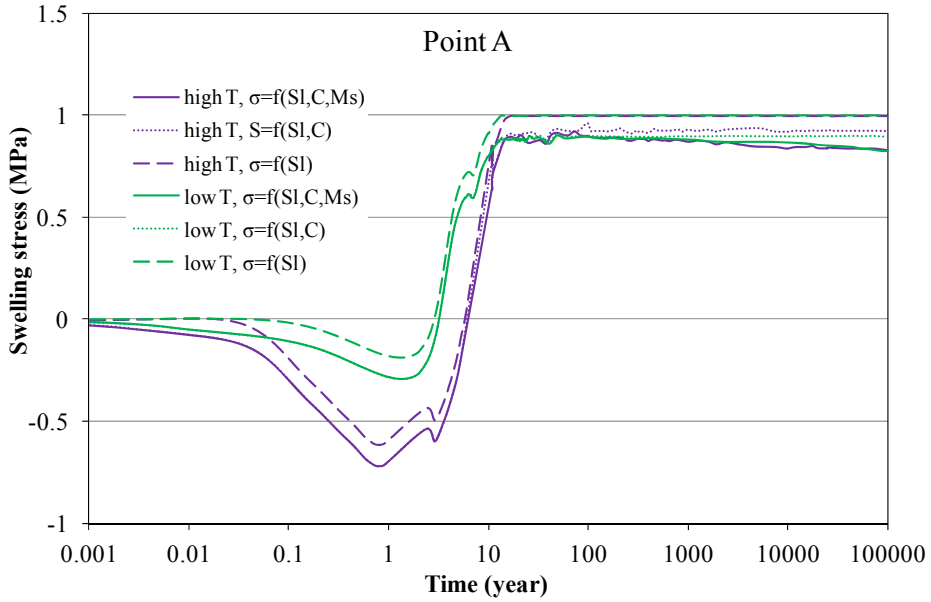

Figure 2-20. Simulation results of swelling stress at point A for the "low T" and "high T" scenarios, respectively.

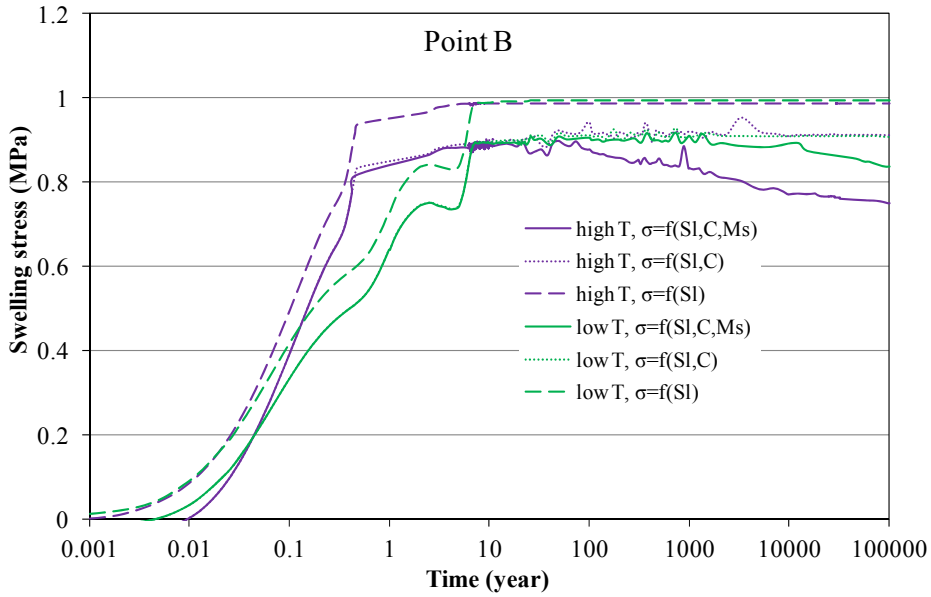

Figure 2-21. Simulation results of swelling stress at point B for the "low T" and "high T" scenarios, respectively.

Figures 2-22 and 2-23 show the evolution of total stress and pore pressure at points C and D in the clay formation. After a sharp increase in stress at about 100 years, stress decreases. After 20,000 to 30,000 years the stress field become stable and the difference between the "high T" and "low T" case is fairly small.

In FY15, the mechanical model for clay formation is also linked to the chemical changes with a similar coupling scheme to that used for bentonite, which provides an opportunity to check the effect of chemical change in the clay formation on stress. In the "high T" base case the effect of ion concentration and smectite change on stress are considered. We developed two sensitivity runs in which the contribution of ion concentration and smectite volume fraction change to stress are alternatively neglected to check on the contribution of chemical changes on the stress. The "high T, no Sc" case in which the contribution of smectite change to stress is neglected and the "high T, no C, no Sc" case in which both the contribution of smectite change and ion concentration to stress is neglected, are shown in Figures 2-24 and 2-25. Model results for these three cases show that the effects on stress are very small, especially at point D. By the end of 100,000 years at point C, the dissolution of smectite leads to a decrease in stress of about 0.14 MPa and ion concentration change cause another decrease in stress of about 0.14 MPa. Therefore, in total, the chemical changes in the clay formation result in about a 0.28 MPa decrease in stress, or 2.6%. At point D, chemical changes account for only about a 0.1 MPa difference in stress.

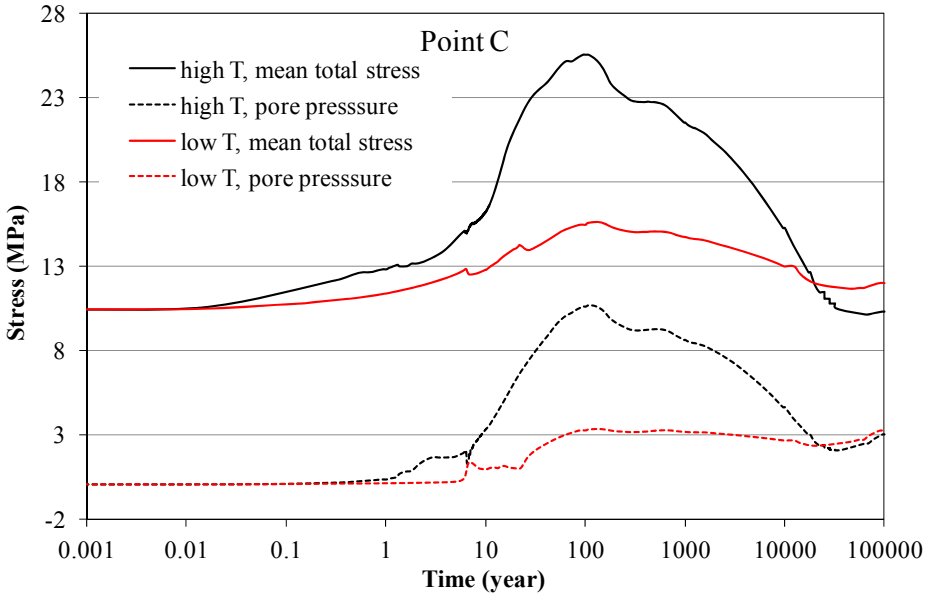

Figure 2-22. Simulation results of mean total stress, pore pressure, and thermal stress at point C for the "low T" and "high T" scenario, respectively.

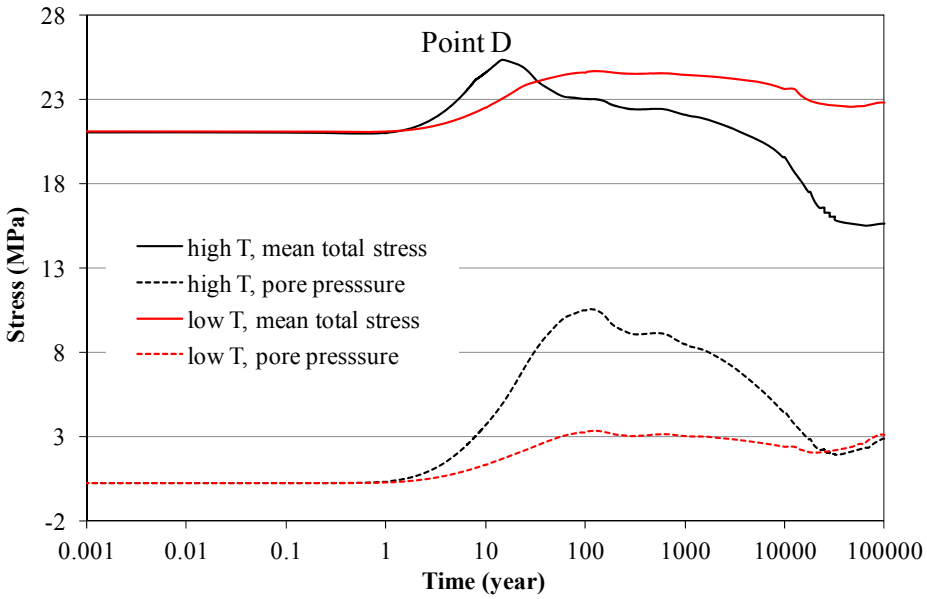

Figure 2-23. Simulation results of mean total stress, pore pressure, and thermal stress at point D for the "low T" and "high T" scenario, respectively.

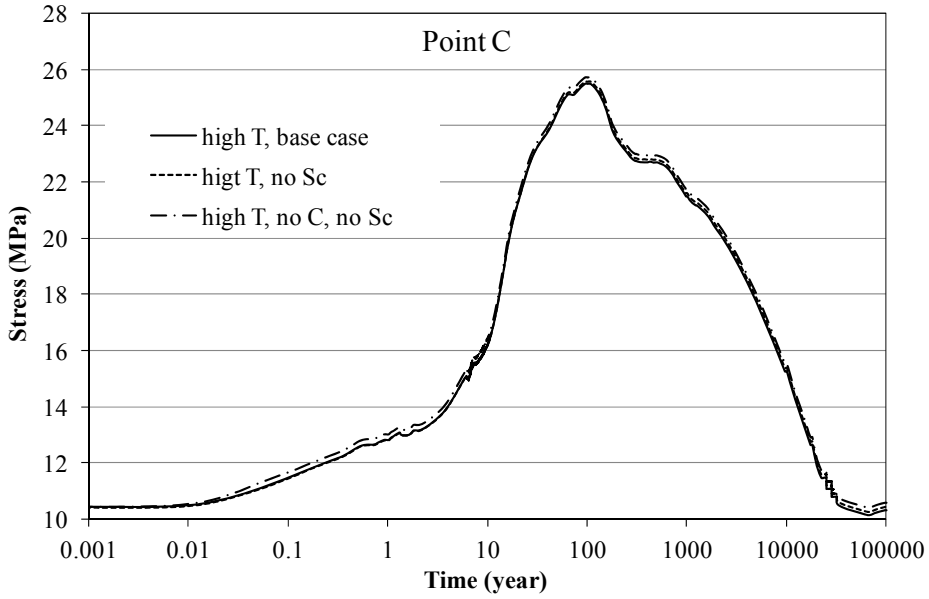

Figure 2-24. Simulation results of mean total stress at point C for the "high T" scenarios in three cases: the 'high T, base case" in which the effect ion concentration and smectite change on stress are considered; the "high T, no Sc" case in which the contribution of smectite change to stress is neglected and the "high T, no C, no Sc" case in which both the contribution of smectite change and ion concentration to stress are neglected.

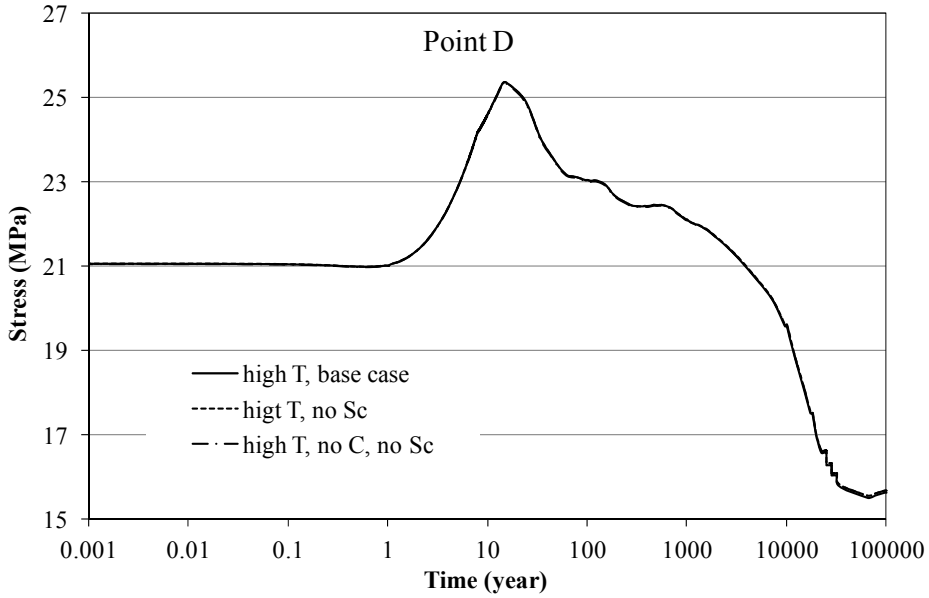

Figure 2-25. Simulation results of mean total stress at point D for the "high T" scenarios in three cases: the 'high T, base case" in which the effect ion concentration and smectite change on stress are considered; the "high T, no Sc" case in which the contribution of smectite change to stress is

neglected and the "high T, no C, no Sc" case in which both the contribution of smectite change and ion concentration to stress are neglected.

2.3.2 Cases for FEBEX Bentonite

In order to understand the change in THMC properties under high temperature for different conditions, models were also developed for FEBEX bentonite as an alternative to Kunigel-VI bentonite discussed in Section 2.3.1. Kunigel-VI bentonite (Ochs et al., 2004) is one of those that have low smectite content and relative low swelling capacity, whereas FEBEX bentonite (ENRESA, 2000) represents a type of bentonite that has high fraction of smectite and high swelling capacity. Kunigel-VI bentonite differs from the FEBEX bentonite in the following aspects (Zheng et al., 2014):

1. In terms of mineralogical composition, the most pronounced and relevant difference between FEBEX and Kunigel-VI bentonite is content of smectite, with FEBEX bentonite containing about 60 vol% smectite and Kunigel-VI bentonite having only about 31 vol% smectite (see Table 2-1). FEBEX bentonite also has less K-feldspar, which could affect illitization. The published mineralogical compositions vary slightly (Zheng et al., 2014), and the average was used in the model. Note that Table 2-1 lists the volume fraction whereas most published values are mass fraction.
2. In terms of aqueous chemistry, FEBEX bentonite has a higher ion concentration in pore water than Kunigel-VI bentonite, as shown in Table 2-2. The concentration of major cations, i.e. Ca, Mg, Na, K for FEBEX bentonite is about 2 orders of magnitude higher than that for Kunigel-VI bentonite, which could affect illitization over the course of heating and hydration.
3. The swelling pressure for FEBEX bentonite, ranging from 4.5 MPa (Castellanos et al., 2008) to 7 MPa (ENRESA, 2000), is higher than the swelling pressure for Kunigel-VI bentonite, with a swelling pressure of around 1 MPa (Börgesson et al. 2001; Komine and Ogata, 1996) measured using distilled water. Therefore the β_{SW} in Equation (2-4) for FEBEX bentonite is 0.238 (Rutqvist et al., 2011), which is higher than that used for Kunigel-VI bentonite (0.048).
4. Another difference between FEBEX and Kunigel-VI bentonite is the parameter A_{sc} that relates swelling stress with the abundance of smectite. For FEBEX bentonite, A_{sc} is 6.5E+6 Pa^{-1} (Zheng et al., 2014), which is higher than 2.5E+6 Pa^{-1} used for Kunigel-VI bentonite.

2.3.2.1 Chemical Evolution

In order to delineate the effect of differences in chemical and mechanical properties on the long term chemical changes and the subsequent mechanical changes, the same thermal conductivity and permeability are used for FEBEX bentonite as used for Kunigel-VI bentonite. The temperature, water saturation and pore pressure for FEBEX bentonite are therefore the same as shown in Figures 2-4 through 2-6. Changes in smectite and illite volume fractions are shown in Figures 2-26 and 2-27. An examination of the model results for Kunigel-VI and FEBEX

bentonite reveals that some changes are common to both bentonites and some are distinct. Some common observations for both bentonites are as follows:

- Illitization (dissolution of smectite and precipitation of illite) occurs in bentonite and is enhanced at higher temperature.
- Bentonite near the NS-EBS interface undergoes more illitization than that near the waste package.
- Starting from about 1,600 years for the "high T" case, coincident with the time that smectite is depleted and illitization ceases in the clay formation near the NS-EBS interface, the dissolution of smectite is accelerated.
- In the far field of the clay formation (e.g. point D), it takes about 3,400 years to transform all smectite to illite for the "high T" case, but there is still 60% left after 100,000 years for the "low T" case.

However, in comparison with the model results for Kunigel-VI bentonite, several distinct features have been observed for FEBEX bentonite.

- There is less smectite dissolution for FEBEX bentonite for both "high T" and "low T" scenarios after 100,000 years. For the "high T" case, smectite volume fraction decreases about 0.03 at point A and 0.14 at point B, about 5% and 23% of the initial smectite volume fraction, respectively. These changes are significantly lower than a decrease of 0.05 (17% of initial amount) at point A and 0.19 (60% of the initial amount) for Kunigel-VI bentonite.
- The enhancement of illitization (expressed as smectite dissolution and illite dissolution) by temperature is less pronounced for FEBEX, i.e. the difference between the amount of smectite dissolving for the "low T" and "high T' scenarios is less significant for FEBEX bentonite than for Kunigel-VI bentonite.
- Although the different types of EBS bentonite have almost no impact on the chemical changes in the clay formation away from the EBS-NS interface (illustrated by results at point D Figures 2-26 and 2-27), the type of bentonite does have a moderate impact on the clay formation near the EBS interface. As shown by the results at point C in Figures 2-26 and 2-27, with FEBEX bentonite, smectite dissolution occurs earlier in the clay formation. The reason is that FEBEX bentonite has a higher K concentration (see Table 2-2) so that the diffusion of K from the clay formation into the bentonite is at lower rate, and subsequently more K is available in the clay formation for illitization.

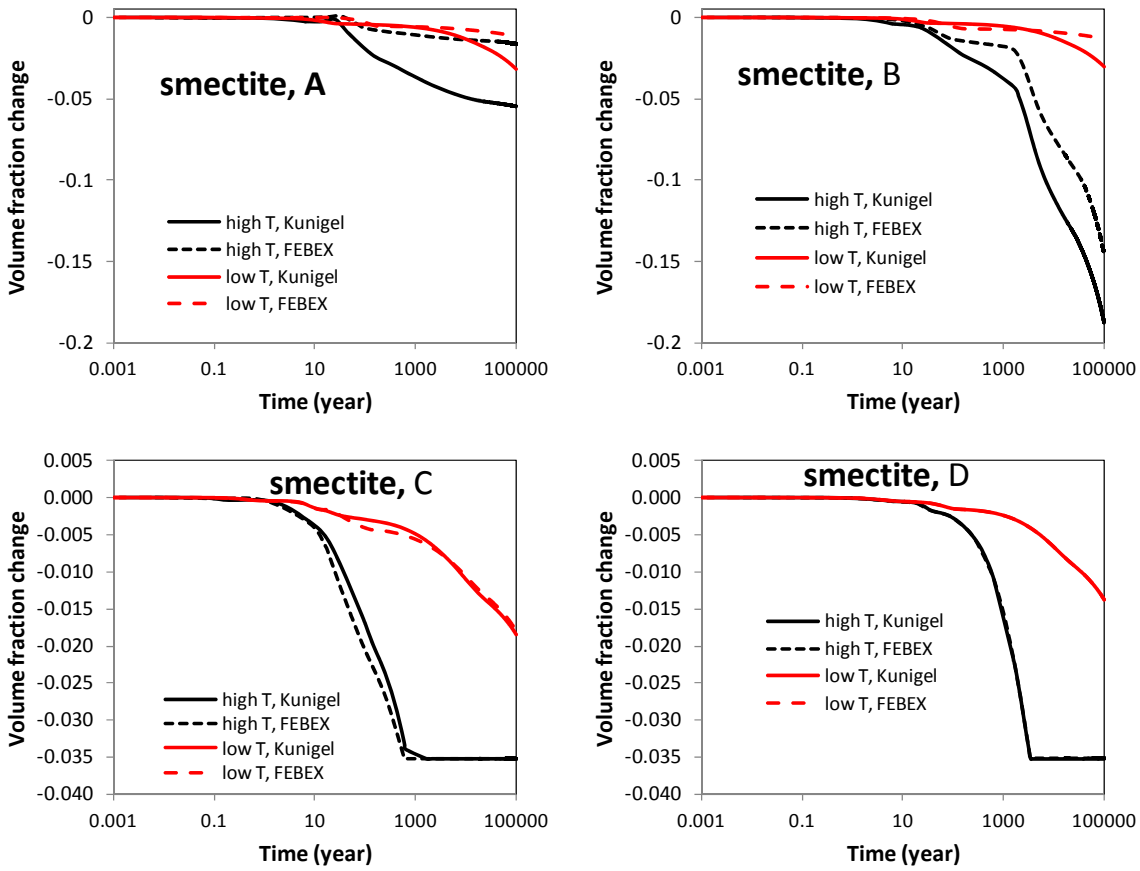

Figure 2-26. The temporal evolution of smectite volume fraction at points A, B, C, and D for Kunigel and FEBEX bentonite.

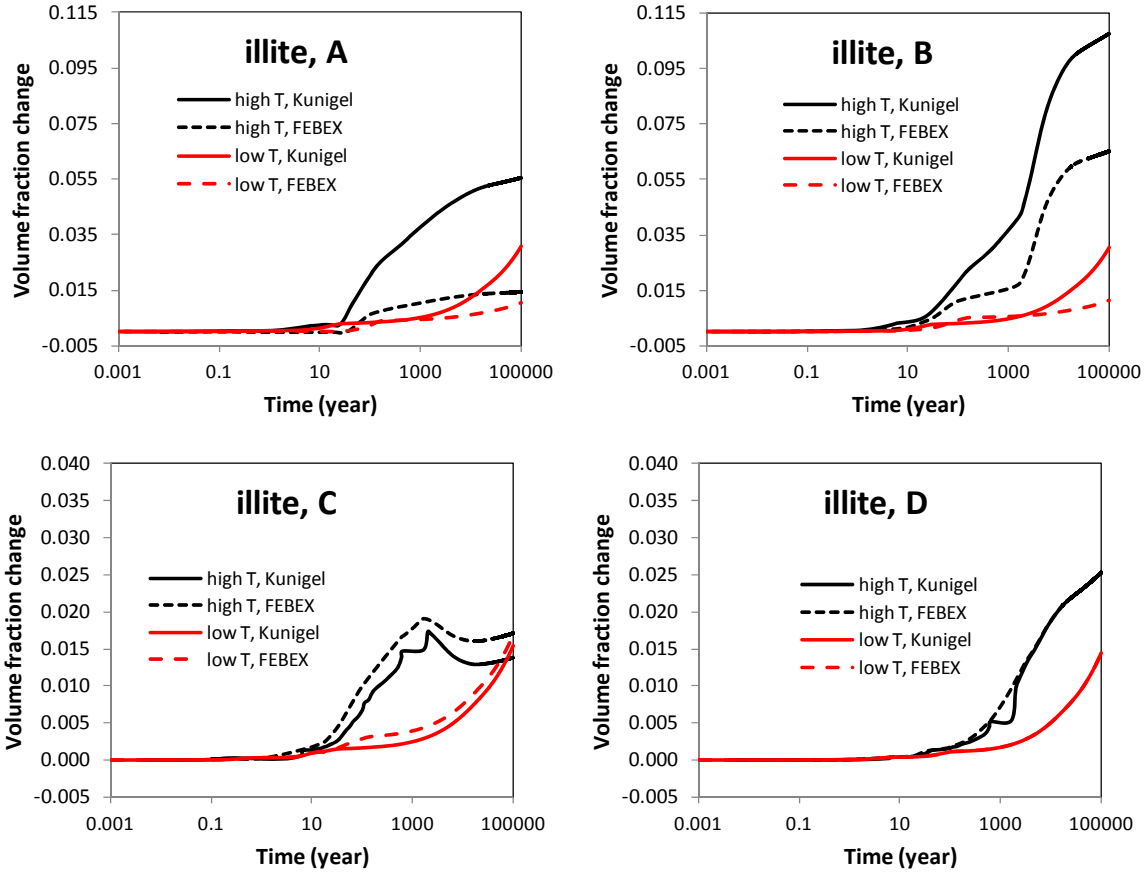

Figure 2-27. The temporal evolution of illite volume fraction at points A, B, C, and D for Kunigel and FEBEX bentonite.

A sensitivity analysis of illitization in the EBS to key chemical parameters was documented in Liu et al. (2013), which confirms the importance of available K to illitization. This sensitivity has also been widely observed in geological formations (e.g. Cuadros, 2006), which further demonstrates that the source of K is actually the dissolution of K-feldspar. When FEBEX bentonite is used as the EBS material, much less K-feldspar dissolution occurs compared with the case using Kunigel-VI bentonite, as illustrated in Figure 2-28. This is the reason why in Figure 2-26 there is less smectite dissolution for FEBEX bentonite that that for Kunigel-VI bentonite. Less dissolution of K-feldspar for FEBEX bentonite can be attributed to two factors: a lower content of K-feldspar and a higher K concentration in pore water for FEBEX bentonite.

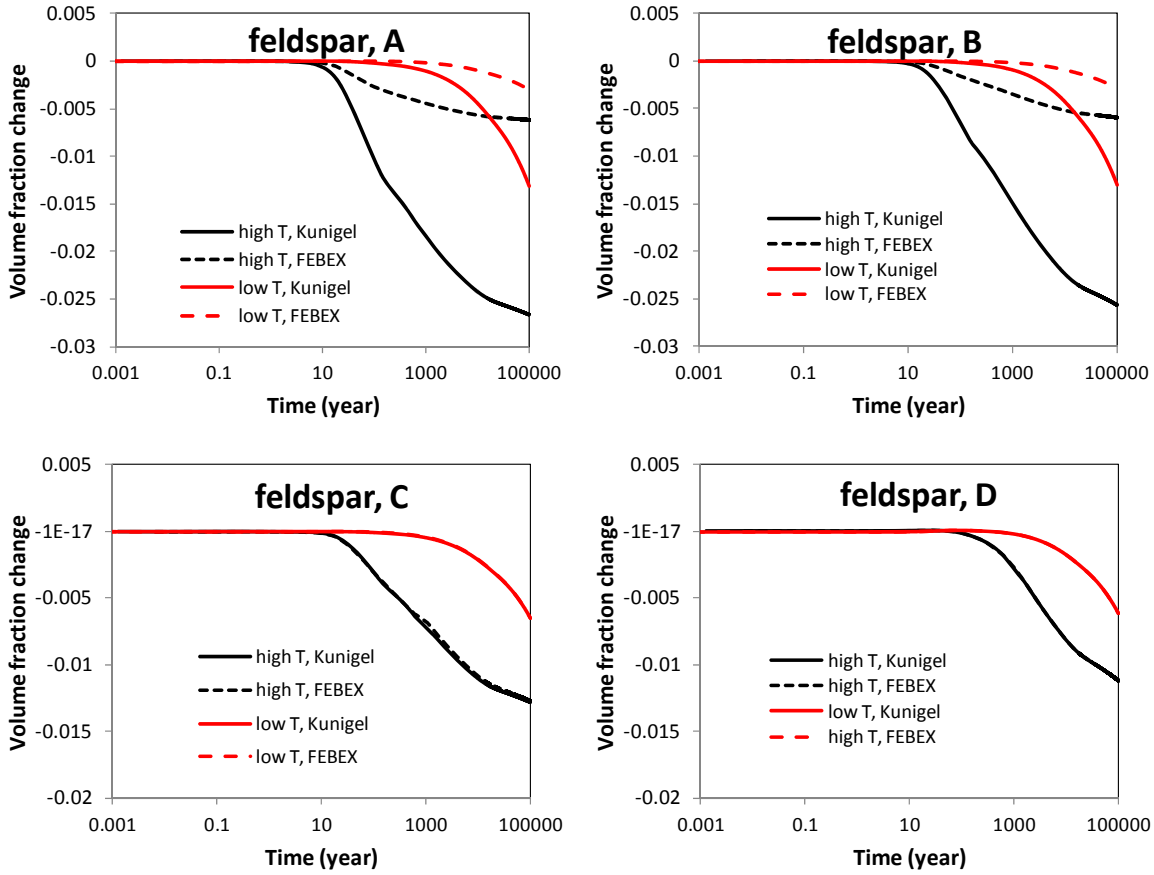

Figure 2-28. The temporal evolution of K-feldspar volume fraction at points A, B, C, and D in the base case with Kunigel bentonite and a sensitivity case with FEBEX bentonite.

One of the byproducts of illitization is the precipitation of quartz as shown in the following reactions:

$$\text{Smectite} + 0.52H^{+} + 0.63AlO_2^{-} + 0.6K \Leftrightarrow \text{illite} + 0.26H_2O + 0.08Mg^{+2} + 0.33Na^{+} + 0.5\text{quartz} \quad (2\text{-}12)$$

The cementation by quartz (or amorphous SiO_2 minerals) might lower the swelling of bentonite and increase the brittleness of the bentonite. In comparison with Kunigel-VI bentonite, there is less quartz precipitation for the case with FEBEX bentonite (see Figure 2-19). For the "high T" scenario, the amount of quartz formed in FEBEX bentonite is only about 30% of that for Kunigel-VI bentonite.

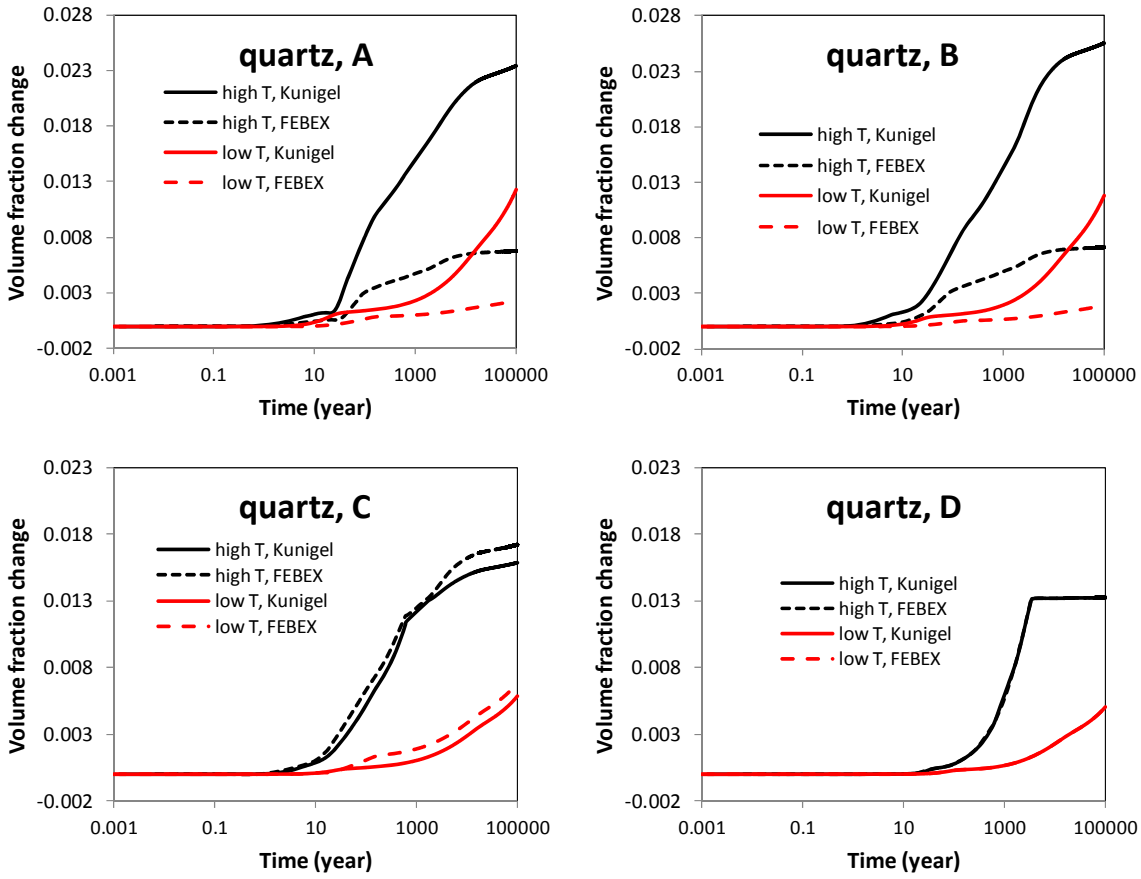

Figure 2-29. The temporal evolution of quartz volume fraction at points A, B, C, and D in the base case with Kunigel bentonite and a sensitivity case with FEBEX bentonite.

We also tested the behavior of FEBEX bentonite containing Na-smectite versus Ca-smectite to investigate the effects of calcite dissolution on long term illitization, as done for Kunigel-VI bentonite in Section 2.3.1. The reaction of Ca-smectite is given in Equation (2-10) above.

Calcite dissolution is a fairly fast process. For the "low-T" case, it takes about 7 years to dissolve all the calcite initially present, as manifested by the plateau of the volume fraction change in Figure 2-30. For the "high-T" case, higher temperature leads to a faster reaction rate, so it takes only about 3 years to deplete calcite if Ca-smectite is considered in the model compared with 5 years if Na-smectite is modeled. Because there is only a small amount of calcite initially in the bentonite and the dissolution of calcite is fast, the effect of calcite on the illitization is short-lived. In Figure 2-31, the volume fraction of illite in the first 200 years is plotted to highlight this effect. If Ca-smectite is used, because of the dissolution of calcite, the formation of illite is delayed in comparison with the case that Na-smectite is used because calcite interferes with illitization. But after 200 years (see Figures 2-32 and 2-33), the difference in illitization between the Ca-smectite and Na-smectite is very small.

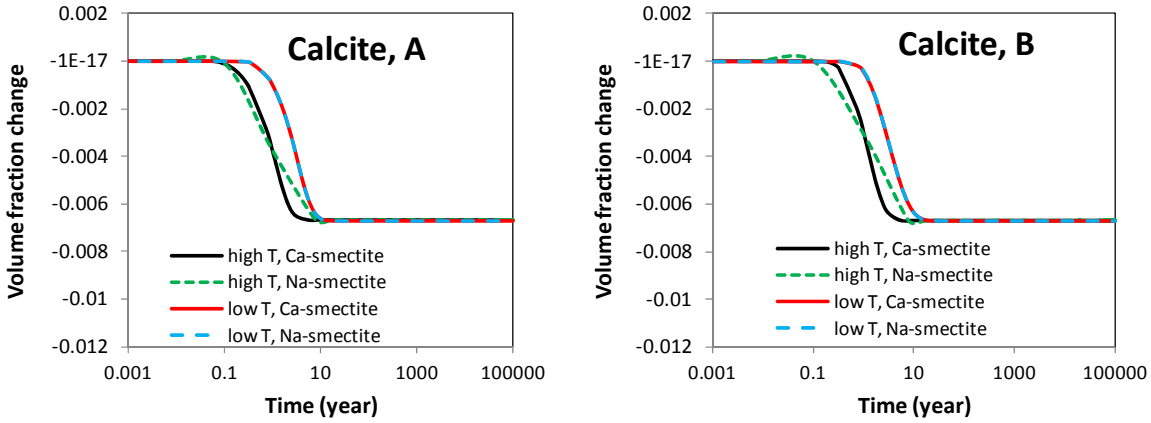

Figure 2-30. The temporal evolution of calcite volume fraction at points A and B for the case with Ca-smectite and Na-smectite in FEBEX bentonite.

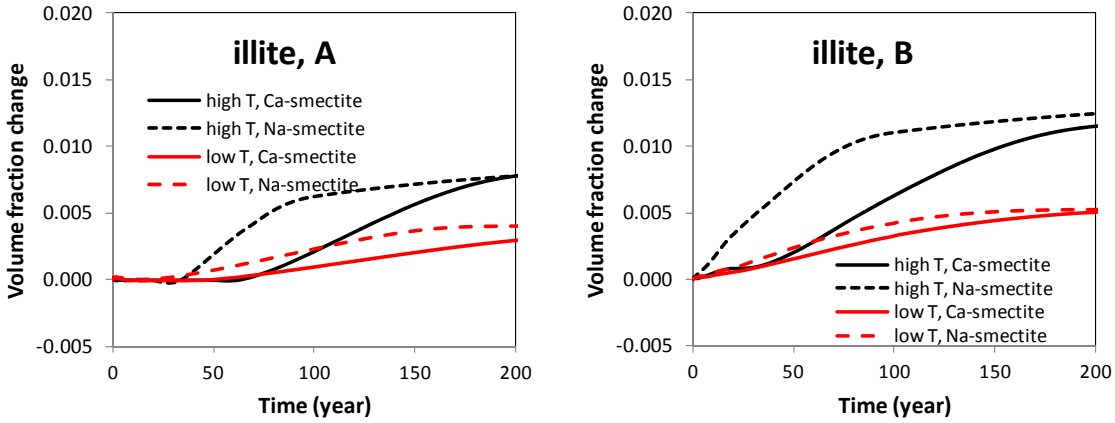

Figure 2-31. The temporal evolution of Ca-smectite/Na-smectite volume fraction for 200 years at points A and B for the case with Ca-smectite and Na-smectite in FEBEX bentonite.

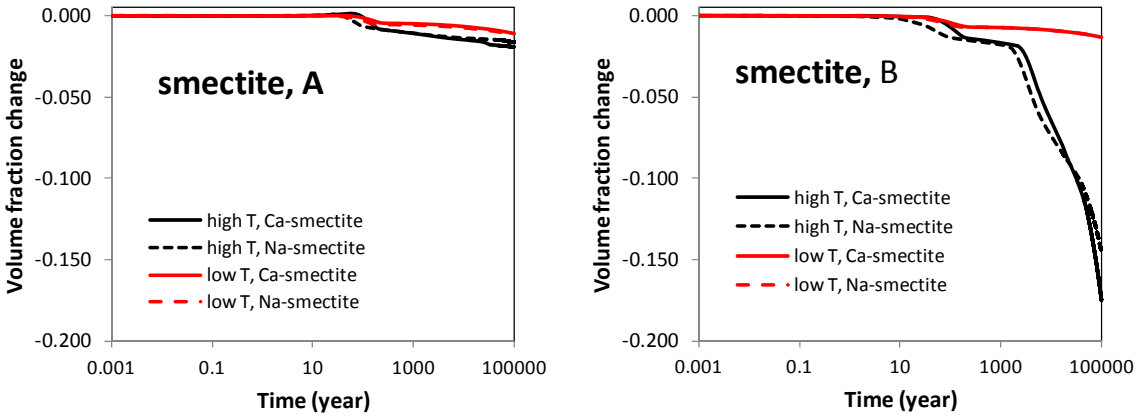

Figure 2-32. The temporal evolution of illite volume fraction at points A and B for the case with Ca-smectite and Na-smectite in FEBEX bentonite.

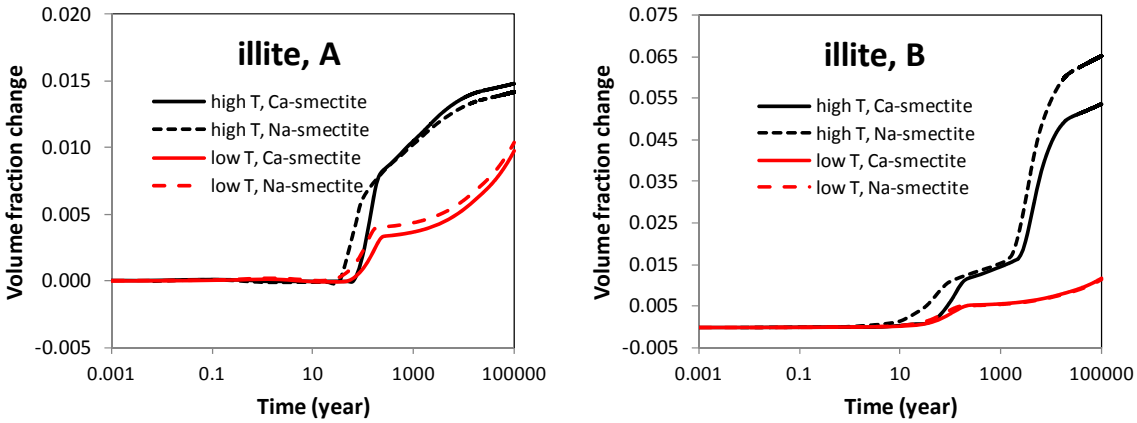

Figure 2-33. The temporal evolution of illite volume fraction at points A, B for the case with Ca-smectite and Na-smectite in FEBEX bentonite.

2.3.2.2 Stress Evolution

Figures 2-34 and 2-35 show the stress changes in the sensitivity run using FEBEX bentonite at points A and B for both "low T" and "high T" cases. As discussed in Section 2.3.1.2, the increase in pore pressure due to hydration and thermal pressurization (a processes caused by the difference in thermal expansion of the fluid and solid host rock), bentonite swelling, and thermal expansion are the main driving force for the increase in total stress in bentonite. In comparison with the "low T" case, the stronger thermal pressurization in the "high T" case clearly leads to much higher stress in the bentonite. For both the "high T" and "low T" cases, the major contribution to the total stress within the buffer is from pore pressure, with smaller contributions from swelling and thermal stress. As observed for Kunigel-VI bentonite, the stress peak occurs at around 100 years and then decreases thereafter. After 20,000 to 30,000 years, the stress seems to reach a stable state.

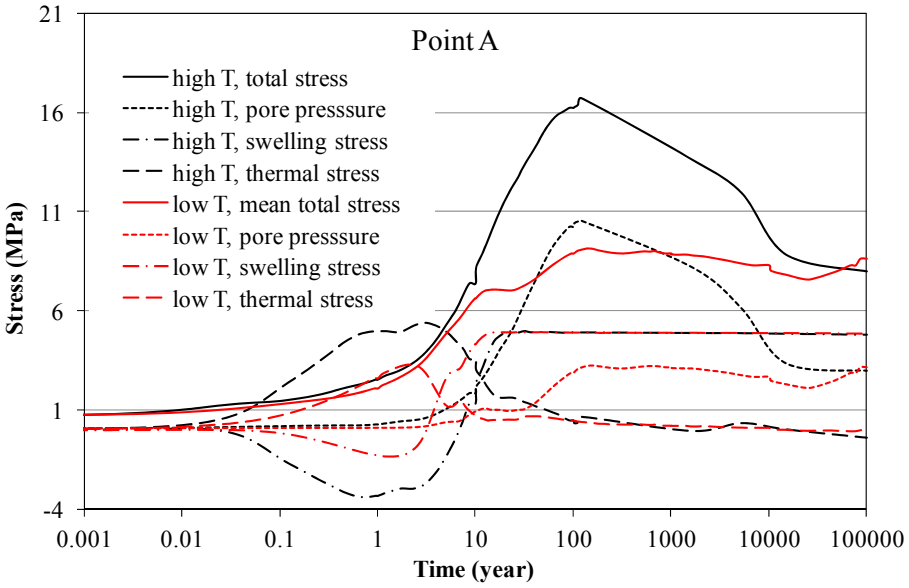

Figure 2-34. Simulation results of mean total stress, pore pressure, swelling stress, and thermal stress at point A in the sensitivity case with FEBEX bentonite for the "low T" and "high T" scenarios, respectively.

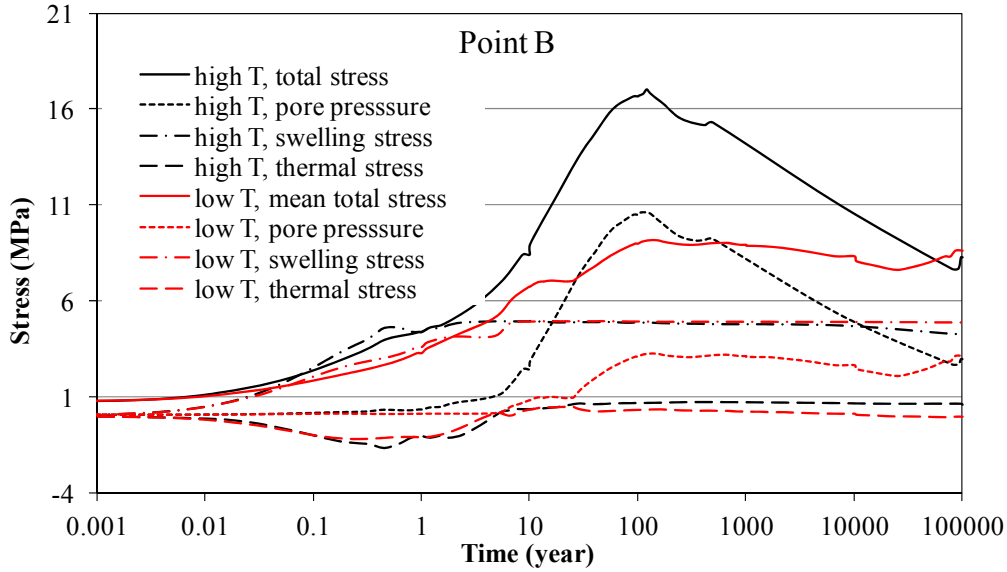

Figure 2-35. Simulation results of mean total stress, pore pressure, swelling stress, and thermal stress at point B in the sensitivity case with FEBEX bentonite for the "low T" and "high T" scenarios, respectively.

Figures 2-36 and 2-37 compare the total stress calculated for the Kunigel-VI and FEBEX bentonite. Because FEBEX bentonite has higher swelling pressure, the total stress for FEBEX bentonite at points A and B are 3-4 MPa higher than that for Kunigel bentonite at the peak (100 years) and this difference persists until the end of the simulation at 100,000 years.

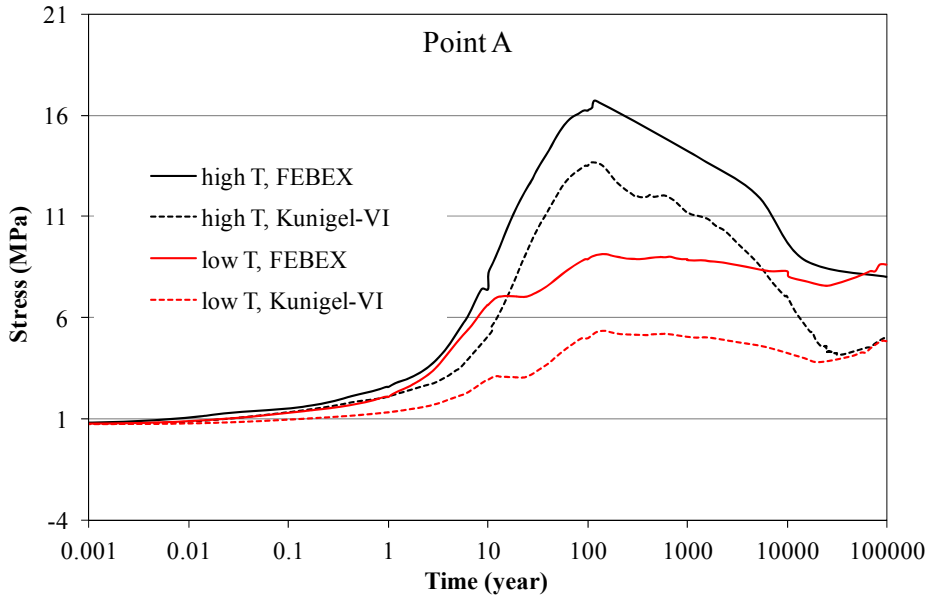

Figure 2-36. Simulation results of mean total stress at point A for Kunigel-VI and FEBEX bentonite for the "low T" and "high T" scenarios, respectively.

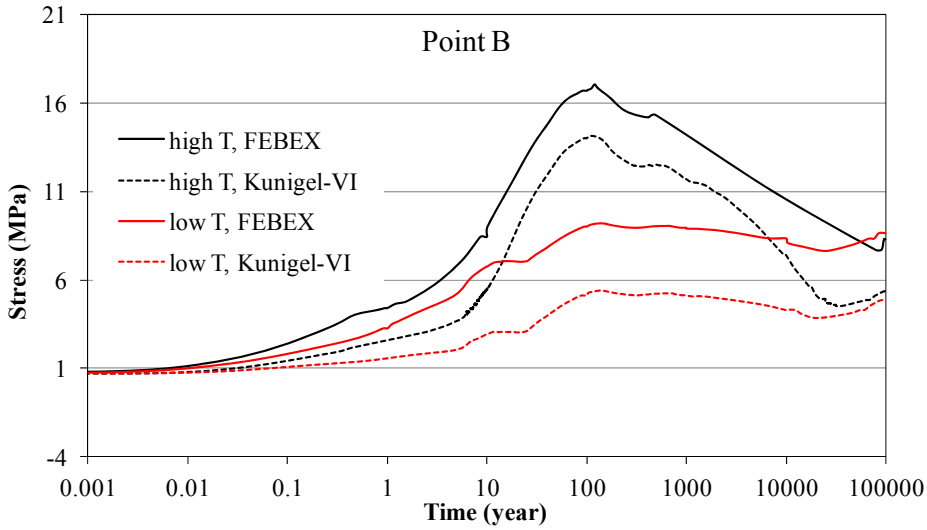

Figure 2-37. Simulation results of mean total stress at point B for Kunigel-VI and FEBEX bentonite for the "low T" and "high T" scenarios, respectively.

The constitutive relationship described by Equation (2-5) shows that the swelling stress changes have contributions from moisture, ion concentration and smectite changes. Similar to what has been done for the Kunigel-VI bentonite, we also present three sets of calculated swelling stresses for FEBEX bentonite to delineate the contribution from each process. In the first set, denoted in Figures 2-38 to 2-41 as "σ=f(Sl,C,Ms)", the swelling stress is calculated according to Equation (2-5) as a function of liquid saturation changes (Sl), ion concentration (C) changes, and smectite

(Ms) changes. In the second set, denoted as "σ=f(Sl,C)", the contribution from smectite changes in Equation (2-5) is disregarded, and the swelling stress is only a function of liquid saturation and ion concentration. In the third set, denoted as "σ=f(Sl)", all chemical effects are neglected, and the swelling stress is only a function of liquid saturation changes. At point A near the canister, pore water in the bentonite evaporates causing the liquid saturation to decrease. This results in a decrease of swelling stress (shrinkage) until about 4 years for "low T" scenario and 8 years for "high T" scenario (Figure 2-38). After that, increases in liquid saturation induce swelling and swelling stress keeps increasing until reaching the swelling capacity of 5 MPa. Figure 2-39 zooms in to show the stress from 4.5 to 5 MPa and illustrate the contribution from ion concentration and smectite changes. In comparison with the swelling stress for Kunigel-VI bentonite at point A, presented in Section 2.3.1.2, the swelling stress for FEBEX bentonite has two distinct features. First, ion concentration has a minimal effect on the swelling stress because the ion concentration of the pore water in FEBEX bentonite is fairly close to that in the clay formation. Second, a greater stress reduction due to smectite dissolution has been observed for FEBEX bentonite. Despite that, less smectite dissolution has been observed for FEBEX bentonite (Figure 2-26) and a higher A_{sc} (a parameter that relates swelling stress with the abundance of smectite) for FEBEX bentonite leads to slightly higher reduction in swelling stress. Table 2-5 lists the stress reduction by ion concentration and smectite dissolution at point A for Kunigel-VI and FEBEX bentonites. In total, chemical changes leads to about 0.17 MPa stress change for Kunigel-VI bentonite and 0.18 MPa for FEBEX bentonite. In comparison with the swelling stress obtained with "σ=f(Sl)", chemical change causes about 16% reduction in swelling stress for Kunigel-VI bentonite, but only 3.4% for FEBEX bentonite.

Model results at point B (Figures 2-40 and 2-41) lead to the same observation in terms of the difference between Kunigel-VI and FEBEX bentonite, although the specific values differ significantly from those at point A. As we discussed in the previous section, because of the interaction between bentonite and the clay formation, bentonite near the interface goes through further dissolution of smectite after about 20,000–30,000 years when the dissolution of smectite in bentonite near the waste package become stable, which lead to further decrease in swelling stress. By the end of 100,000 years, as illustrated in Figure 2-41 and articulated in the Table 2-5, Kunigel-VI bentonite has lost more than half of its swelling capacity whereas FEBEX bentonite has lost about 13% of its swelling capacity. Generally speaking, in absolute numbers, Kunigel-VI and FEBEX bentonites undergo similar magnitudes of reduction in swelling stress, but relative to their swelling capacity (the maximum swelling stress which is typically measured by hydrating bentonite with deionized water), chemical changes cause a stronger reduction in swelling capacity for Kunigel-VI than for FEBEX bentonite. Therefore, using bentonite with a high swelling capacity such as FEBEX bentonite is always beneficial with respect to stress reduction caused by illitization.

Table 2-5. The geochemically induced swelling stress for Kunigel and FEBEX bentonite at points A and B for "high T" scenario. Stress reduction by ion concentration is the difference between the swelling stress obtained with "σ=f(Sl)" and "σ=f(Sl,C)", and the stress reduction by smectite dissolution is the difference between the swelling stress obtained with "σ=f(Sl,C)" and "σ=f(Sl,C,Ms)" (see Figure 2-26), where the relative amount (%) use the results from "σ=f(Sl)" as the basis.

	Kunigel-VI bentonite				FEBEX bentonite			
	Stress reduction by ion concentration		Stress reduction by smectite dissolution		Stress reduction by ion concentration,		Stress reduction by smectite dissolution	
	MPa	%	MPa	%	MPa	%	MPa	%
Point A	0.07	7%	0.09	9%	0.006	0.1%	0.17	3.4%
Point B	0.08	8%	0.45	45%	0.06	1.1%	0.6	12%

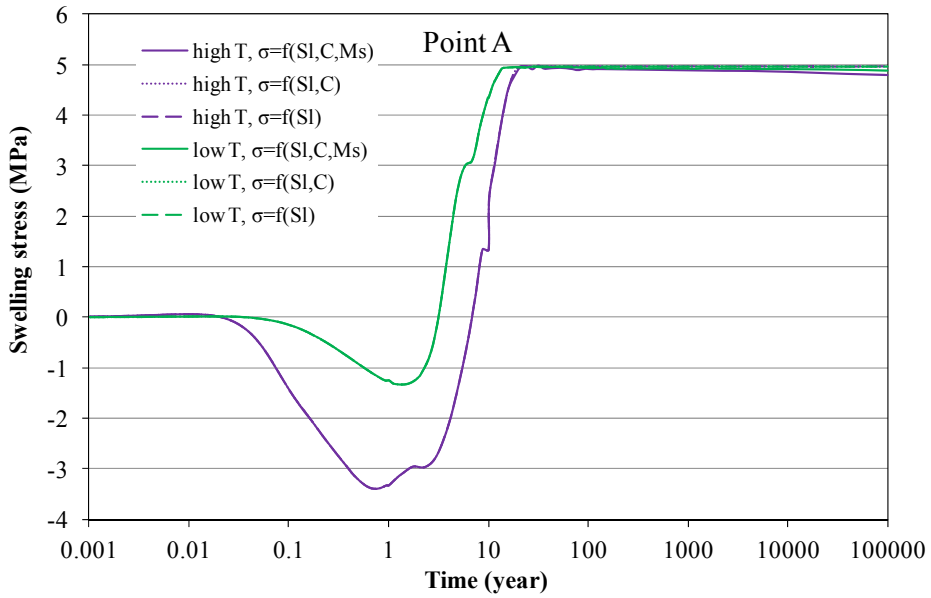

Figure 2-38. Simulation results of swelling stress at point A for the FEBEX bentonite for the "low T" and "high T" scenarios, respectively, focusing on the stress range from 4.5 to 5 MPa.

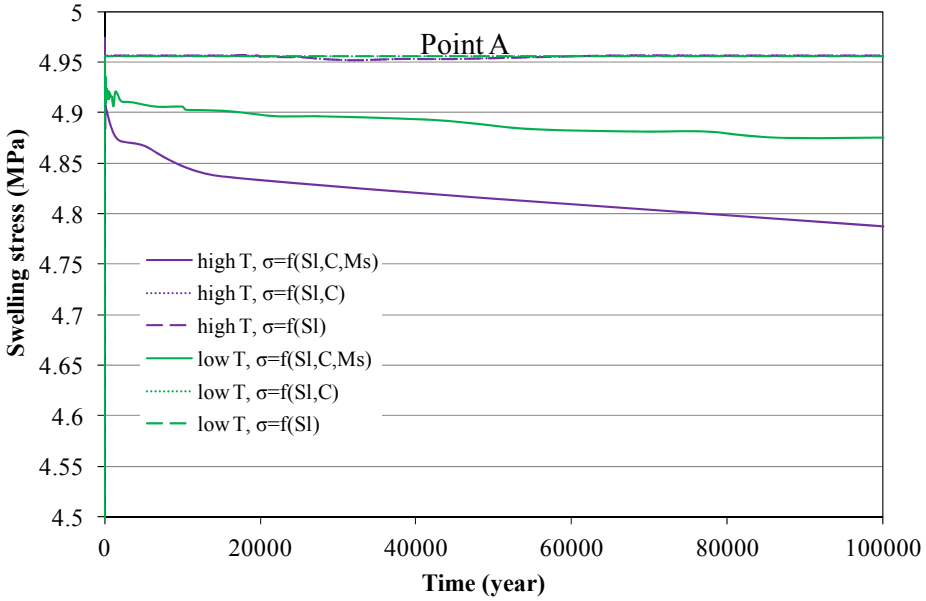

Figure 2-39. Simulation results of swelling stress at point A for the FEBEX bentonite for the "low T" and "high T" scenarios, respectively, focusing on the stress range from 4.5 to 5 MPa.

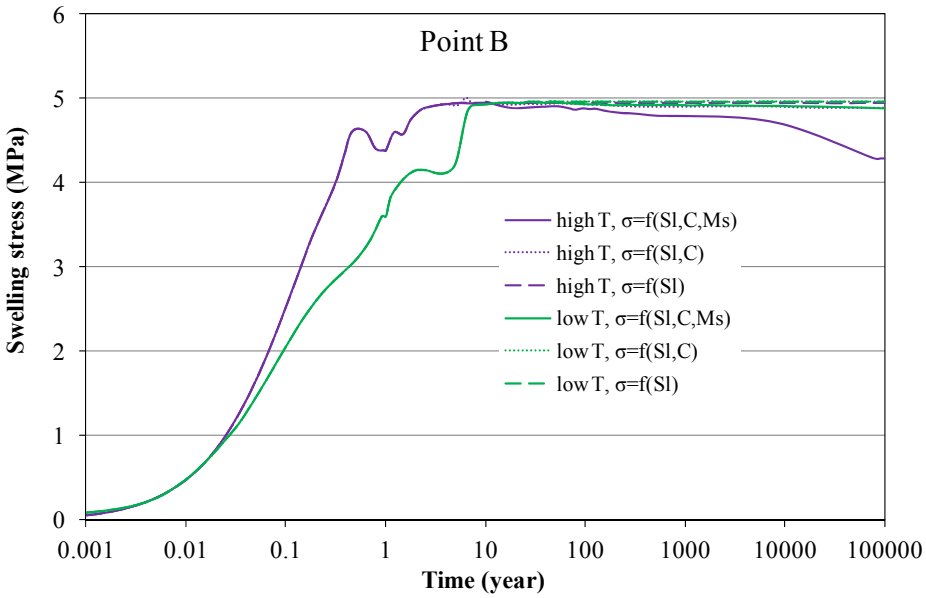

Figure 2-40. Simulation results of swelling stress at point B for the FEBEX bentonite for the "low T" and "high T" scenarios, respectively, focusing on the stress range from 4.5 to 5 MPa.

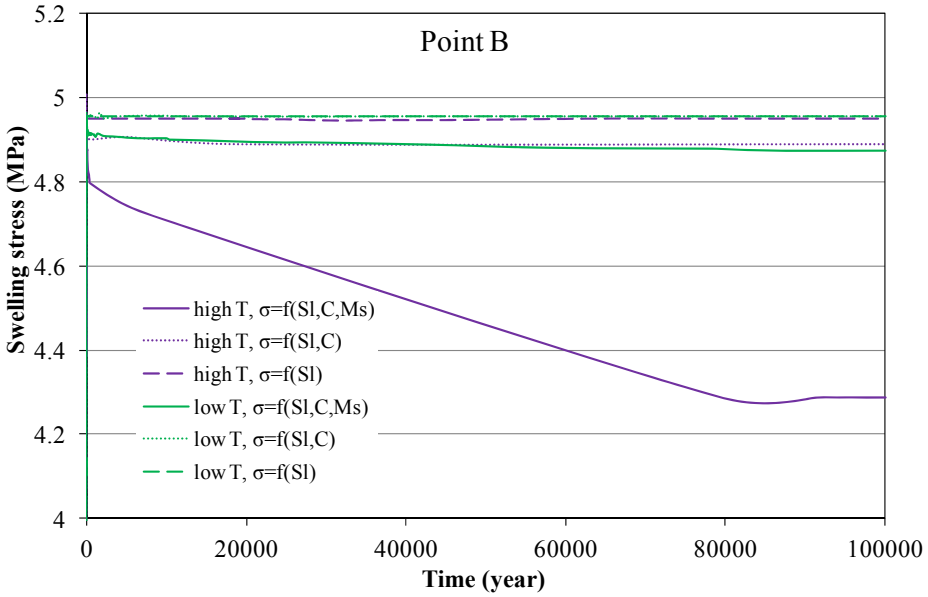

Figure 2-41. Simulation results of swelling stress at point B for the FEBEX bentonite for the "low T" and "high T" scenarios, respectively, focusing on the stress range from 4.5 to 5 MPa.

2.4 Conclusions

2.4.1 Summary of current modeling work

This report documents our progress in FY15 to investigate the impact of strongly elevated temperature on the bentonite backfill and near-field clay host rock in a geologic repository for radioactive waste. Since FY13, we have been using coupled THMC modeling to evaluate the chemical alteration and associated mechanical changes in a generic repository to consider the interaction between EBS bentonite and the NS clay formation. Two main scenarios were developed for comparison: a "high T" case in which the temperature near the waste package can reach about 200 ^{o}C and a "low T" scenario in which the temperature peaks at about 100 ^{o}C. Conducting coupled THMC modeling is very challenging — it requires significant expansion of our modeling capability in terms of considering more processes and improving the numerical stability and efficiency of the current simulator TOUGHREACT-FLAC3D. One of the major achievements in FY15 is the implementation of a time-step management scheme in the TOUGHREACT-FLAC3D simulator to reduce the simulation time, which enables us to extend the simulations from 1,000 years to 100,000 years. The simulator was also revised to include chemical-mechanical coupling for clay formations. We also performed an evaluation of Ca-smectite illitization, which sheds light on the potential for calcite to interfere with smectite illitization.

Our model results for 100,000 years confirm some findings from the 1,000-year simulations (Liu et al., 2013; Zheng et al., 2014). There is some degree of illitization in the EBS bentonite and NS clay formation and illitization is enhanced under higher temperature. In addition to illitization, major chemical alterations include the dissolution of K-feldspar and calcite, the precipitation of quartz, chlorite, and kaolinite. The quantity of illitization, expressed as the smectite volume

fraction change, is affected by many chemical factors and as a result varies over a wide range. The most important chemical factors for illitization are the concentration of K and dissolution rate of K-feldspar. However, 100,000-year simulations also lead to some distinct observations regarding illitization, especially for the high temperature condition:

- Model results reveals that for the "high T" scenario, illitization is stabilized after about 2,000 years in bentonite near the waste package, but continues in bentonite near the EBS-NS interface. For the "low T' scenario, illitization is nearly stabilized after 2,000 years for the entire volume of EBS bentonite.
- The geochemical interaction between EBS bentonite and the clay formation has a strong effect on long term illitization in bentonite. Previous simulations, namely the 1,000-years simulations in Liu et al., (2013) and Zheng et al., (2014), showed that illitization reactions in bentonite are tied to the dissolution rate of K-feldspar that occurs locally, and as a result, illitization is fairly homogeneous in the entire bentonite barrier. However, the 100,000-year simulations show that bentonite near the EBS-NS interface undergo more illitization than that near the waste package by the end of 100,000 years for the "high T' scenarios. The reason is that after 2,000–3,000 years, the illitization process ceases in the clay formation and the K ion is not consumed by the local illitization and is, therefore, transported into the EBS bentonite to facilitate further illitization.
- The dissolution rate of K-feldspar, which was thought to be critical for illitization as revealed by the 1,000-years simulations, is not as important as the amount of K-feldspar available for longer time periods. The reason is that fast dissolution of K-feldspar leads to a quicker depletion of K-feldspar (in about 1,000 years) that permits greater illitization to occur within 1,000 years. However, for the 100,000 year time period, the amount of K-feldspar available controls how much illitization can occur rather than the dissolution rate of K-feldspar.

The simulations conducted in FY15 also reveal that the dissolution of calcite delays illitization by around 30 to50 years for the case of Kunigel-VI and FEBEX bentonite if Ca-smectite is the major smectite phase in the bentonite. Although this effect is short-lived and not important as far as long-term illitization is concerned, calcite dissolution might explain why illitization was not observed in some laboratory and field experiments.

In terms of the effect of chemical changes on swelling stress for bentonite, the current modeling results show a more significant reduction in swelling stress as a result of smectite dissolution after 100,000 years than previously revealed by the 1,000-years simulations. This is particularly true for bentonite near the EBS-NS interface as illitization continues in these areas. For the "high T" case, Kunigel-VI bentonite near the EBS-NS loses as much as 53% swelling capacity and FEBEX bentonite near the EBS-NS has about 13% reduction in swelling stress, whereas bentonite near the waste package undergoes a small reduction in swelling stress — 16% reduction for Kunigel-VI and 3.4% for FEBEX bentonite, respectively. For the "low T" case, the stress reduction by chemical change is relatively homogeneous, 16% reduction for Kunigel-VI bentonite and around 3% reduction for FEBEX bentonite after 100,000 years.

In FY15, chemical effects were incorporated in the mechanical model for the clay formation and the effect of chemical change in clay formation on the total stress was evaluated. Chemical change leads to about a 2.6% decrease in stress near the EBS-NS interface and about 0.7% in the

far field. In general, chemical change does not have significant impact on the stress in the clay formation.

2.4.2 FUTURE WORK

The current coupled THMC model greatly improves our understanding of the coupled processes contributing to chemical and mechanical alteration in EBS bentonites and NS argillite formations and answers questions regarding the thermal limit of EBS bentonite in clay repository. However, more questions remain to be answered regarding the THMC alteration of bentonites and clay formations under high temperature. Further refinement of current models and improvements for the TOUREACT-FLAC3D simulator are needed in the future. In the remaining months of FY15 and FY16 the following activities are proposed:

- A more rigorous approach to link chemistry to mechanics is needed for more accurate calculations than the current extended linear elastic swelling model. More comprehensive links between chemistry and mechanics, taking advantage of the framework provided by a dual-structure model, was implemented in TOUGHREACT-FLAC (Rutqvist et al., 2014), and could be used to simulate the chemical-mechanical coupling for EBS bentonite in the future.
- In the current model, the canister serves only as a heat source; chemical changes on the surface of the canister are neglected for simplification. Further model analysis is needed to consider chemical changes in the canister, specifically the release of Fe^{+2}, which might enhance the dissolution of smectite by forming chlorite.
- Current models show significant precipitation of silicate minerals during illitization, which could result in the cementation of bentonite and subsequently lead to change in the mechanical properties of bentonite. While the current model can quantify the formation of silicate minerals, the change of mechanical properties as result of cementation needs to be quantified. This requires a mechanical-chemical coupling scheme for cementation to be incorporated and tested in the next version of the simulator.

References

Alonso, E. E., J. Vaunat and A. Gens 1999. Modeling the mechanical behaviour of expansive clays. Engineering Geology 54: 173-183.

Bossart P. (2011) Characteristics of the Opalinus Clay at Mont Terri, http://www.mont-terri.ch/internet/mont-terri/en/home/geology/key_characteristics.html

Börgesson, L., Chijimatsu, M., Nguyen, T.S., Rutqvist, J., Jing L. (2001) Thermo-hydro-mechanical characterization of a bentonite-based buffer material by laboratory tests and numerical back analyses. Int. J. Rock Mech. & Min. Sci. 38, 105-127.

Bucher, F., and Müller-Vonmoos, M. (1989) Bentonite as a containment barrier for the disposal of highly radioactive waste. Applied Clay Science, 4(2): 157–177.

Castellanos, E., M. V. Villar, E. Romero, A. Lloret and A. Gens 2008. Chemical impact on the hydro-mechanical behaviour of high-density FEBEX bentonite. Physics and Chemistry of the Earth, Parts A/B/C 33, Supplement 1(0): S516-S526.

Chen, Y., C. Zhou and L. Jing 2009. Modeling coupled THM processes of geological porous media with multiphase flow: Theory and validation against laboratory and field scale experiments. Computers and Geotechnics 36(8): 1308-1329.

Cuadros, J. 2006. Modeling of smectite illitization in burial diagenesis environments. Geochimica et Cosmochimica Acta 70(16): 4181-4195.

ENRESA 2000. Full-scale engineered barriers experiment for a deep geological repository in crystalline host rock FEBEX Project, European Commission: 403.

Fernández, A. M., B. Baeyens, M. Bradbury and P. Rivas (2004). Analysis of the porewater chemical composition of a Spanish compacted bentonite used in an engineered barrier. Physics and Chemistry of the Earth, Parts A/B/C 29(1): 105-118.

Fernández, A., Cuevas, J., Rivas, P., 2001. Pore water chemistry of the FEBEX bentonite. Mat. Res. Soc. Symp. Proc. 663, 573–588.

Fernández, A. M., Turrero, M. J., Sánchez, D. M., Yllera, A., Melón, A. M., Sánchez, M., Peña, J., Garralón, A., Rivas, P., Bossart, P. and Hernán, P. (2007) On site measurements of the redox and carbonate system parameters in the low-permeability Opalinus Clay formation at the Mont Terri Rock Laboratory. Physics and Chemistry of the Earth, Parts A/B/C 32(1-7): 181-195.

Horseman S.T. and McEwen, T. J. (1996) Thermal constrains on disposal of heat-emitting waste in argillaceous rocks, Engineering Geology 41, 5-16.

Hicks, T.W., White, M.J. and Hooker, P.J. (2009) Role of Bentonite in Determination of Thermal Limits on Geological Disposal Facility Design, Report 0883-1, Version 2, Falson Sciences Ltd., Rutland, UK, Sept. 2009.

Itasca, 2009. FLAC3D, Fast Lagrangian Analysis of Continua in 3 Dimensions, Version 4.0, Minneapolis, Minnesota, Itasca Consulting Group.

JNC, Japan Nuclear Cycle Development Institute. (1999) H12: project to establish the scientific and technical basis for HLW disposal in Japan: supporting report 2 (respiratory design and engineering Technology). Japan Nuclear Cycle Development Institute, Tokyo.

Komine, H., and Ogata, N. (1996) Prediction for swelling characteristics of compacted bentonite. Canadian Geotechnical Journal, 33: 11–22.

Karnland, O., Olsson, S. and Nilsson, U. (2006) Mineralogy and sealing properties of various bentonites and smectite-rich clay materials, SKB Technical Report TR-06-30.

Laredj, N., Missoum, H. and Bendani, K. (2010) Modeling the effect of osmotic potential changes on deformation behavior of swelling clays. Journal of Porous Media 13(8): 743-748.

Lasaga, A. C., J. M. Soler, J. Ganor, T. E. Burch and K. L. Nagy 1994. Chemical weathering rate laws and global geochemical cycles. Geochimica et Cosmochimica Acta 58: 2361-2368.

Lauber, M., B. Baeyens and Bradbury, M. H. (2000) Physico-Chemical Characterisation and Sorption Measurements of Cs, Sr, Ni, Eu, Th, Sn and Se on Opalinus Clay from Mont Terri. PSI Bericht Nr. 00-10 December 2000 ISSN 1019-0643.

Liu, H.H., J. Houseworth, J. Rutqvist, L. Zheng, D. Asahina, L. Li, V. Vilarrasa, F. Chen, S. Nakagawa, S. Finsterle, C. Doughty, T. Kneafsey and J. Birkholzer. (2013) Report on THMC modeling of the near field evolution of a generic clay repository: Model validation and demonstration, Lawrence Berkeley National Laboratory, August, 2013, FCRD-UFD-2013-0000244.

Nguyen, T. S., A. P. S. Selvadurai and G. Armand 2005. Modelling the FEBEX THM experiment using a state surface approach. International Journal of Rock Mechanics and Mining Science 42(5-6): 639-651.

Ochs, M., Lothenbach, B., Shibata, M. and Yui, M. (2004) Thermodynamic modeling and sensitivity analysis of porewater chemistry in compacted bentonite. Physics and Chemistry of the Earth, Parts A/B/C 29(1): 129-136.

Pusch R. and Karnland, O. (1996) Physico/chemical stability of smectite clays, Engineering Geology 41: 73-85.

Pusch, R., Kasbohm, J. and Thao, H. T. M. (2010) Chemical stability of montmorillonite buffer clay under repository-like conditions—A synthesis of relevant experimental data. Applied Clay Science 47(1–2): 113-119.

Pusch, R. and Madsen, F. T. (1995) Aspects on the illitization of the kinnekulle bentonites. Clays and Clay Minerals 43(3): 261-270.

Ramírez, S., J. Cuevas, R. Vigil and S. Leguey 2002. Hydrothermal alteration of "La Serrata" bentonite (Almeria, Spain) by alkaline solutions. Applied Clay Science 21(5–6): 257-269.

Rutqvist, J., Y. Ijiri and H. Yamamoto 2011. Implementation of the Barcelona Basic Model into TOUGH–FLAC for simulations of the geomechanical behavior of unsaturated soils. Computers & Geosciences 37(6): 751-762.

Rutqvist, J., Zheng, L., Chen, F., Liu, H.-H. and Birkholzer, J. (2013). Modeling of Coupled Thermo-Hydro-Mechanical Processes with Links to Geochemistry Associated with Bentonite-Backfilled Repository Tunnels in Clay Formations. Rock Mechanics and Rock Engineering: 1-20.

Rutqvist, J., Zheng, L., Chen, F., Liu, H.-H. and Birkholzer, J. (2014) Modeling of Coupled Thermo-Hydro-Mechanical Processes with Links to Geochemistry Associated with Bentonite-Backfilled Repository Tunnels in Clay Formations. Rock Mechanics and Rock Engineering: 47(1): 167-186.

Sánchez, M., A. Gens, L. J. D. N. Guimarães and S. Olivella 2005. A double structure generalized plasticity model for expansive materials. International Journal for numerical and analytical methods in geomechanics 29: 751-787.

Soler, J. M. 2001. The effect of coupled transport phenomena in the Opalinus Clay and implications for radionuclide transport. Journal of Contaminant Hydrology 53: 63-84.

Sonnenthal, E. Chapter 5 in: Birkholzer, J. Rutqvist, E. Sonnenthal, and D. Barr, Long-Term Permeability/Porosity Changes in the EDZ and Near Field due to THM and THC

Processes in Volcanic and Crystalline-Bentonite Systems, DECOVALEX-THMC Project Task D Final Report, 2008.

Wersin P., Johnson, L.H. and McKinley, I.G. (2007) Performance of the bentonite barrier at temperature beyond 100oC: A critical review, Physics and Chemistry of the Earth 32: 780-788.

Wolery, T. J. 1993. EQ3/6, A software package for geochemical modelling of aqueous systems (Version 7.2). , Lawrence Livermore National Laboratory.

Xu, T., E. Sonnenthal, N. Spycher and K. Pruess 2006. TOUGHREACT: A Simulation Program for Non-isothermal Multiphase Reactive Geochemical Transport in Variably Saturated Geologic Media. Computers and Geosciences 32: 145-165.

Xu, T., Spycher, N., Sonnenthal, E., Zhang, G., Zheng, L. and Pruess, K. (2011) TOUGHREACT Version 2.0: A simulator for subsurface reactive transport under non-isothermal multiphase flow conditions. Computers & Geosciences 37(6): 763-774.

Zheng, L., Li, L., Rutqvist, J., Liu, H. and Birkholzer, J.T., (2012). Modeling Radionuclide Transport in Clays. Lawrence Berkeley National Laboratory. FCRD-URD-2012-000128

Zheng, L., J. Samper and L. Montenegro 2011. A coupled THC model of the FEBEX in situ test with bentonite swelling and chemical and thermal osmosis. Journal of Contaminant Hydrology 126(1–2): 45-60.

Zheng, L., Jonny Rutqvist, Carl Steefel, Kunhwi Kim, Fei Chen, Victor Vilarrasa, Seiji Nakagawa, Jiangtao Zheng, James Houseworth, Jens Birkholzer. (2014) Investigation of Coupled Processes and Impact of High Temperature Limits in Argillite Rock. FCRD-UFD-2014-000493, LBNL-6719E.

3. DEVELOPING THMC MODELS FOR FEBEX-DP

3.1 Introduction

The multi-barrier system in a nuclear waste repository typically consists of the natural barrier system (NBS), which includes the repository host rock and its surrounding subsurface environment, and the engineered barrier system (EBS). The EBS represents the man-made, engineered materials placed within a repository, including the waste form, waste canisters, buffer materials, backfill, and seals (OECD 2003).

The most common buffer material for EBS is compacted bentonite, which features low permeability and high retardation of radionuclide transport. The safety functions of EBS bentonite include limiting transport in the near field; damping the shear movement of the host rock; preventing the sinking of canisters (if emplaced in the center of the tunnel), limiting pressure on the canister and rock, and reducing microbial activity. To assess whether EBS bentonite can maintain these favorable features when undergoing heating from the waste package and hydration from the host rock, we need a thorough understanding of the thermal, hydrological, mechanical, and chemical evolution of bentonite under disposal conditions. While numerous laboratory experiments, field tests, and numerical models have been conducted to improve the understanding of each individual process or coupled THC/THM processes, there is a lack of studies on coupled THMC processes due to the challenges of conducting experiments and developing models that can cover all the THMC processes. Recently in the UFD program, coupled THMC models have been developed for a generic disposal system in clayey host rock with EBS bentonite (Liu et al., 2013; Zheng et al., 2014). However, model validation was difficult for lack of THMC data from long-term, large-scale experiments. The FEBEX (Full-scale Engineered Barrier EXperiment) *in situ* test, which has been operated for 18 years, provides a unique opportunity of validating coupled THMC models.

In the FEBEX *in situ* test, two heaters surrounded by bentonite blocks about 0.7 m thick were emplaced in a tunnel excavated in granite. The heaters were switched on in 1997. In 2002, heater 1 was dismantled; in 2015, the second heater is being dismantled in the FEBEX-DP project, which is comprised of extensive THMC and biological characterization of bentonite, and development of numerical models. LBNL/DOE joined FEBEX-DP project in FY15. The ultimate goal is to use THMC data from FEBEX-DP to validate THMC models and therefore enhance our understanding of coupled THMC process. In this section, we describe our progress in FY15, which includes the development of a TH model with Non-Darcian flow, a coupled THC model, and evaluation of these models with TH data obtained from the bentonite surrounding heater 2 and chemical data obtained from the dismantling of heater 1.

3.2 A Brief Description of FEBEX Experiments

The objective of the FEBEX experiment was to study the behavior of components in the near-field for a high-level radioactive waste (HLW) repository in crystalline rock. Specifically, the project aimed to demonstrate the feasibility of fabricating and assembling the EBS and developing methodologies and models for evaluation of the thermo-hydro-mechanical (THM) and thermo-hydro-chemical (THC) behavior of the near-field (ENRESA, 2000). These objectives

were to be attained through the combination of *in situ* and mock-up tests, and numerous small scale laboratory tests, and THC/THM modeling. The project was initially scheduled for a period of 7 years, from 1994 to 2001, but was extended several times as the experiments continued. Figure 3-1 shows the history of FEBEX projects, with different project names representing different operational stages. In 2002, the *in situ* test was partially dismantled — the heater 1 was turned off and the bentonite blocks surrounding heater 1 were sampled for THM/THC characterization. The final dismantling started in April 2015 and is expected to finish in August 2015.

Figure 3-1. The operational stages of FEBEX *in situ* test (Vomvoris, personal communication).

The bentonite used in the FEBEX project was from the Cortijo de Archidona deposit in the south of Spain. It has about 92% mass fraction of smectite, with a dry density of 1.6–1.7 g/cm^3 and a swelling pressure of around 5 MPa. The average permeability of FEBEX bentonite is on the order of 10^{-21} m^2. Extensive THMC characterization of FEBEX bentonite was conducted at the early stage of the FEBEX project.

Small scale THM/THC experiments were also conducted to improve the understanding of the THM/THC changes in bentonite under simultaneous heating and hydration, which facilitated the design of large scale experiments and helped the calibration of key parameters for THM/THC models. Figure 3-2 shows an example of a THC experiment. A 4.29 kg FEBEX bentonite block 13 cm in height and 15 cm in diameter was placed in a stainless steel cylindrical hermetic cell (Figure 3-2). A heater maintained a constant temperature of 87.5 °C in the upper part of the cell. At the same time, the lower part of the bentonite block was hydrated with distilled water injected at a pressure of 1 MPa through a 2.4 cm thick porous stone. After 183 days of heating and hydration, the heater was switched off, hydration was stopped and the bentonite sample was allowed to reach the ambient temperature. Then, the bentonite block was sliced into five sections to measure the aqueous concentration of pore water.

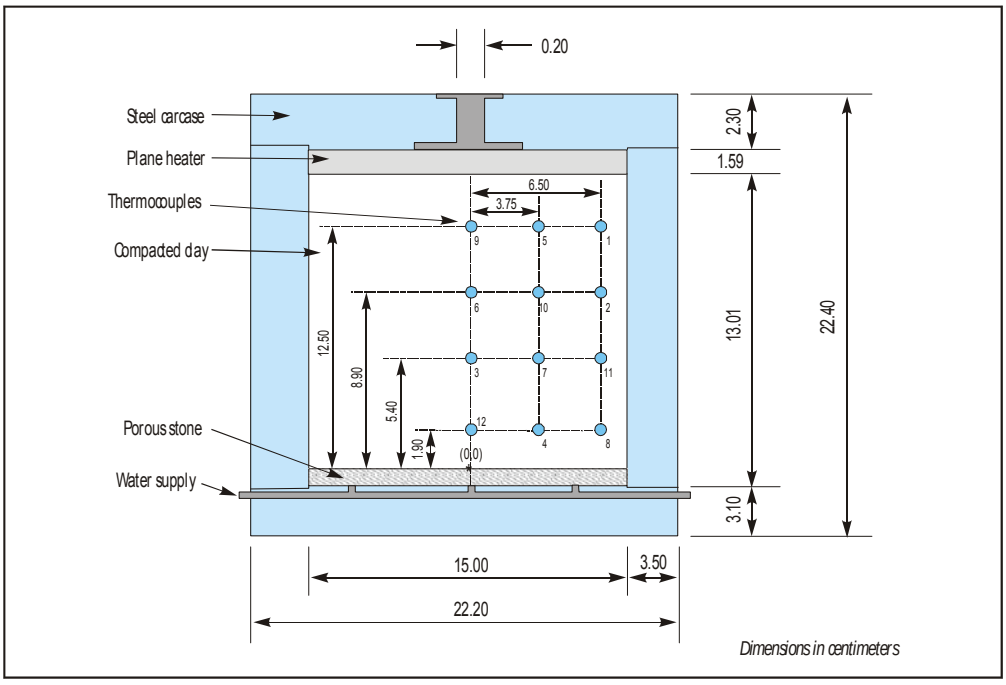

Figure 3-2. Schematic design of the heating and hydration laboratory experiment in the cell CT23 (ENRESA, 2006a).

In parallel with the *in situ* test, a mock-up test was conducted at CIEMAT facilities in Madrid, Spain (Martín and Barcala, 2005; Martín et al., 2006). Components of the mock-up test (Figure 3-3) are similar to those of *in situ* test: two electric heaters, a 0.64 m-thick bentonite barrier, instrumentation, automatic control of heaters, and a data-acquisition system. In the mock-up test the buffer is confined in a steel structure which ensures a uniform temperature and water pressure around the external surface of the buffer (Figure 3-3). The clay barrier is made of compacted bentonite blocks of dry density of 1.7 Mg/m^3. Heating and hydration of the clay buffer started in February 1997 and has continued uninterruptedly until now.

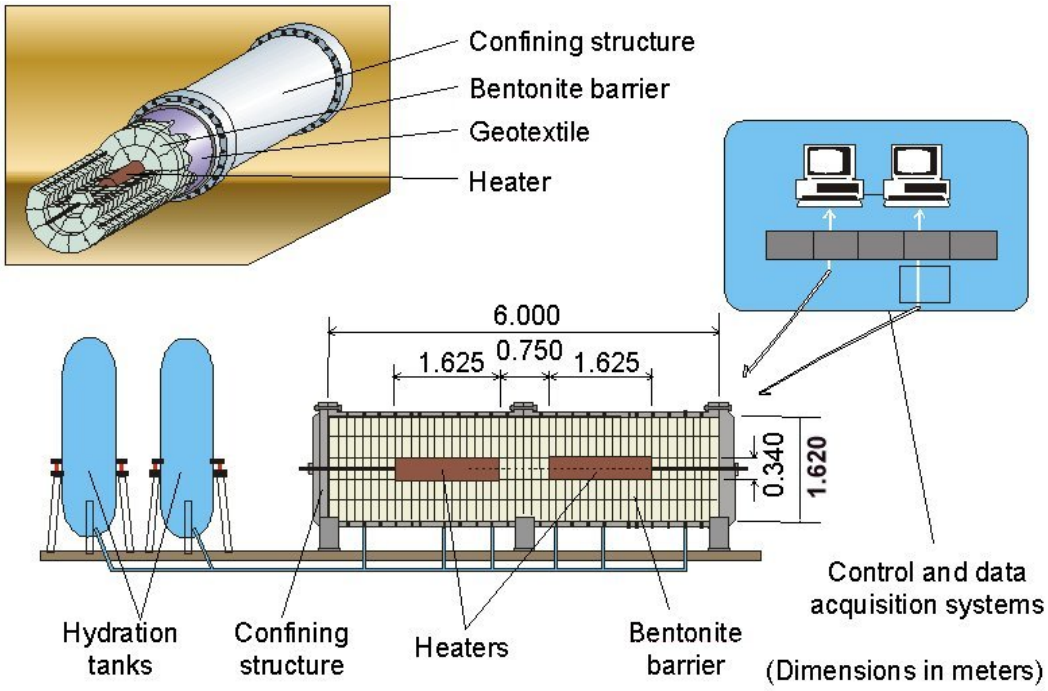

Figure 3-3. Schematic design of mock-up test (Martín et al., 2006).

The centerpiece of FEBEX experiments is, of course, the *in situ* test conducted at the Grimsel underground laboratory, Switzerland. The test consists of five basic units: the drift, the heating system, the bentonite barrier, the instrumentation, and the monitoring and control system (Figure 3-4). The drift is 70.4 m long and 2.28 m in diameter. The test area which was sealed with a concrete plug is located at the last 17.4 m of the drift where heaters, bentonite and instrumentation were installed. The main elements of the heating system are two heaters (1 and 2), 1 m apart, which simulate full-sized canisters. Heaters were placed inside a cylindrical steel liner. Each heater is made of carbon steel, measures 4.54 m in length and 0.9 m in diameter, and has a wall thickness of 0.1 m. Heaters were operated at a constant power output of 1200 W/heater during the first 20 days and 2000 W/heater for the following 33 days. Afterwards, the heaters were switched to a constant-temperature control mode to maintain a maximum temperature of 100 ºC at the steel liner/bentonite interface.

The bentonite barrier is made of blocks of highly compacted bentonite, situated in vertical sections normal to the axis of the tunnel. The average values of the initial dry density and the water content of bentonite blocks are 1.7 g/cm^3 and 14.4%, respectively.

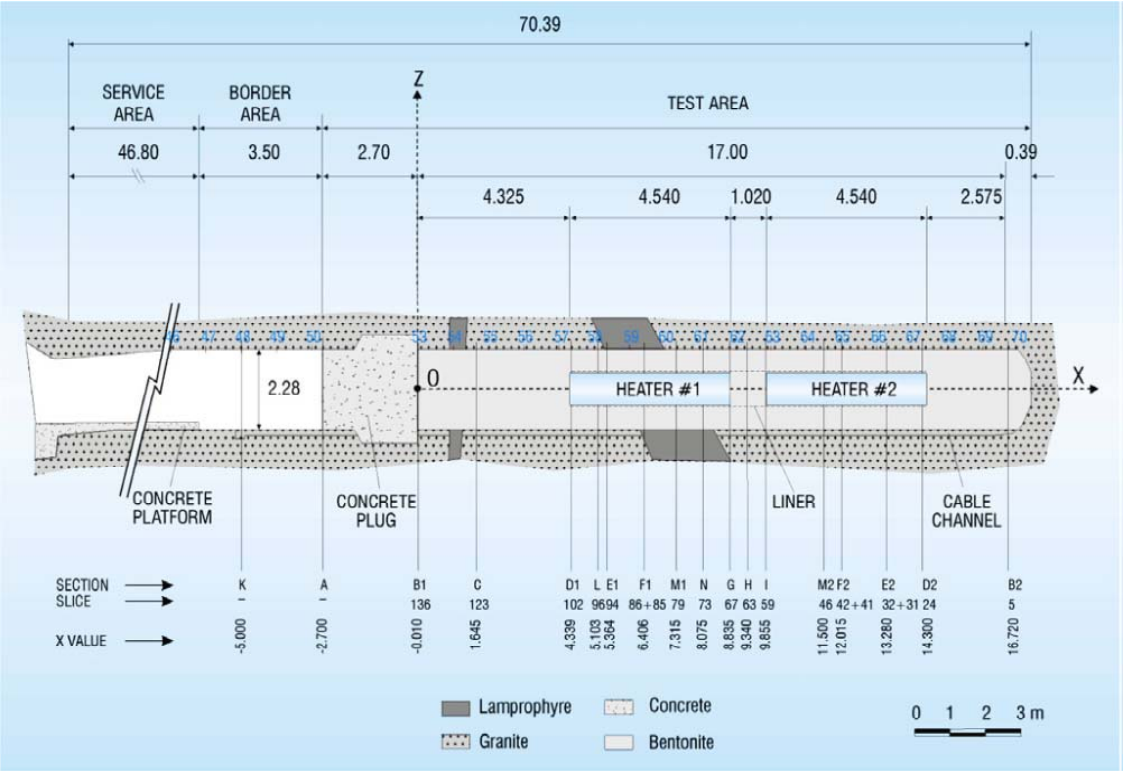

Figure 3-4. The initial configuration of FEBEX in situ test at the Grimsel underground laboratory (Switzerland) (ENRESA, 2000).

The *in situ* test began on February 27, 1997. Heater 1 was switched off in February 2002 and dismantled from May to September 2002. A comprehensive post-mortem bentonite sampling and analysis program was performed on the solid and liquid phases to check the physical and chemical changes induced by the combined effect of heating and hydration and to test THM and THC model predictions (ENRESA 2006a, b). Figure 3-5 shows the moisture content at section 15 after the dismantling of heater 1. The location of section 15 is shown in Figure 3-6. Note that the sections during dismantling of heater 1 are different from that was originally designated in the initial configuration as shown in Figure 3-4.

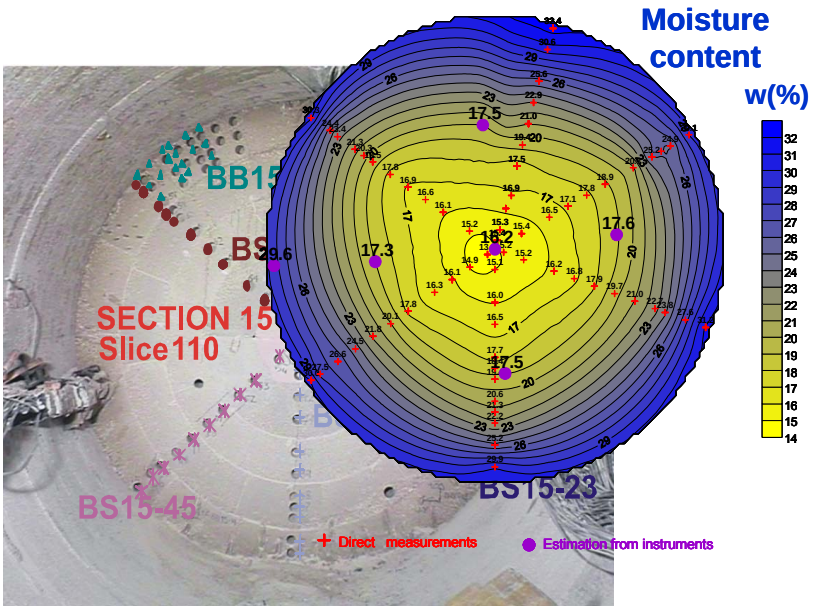

Figure 3-5. The moisture content (gravimetric water content) at section 15(Vomvoris, personal communication).

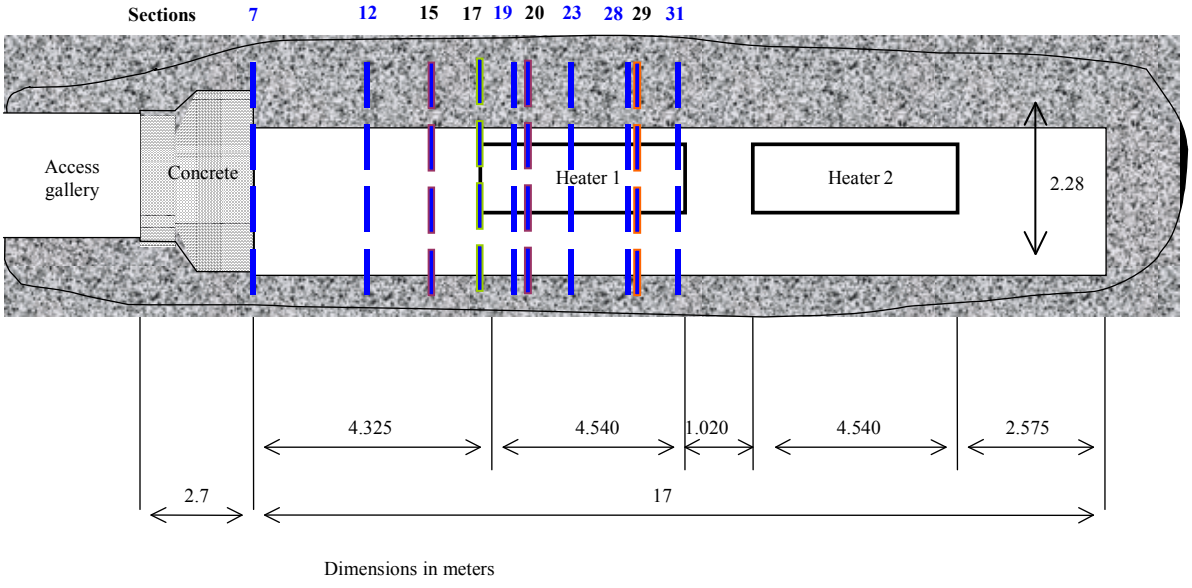

Figure 3-6. Layout of the sampling sections during the dismantling of heater 1 in 2002. In blue color are the common sections for THG and THM analyses (Fernandez and Rivas, 2003)

After the dismantling of heater 1, the tunnel was plugged with shotcrete (Figure 3-7) and heater 2 was kept working under normal conditions to maintain a constant 100 ^{o}C at the steel liner/bentonite interface. In 2014, considering that changes in the state of bentonite buffer is very slow and it is unlikely for bentonite to reach fully saturation in the project lifetime, decision was

made to dismantle the heater 2. On April 24, 2015, heater 2 was switched off. After a short cool off time period, samples were taken for THMC and microbiological characterization.

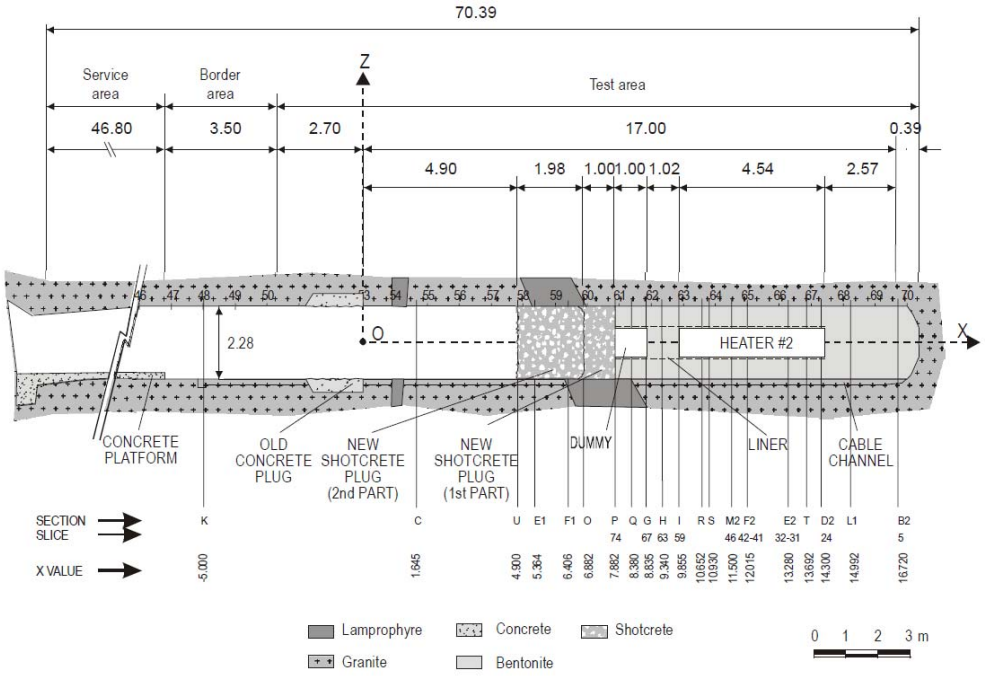

Figure 3-7. *In situ* test configuration following dismantling of heater 1 (Huertas et al., 2005)

The long-term FEBEX *in situ* test with comprehensive THMC data provides a unique opportunity to validate coupled THMC models and strengthen our understanding of the coupled processes in bentonite. In addition, experiments at different scales with the same type of bentonite are also very useful to evaluate the key parameters obtained at different scales and study the scaling effect of modeling THMC processes. Up to now, several THM/THC models have been developed to interpret the FEBEX experiments, including the THM model for the mock-up test (Sánchez et al., 2005; 2012a) and *in situ* test (Sánchez et al., 2012b), and THC models for the small scale heating and hydration experiment (Zheng et al., 2010), mock-up test (Zheng and Samper, 2008), and *in situ* tests (Samper et al., 2008a; Zheng et al., 2011).

3.3 Model Development

In this section, we describe the model development effort so far in FY15, starting from a TH model and then building THC models; eventually a coupled THMC models will be completed in the future.

3.3.1 Simulator

The numerical simulations are conducted with TOUGHREACT-FLAC3D, which sequentially couples the multiphase fluid flow and reactive transport simulator, TOUGHREACT (Xu et al., 2011), with the finite-difference geomechanical code FLAC3D (Itasca, 2009). The coupling of TOUGHREACT and FLAC was initially developed in Zheng et al. (2012) to provide the necessary numerical framework for modeling fully coupled THMC processes. It was equipped

with a linear elastic swelling model (Zheng et al., 2012; Rutqvist et al., 2013) to account for swelling as a result of changes in saturation and pore-water composition and the abundance of swelling clay (Liu et al., 2013; Zheng et al., 2014). A recent addition to the code is the capability of simulating Non-Darcian flow.

Non-Darcian flow refers to a phenomenon where the flux is not linearly proportional to the hydraulic gradient. It has been fairly well known for clay media, as manifested in the "pressure seal" studies in the petroleum literature (Deming, 1994). Researchers have proposed different relationship to describe non-Darcian flow, such as the flux being proportional to a power function (Hansbo, 1960; 2001), or exponential function (Swartzendruber,1963), of hydraulic gradient. Zou (1996) developed a nonlinear flux-gradient relationship depending on the activation energy of pore liquid. Liu and Birkholzer (2012) proposed more generalized equations that encompass the relationship proposed by other researchers, which are given below and implemented in the simulator.

$$q = K[i - \frac{I}{\gamma(\frac{1}{\alpha})}\gamma(\frac{1}{\alpha},\left(\frac{i}{I*}\right)^{\alpha})] \tag{3-1}$$

where q (m/s) is the water flux, K(m/s) is the hydraulic conductivity, and I is the threshold gradient. I* is calculated as:

$$I* = \frac{I \cdot \alpha}{\gamma\left(\frac{1}{\alpha}\right)} \tag{3-2}$$

γ refers to Gamma functions

$$\gamma(a,x) = \int_0^x t^{a-1}e^{-t}dt \tag{3-3}$$

$$\gamma(a) = \int_0^\infty t^{a-1}e^{-t}dt \tag{3-4}$$

where α and I are fitting parameters. Liu and Birkholzer (2012) found out that α = 5 leads to a good match between Equation (3-1) and data. How to calculate the threshold gradient will be discussed later.

3.3.2 Modeling Setup

As shown in Figure 3-5, the hydration of bentonite is fairly symmetrical, and radial symmetry has also been observed for heating (as shown later in Figures 3-9 to 3-12). We therefore use an axi-symmetrical mesh (Figure 3-8) to save computation time so that we can focus on the key coupling processes. However, such a model can only be used to interpret and predict the THMC behavior in the "hot" sections, i.e. sections of bentonite block surrounding the heater such as section F1 and F2 in Figure 3-4. 3-D models that have both "hot" and "cold" sections could be developed in the future.

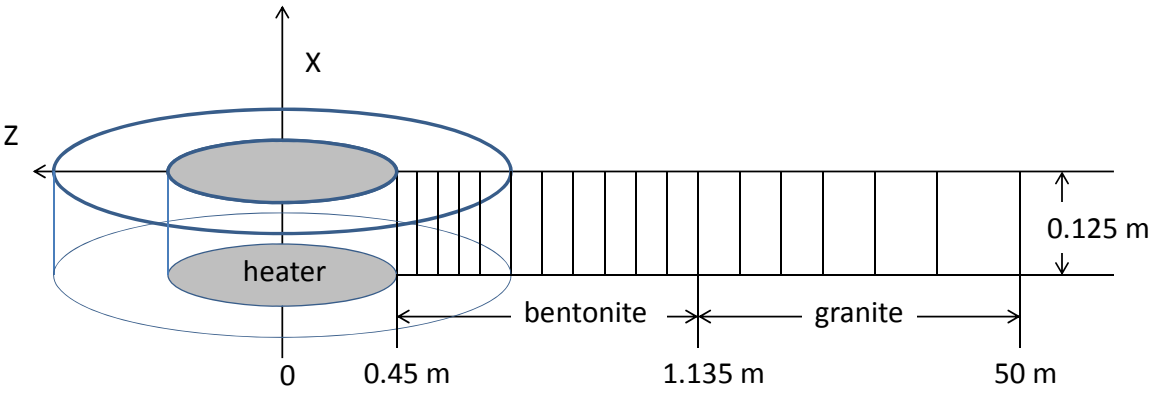

Figure 3-8. Mesh used for the model, not to the scale.

The model considers two material zones for the bentonite and granite. The first two nodes (1 and 2) are located on the external wall of the heater (r = 0.45-0.46 m). Bentonite is located within 0.45 m < r < 1.135 m. The remaining domain up to 50 m is used to simulate the granite. The simulation time starts on February 27, 1997 and ends on July 1, 2015, a total of 6,698 days.
The initial temperature is uniform and equal to 12 ºC. A constant temperature of 100 ºC is prescribed at the heater/bentonite interface (r = 0.45 m) while temperature is assumed to remain constant at its initial value of 12 ºC at the external boundary (r = 50 m) because the thermal perturbation induced by the heaters does not extend to this boundary.

The bentonite has initially a gravimetric water content of 14% which corresponds to a saturation degree of 59% and a suction of 1.11×10^5 kPa. The boundary conditions for flow include: 1) no flow at r = 0.45 m and 2) a prescribed liquid pressure of 7 bars at r = 50 m.

3.3.3 The TH model

In previous modeling work (e.g. Sánchez et al., 2012b; Zheng and Samper, 2008), significant effort has been invested to find out why the hydration of FEBEX bentonite is slower than predicted by the typical Darcy flow model. Several processes have been proposed to explain the discrepancy between measured data and predictions by the Darcy flow model. These include the permeability decrease due to the dual-structural behavior of bentonite (Sánchez et al., 2005, 2012b), thermal osmosis, in which a moisture flux induced by the thermal gradient in the

bentonite is in the opposite direction of water infiltration from the granite (Zheng et al., 2011), and permeability decrease due to swelling (Zheng and Samper, 2008). Another possibility could be the Non-Darcian flow (Liu and Birkholzer, 2012) which has been observed for clay rock and shale. However, before we use a more complex THMC model to identify exactly which processes are at play, we should keep in mind that uncertainty in the parameters could also affect the hydration of bentonite. Therefore, for this work we started first with a TH model. Parameters for the base case are listed in Table 3-1. Sensitivity analyses to key parameters are given in the following sections. The parameters in Table 3-1 are largely based on the information from ENRESA (2000), Sánchez et al. (2012) and Zheng et al. (2011), with more detailed discussion about their uncertainties in Section 3.4.1.2 when we present the sensitivity analyses.

Table 3-1. Thermal and hydrodynamic parameters.

Parameter	Granite	Bentonite
Grain density [kg/m^3]	2700	2700
Porosity ϕ	0.01	0.41
Saturated permeability [m^2]	2.0×10^{-18}	3.75×10^{-21}
Relative permeability, k_{rl}	$k_{rl} = S$	$k_{rl} = S^3$
Van Genuchten α [1/Pa]	1.1×10^{-8}	4.76×10^{-4}
Van Genuchten m	0.45	0.7
Compressibility, β [1/Pa]	3.2×10^{-9}	5.0×10^{-8}
Thermal expansion coeff., [1/^{o}C]	1.0×10^{-5}	1.5×10^{-4}
Dry specific heat, [J/kg-^{o}C]	793	1091
Thermal conductivity [W/m-^{o}C] dry/wet	3.2/3.3	0.47/1.15
effective vapor diffusion coefficient (m^2/s)	1.03×10^{-4}	1.03×10^{-4}

3.3.4 Chemical Model

The establishment of the chemical model requires first the knowledge of initial chemical conditions in bentonite and granite, i.e. the initial mineralogical and pore water composition. Extensive mineralogical characterization had been conducted by ENRESA (2000) and Fernández et al. (2004). Ramírez et al. (2002) also reported the mineralogical composition of FEBEX bentonite, which is slightly different from that in ENRESA (2000). In the report, we take the average of mass fraction reported in ENRESA (2000), Fernández et al. (2004) and Ramírez et al. (2002) (all listed in Table 3-2) and transformed mass fraction to volume fraction (ratio of the volume for a mineral to the total volume of medium) using a porosity of 0.41 (see Table 3-3). Note the minerals that have zero volume fractions are the secondary minerals that could be formed. Detailed mineralogical composition of granite has not been found in current literature search, probably because the chemical conditions in granite are not supposed to be actively changed by repository conditions. Previous THC models for the *in situ* test (Samper et al., 2008a; Zheng et al., 2011) only include quartz in the minerals assemblage in granite. Siitari-Kauppi et al., (2007) reported that Grimsel granite is composed of quartz, K-feldspar, plagioclase and a

small amount of "dark material". In the current model, we consider quartz, K-feldspar, plagioclase in granite with their volume fractions listed in Table 3-3.

Table 3-2. Mass fraction of minerals for FEBEX bentonite from different publications (%)

Mineral	ENRESA (2000), Fernández et al. (2004)	Ramírez et al. (2002)
Calcite	trace	1 ± 0.7
Dolomite	0.0	0
Illite	0.0	0
Kaolinite	0.0	0
Smectite	92 ± 3	93 ± 3
Chlorite	0.8	-
Quartz	2 ± 1	2 ± 0.5
K-Feldspar	trace	2 ± 1
Siderite	0.0	0
Ankerite	0.0	0

Table 3-3. Mineral volume fraction (dimensionless, ratio of the volume for a mineral to the total volume of medium) FEBEX bentonite (ENRESA, 2000; Fernández et al., 2004; Ramírez et al., 2002) and granite (Zheng et al., 2011).

Mineral	**FEBEX Bentonite**	**Granite**
Calcite	0.00472	0
Smectite	0.546	0.
Chlorite	0.0024	0
Quartz	0.012	0.37
K-Feldspar	0.0059	0.35
Plagioclase	0	0.27
Dolomite	0.0	0
Illite	0.0	0
Kaolinite	0.0	0
Siderite	0.0	0
Ankerite	0.0	0

FEBEX bentonite blocks have an initial gravimetric water content of 13.5–14% (ENRESA 2000). As described in Bradbury and Baeyens (2003), obtaining the pore-water chemistry of compacted bentonite with such a low water content is difficult. Because the concentration of ions for the initial state of compacted bentonite cannot be measured directly, indirect measurement methods must be used. Squeezing and aqueous extract are the most commonly used methods. Squeezing is a straight forward method — pore-water is squeezed out and concentrations are measured. However, pore water cannot be extracted by squeezing from clay samples with gravimetric water contents less than 20% (Fernández et al. 2001, 2004), which means that squeezing cannot be done for FEBEX bentonite blocks. In an aqueous extract test, a crushed

sample is placed in contact with water at a low solid/liquid ratio (ranging from 1:16 to 1:1). After establishing equilibrium, the solid phase is separated and the liquid phase is analyzed (Fernández et al., 2001). Geochemical modeling was needed to retrieve the aqueous ion concentrations at low water content (Zheng et al. 2008). Therefore, any uncertainties associated with the geochemical models affect the evaluation of initial aqueous concentration levels at low water content (the water content at the initial state). The model presented in this report uses the pore water composition (see Table 3-4) inferred by Fernández et al. (2001) from aqueous extract data. The pore water composition for granite (Table 3-4) is taken from Zheng et al., (2011).

Table 3-4. Pore-water composition (mol/kg water except for pH) of FEBEX bentonite (Fernández et al., 2001) and granite (Zheng et al., 2011).

	EBS Bentonite: FEBEX	**Granite**
pH	7.72	8.35
Cl	1.60E-01	1.31E-05
SO_4^{-2}	3.20E-02	7.86E-05
HCO_3^-	4.1E-04	3.97E-04
Ca^{+2}	2.2E-02	1.81E-04
Mg^{+2}	2.3E-02	1.32E-06
Na^+	1.3E-01	3.76E-04
K^+	1.7E-03	7.80E-06
Fe^{+2}	2.06E-08	2.06E-08
$SiO_2(aq)$	1.1E-04	6.07E-04
AlO_2^-	1.91E-09	3.89E-08

In the chemical model, we consider aqueous complexation, cation exchange, surface complexation and mineral dissolution/precipitation. Aqueous complexes and their disassociation constants for reactions that are written in terms of the primary species in Table 3-4 are listed in Table 3-5. These thermodynamic data were taken from Data0.dat.YMPv4.0, an EQ3/6 (Wolery, 1993) database qualified by the U.S. Department of Energy for the Yucca Mountain project. Surface protonation reactions are given in Table 3-6 and cation exchange reactions are given in Table 3-7.

Table 3-5. Aqueous complexes and their dissociation constants

Species	Log K (25^oC)	Species	Log K (25^oC)
OH^-	13.99	$MgHCO_3^+$	-1.03
Al^{+3}	-22.88	$CO_2(aq)$	-6.34
$HAlO_2(aq)$	-6.45	CO_3^{-2}	10.33
$NaAlO_2(aq)$	0.75	$CaCO_3(aq)$	7.01
$AlOH^{+2}$	-17.87	KCl(aq)	1.50
$Al(OH)_2^+$	-12.78	$MgCl^+$	0.14
$Al(OH)_3(aq)$	-6.72	$MgSO_4(aq)$	-2.38
$CaCl^+$	0.70	$NaSO_4^-$	-0.81

$CaCl_2$(aq)	0.65	KSO_4^-	-0.88
$CaSO_4$(aq)	-2.10	$NaHSiO_3$(aq)	8.30
NaCl(aq)	0.78	$CaOH^+$	12.85
$FeCl^+$	0.17	NaOH(aq)	14.15
$FeHCO_3^+$	-2.04	$NaCO_3^-$	9.82
$FeCO_3$(aq)	4.88	$NaHCO_3$(aq)	-0.17
$FeCl_4^{-2}$	1.94	$CaHCO_3^+$	-1.04

Table 3-6. Surface protonation reactions on montmorillonite (Bradbury and Baeyens, 2005)

Surface complexation	**Log K**
mon_sOH_2^+ = mon _sOH + H^+	-4.5
mon_sO^- + H^+ = mon _sOH	7.9
mon_$w1OH_2^+$ = mon_w1OH + H^+	-4.5
mon_$w1O^-$ + H^+ = mon_w1OH	7.9
mon_$w2OH_2^+$ = mon_w2OH + H^+	-6
mon_$w2O^-$ + H^+ = mon_w2OH	10.5

Table 3-7. Cation exchange reactions on montmorillonite and illite (Bradbury and Baeyens, 2005)

Cation exchange reaction	**$K_{Na/M}$**
Na^+ + mon-H = mon -Na + H^+	1
Na^+ + mon -K = mon -Na + K^+	0.0775
Na^+ + 0.5 mon -Ca = mon -Na + 0.5Ca^{+2}	0.302
Na^+ + 0.5 mon -Mg = mon -Na + 0.5Mg^{+2}	0.302

Table 3-8. Equilibrium constants for mineral precipitation/dissolution

Primary Mineral	log(*K*)	Secondary Mineral	log(*K*)
Calcite	1.85	Siderite	1.543
Smectite-Na	-34.62	Dolomite	2.524
Quartz	-3.75	Ankerite	-1.035
K-feldspar	-22.91	Illite	-47.33
Albite	-20.133	Chlorite	4.298
Anorthite	-19.19	Kaolinite	-39.9

The equilibrium constants for precipitation/dissolution of primary minerals (minerals that are present initially) and secondary minerals are listed in Table 3-8. Note that plagioclase is a solid solution with albite and anorthite as its end members. In the current model, we assume plagioclase contains 10% anorthite and 90% albite so that there is a quasi-equilibrium between pore water and plagioclase.

Mineral dissolution/precipitation is kinetically controlled. The kinetic law for mineral dissolution/precipitation is given in Xu et al. (2011). The kinetic rates and surface areas for the

minerals considered in the model were taken mostly from Xu et al. (2006) (Table 3-9). However, the illitization rate (the rate of illite precipitation and smectite dissolution) was calibrated (Liu et al., 2013) based on the measured illite percentage in an illite/smectite (I/S) mixed layer from Kinnekulle bentonite, Sweden (Pusch and Madsen, 1995).

Table 3-9. Kinetic properties for minerals considered in the model (Xu et al., 2006).

Mineral	A (cm^2/g)	Parameters for Kinetic Rate Law							
		Neutral Mechanism		Acid Mechanism			Base Mechanism		
		k_{25} (mol/m^2-s)	E_a (kJ/mol)	k_{25} (mol/m^2-s)	E_a (kJ/mol)	$n(H^+)$	k_{25} (mol/m^2-s)	E_a (kJ/mol)	$n(H^+)$
Quartz	9.8	1.023×10^{-14}	87.7						
K-feldspar	9.8	3.89×10^{-13}	38	8.71×10^{-11}	51.7	0.5	6.31×10^{-12}	94.1	-0.823
Kaolinite	151.6	6.91×10^{-14}	22.2	4.89×10^{-12}	65.9	0.777	8.91×10^{-18}	17.9	-0.472
Illite	1.18×10^{4} (1)	1.66×10^{-13}	105 (2)						
Chlorite	9.8	3.02×10^{-13}	88	7.76×10^{-12}	88	0.5			
Calcite	3.5	1.63×10^{-7}	23.5						
Dolomite	12.9	2.52×10^{-12}	62.76	2.34×10^{-7}	43.54	1			
Ankerite	9.8	1.26×10^{-9}	62.76	6.46×10^{-4}	36.1	0.5			
Smectite - Na	1.18×10^{4} (1)	1.66×10^{-13}	105 (2)						

(1) calibrated based on the field illitization data (Liu et al., 2013)
(2) from Pusch and Madsen (1995)

3.4 Model Results

The ultimate goal of modeling the FEBEX *in situ* test is to develop a coupled THMC model that can simultaneously match the measured temperature, relative humidity, water content, stress, aqueous concentrations, and minerals phase change. While the development of a mechanical model is still under way, we report here the results from THC models. First, result from TH models and sensitivity analyses to key hydrological parameters are presented and then preliminary model results for the chemical changes in bentonite are discussed.

3.4.1 The TH model

3.4.1.1 The TH base model

Figures 3-9 through 3-12 compare the measured temperatures to simulation results. Because the current model simulates only the "hot" sections that normally are located at the middle of the 4.5 m long heater, we used temperature measured at section F2 and E2 (see Figure 3-4) surrounding heater 2 to constrain the thermal calculation. Starting February 27, 1997, a constant power of 1200 W was applied to each heater for 20 days and then a constant power of 2000 W for another 33 days. After that, the system was switched to the constant temperature mode, allowing the power to fluctuate freely, but the maximum temperature at the surface of steel liner of the heater

was maintained at 100 °C. After the shutdown of heater 1 on February 2, 2002 (1827 days), the temperature field changed, as manifested by the temperature evolution after 1827 days in Figures 3-9 to 3-12. Unfortunately the thermal sensors at radial distances of 0.48 m and 1.09 m failed shortly after1827 days, but the temperature data from some sensors at radial distance of 0.8 m (Figure 3-10) and 1.05 m (Figure 3-11) show the decrease in temperature after the shutdown of heater 1. Models results match well the temperature data at all the radial distances. Near the steel liner, e.g., radial distance of 0.48 m in Figure 3-9, the temperature is almost the same as at the surface of the steel liner, but it decreases noticeably at radial distance of 1.09 m (very close to the bentonite/granite interface) after the shutdown of heater 1 (Figure 3-12). The current model is a 1-D axi-symmetrical model that is designed to simulate the conditions of "hot" sections around heater 2. In order to account for the heat dissipation from "hot" sections to "cold" sections (located outside of the heater in X direction, such as sections B1 and B2 in Figure 3-4) , we used a semi-analytical solution implemented in TOUGH2 (Pruess et al., 1999) with an adjusted heat exchange surface area to match the temperature data. After 1827 days, the heat exchange surface area was adjusted again to match the data to mimic further heat loss from heater 2 when heater 1 was removed. In general, a fairly good match between the model and data was archived.

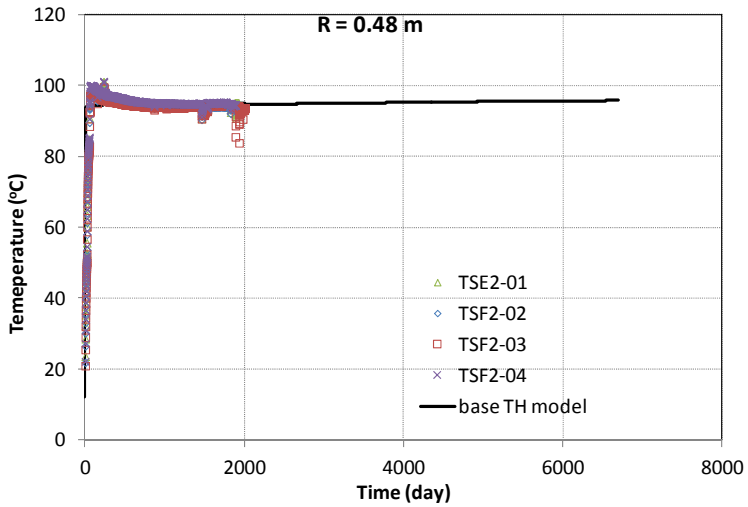

Figure 3-9. Measured temperature by sensors located at radial distance of 0.48 m in sections E2 and F2 and model results from the base TH model.

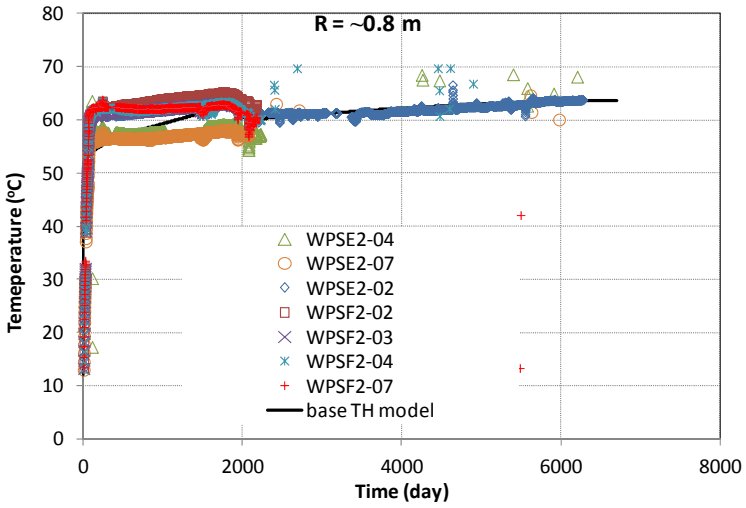

Figure 3-10. Measured temperature by sensors located at radial distance of 0.8 m in sections E2 and F2and model results from the base TH model.

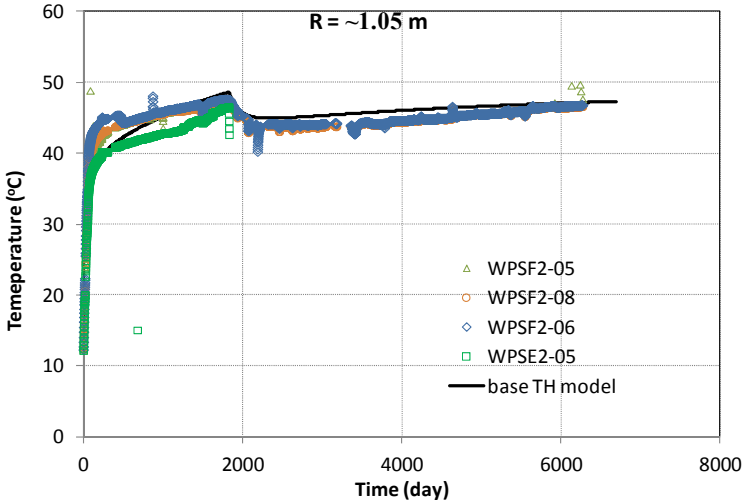

Figure 3-11. Measured temperature by sensors located at radial distance of 1.05 m in sections E2 and F2 and model results from the base TH model.

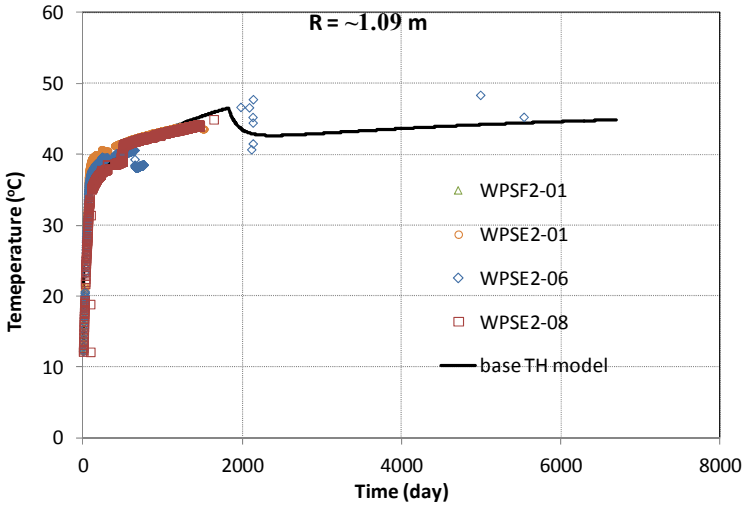

Figure 3-12. Measured temperature by sensors located at radial distance of 1.09 m in sections E2 and F2 and model results from the base TH model.

Relative humidity data measured by sensors at various positions in the bentonite were compared with models results. These data were grouped by the radial distance of the sensors. Previous modeling exercises (e.g. Zheng et al., 2011) showed that relative humidity near the heater has been overestimated and was the key data to test the models. Unfortunately, most sensors for relative humidities failed for sections around heater 2, especially near the heater. For example, as shown in Figure 3-13, sensors at section E2 (WCSE2-03, WCSE2-04) only provide data until 147 days. We therefore have to rely on the relative humidity data measured at section E1 (located around heater 1) to constrain our model. A fairly good match between model results and relative humidity was achieved. A better fit between the model and data was obtained at the outer rings of the bentonite barrier (large radial distance, see Figure 3-15 and 16) and in the middle of the bentonite barrier (radial distance of 0.8 m, Figure 3-14). However, the match between the model and data near the heater (radial distance of 0.52 m, Figure 3-13) was slightly worse.

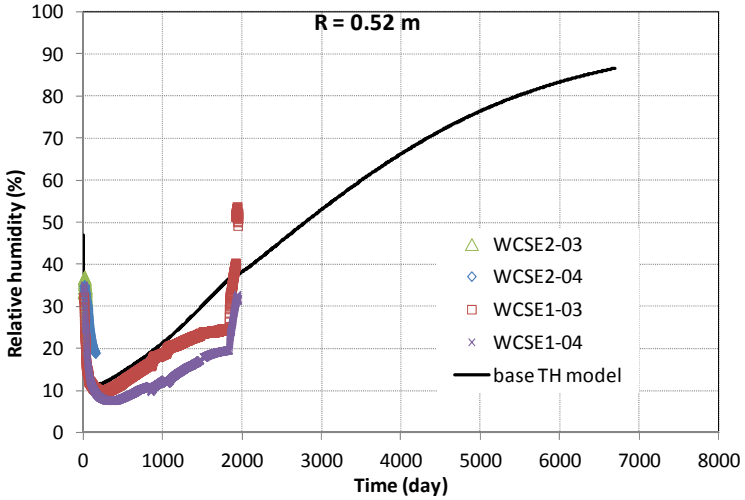

Figure 3-13. Measured relative humidity by sensors located at radial distance of 0.52 m in sections E2 and E1 and model results from the base TH model.

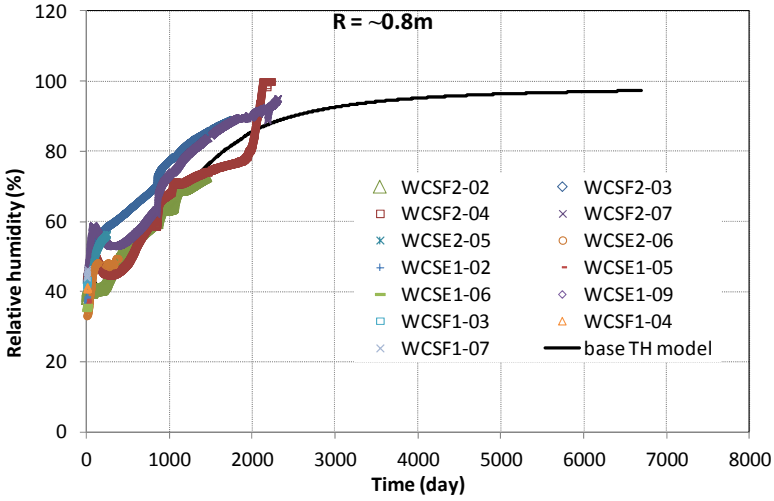

Figure 3-14. Measured relative humidity by sensors located at radial distance of ~0.8 m in sections E1, E2, F1 and F2 and model results from the base TH model

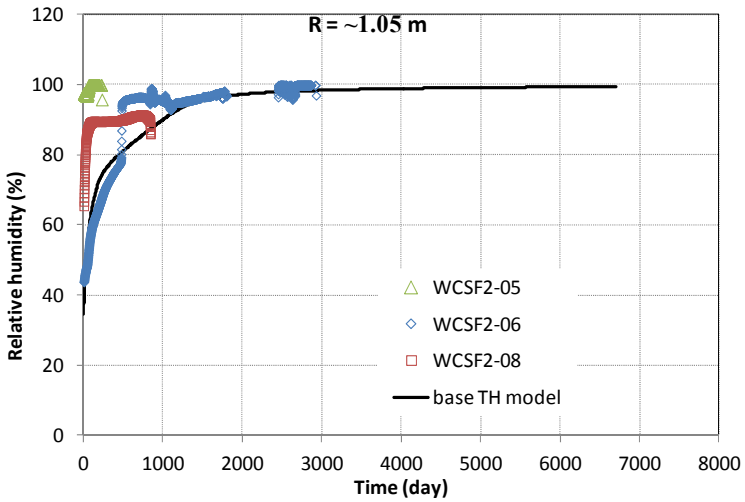

Figure 3-15. Measured relative humidity by sensors located at radial distance of ~1.05 m in section F2 and model results from the base TH model

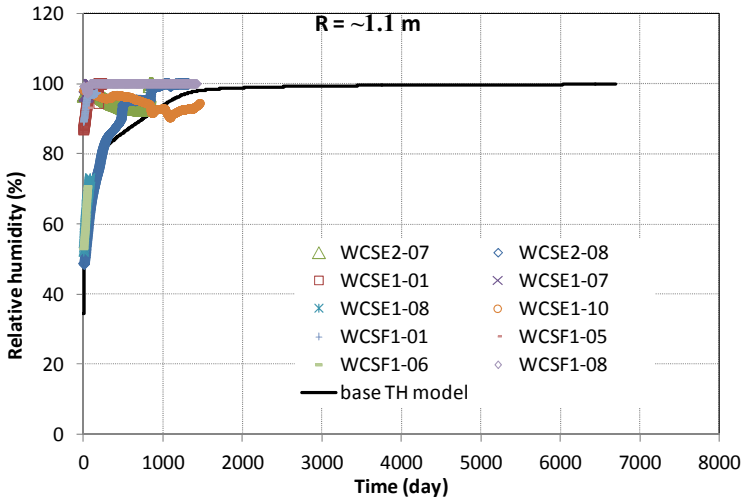

Figure 3-16. Measured relative humidity by sensors located at radial distance of ~1.1 m in sections E1, E2 and F1 and model results from the base TH model

3.4.1.2 Sensitivity analyses to key hydrological parameters

The key parameters affecting the hydration of bentonite are the permeability of granite, the relative permeability and retention curves of bentonite, and the vapor diffusion coefficient. In this section, we discuss the most plausible values for these parameters and illustrate how they affect the simulated relative humidity.

Granite is a fractured medium and should ideally be represented by fractures and matrix. Just as previous models for *in situ* tests (Samper et al., 2008a; Sánchez et al., 2012b), current model also assumes granite is a homogeneous porous medium, which requires us to use an equivalent permeability. Based on the total water flow at the entire test zone (17.4 m, see Figure 3-4)

(ENRESA, 2000), the permeability of granite is around 5×10^{-18} to 8×10^{-18} m^2. ENRESA (2000) also reports that the most frequent permeability is 1×10^{-18} but deems it is more representative of rock matrix. Zheng et al., (2011) used 8×10^{-18} m^2, Kuhlman and Gaus (2014) estimated a permeability of 6.8×10^{-19} m^2, and Sanchez et al., (2012b) used a surprisingly small value, 8.18×10^{-21} m^2. Based on the published values, it seems that a permeability between 7×10^{-19} to 8×10^{-18} m^2 is plausible. In the base model, a permeability of 2×10^{-18} m^2 is used and Figure 3-17 shows the relative humidity results obtained with permeability of 6.8×10^{-19} m^2 and 8×10^{-18} m^2 for granite. Lower granite permeability significantly limits the water infiltration into bentonite, and subsequently lowers the computed relative humidity. A permeability of 6.8×10^{-19} for granite actually leads to a better match of measured relative humidity data at radial distance of 0.52 m (near the heater, Figure 3-17); however, it results in a marked underestimation of the relative humidity in the middle of bentonite barrier (radial distance of 0.8 m, Figure 3-18) and near the bentonite/granite interface (radial distance of 1.05, 1.21 m). A permeability of 8×10^{-18} m^2 for granite leads to reasonable fit of the relative humidity in the middle of bentonite barrier and near the bentonite/granite interface, but causes overestimation of the relative humidity near the heater. Permeability of granite is certainly a very important parameter for determining the hydration rate of bentonite, but adjusting it will not result in a good match of the relative humidity data over the entire bentonite barrier.

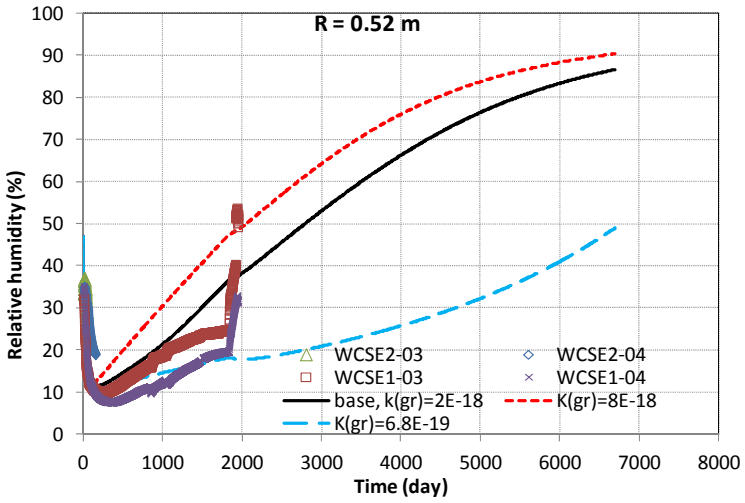

Figure 3-17. Measured relative humidity by sensors located at radial distance of 0.52 m and model results from the base model and two sensitivity runs with different permeability for granite.

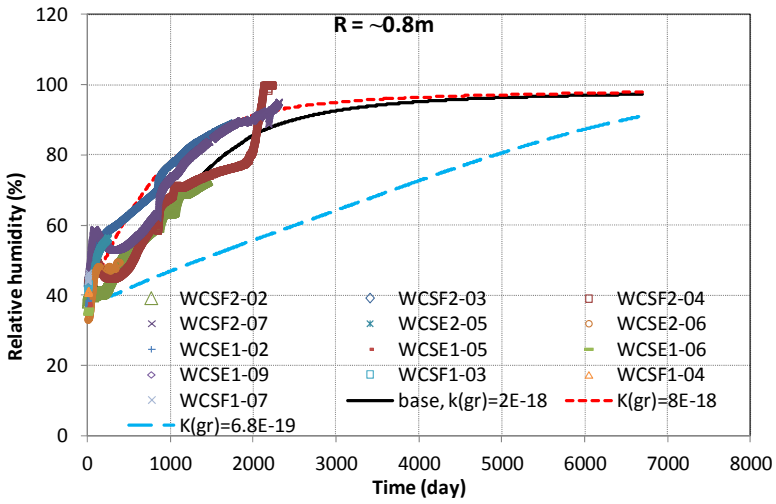

Figure 3-18. Measured relative humidity by sensors located at radial distance of 0.8 m and model results from the base model and two sensitivity runs with different permeability for granite.

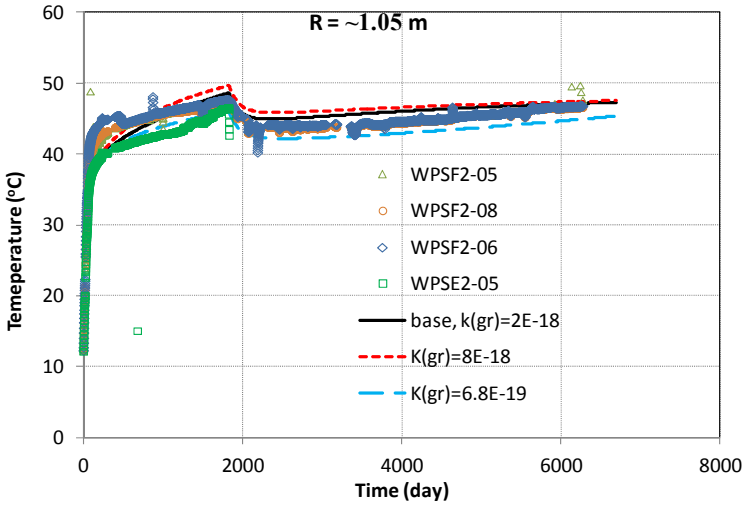

Figure 3-19. Measured temperature by sensors located at radial distance of ~1.05 m and model results from the base model and two sensitivity runs with different permeability for granite.

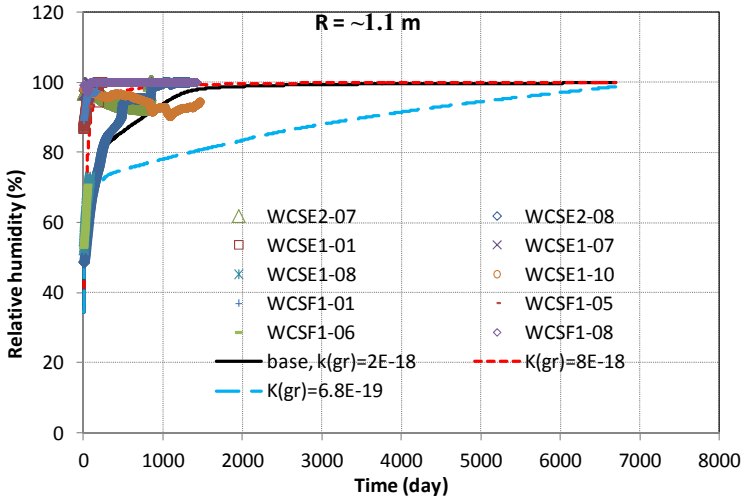

Figure 3-20. Measured relative humidity by sensors located at radial distance of 1.1 m and model results from the base model and two sensitivity runs with different permeability for granite.

The effective permeability of bentonite has been under scrutiny by modelers (e.g. Zheng et al., 2011) due to its critical role in determining the hydration of bentonite. It is the product of saturated permeability (k) and relative permeability (k_r). Because $k_r=S_l^3$ (where S_l is water saturation degree) has been consistently used by different models (Zheng et al., 2011; Sánchez et al., 2012b; Kuhlman and Gaus, 2014), we focus here on the impact of saturated permeability on relative humidity. Dry density is the primary factor that affects the permeability of bentonite, as shown in Figure 3-21. The bentonite blocks used in the *in situ* test initially have a dry density of 1.7 g/cm^3, which gives a saturated permeability of around 2.5×10^{-21} m^2 (2.5×10^{-14} m/s in term of saturated hydraulic conductivity). In addition to dry density, the water (distilled, granitic or saline water) used to measure the permeability also give different values (see Figure 3-21). Considering the possible small variation in the initial dry density and impact of water type on the permeability, the plausible saturated permeability for FEBEX bentonite could be in a range from 1×10^{-21} to 9×10^{-21} m^2. In a THM model for the *in situ* test Chen et al., (2009) use 2×10^{-21} m^2 which is within that range, but a permeability of 9.4×10^{-22} estimated based on inverse modeling by Kuhlman and Gaus (2014) seems a bit low. Results from two sensitivity runs using permeabilities of $1\times10^{-21}$and 9×10^{-21} m^2 for bentonite are shown in Figures 3-22 to 3-24. The impact of permeability of bentonite on the computed relative humidity is not obvious: higher permeability leads to higher relative humidity near the heater but actually lower relative humidity near the bentonite/granite interface. The reason is that higher permeability, on the one hand, accelerates the water infiltration overall, which leads to higher relative humidity near the heater; on the other hand, it also induces stronger suction that causes desaturation in granite and maintains the unsaturated state in bentonite near the bentonite/granite for longer time.

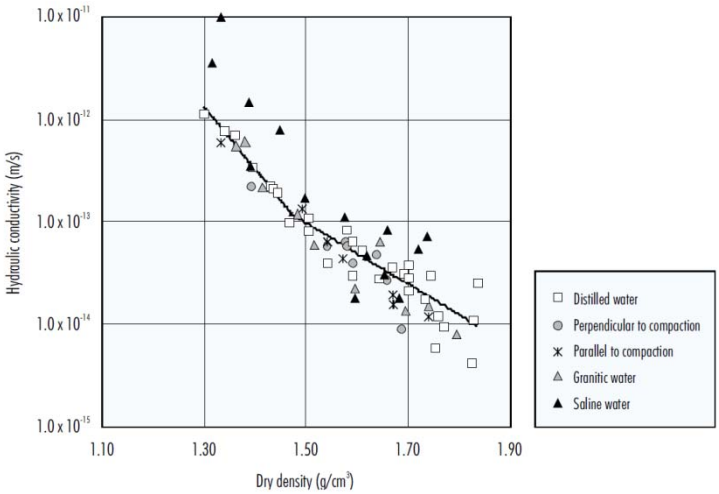

Figure 3-21. Saturated hydraulic conductivity as a function of dry density (ENRESA, 2000)

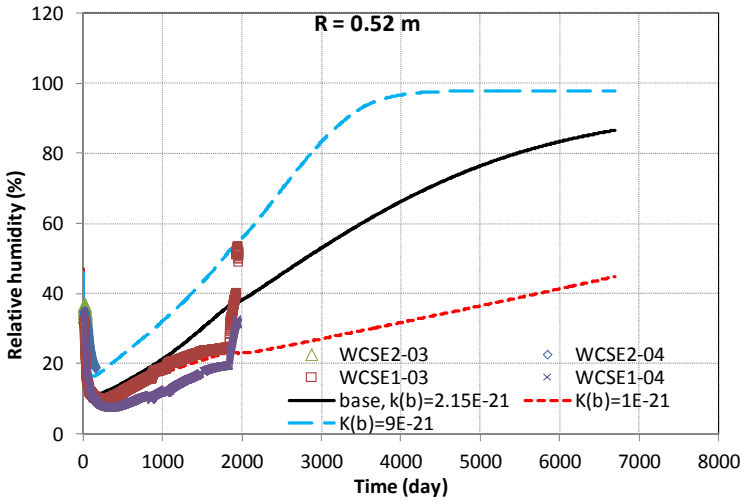

Figure 3-22. Measured relative humidities by sensors located at radial distance of 0.52 m and model results from the base model and two sensitivity runs with different permeability for bentonite.

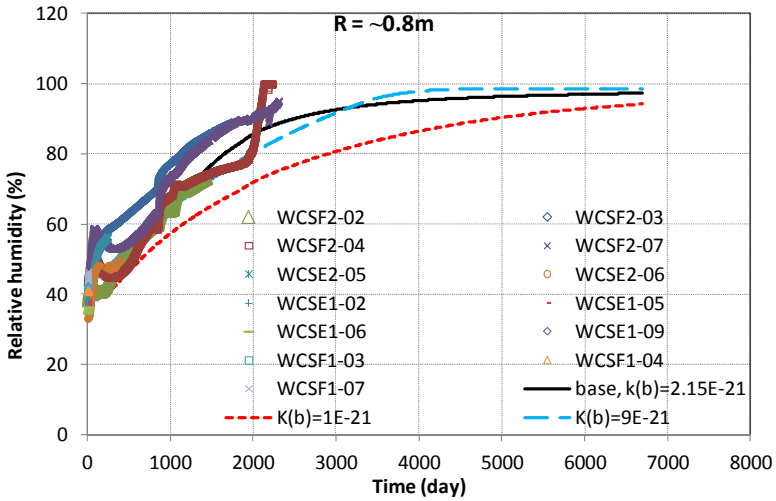

Figure 3-23. Measured relative humidities by sensors located at radial distance of 0.8 m and model results from the base model and two sensitivity runs with different permeability for bentonite.

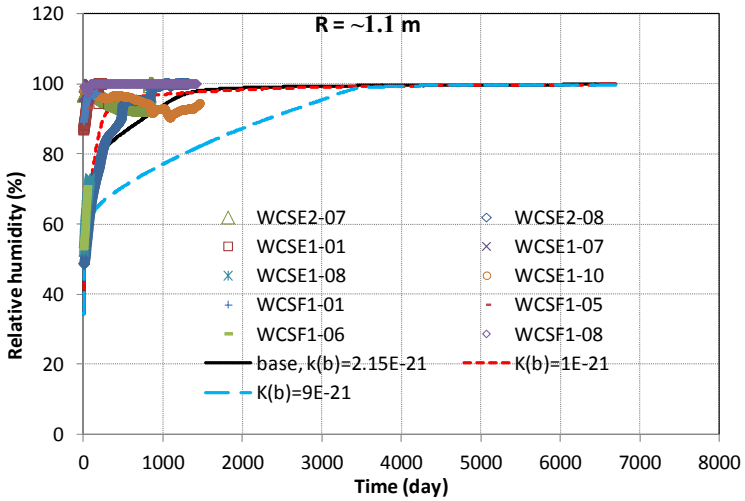

Figure 3-24. Measured relative humidities by sensors located at radial distance of 1.1 m and model results from the base model and two sensitivity runs with different permeability for bentonite.

While it is obvious that permeability has a strong effect on the hydration of bentonite, it is also clear that a constant saturated permeability cannot lead to a satisfactory match of relative humidity data at all the locations. Then the question is how saturated permeability changes over the course of hydrating bentonite. Zheng et al. (2011) related saturated permeability to porosity using the Kozeny-Carman (KC) equation (Bear, 1972):

$$k = k_0 \frac{\phi^3}{(1-\phi)^2} \frac{(1-\phi_0)^2}{\phi_0^3} \quad (3\text{-}5)$$

where k_0 (m^2) and ϕ_0 are the reference values of bentonite permeability and porosity, respectively, with $k_0 = 3.75 \cdot 10^{-21}$ m^2 and $\phi_0 = 0.41$. The porosity changes were calculated by a mechanical model using a state surface approach (Nguyen *et al.*, 2005). Although the Kozeny-Carman (KC) equation was derived for granular material, other studies have shown (Odong, 2007) that it can be used for a wide range of soils. Eventually Zheng et al. (2011) managed to achieve a good match between models and data using Equation (3-1) and thermal osmosis which leads to outward (from heater to granite) moisture flux. Sanchez et al. (2102b) used also the KC equation to relate porosity change with permeability, with $k_0 = 1.9 \cdot 10^{-21}$ m^2 and $\phi_0 = 0.40$, and the porosity changes as a result of swelling which is calculated based on the BBM. In the near future, when mechanical models are developed, we can explore which one leads to a better fit of the measured data.

3.4.2 The relevance of Non-Darcian flow to the hydration of bentonite

THM/THC models for mock-up tests (Zheng and Samper, 2008; Sánchez et al., 2012b) clearly showed that the typical Darcy flow model overestimated the hydration of FEBEX bentonite. While summarizing the main findings from 15 years of operation of the mock-up and *in situ* tests, Lanyon et al. (2013) identified three second-order processes that may be relevant: thermal osmosis, threshold gradient for flow (i.e. the Non-Darcian flow) within bentonite, and the evolution of pore structure during hydration. One of the objectives of conducting THMC simulations is to sort out which one (or ones) of these processes plays an important role in slowing down the hydration of bentonite. In this section, we tested a TH model with Non-Darcian flow.

3.4.2.1 Calibrating threshold gradient with a permeability test

The key of having Non-Darcian flow model is to be able to calculate the threshold gradient reliably. Based on data from various sources, the threshold gradient I and permeability k (m^2) have the following relationship (Liu and Birkholzer, 2012):

$$I = Ak^B \quad (3\text{-}6)$$

with A= 4.0E-12 and B =-0.78. However, as the data set have some scatter, A and B have to be calibrated for a particular case, even though Equation (3-6) with A= 4.0E-12 and B =-0.78 can give a good first-cut estimate. The uncertainties regarding threshold gradient likely dictate the relevance of Non-Darcian flow to the hydration of bentonite. Fortunately, a permeability test using FEBEX bentonite (Samper et al., 2008b) provides a great opportunity for calculating the threshold gradient (parameters A and B) that can be applied to the FEBEX *in situ* test. In this report, we first developed a Non-Darcian flow model for the permeability test and then applied the calibrated parameters to the TH model for *in situ* test.

The experimental column used for the permeability test consists of a stainless steel cell in which a sample of FEBEX compacted bentonite is subjected to water flow (Figure 3-25). The cell has an internal diameter of 5 cm and a length of 2.5 cm. It contains 99.7 g of dry bentonite and 19.09

mL of water. A HPLC pump injects a solution at a pressure of 4 MPa through a porous stainless steel filter providing a nearly-constant flow rate of approximately 2 mL/month. Outflowing water comes out through another stainless steel filter and is sampled inside a syringe. The test lasted for 1393 days, during which a total volume of 106 mL (which amounts to 5 pore volumes) was collected. The saturated hydraulic conductivity of the clay is 2.9×10-14 m/s.

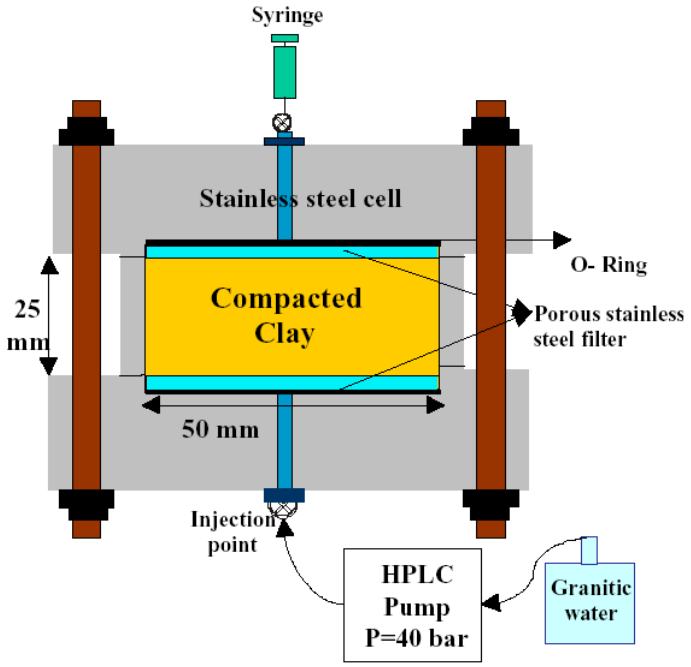

Figure 3-25. Schematic design of the permeation test (Samper et al., 2008b).

Darcy flow models with this measured hydraulic conductivity and the Non-Darcian flow model with different parameters were developed to match the cumulative water flux measured in the test. As shown in Figure 3-26, a Darcy flow model overestimates the water flux data and Non-Darcian flow with A of 4E-12 completely shuts down the water flow through the bentonite sample. Eventually we calibrated that A of 2×10^{-13} gives the best fit of measured data. Model results are very sensitive the choice of B as well, as illustrated in Figure 3-27, and the best value for B is -0.78.

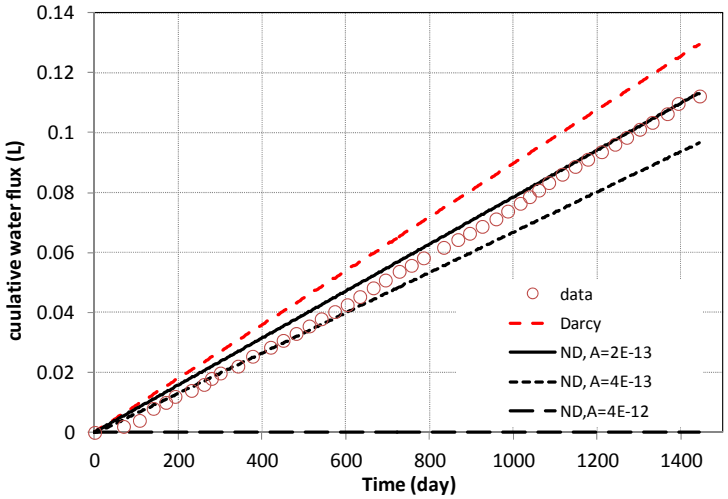

Figure 3-26. Measured cumulative water flux data and Darcy flow model, marked "Darcy" in the figure and Non-Darcian flow model, marked as "ND" in the figure with different A values while keeping B equal to -0.78.

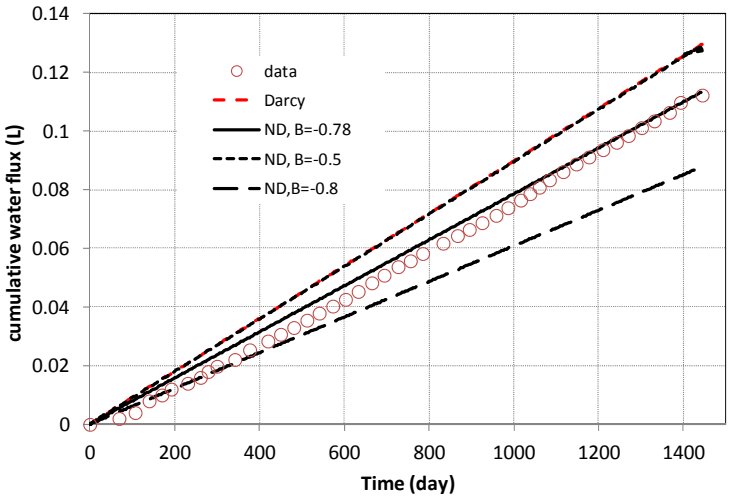

Figure 3-27. Measured cumulative water flux data and Darcy flow model, marked "Darcy" in the figure and Non-Darcian flow model, marked as "ND" in the figure with different B values while keeping A equal to 2×10^{-13}.

3.4.2.2 TH model with Non-Darcian flow

After we obtained the optimal A and B to reliably calculate the threshold gradient for FEBEX bentonite, a Non-Darcian flow model was developed for the FEBEX *in situ* test. Except for Non-Darcian flow, all the rest of the parameters remain the same as in the base model presented in 3.4.1.1. Comparison between relative humidity data and model results from the Darcy and Non-Darcian flow models at several radial distances are presented in Figures 3-28-3-30. The Non-Darcian flow models significantly underestimate the relative humidity data, even in bentonite near the bentonite/granite interface (at the radial distance of 1.1 m in Figure 3-30).

The relevance of Non-Darcian behaviour is clear for saturated flow in clay rock (Liu and Birkholzer, 2012 and references cited therein) and intuitively one would think that Non-Darcian behaviour should also be relevant to unsaturated flow in clay rock. However, when the numerical model is used to demonstrate such relevance, there are a couple of issues that might prevent us from clearly delineating the contribution of Non-Darcian flow to unsaturated clay or bentonite. First and foremost, the calibration of the relative permeability and retention curves overshadows the effect of Non-Darcian flow. The non-linear relationship between water flux and hydraulic gradient which motivates the relevance of Non-Darcian behaviour to water flow, is already accounted for, at least partially, by the relative permeability (which in turn is a function of the retention curve) in the flux-gradient relationship for unsaturated flow. In other words, the non-linear relationship between water flux and hydraulic gradient for unsaturated flow might be affected by two features: Non-Darcian flow and relative permeability. However, in most modelling exercises, relative permeability is calibrated based on a Darcy-type flow. As a result, the calibration of the parameters associated with relative permeability overshadows the contribution of Non-Darcian flow— the parameters for relative permeability might be "over-calibrated" so that the effect of Non-Darcian flow looks irrelevant. For FEBEX bentonite, the relative permeability and retention curve were calibrated based on Darcy type of flow model (ENRESA, 2000), which essentially obviates the Non-Darcian flow for unsaturated bentonite. Thus, if Darcian flow is added on top of relative permeability that is calibrated based on Darcy flow, as in the model presented in this section, we double count the non-linearity between flux and gradient, and consequently the model significantly underestimates the water inflow from granite to bentonite, as shown in Figures 3-28 to 3-30. This is essentially an issue of process uncertainty versus parameter uncertainty, which is faced by many complex models. Second, Cui et al., (2008) reported that threshold gradients are different for different capillary pressure. In this report, we used the equation proposed in Liu and Birkholzer (2012) in which threshold gradient is solely a function of saturated permeability. Further research is needed to take into account the effect of capillary pressure when a threshold gradient is calculated. However, even though we can improve our threshold gradient calculation by taking into account capillary pressure, it is unlikely to eliminate the aforementioned issue of process uncertainties versus parameter uncertainties.

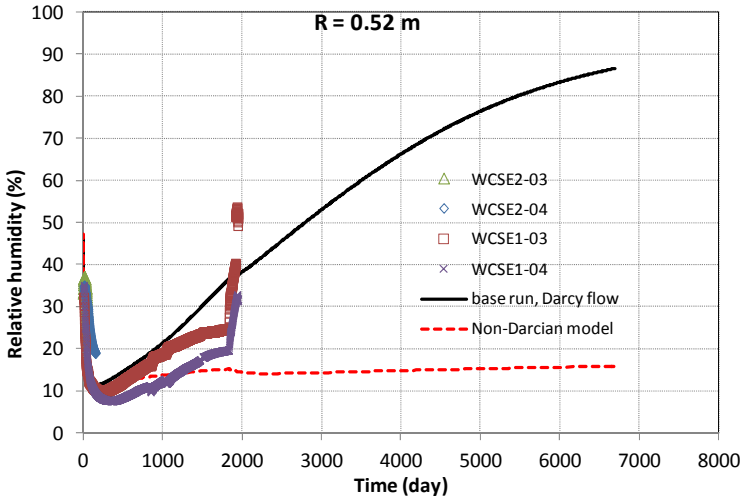

Figure 3-28. Measured relative humidities by sensors located at radial distance of 0.52 m and model results from the base model and the Non-Darcian flow model.

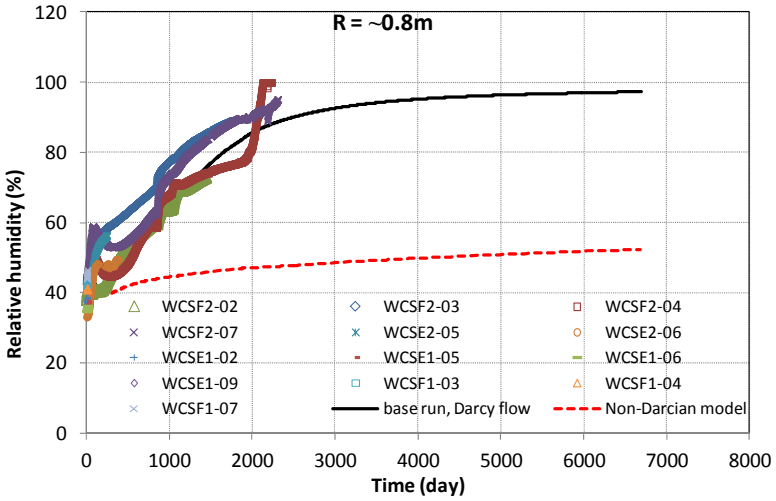

Figure 3-29. Measured relative humidities by sensors located at radial distance of 0.8 m and model results from the base model and the Non-Darcian flow model.

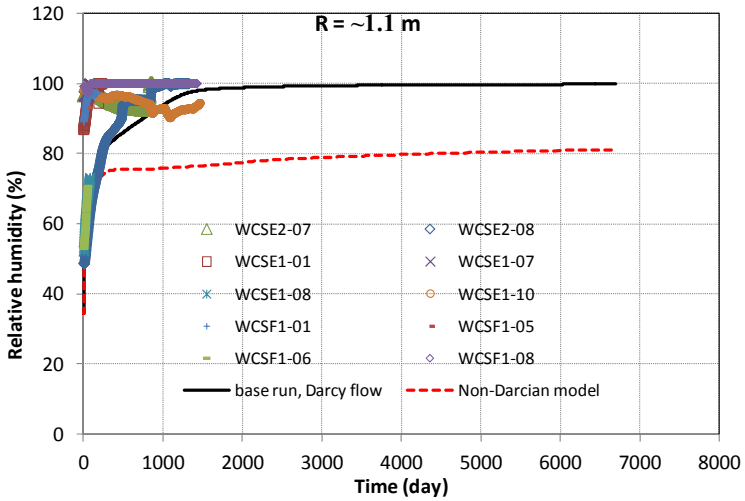

Figure 3-30. Measured relative humidities by sensors located at radial distance of 1.1 m and model results from the base model and the Non-Darcian flow model.

Figures 3-31 and 3-32 show the temperature computed by the TH model with Non-Darcian flow. The model results illustrate perfectly the coupling between thermal and hydrological processes — underestimation of relative humidity by Non-Darcian flow model is accompanied by underestimation of temperature because thermal conductivity of bentonite is a function of water saturation.

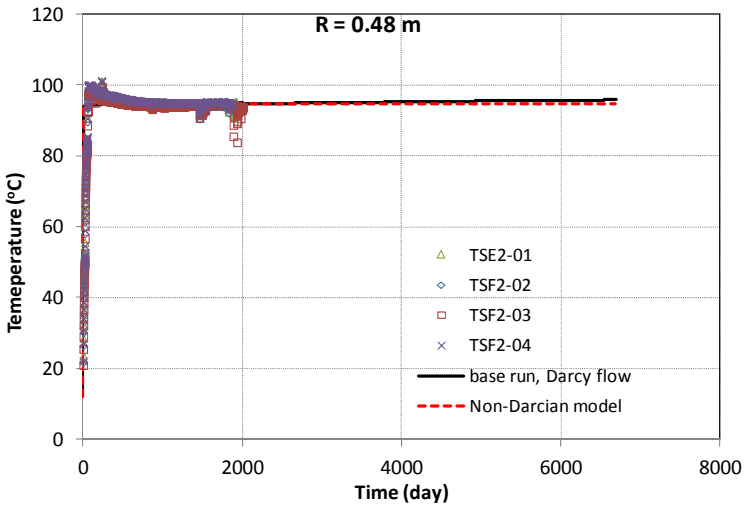

Figure 3-31. Measured temperature by sensors located at radial distance of 0.48 m and model results from the base model and the Non-Darcian flow model.

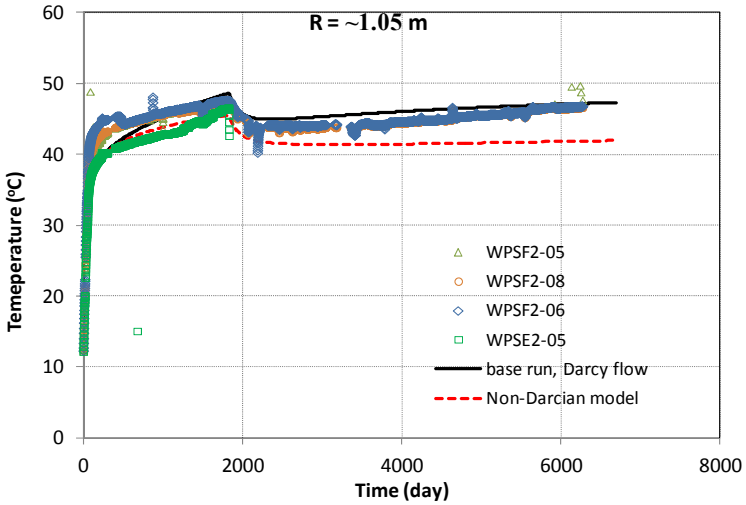

Figure 3-32. Measured temperature by sensors located at radial distance of 1.1 m and model results from the base model and the Non-Darcian flow model.

3.4.3 The THC model

Previous THC modeling work focused on the interpretation of the aqueous concentration of major cations and anions measured after the dismantling of heater 1. In this section, these data are compared with the results from the preliminary THC model as well. Because the TH model cannot match perfectly the hydrological data, namely relative humidity, which means the water inflow to bentonite still needs improvement (with the permeability change due to swelling being the last piece of the puzzle), it is expected that the THC model cannot match the chemical data perfectly. The comparison between chemical data and results from the THC model will illustrate

how much discrepancy can be introduced by neglecting the mechanical changes and the subsequent permeability decrease in bentonite. However, because hydrological and mechanical processes shape the concentration profile very differently from chemical processes, as will be discussed below, the THC model is still very useful to test the chemical model and guide its future refinement.

3.4.3.1 Geochemical data after dismantling of heater 1

Bentonite samples were taken from vertical sections normal to the axis of the tunnel. Samples were taken along several radii in each section (Zheng et al., 2011). Bentonite samples were taken for THC analyses from three sections surrounding the heater 1: s19, s28, and s29; see Figure 3-6 for the positions of these sections. Each sampling section consists of an outer, central and inner layer of bentonite blocks. The locations of bentonite blocks in section 29 collected after dismantling of heater 1 are shown in Figure 3-33. A total of 9 bentonite blocks were sampled at several radial distances. Bentonite blocks were preserved immediately after their extraction in plastic films, with two layers of aluminized PET sheets and vacuum-sealed plastic bags. Protection against mechanical damage was used to ensure the integrity of the material (ENRESA, 2006a).

Aqueous extract tests (AET) were used to obtain pore water chemistry for compacted FEBEX bentonite. AET is a method to quantify the total content of soluble salts of a clay sample. A *1:R* AET consists on adding to a mass M_s of powdered clay sample a mass of distilled water equal to R times M_s. The clay sample and water are stirred during a period of time, usually 2 days, during which water and clay are allowed to equilibrate. Chemical analyses are performed on the supernatant solution after phase separation by centrifugation (Sacchi et al., 2001). In addition to dilution, chemical reactions take place during pore water extraction which changes the concentrations of dissolved species in a complex nonlinear manner. This makes it difficult to derive the chemical composition of the original pore water from the aqueous extract data (Bradbury and Baeyens, 1998; Sacchi et al., 2001). The inference of dissolved concentrations for reactive species requires geochemical modeling based on mineralogical data (Fernández and Rivas, 2005; Zheng et al., 2008). Aqueous extract tests and concentration of exchangeable cations are available for sections 19, 28 and 29 (Fernández and Rivas, 2003). Aqueous extract data from sections 29 and 19 (see Figure 3-6) were interpreted by inverse geochemical modeling (Zheng et al., 2008) and used to test the model predictions (Zheng et al., 2011). In this report, we use the same data set to evaluate our THC models.

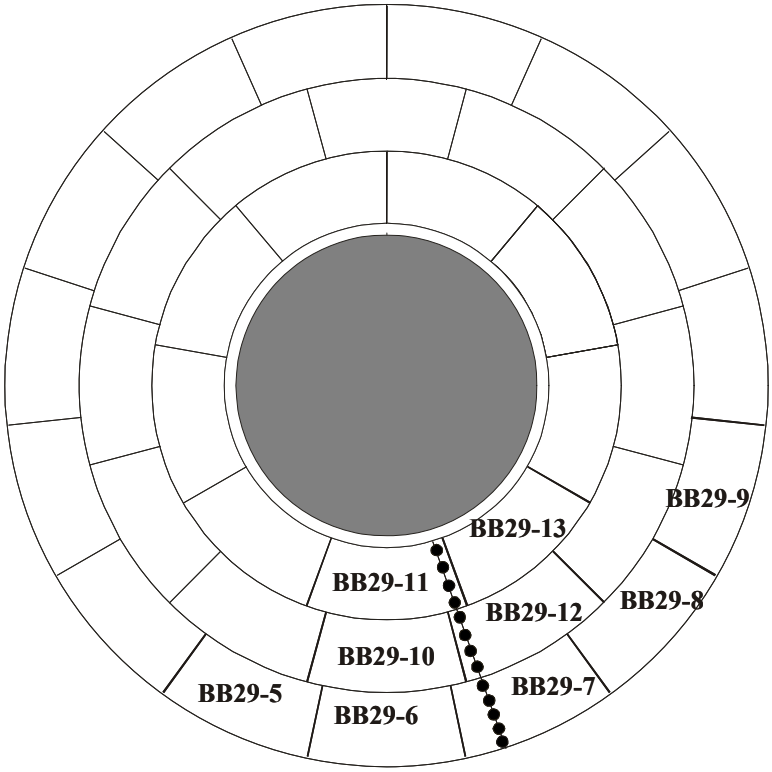

Figure 3-33. The positions where samples were taken for geochemical analyses at section 29 after the dismantling of heater 1 in 2002 (Zheng et al., 2011).

3.4.3.2 Testing the THC model with data and predictions

In Figure 3-34, we compare the chloride data and model results at 1930 days. Note that heater 1 was turned off after 1827 days, but the sample for THC analyses ware actually taken at 1930 days after a three- month cooling period. The model captures the general trend of the measured profiles, but overestimates the concentration near the heater and the bentonite/granite interface. A similar discrepancy has been observed for the THC models in Zheng et al. (2011). When water infiltrates into bentonite, the swelling of bentonite allows more water to reside near the bentonite/granite interface and this dilutes the chloride. The current THC model cannot capture such behavior, but it is expected that including swelling in the model would alleviate the discrepancy.

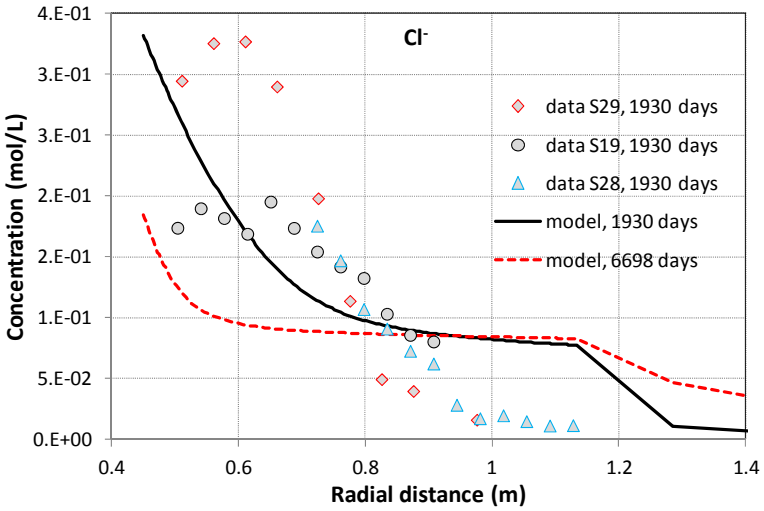

Figure 3-34. The concentration profile of chloride at 1930 days (Zheng et al., 2011) and model results from the base model.

The concentration profiles of major cations are shown in Figures 3-35 through 3-38. In addition to the base model results at 1930 days when samples were taken after the dismantling of heater 1, also shown in the figures are the results from a sensitivity run that does not consider chemical reactions. The comparison between the base model and sensitivity run allows one to distinguish the contribution of chemical reactions in shaping the concentration profile along the bentonite barrier. Concentration profiles of major cations largely follow the profile of conservative species such as chloride, indicating that flow and transport play major roles in shaping the profile. Similarly, just as the model overestimates the concentration of chloride near the bentonite/granite interface and near the heater, it also overestimates the concentration of sodium, calcium, magnesium, and potassium as well. In addition to the transport processes, sodium concentration could also be affected by cation exchange and dissolution of smectite (Figure 3-39). However, because sodium concentration is much higher than other cations and the concentration perturbation of other cations is fairly small, sodium concentration is not impacted noticeably by cation exchange, and the amount of smectite dissolved is too small to meaningfully alter the sodium concentration; the results from the base model and sensitivity run are almost indistinguishable as shown in Figure 3-35.

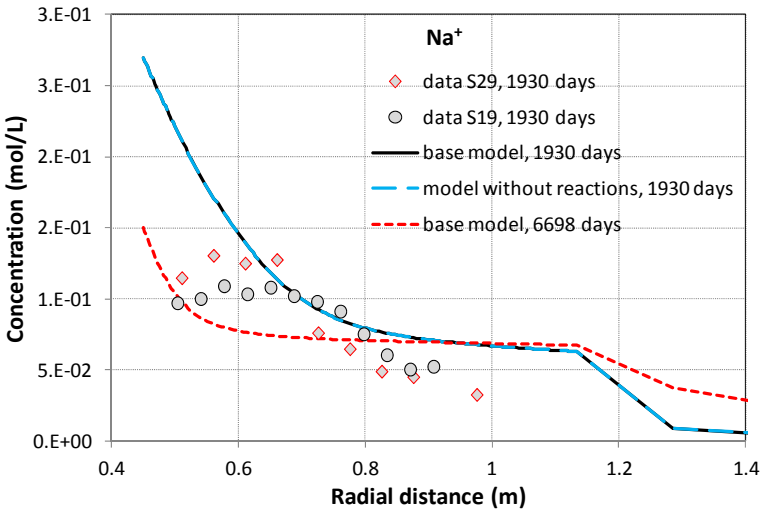

Figure 3-35. The concentration profile of sodium at 1930 days (Zheng et al., 2011) and model results from the base model and sensitivity run that does not consider any chemical reaction.

The base model leads to slightly lower calcium concentration than the sensitivity run (Figure 3-36). This is because of precipitation of dolomite (which decreases calcium concentration) (Figure 3-40), which outperforms the dissolution of calcite (which increases calcium concentration) (Figure 3-41). Eventually the model needs to delicately balance the pH, bicarbonate, calcium concentration, calcite dissolution, and dolomite precipitation to capture the concentrations of all of them.

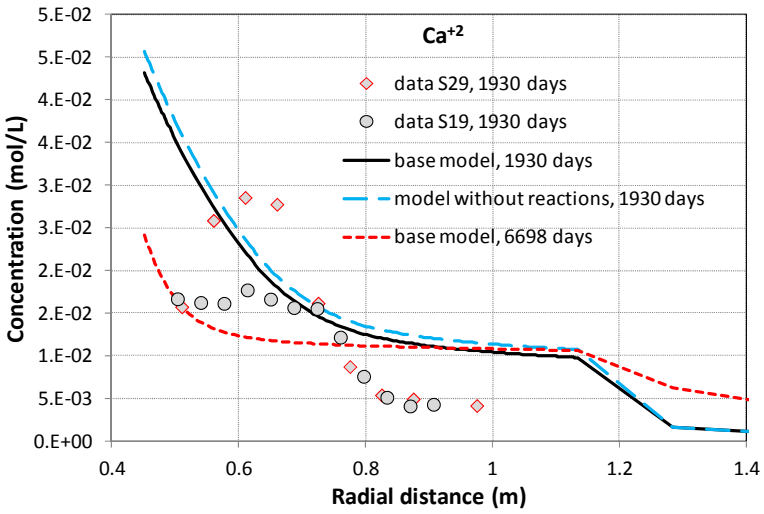

Figure 3-36. The concentration profile of calcium at 1930 days (Zheng et al., 2011) and model results from the base model and sensitivity run that does not consider any chemical reaction.

Magnesium is involved in the dissolution/precipitation of smectite, the precipitation of dolomite, and cation exchange (Figure 3-37). Eventually these reactions seem to cancel each other out, and

magnesium concentration in the base model is just slight lower than that from the sensitivity run without any reactions.

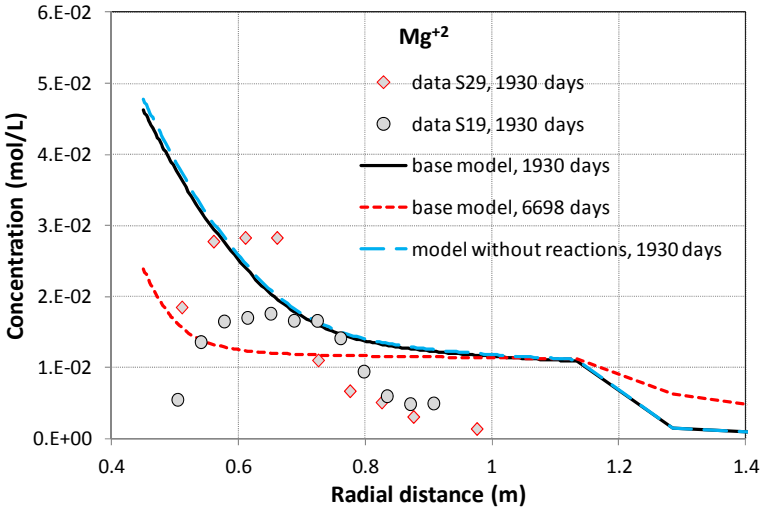

Figure 3-37. The concentration profile of magnesium at 1930 days (Zheng et al., 2011) and model results from the base model and sensitivity run that does not consider any chemical reaction.

The computed concentration of potassium from the base model is actually lower than that from the sensitivity run (Figure 3-38), suggesting that some reactions consume potassium in the pore water, which aligns well with the precipitation of illite (Figure 3-42). However, the fact that measured concentration is just slightly lower than computed from the sensitivity run (which has no reactions) seems to suggest there is only minimal precipitation of illite. In Figure 3-44, the maximum volume fraction increase is about 2E-6 after 1930 days, which could be too small to be detected.

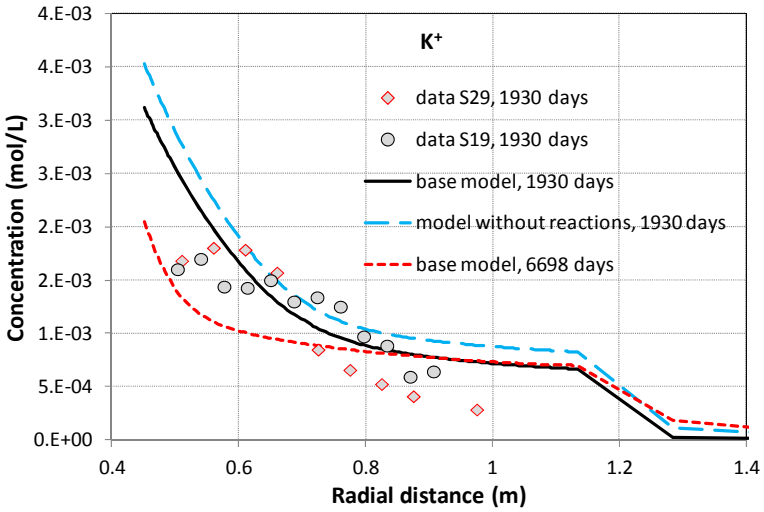

Figure 3-38. The concentration profile of potassium at 1930 days (Zheng et al., 2011) and model results from the base model and sensitivity run that does not consider any chemical reaction.

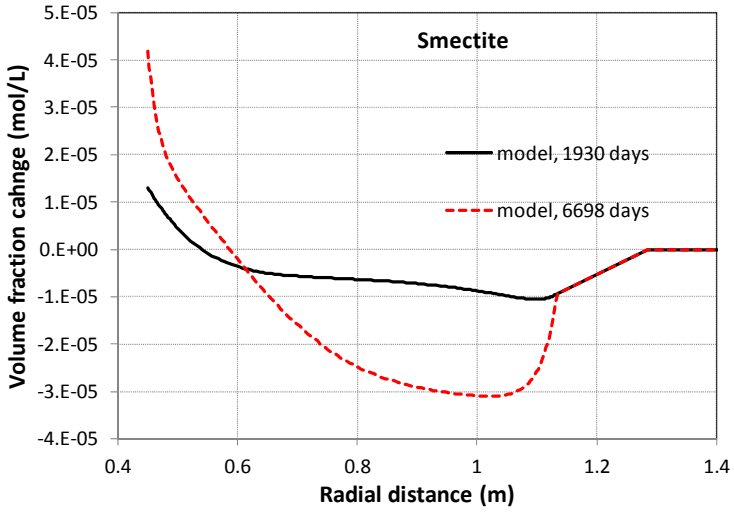

Figure 3-39. Computed profile of volume fraction change of smectite at the 1930 days (after the dismantling of heater 1) and at 6698 days (July 1, 2015).

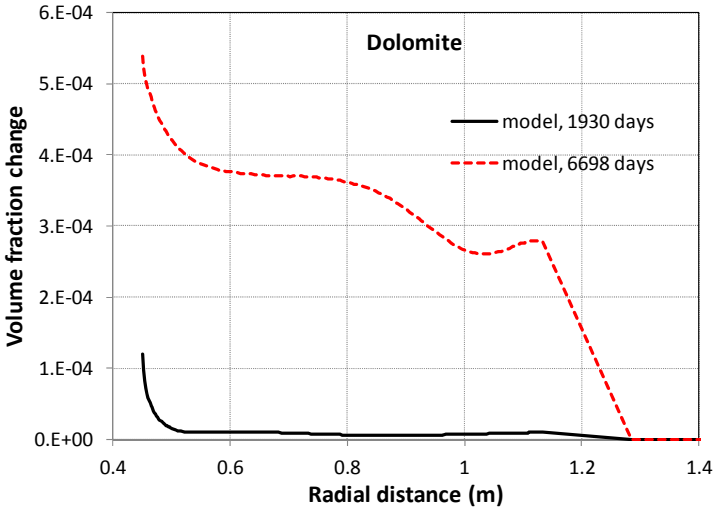

Figure 3-40. Computed profile of volume fraction change of dolomite at the 1930 days (after the dismantling of heater 1) and at 6698 days (July 1, 2015).

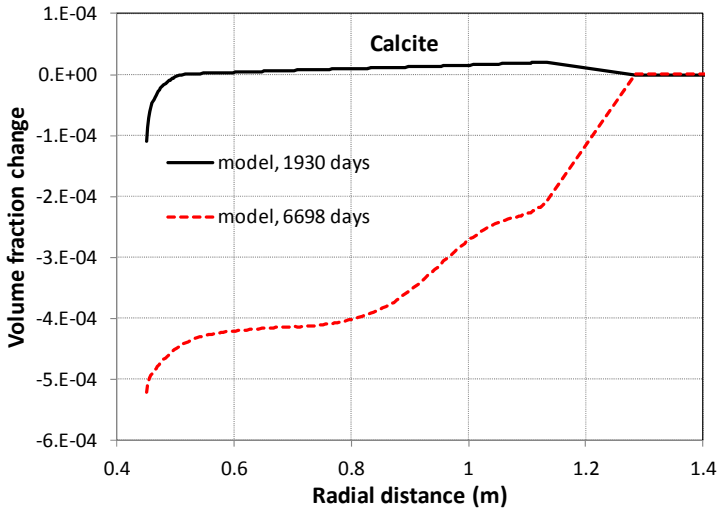

Figure 3-41. Computed profile of volume fraction change of calcite at the 1930 days (after the dismantling of heater 1) and at 6698 days (July 1, 2015).

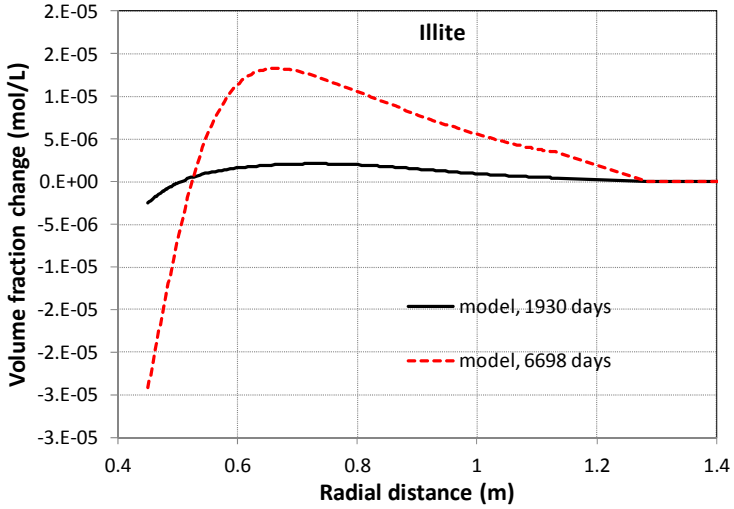

Figure 3-42. Computed profile of volume fraction change of illite at the 1930 days (after the dismantling of heater 1) and at 6698 days (July 1, 2015).

pH is usually very difficult to predict because it involves many reactions. As shown in Figure 3-43, in the sensitivity run that has no reactions, the computed pH is too low. For FEBEX bentonite, pH is mainly regulated by carbonate reactions involving calcite and dolomite and surface protonation reactions. Zheng et al. (2011) showed that surface protonation has strong pH buffering capacity and the model in this report confirms that observation. However, the base model still underestimates the measured pH slightly by 0.1 unit, which may be attributed to the uncertainties in the initial amount of calcite. Figure 3-44 shows the concentration profile of bicarbonate. The base model produces lower bicarbonate concentration than the sensitivity run and results from the base model are lower than measured data. Previous modeling work (e.g.

Samper et al., 2008) showed that bicarbonate concentration is very sensitive to the alteration of calcite and dolomite and is entangled with pH changes. The current model does not consider the dissolution/exsolution of CO_2 gas, which may be a key reaction to explain the underestimation of pH and bicarbonate by the model. Also as mentioned above, inference processes using geochemical modeling were needed to obtain the chemical composition of pore water in bentonite under *in situ* conditions based on the measured concentrations by aqueous extract (Zheng et al., 2008a). However, during the aqueous extract, there was CO_2 exsolution that changed the inventory of total carbonate, which was difficult to capture accurately in the geochemical model that was used to infer the concentration under the *in situ* conditions (Zheng et al., 2008). This is another source of uncertainty regarding the pH and concentration of bicarbonate.

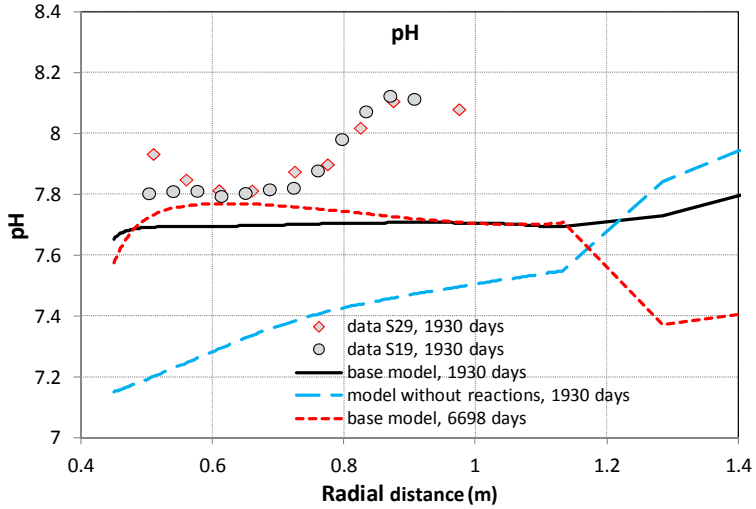

Figure 3-43. The profile of pH at 1930 days (Zheng et al., 2011) and model results from the base model.

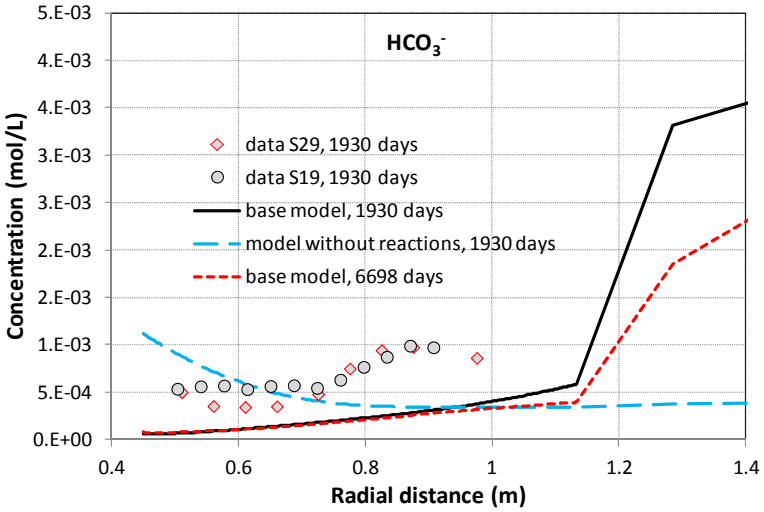

Figure 3-44. The concentration profile of bicarbonate at 1930 days (Zheng et al., 2011) and model results from the base model.

FEBEX bentonite contains a small amount of gypsum (ENRESA, 2000). But the amount is very small and gypsum is very soluble, so a small change in the water saturation may make gypsum disappear, which makes it debatable whether there is gypsum initially in the bentonite. The presence of gypsum had been one of the major uncertainties when the pore water compositions under in situ conditions were inferred from aqueous extract data (Zheng and Samper, 2008). Figure 3-45 shows the inferred data and model results. Unlike cations, the data for sulfate does not follow the trend of chloride, which indicated strong interference by chemical reactions. In the current model, no gypsum is present in the bentonite. Model results underestimate the data. Refinement of the current chemical model is warranted when the swelling of bentonite is properly accounted for.

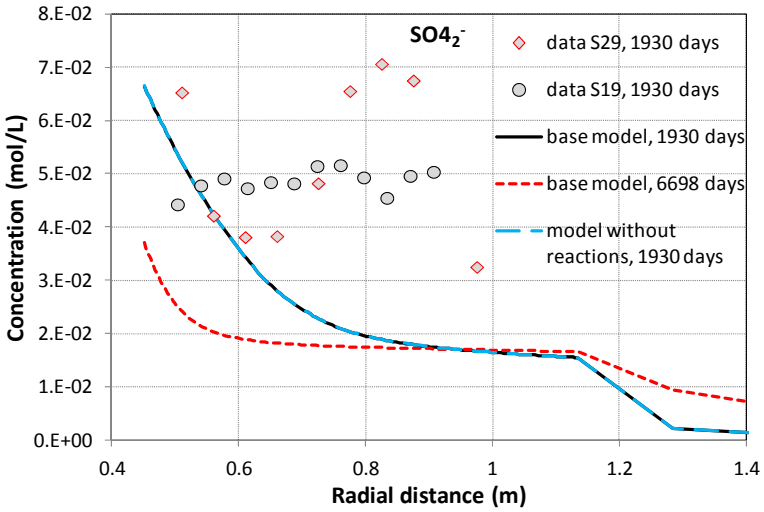

Figure 3-45. The concentration profile of sulfate at 1930 days (Zheng et al., 2011) and model results from the base model.

The concentration profile along the EBS bentonite is the result of complex reaction networks under the influence of coupled THMC processes. For FEBEX bentonite, the inability to obtain concentrations directly (Zheng et al., 2008) adds another layer of uncertainty. In this report, we conducted a few sensitivity analyses to illustrate how these parameters affect the concentration profile in bentonite after the dismantling of heater 1; more analyses will be conducted in the future.

In section 3.4.1.2, we explore the sensitivity of relative humidity to several hydrological parameters. One of these is the permeability of granite, which significantly affects the hydration of bentonite; consequently it will affect profiles of concentration. As we can see from Figure 3-46, lower permeability for granite leads to higher concentration of chloride because less infiltration of granite water leads to less dilution of bentonite pore water, and vice versa, higher permeability of granite leads to lower concentration of chloride in bentonite.

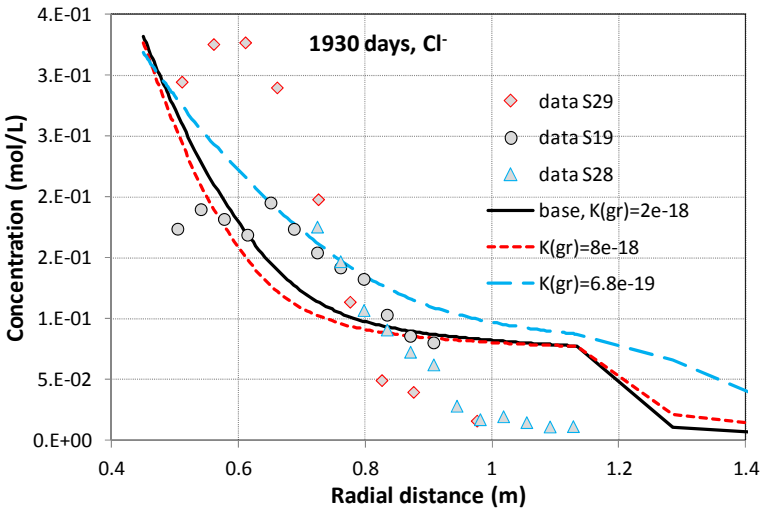

Figure 3-46. The concentration profile of chloride at 1930 days (Zheng et al., 2011) and model results from the base model and two sensitivity runs with different permeability for granite.

Another uncertainty is the initial concentration of major cations and anions in pore water, which stems mostly from the complex pore structure of bentonite. While defining the right pore structure and modeling approach has been, and will be, a challenge for modeling the chemical change in bentonite, here we simply vary the initial concentration of chloride to illustrate how important the initial concentration is in term of controlling the concentration profile for the FEBEX in situ test. Figure 3-47 shows the concentration profile of chloride with three different initial concentrations. Differences in initial concentrations change the overall level of concentration but not the general trend of concentration profile across the bentonite barrier.

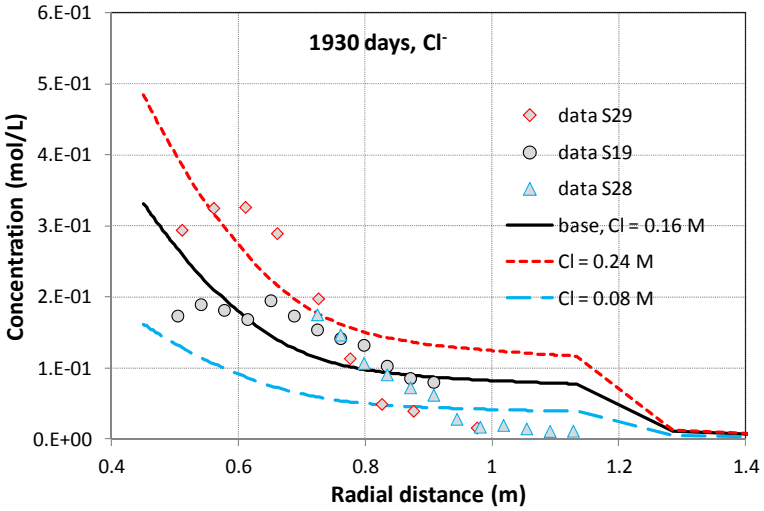

Figure 3-47. The concentration profile of chloride at 1930 days (Zheng et al., 2011) and model results from the base model and two sensitivity runs with different chloride initial concentrations.

Figures 3-34 to 3-45 also show the concentration profiles of major cations and anion and minerals phase changes at 6698 days, corresponding to July 1, 2015. The dismantling of heater 2 started on April 2015 and is expected to finish in August, 2015. July 1, 2015 is just an approximation of the time that samples for geochemical analyses were to be taken. When we know the time that samples are taken, the appropriate simulation data will be used for comparison. Regarding the evolution of concentration of major cations in pore water, after 6698 days (18.3 years) the model predicts lower concentrations near the heater than after 1930 days, but concentration near granite similar to the level of 1930 days (Figures 3-35 through 3-38). Sulfate concentration will be further diluted as more water coming to saturate bentonite (Figure 3-45), but pH and bicarbonate at 6698 days stay roughly the same level as at1930 days (Figures 3-43, 3-44). Regarding the mineral change at 6698 days, calcite continues dissolving and dolomite keeps precipitating; smectite dissolves more in the bentonite blocks near the bentonite/granite interface and start to precipitate in bentonite blocks near the heater. Illite acts the opposite — wherever smectite dissolve it precipitates and vice versa. However, the amount that smectite dissolves and illite precipitates is still very small, which might be difficult to detect.

3.5 Summary and Future Work

The FEBEX *in situ* test that lasted more than 18 years is extremely valuable for validating coupled the THMC model. In the FEBEX-DP project, heater 2 will be dismantled and extensive THMC characterization will be conducted to evaluate the THMC alteration of the bentonite block. LBNL/DOE joins the FEBEX-DP in FY15 and aims to develop a THMC model and test it with data from FEBEX-DP. Specifically we would like to answer the following questions:

- What causes the hydration of bentonite to be slower than typically predicted by a Darcy flow model: Non-Darcian flow behavior, thermal osmosis that counteracts flow towards the heater, decrease of intrinsic permeability of the buffer due to changes in microstructure, or a combination of all these processes?
- What is the spatial density variation of the bentonite as a result of long term hydration and swelling?
- What is the chemical evolution in the bentonite, especially the changes of more soluble minerals (gypsum, calcite and pyrite) and aqueous concentration, evolution of pH and Eh and alteration of smectite?

We planned to start the development of the TH model, then expand the TH model to a THC or THM model and eventually establish the coupled THMC model. This report documents our modeling effort so far in FY15, which encompasses the development the TH model with Non-Darcian flow and the THC model, and comparison between model results with TH data from the bentonite surrounding heater 2 and chemical data obtained from the dismantling of heater 1. The key findings from current modeling work are as follows:

- Adjusting key hydrological parameters such as permeability of bentonite and granite may lead to a good fit of measured relative humidity at given location, but cannot explain relative humidity across the entire bentonite barrier. Mechanical change (especially swelling) has to be considered.

- Including Non-Darcian flow into the TH model leads to a significant underestimation of the relative humidity data in the entire bentonite barrier (even in bentonite near the bentonite/granite interface). The reason could be that the calibration of relative permeability (and retention curve) already encompasses the nonlinear relationship between gradient and flux for bentonite, which would obviate the consideration of Non-Darcian flow in the model. Non-Darcian flow under unsaturated conditions still needs more study.
- In comparison with the chemical data obtained after the dismantling of heater 1 in 2002, the THC model captures the general trend of the concentration profiles of major cations and anions. However, the model overestimates the concentration level in bentonite near the bentonite/granite interface; this effect will be reduced when mechanical change is included in the model, i.e. with THMC models.
- The preliminary prediction of the chemical change after the dismantling of heater 2 shows that concentration levels of aqueous species will continue going down in bentonite near the heater; calcite dissolves and dolomite forms, and illite precipitates in bentonite near the bentonite/granite interface, accompanied by the dissolution of smectite at the same place.

In the remaining months of FY15 and FY16, the following work is planned:

- The mechanical processes will be added to the current THC model. Once the coupled THMC model is developed, mechanical-hydrological coupling will be calibrated again measured stress, dry density, water content and relative humidity data.
- The chemical model will be further refined. Once the concentration profile of chloride can be matched by the THMC model, predictions will be made for other chemical species and mineral phases.
- Once the corrosion of the steel liner is analyzed, chemical changes of steel will be included in the chemical model to evaluate the interaction of steel and bentonite.

Ultimately, after the THMC models for FEBEX *in situ* test are fully validated with data, they will used to explore THMC changes in the long run under higher temperature.

References

Bear, J., (1972). Dynamics of fluids in porous media. American Elsevier Publishing Company Inc., New York. ISBN 0-486-65675-6.

Bradbury, M.H., Baeyens, B., (1998). A physicochemical characterization and geochemical modelling approach for determining porewater chemistries in argillaceous rocks. Geochimica et Cosmochimica Acta 62, 783–795.

Bradbury, B., Baeyens, B., (2003). Porewater chemistry in compacted resaturated MX-80 bentonite. Journal Contaminant Hydrology 61, 329–338.

Bradbury, M. H. and B. Baeyens (2005). Modelling the sorption of Mn(II), Co(II), Ni(II), Zn(II), Cd(II), Eu(III), Am(III), Sn(IV), Th(IV), Np(V) and U(VI) on montmorillonite: Linear free energy relationships and estimates of surface binding constants for some selected heavy metals and actinides. Geochimica et Cosmochimica Acta 69(4): 875-892.

Chen, Y., Zhou, C., Jing, L., (2009). Modeling coupled THM processes of geological porous media with multiphase flow: theory and validation against laboratory and field scale experiments. Computers and Geotechnics 36 (8), 1308–1329.

Cui YJ, Tang AM, Loiseau C, Delage P (2008). Determining the unsaturated hydraulic conductivity of a compacted sand-bentonite mixture under constant-volume and free-swell conditions. Physics and Chemistry of the Earth 33, S462-S471

Deming D (1994). Factors necessary to define a pressure seal. AAPG Bulletin 78(6): 1005-1009

ENRESA (2000). Full-scale engineered barriers experiment for a deep geological repository in crystalline host rock FEBEX Project, European Commission: 403.

ENRESA, (2006a). FEBEX: Updated final report. ENRESA Tech. Publ. PT 05-0/2006, 589 pp.

ENRESA, (2006b). FEBEX: Final THG modelling report. ENRESA Tech. Publ. PT 05-3/2006, 155 pp.

Fernández, A., Rivas, P., (2003). Task 141: post-mortem bentonite analysis. geochemical behaviour. CIEMAT/DIAE/54520/05/03, Internal Note 70-IMA-L-0-107 v0.

Fernández, A.M., Rivas, P., (2005). Pore water chemistry of saturated FEBEX bentonite compacted at different densities. In: Alonso, E.E., Ledesma, A. (Eds.), Advances in Understanding Engineered Clay Barriers. A.A Balkema Publishers, Leiden, The Netherlands, pp. 505–514.

Fernández, A. M., B. Baeyens, M. Bradbury and P. Rivas (2004). Analysis of the porewater chemical composition of a Spanish compacted bentonite used in an engineered barrier. Physics and Chemistry of the Earth, Parts A/B/C 29(1): 105-118.

Fernández, A.M., Cuevas, J., Rivas, P. (2001). Pore water chemistry of the FEBEX bentonite. Mat. Res. Soc. Symp. Proc. 603, 573-588.

Hansbo S (1960). Consolidation of clay, with special reference to influence of vertical sand drains. Swed Geotech Inst Proc 18, Stockholm

Hansbo S (2001). Consolidation equation valid for both Darcian and non-Darcian flow. Geotechnique 51(1): 51-54

Huertas, F. B. de la Cruz, J. L. Fuentes-Cantillana, et al. (2005). Full-Scale Engineered Barriers Experiment for a Deep Geological Repository for High-Level Waste in Crystalline Host Rock – Phase II. EUR 21922

Itasca, (2009). FLAC3D, Fast Lagrangian Analysis of Continua in 3 Dimensions, Version 4.0, Minneapolis, Minnesota, Itasca Consulting Group.

Kuhlman U., Gaus I. (2014). THM Model validation modelling of selected WP2 experiments:
Inverse Modelling of the FEBEX in situ test using iTOUGH2. DELIVERABLE-N°: D3.3-1, NAGRA.

Lanyon, G. W., I. Gaus, M. Villar, P.L.Martín, A. Gens, J. García-Siñeriz, I. Bárcena, (2013). Main outcomes and review of the FEBEX In Situ Test (GTS) and Mock-Up after 15 years of operation, Arbeitsbericht NAB 13-96

Liu, H.H., J. Houseworth, J. Rutqvist, L. Zheng, D. Asahina, L. Li, V. Vilarrasa, F. Chen, S. Nakagawa, S. Finsterle, C. Doughty, T. Kneafsey and J. Birkholzer. (2013). Report on THMC modeling of the near field evolution of a generic clay repository: Model validation and demonstration, Lawrence Berkeley National Laboratory, August, 2013, FCRD-UFD-2013-0000244.

Liu, H.-H. and J. Birkholzer (2012). On the relationship between water flux and hydraulic gradient for unsaturated and saturated clay. Journal of Hydrology 475: 242-247.

Martín, P.L. and J.M. Barcala, (2005). Large scale buffer material test: Mock-up experiment at CIEMAT, Engineering Geology 81, 298– 316.

Martín, P.L., J.M. Barcala, and F. Huertas, (2006). Large-scale and long-term coupled thermo-hydro-mechanic experiments with bentonite: the FEBEX mock-up test, Journal of Iberian Geology 32 (2) 259-282.

Nguyen, T. S., A. P. S. Selvadurai and G. Armand (2005). Modelling the FEBEX THM experiment using a state surface approach. International Journal of Rock Mechanics and Mining Science 42(5-6): 639-651.

Odong, J. (2007). Evaluation of empirical formulae for determination of hydraulic conductivity based on grain-size analysis. The Journal of American Science 3 (3), 54–60.

Pusch, R. and Madsen, F. t. (1995). Aspects on the illitization of the kinnekulle bentonites. Clays and Clay Minerals 43(3): 261-270.

Pruess, K., C. Oldenburg and G. Moridis (1999). TOUGH2 User's Guide, Version 2.0, Lawrence Berkeley National Laboratory, Berkeley, CA.

Ramírez, S., J. Cuevas, R. Vigil and S. Leguey (2002). Hydrothermal alteration of "La Serrata" bentonite (Almeria, Spain) by alkaline solutions. Applied Clay Science 21(5–6): 257-269.

Rutqvist, J., Zheng, L., Chen, F., Liu, H.-H. and Birkholzer, J. (2013). Modeling of Coupled Thermo-Hydro-Mechanical Processes with Links to Geochemistry Associated with Bentonite-Backfilled Repository Tunnels in Clay Formations. Rock Mechanics and Rock Engineering: 1-20.

Sacchi, E., Michelot, J.L., Pitsch, H., Lalieux, P., Aranyossy, J.F., (2001). Extraction of water and solution from argillaceous rock for geochemical characterisation: methods, processes, and current understanding. Hydrogeology Journal 9, 17–33.

Sánchez, M., A. Gens, L. J. D. N. Guimarães and S. Olivella (2005). A double structure generalized plasticity model for expansive materials. International Journal for numerical and analytical methods in geomechanics 29: 751-787.

Sánchez, M., A. Gens and L. Guimarães (2012a). Thermal–hydraulic–mechanical (THM) behaviour of a large-scale in situ heating experiment during cooling and dismantling. Canadian Geotechnical Journal 49(10): 1169-1195.

Sánchez, M., A. Gens and S. Olivella (2012b). THM analysis of a large-scale heating test incorporating material fabric changes. International Journal for Numerical and Analytical Methods in Geomechanics 36(4): 391-421.

Samper, J., L. Zheng, L. Montenegro, A. M. Fernández and P. Rivas (2008a). Coupled thermo-hydro-chemical models of compacted bentonite after FEBEX in situ test. Applied Geochemistry 23(5): 1186-1201.

Samper, J., L. Zheng, A. M. Fernández and L. Montenegro (2008b). Inverse modeling of multicomponent reactive transport through single and dual porosity media. Journal of Contaminant Hydrology 98(3–4): 115-127.

Siitari-Kauppi, M.; Leskinen, A., Kelokaski, M.; Togneri, L. Alonso, U.; Missana, T.; García - Gutiérrez, (2007). Physical Matrix Characterisation: Studies of Crystalline Rocks and Consolidated Clays by PMMA Method and Electron Microscopy as Support of Diffusion Analyses. CIEMAT Technical Report, 1127, December 2007.

Swartzendruber D (1961). Modification of Darcy's law for the flow of water in soils. Soil Science 93: 22-29

Wolery, T. J., (1993). EQ3/6, A software package for geochemical modelling of aqueous systems, Version 7.2. Lawrence Livermore National Laboratory, USA.

Xu, T., Spycher, N., Sonnenthal, E., Zhang, G., Zheng, L. and Pruess, K. (2011). TOUGHREACT Version 2.0: A simulator for subsurface reactive transport under non-isothermal multiphase flow conditions. Computers & Geosciences 37(6): 763-774.

Xu, T., E. Sonnenthal, N. Spycher and K. Pruess (2006). TOUGHREACT: A Simulation Program for Non-isothermal Multiphase Reactive Geochemical Transport in Variably Saturated Geologic Media. Computers and Geosciences 32: 145-165.

Zheng, L. and J. Samper (2008). A coupled THMC model of FEBEX mock-up test. Physics and Chemistry of the Earth, Parts A/B/C 33, Supplement 1: S486-S498.

Zheng, L., J. Samper and L. Montenegro (2008). Inverse hydrochemical models of aqueous extracts tests. Physics and Chemistry of the Earth, Parts A/B/C 33(14–16): 1009-1018.

Zheng, L., J. Samper, L. Montenegro and A. M. Fernández (2010). A coupled THMC model of a heating and hydration laboratory experiment in unsaturated compacted FEBEX bentonite. Journal of Hydrology 386(1–4): 80-94.

Zheng, L., J. Samper and L. Montenegro (2011). A coupled THC model of the FEBEX in situ test with bentonite swelling and chemical and thermal osmosis. Journal of Contaminant Hydrology 126(1–2): 45-60.

Zheng, L., Li, L., Rutqvist, J., Liu, H. and Birkholzer, J.T., (2012). Modeling Radionuclide Transport in Clays. Lawrence Berkeley National Laboratory. FCRD-URD-2012-000128

Zheng,L. Jonny Rutqvist, Carl Steefel, Kunhwi Kim, Fei Chen, Victor Vilarrasa, Seiji Nakagawa, Jiangtao Zheng, James Houseworth, Jens Birkholzer. (2014). Investigation of Coupled Processes and Impact of High Temperature Limits in Argillite Rock. FCRD-UFD-2014-000493, LBNL-6719E

Zou Y (1996). A non-linear permeability relation depending on the activation energy of pore liquid. Geotechnique 46(4): 769-774

4. THM MODELING: FE HEATER TEST AND DECOVALEX

In this section, we present LBNL's activities related to THM modeling of underground heater experiments in clay formations, including studies related to the Development of Coupled Models and their Validation against Experiments (DECOVALEX)-2015 project and the Mont Terri FE (Full-scale Emplacement) Experiment. DECOVALEX-2015 is an acronym for the sixth and current phase of the "Development of Coupled Models and their Validation against Experiments" project, ongoing from 2012 through 2015. In DECOVALEX-2015, LBNL participates in Task B, which includes:

Subtask B1—Mont Terri HE-E Experiment: A heating experiment to evaluate sealing and clay-barrier performance, in a micro-tunnel at the Mont Terri URL in Switzerland; and

Subtask B2—Horonobe Engineered Barrier System (EBS) Experiment: A heating experiment to study the thermo-hydro-mechanical-chemical (THMC) behavior of the EBS and its interaction with the mudstone host rock, in a vertical emplacement hole at the Horonobe URL in Japan

In addition to the modeling work in these two DECOVALEX tasks; LBNL participates in the Mont Terri FE Experiment as one of the participating modeling teams. The FE Experiment is undertaken as an ultimate test for the performance of geologic disposal in Opalinus Clay, focusing on both the EBS components and the host-rock behavior; it will be one of the largest and longest running heater tests worldwide.

UFD objectives for participating in these international activities are to develop expertise and test advanced models of coupled processes in clay-based backfill in interaction with clay host rock. Through participation in modeling these field experiment, the models will be developed and experience will be gained for a range of different backfill materials (e.g., bentonite pellets and sand/bentonite mixture), as well as different host rocks (e.g., Opalinus clay and mudstone).

The main software developed and used for these simulations is the TOUGH-FLAC (Rutqvist et al. 2002; 2011; 2014). For nuclear waste isolation, TOUGH-FLAC provides UFD with a model framework for modeling coupled THM processes in the EBS and host rock and their interactions using state-of-the-art macroscopic constitutive models for bentonite, crushed rock salt backfill, clay, salt and crystalline host rocks. For rigorous modeling of the THM behavior of bentonite-based (swelling) buffer and back-fill materials, the BBM (Barcelona Basic Model) and BExM (Barcelona Expansive Model) have been implemented into TOUGH-FLAC. Modeling of the in situ heater experiments provides a unique opportunity to validate and test the models at realistic, large-scale, in-situ conditions, including the interactions between the host rock and EBS. Finally, through the numerical modeling of these experiments and being at the forefront of modeling coupled THMC processes our goal is also to advance the state-of-the-sciences in the field of coupled processes modeling of clay barriers.

In the following Subsection 4.1, the modeling approach and the status of model development will be summarized. Then the modeling work conducted associated with field experiments is presented in Subsections 4.2 through 4.4. Finally, in Subsection 4.5, the current status and future plans for THM m modeling are summarized.

4.1 Modeling Approach

LBNL uses two independent numerical simulators (TOUGH-FLAC and ROCMAS) for modeling of coupled THM processes associated with nuclear waste disposal and for modeling of the aforementioned heater experiments. The TOUGH-FLAC simulator developed at LBNL is the primary analysis tool, because this simulator has the required capabilities to model a large variety of problems associated with nuclear waste disposal for various engineering and natural systems. The ROCMAS code, also developed at LBNL, is in this project used for confidence building through code-to-code verification. That is, models of a particular problem might be built in both TOUGH-FLAC and ROCMAS, and if the simulation results agree, that provides confidence in the models.

Both the TOUGH-FLAC and ROCMAS codes solve THM coupled problems, but are two different codes with different characteristics. TOUGH-FLAC can simulate coupled THM processes under multiphase flow conditions through a sequential coupling of the TOUGH2 multiphase flow simulator with the FLAC3D geomechanical code (Rutqvist et al., 2002; Rutqvist 2011). TOUGH-FLAC has recently been modified for applications related with to bentonite-backfilled repositories in clay host formations (Rutqvist et al., 2014). ROCMAS simulates coupled THM processes in unsaturated media, including single-phase liquid flow and vapor diffusion in a static gas phase (Rutqvist et al., 2001a). The code has been extensively applied in earlier phases of the DECOVALEX project for THM analysis in bentonite-rock systems (Rutqvist et al., 2001b, 2005, 2009). In the following, the TOUGH-FLAC simulator (primary analysis tool) is described in more detail.

The TOUGH-FLAC simulator (Rutqvist 2011), is based on linking the TOUGH2 multiphase flow and heat transport simulator (Pruess et al., 2011) with the FLAC3D geomechanical simulator (Itasca 2011). In this approach, TOUGH2 (Pruess et al., 2011) is used for solving multiphase flow and heat transport equations, whereas FLAC3D (Itasca, 2011) is used for solving geomechanical stress-strain equations. The two codes are sequentially coupled so that a TOUGH-FLAC simulation runs seamlessly.

For analysis of coupled THM problems, TOUGH2 and FLAC3D are executed on compatible numerical grids and linked through a coupled THM model (Figure 4-1) with coupling functions to pass relevant information between the field equations that are solved in the respective codes. In the coupling scheme between TOUGH2 and FLAC3D, the TOUGH2 multiphase pressures, saturation, and temperature are provided to update temperature, and pore pressure to FLAC3D (Figure 4-1). After data transfer, FLAC3D internally calculates thermal expansion, swelling, and effective stress. Conversely, element stress or deformation from FLAC3D is supplied to TOUGH2 to correct element porosity, permeability, and capillary pressure for the fluid-flow simulation in TOUGH2. The corrections of hydraulic properties are based on material-specific functions.

In a TOUGH-FLAC simulation, the calculation is stepped forward in time with the transient multiphase fluid flow analysis in TOUGH2, and at each time step or at the TOUGH2 Newton iteration level, a quasi-static mechanical analysis is conducted with FLAC3D to calculate stress-induced changes in porosity and intrinsic permeability. In this scheme, the fluid-flow sequence is solved first under fixed stress, and the resulting pressure and temperature are prescribed in the mechanical sequence. This corresponds to so-called stress-fixed iterations in the sequential scheme, in which the solution becomes unconditionally stable. The resulting THM analysis may

be explicit sequential, meaning that the porosity and permeability is evaluated only at the beginning of each time step, or the analysis may be implicit sequential, with permeability and porosity updated on the Newton iteration level towards the end of the time step using an iterative process.

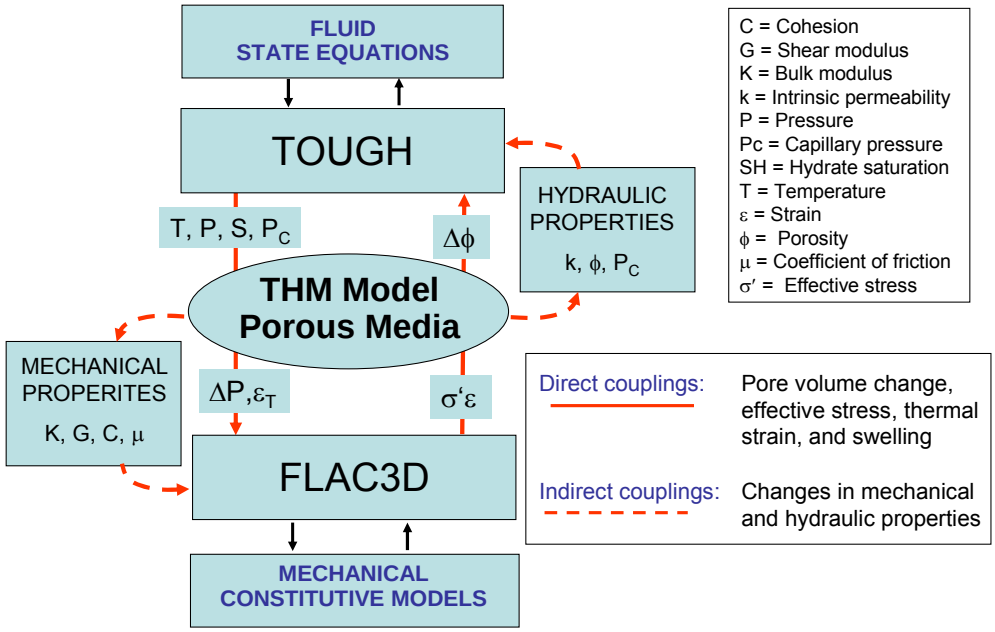

Figure 4-1. Schematic of linking of TOUGH2 and FLAC3D in a coupled TOUGH-FLAC simulation.

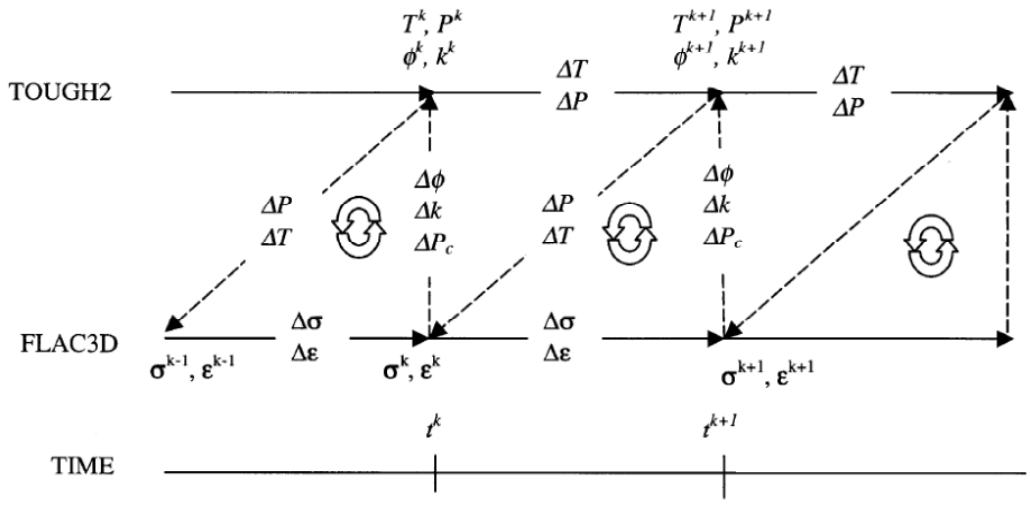

Figure 4-2. Numerical procedure of a linked TOUGH2 and FLAC3D simulation.

A great advantage with this adopted approach is that both codes are continuously developed and widely used in both academia and industry. In TOUGH2, a large number of fluid equation-of-state modules are available, while in FLAC3D, a large number of geomechanical constitutive models are available. This means that the simulator can be relatively easily extended to new application areas.

As part of the UFD effort, the TOUGH-FLAC simulator has been extended and applied to issues related to nuclear waste disposal with bentonite backfilled tunnels (Rutqvist et al., 2011; 2014). This includes implementation of the Barcelona Basic Model (BBM) (Alonso et al., 1990), for the mechanical behavior of unsaturated soils, which has been applied for modeling of bentonite backfill behavior (Rutqvist et al., 2011). The BBM was first developed and presented in the early 1990s as an extension of the Modified Cam Clay (MCC) model to unsaturated soil conditions (Alonso et al., 1990). The model can describe many typical features of unsaturated-soil mechanical behavior, including wetting-induced swelling or collapse strains, depending on the magnitude of applied stress, as well as the increase in shear strength and apparent preconsolidation stress with suction (Gens et al., 2006). Figure 4-3 presents the yield surface of the BBM model in q-p-s space. The shaded surface corresponds to the elastic region at fully water-saturated conditions, which is equivalent to the modified MCC model. The figure also shows how the yield surface expands at unsaturated and dryer conditions when suction increases. There is an increase in both the apparent pre-consolidation pressure along the load collapse (LC) yield surface and by the increasing tensile strength, which in turn leads to an increased cohesion and shear strength.

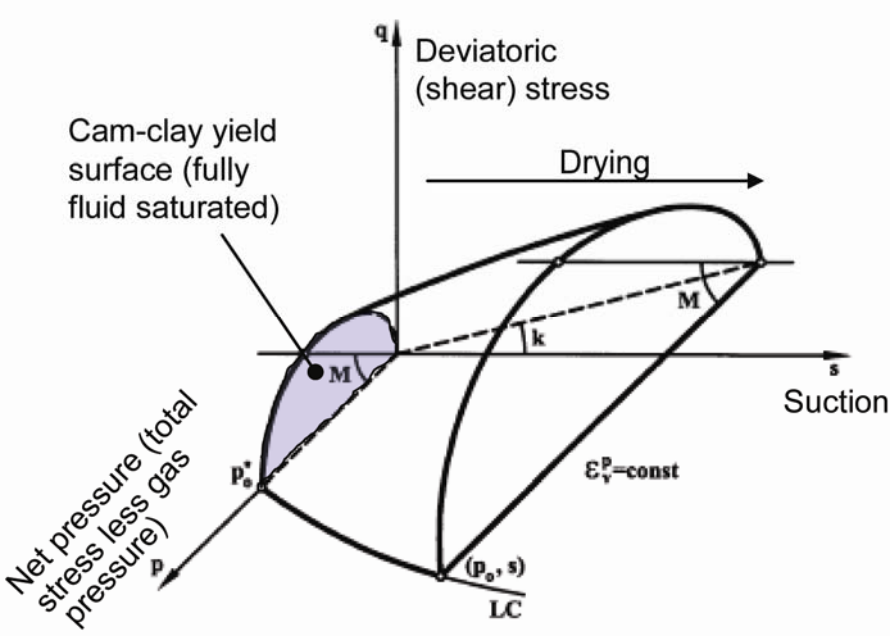

Figure 4-3. BBM constitutive model showing the yield surface in q-p-s space.

The BBM has been used for modeling bentonite-buffer behavior in various national nuclear waste programs in Europe and Japan. For example, the BBM was successfully applied to model the coupled THM behavior of unsaturated bentonite clay associated with the FEBEX *in situ* heater test at the Grimsel Test Site, Switzerland (Gens et al., 2009). The BBM has also been applied to other types of bentonite-sand mixtures based on MX-80, considered as an option for an isolating buffer in the Swedish KBS-3 repository concept (Kristensson and Åkesson 2008). As part of the UFD program, the BBM was also used by Rutqvist et al. (2014), for the modeling of coupled THM processes around a generic repository in a clay host formation.

Recently, as part of the UFD EBS program, the BBM has been extended to a dual structure model, corresponding to the Barcelona Expansive Model (BExM). In a dual-structure model, the material consists of two structural levels: a microstructure in which the interactions occur at the particle level, and a macrostructure that accounts for the overall fabric arrangement of the material comprising aggregates and macropores (Figure 4-4) (Gens et al., 2006, Sánchez et al., 2005, Gens and Alonso 1992). A dual-structure model has important features for modeling the mechanical behavior of a bentonite buffer, such as irreversible strain during suction cycles. However, most importantly, a dual-structure model provides the necessary link between chemistry and mechanics, enabling us to develop a coupled THMC model for the analysis of long-term EBS behavior. This approach enables mechanistic modeling of processes important for long-term buffer stability, including effects of pore-water salinity on swelling (loss of swelling), conversion of smectite to nonexpansive mineral forms (loss of swelling), and swelling pressure versus exchangeable cations. Details of the development, testing and applications of the dual structure model, were presented in the FY2014 milestone report titled “Investigation of Coupled THMC Processes and Reactive Transport: FY14 Progress” (Rutqvist et al. 2014).

Based on model simulation in the DECOVALEX-2015 project with TOUGH-FLAC, considering full multiphase flow (gas and liquid) we found that a gas intrinsic permeability several orders of magnitude higher than the intrinsic permeability related to liquid flow would be required. In the following simulations of the three heater experiments we simulated high intrinsic gas permeability in the bentonite through the Klinkenberg parameter according to:

$$K_g = K_l\left(1 + b/P\right) \tag{4-1}$$

where K_g is intrinsic permeability for gas flow, K_l is intrinsic permeability of water flow, b is the Klinkenberg parameter, and P is pressure. In this case, we assigned a high value of the Klinkenberg parameter of 2.5×10^{11} Pa^{-1}, which means that the intrinsic permeability for gas flow would be about 6 orders of magnitude higher than the intrinsic permeability for water flow. This was necessary as otherwise it is not possible to simulate the drying that usually occurs near the heaters.

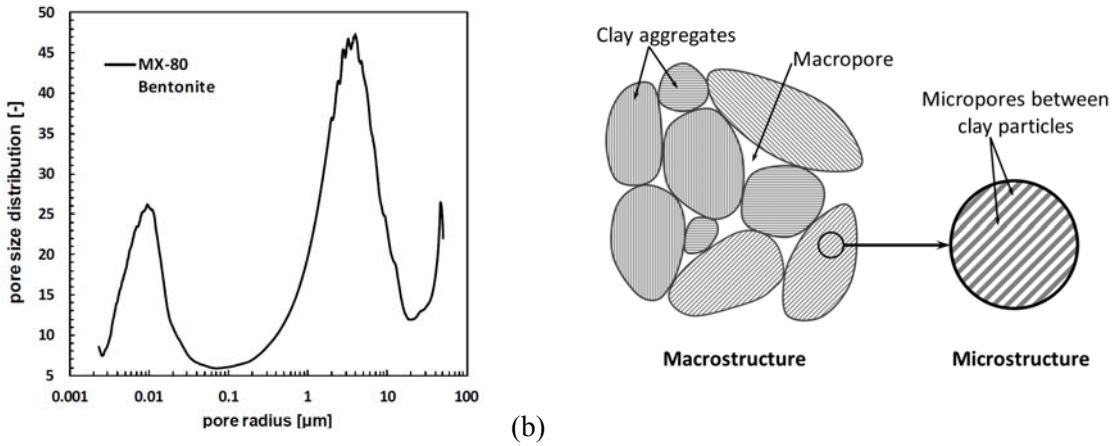

(a) (b)

Figure 4-4. (a) Pore size distribution and (b) schematic representation of the two structural levels considered in the dual structure model. Clay particles are represented by the gray lines.

As will be discussed in Section 4.5, future model developments related to THM process modeling with TOUGH-FLAC will be focused on improving the BExM implementation (especially in terms of efficiency) and to implement and use the model for the evolution of the excavation disturbed zone, starting with implementation and used of the Two-Parts Hooke's Model (TPHM) that has been developed and applied previously in LBNL's work package for UFD.

4.2 Mont Terri HE-E Experiment (DECOVALEX)

The Mont Terri HE-E Experiment focuses on the THM behavior of bentonite barriers in the early nonisothermal resaturation stage and their THM interaction with Opalinus Clay (Figure 4-5). The objective is to better understand the evolution of a disposal system for high level waste in the early post-closure period, with emphasis on the thermal evolution, buffer resaturation (*in situ* determination of the thermal conductivity of bentonite and its dependency on saturation), pore-water pressure in the near field, and the evolution of swelling pressures in the buffer (Gaus et al., 2014). Because the test is conducted in a micro-tunnel (at half scale), it is considered a validation, not a demonstration experiment. The heating test involves two types of bentonite buffer materials (Figure 4-5, left). The heater-buffer interface is heated to a maximum temperature of 135°C and a temperature of 60–70°C is expected at the buffer-rock interface. A dense instrumentation network was in place in the host rock surrounding the micro-tunnel from a previous experiment testing the impact of ventilation on the clay host rock, and has been improved for the purpose of the HE-E Heater Test (up to 40 piezometers in total); various sensors have also been placed in the buffer material. The heating phase started in the late summer of 2011 and is still ongoing.

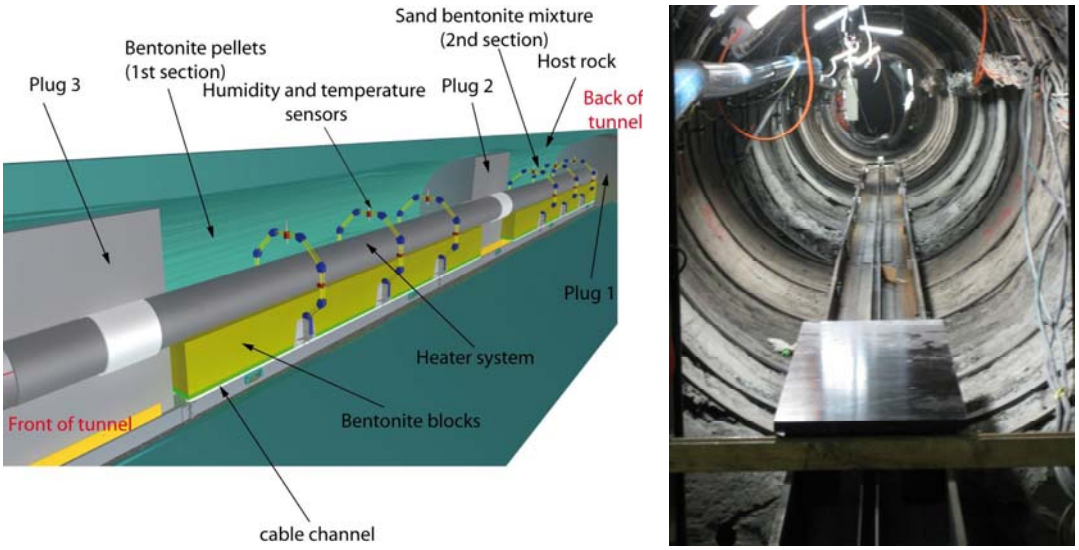

Figure 4-5. Schematic setup of HE-E experiment at Mont Terri and photo of micro-tunnel (Garritte, 2012).

In DECOVALEX-2015 (Task B1), eight international research teams are participating in the modeling of the HE-E experiment. Task B1, which is running over 3 years, is divided into the following steps:

- Step 1a: Opalinus Clay study including HE-D experiment, literature study, processes understanding and parameter determination.
- Step 1b: Buffer material study including CIEMAT column cells, literature study, processes understanding and parameter determination.
- Step 2: HE-E predictive modeling using as-built characteristics and true power load. Modeling is 2-D (axisymmetric, plane strain or combination) and 3-D.
- Step 3: HE-E interpretative modeling when data are made available.

Step 1a started in 2012 with the modeling of the previous HE-D experiment for *in situ* characterization of THM material parameters for the Opalinus Clay and was completed in November 2013. The HE-D experiment involved 1 year of heating of the Opalinus Clay without any bentonite buffer. The modeling of the HE-D experiment and comparison of the TOUGH-FLAC modeling results to the results of other modeling teams were reported in the FY2013 milestone report titled "Report on THMC modeling of the near field evolution of a generic clay repository: Model validation and demonstration" (Liu et al., 2013). Step 1b, which is a study of buffer material properties through modeling of laboratory experiments on buffer material samples, has been completed by all the modeling teams in DECOVALEX-2015. LBNL's final analysis of the CIEMAT column experiments associated with Step 1b was presented in the FY14 milestone report entitled "Investigation of Coupled Processes and Impact of High Temperature Limits in Argillite Rock" (Zheng et al., 2014). In this report we present the results of the predictive analysis of the HE-E experiment, conducted before the field data were available to the

DECOVALEX-2015 participants. We also present a comparison of the model predictions with experimental results. A final interpretive modeling of the field experimental data is also ongoing and will be completed during the rest of FY2015.

4.2.1 TOUGH-FLAC model prediction of the Mont Terri HE-E experiment

Figure 4-6 shows a 3-D model grid for the HE-E experiment and its location within the Mont Terri URL, whereas Figure 4-7 shows more details of the materials in a vertical cross-section that is also the geometry of a 2-D plane strain model. It is a half symmetric model with a vertical symmetry plane along the tunnel axis. In the model, the relevant materials are represented, including the different types of bentonite materials. The most important thermal and hydraulic properties, listed in Table 4-1, were derived from literature data and from material properties derived by modeling of various THM laboratory experiments on bentonite. The intrinsic permeability of gas flow in the bentonite is orders of magnitude higher than the intrinsic permeability for liquid flow and this is simulated in TOUGH2 using a high value of the Klinkenberg parameter (see Section 4.1 and Equation (4-1)). The material properties of the Opalinus Clay are based on the results of the modeling of the HE-D experiment as described Liu et al. (2013).

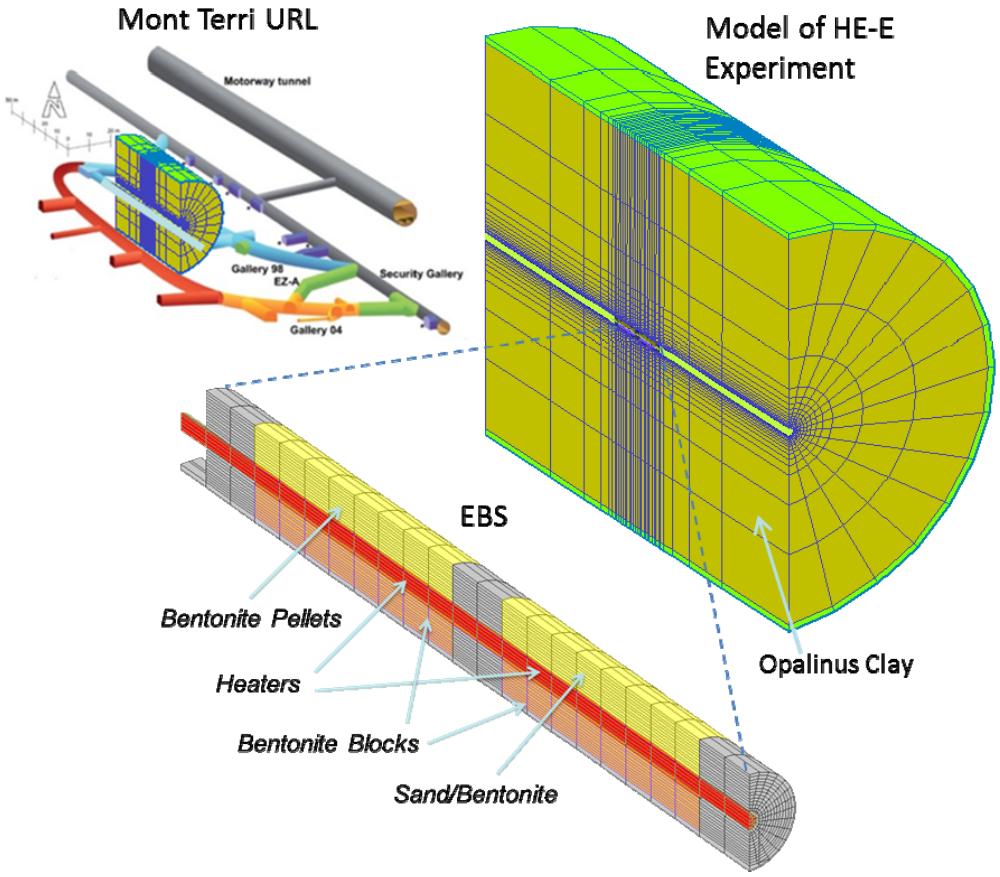

Figure 4-6. TOUGH-FLAC 3-D model of the Mont Terri HE-E experiment.

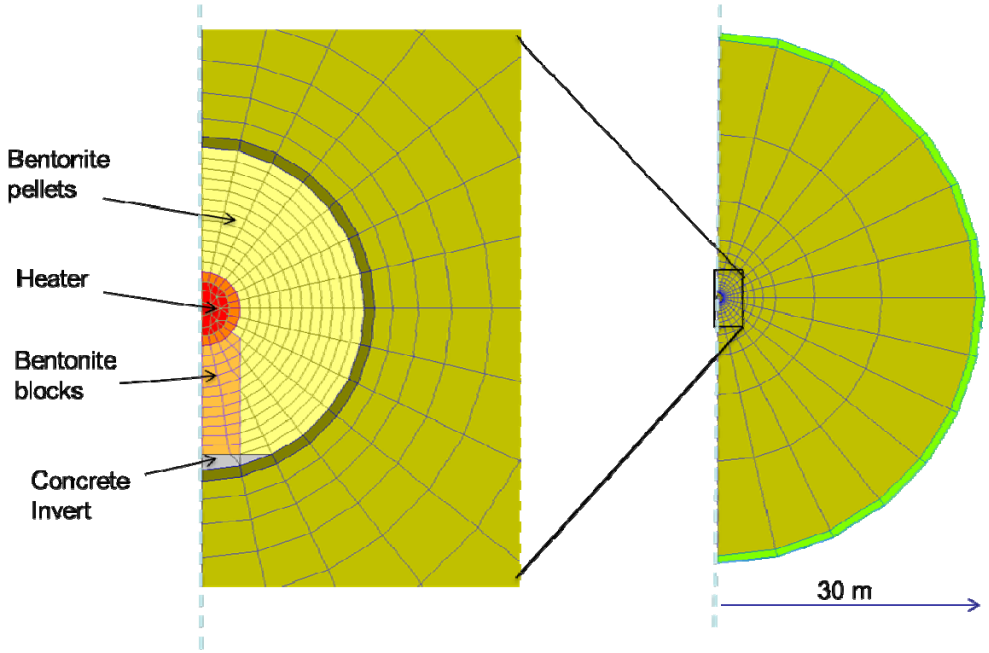

Figure 4-7. Vertical cross-section through the model grid.

Table 4-1. Parameters used in the modeling of the Mont Terri HE-E experiment.

Parameters	Symbol	Opalinus Clay	Granular Bentonite	Bentonite blocks	Concrete (shotcrete and plugs)	Unit
Grain density	ρ_g	2.7×10^3	2.7×10^3	2.7×10^3	2.7×10^3	kg/m^3
Porosity	$Ø$	0.15	0.46	0.389	0.15	-
Intrinsic permeability	k	5.0×10^{-20}	5.0×10^{-21}	2.0×10^{-21}	3.5×10^{-21}	m^2
Liquid relative permeability $k_{rw}(S_w)=\left(\frac{S_w-S_r}{S_m-S_r}\right)^A$	A	-	5	3	-	-
Liquid relative permeability $k_{rw}(S_w)=\left(\frac{S_w-S_r}{S_m-S_r}\right)^{1/2}\left[1-\left\{1-\left(\frac{S_w-S_r}{S_m-S_r}\right)^{1/m}\right\}^m\right]^2$	m	0.52	-	-	0.52	-
Capillary curve $\psi(S_w)=P0\left\{\left(\frac{S_w-S_r}{S_m-S_r}\right)^{-1/m}-1\right\}^{1-m}$	P_0	1.09×10^7	1.0×10^7	3.0×10^7	1.09×10^7	Pa
	m	0.29	0.4	0.32	0.29	-
	S_{ls}	1.0	1.0	1.0	1.0	-
	S_{lr}	0.01	0.0	0.0	0.01	-
Thermal conductivity (wet)	λ_{sat}	1.7	1.3	1.0	1.7	W/m-K
Thermal conductivity (dry)	λ_{dry}	1.06	0.3	0.5	1.06	W/m-K
Grain specific heat	C	800	950	950	800	J/kg-K

The modeling of the HE-E experiment was conducted in several steps (Figure 4-8), including

1) The tunnel being open for 13 years at a constant relative humidity of 98%
2) Bentonite buffer and heaters emplaced for 75 days before start of heating
3) Heating for 1000 days

The simulation of the tunnel open for 13 years at a constant relative humidity of 98% is simulated applying a constant suction value of 2.6 MPa at the tunnel wall. In reality, the tunnel was exposed to a complex history including ventilation experiments, and the average 98% relative humidity was inferred from information in Gaus et al. (2014). This creates a pressure sink around the tunnel with a slight desaturation of the near field rock. The bentonite buffer and heaters where then installed into the model by changing material properties for elements within the tunnel. Also the initial saturation of about 20% in the granular bentonite buffer was assumed based on in-situ observations. Finally, after another 75 days, the heaters were turned on following the heater power used in the actual experiment. In the simplified 2-D model simulations used for the initial model predictions, the actual heat power was scaled down to represent the heat input per meter tunnel.

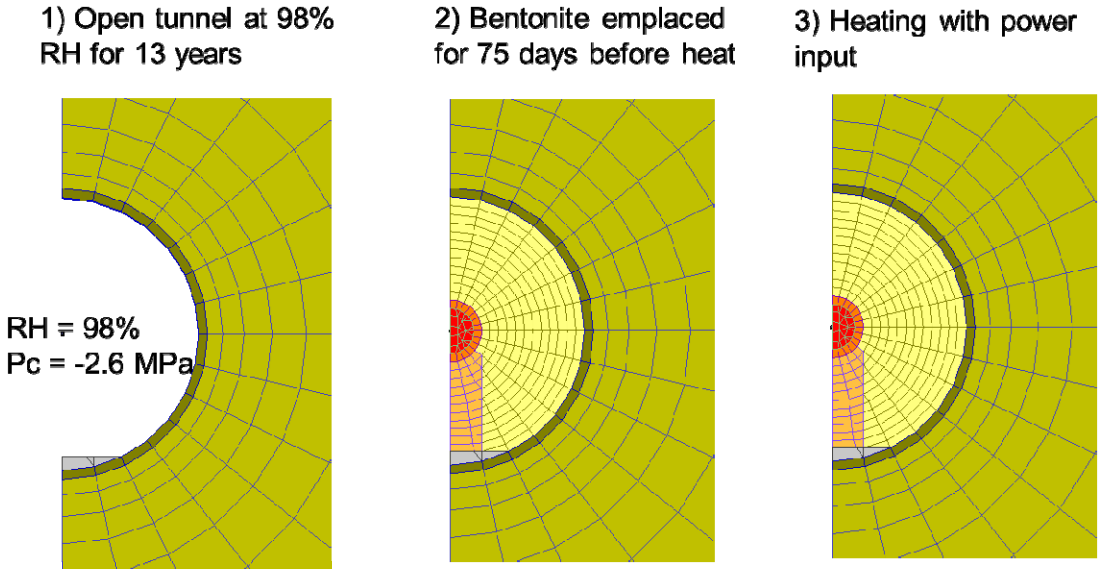

Figure 4-8. Steps for modeling the Mont Terri HE-E experiment.

Figure 4-9 shows the simulation results related to the evolution of liquid saturation and temperature from -100 to 1000 days, i.e. from 100 days before the start of the heating. Figure 4-9a shows that as soon as the bentonite buffer is installed (at -75 day), water is sucked into the bentonite from the adjacent rock. This is seen as a drop in liquid saturation in the rock (orange curve), while the saturation in the bentonite adjacent to the rock wall increases (blue curve). When the heating is turned on, a typical drying occurs at the inner part of the buffer (e.g. red line). Using the given heat power input, the maximum temperature of about 140°C is reached in less than 400 days, while the temperature at the rock wall gradually increases to about 60°C.

In Figure 4-10 compares the simulated responses at two points located in the granular bentonite section with two points located within bentonite blocks, but located at about same distance from the heater. In this case the results are presented in terms of relative humidity and temperature. At the initial saturation of 20% in the granular bentonite, the relative humidity is about 40%, whereas in the bentonite block initial saturation was about 65% with a relative humidity of about 60%. The relative humidity for a given degree of saturation depends on the capillary pressure

and hence the water retention curve. A higher saturation in the bentonite blocks, results in a higher thermal conductivity which explains the difference in the temperature between the monitoring points in the granular bentonite and the bentonite blocks.

A comparison of the predicted and observed evolutions of relative humidity and temperature is shown in Figure 4-11. The figure shows that the general humidity behavior of the bentonite at the rock wall and drying of the inner parts of the bentonite buffer are captured in the modeling. Model results for relative humidity, which is related to saturation, shows very good agreement with measurements for the blue and red curves (i.e. close the rock wall and close to the heater). However, the model overestimates relative humidity in the mid part of the bentonite buffer (green curve). A parameter study was performed as to identify possible reasons for this discrepancy in the wetting of the bentonite buffer. The included variation of buffer absolute permeability (no significant effect), diffusion coefficient (did not help) and buffer relative permeability (tried to reduce relative permeability, but this did not help). A possible reason that will be investigated next is the high suction part of the water retention curve with the van-Genuchten water retention model may cause important deviations from the experimental data at low saturation. Nevertheless, the overall evolution of relative humidity was reasonably predicted by the modeling.

Figure 4-12 shows the evolution of fluid pressure within Opalinus Clay at a monitoring point located 3.54 m from the tunnel wall. This increase in fluid pressure is a result of so-called thermal pressurization, caused by thermal expansion of the pore fluid that cannot escape in the relatively low-permeability host rock. The magnitude and duration of this excess pressure pulse depends on parameters such as rock permeability, and compressibility of water and rock (Rutqvist et al., 2014). Using the Opalinus Clay properties determined from the modeling of the HE-D experiments, it appears that the model could predict this pressure increase fairly well.

The next step will be to complete the interpretive analysis by detailed comparison to measured data for final model comparison within the DECOVALEX-2015 project.

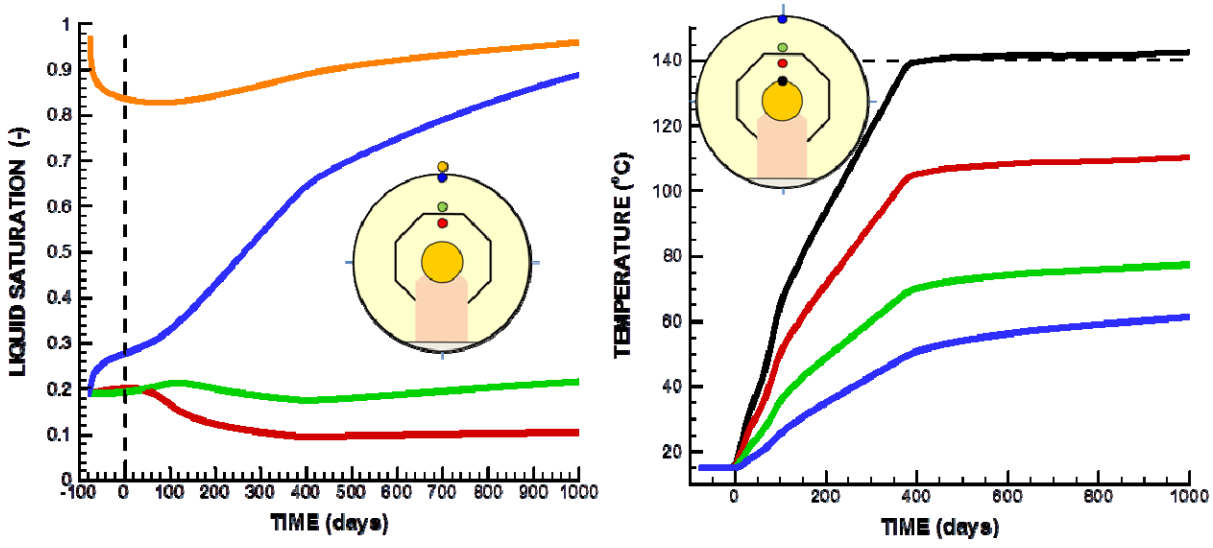

(a) (b)

Figure 4-9. Calculated evolution of (a) liquid saturation and (b) temperature.

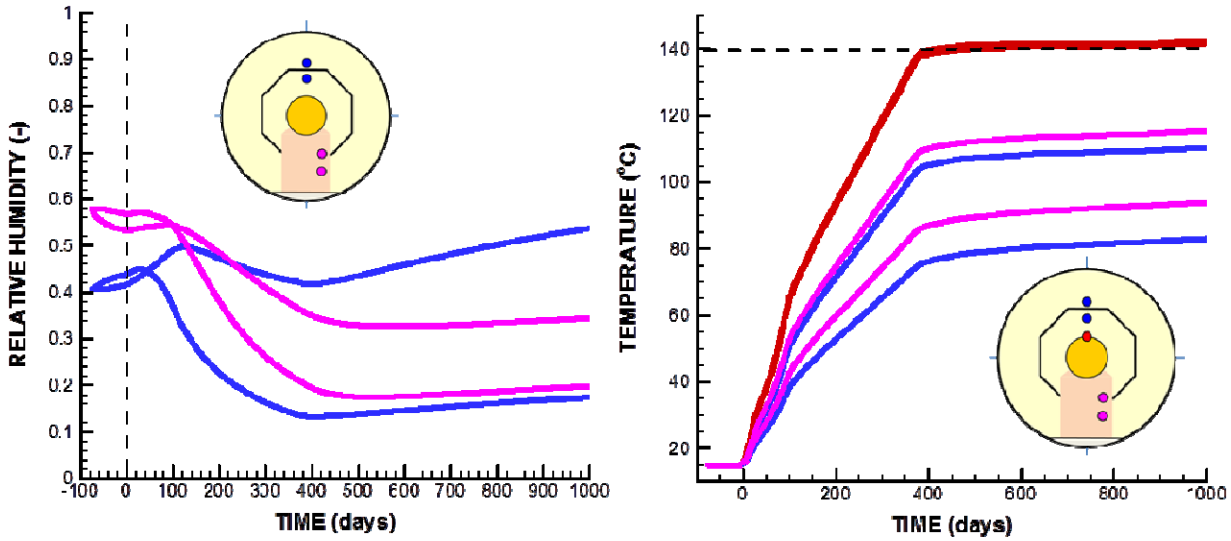

Figure 4-10. Calculated evolution of (a) liquid saturation relative humidity and (b) temperature at monitoring points in the granular bentonite (above heater) and bentonite blocks (below heater).

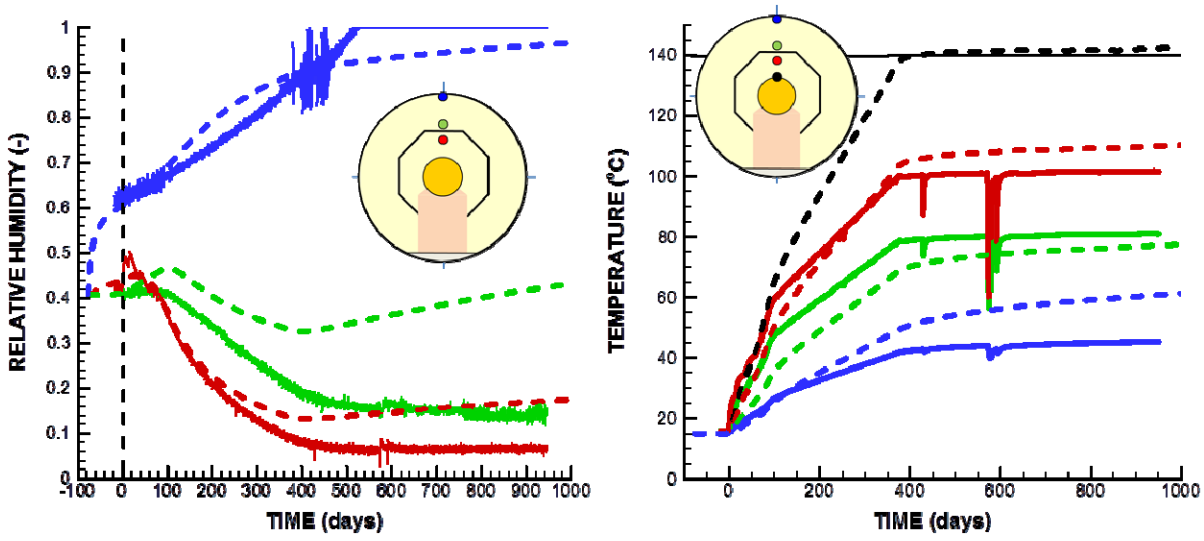

Figure 4-11. Comparison of predicted (dashed lines) and measured (solid lines) evolutions of (a) liquid saturation relative humidity and (b) temperature.

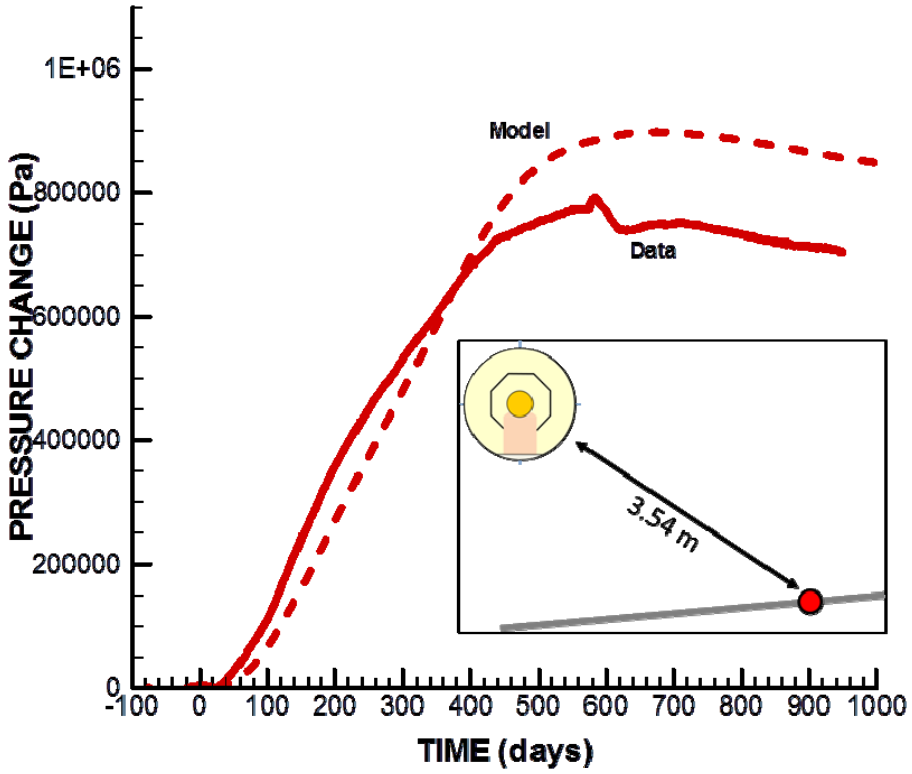

Figure 4-12. Comparison of predicted (dashed lines) and measured (solid lines) evolutions of pore pressure in Opalinus Clay at a point located 3.54 m from the tunnel wall.

4.3 Horonobe EBS Experiment (DECOVALEX)

This task focuses on coupled THMC modeling of a planned full-scale EBS experiment conducted by the Japan Atomic Energy Agency (JAEA) at the Horonobe URL, Hokkaido, Japan (Figure 4-13). The EBS experiment is carried out at a depth of 350 m in a very porous and soft, siliceous mudstone with the following basic properties:

- Porosity 35-60%
- Permeability 10^{-20} – 10^{-18} m^2
- UCS (Strength) 5-25 MPa
- Young's Modulus 1-4 GPa
- Thermal Conductivity 1.34-1.53 W/mK

Figure 4-14 shows the experimental layout with a vertical heater emplacement installed in a test pit at the bottom of an experimental drift. The detailed sequence of the experiment is given in Table 4-2. The experimental drift was backfilled after the installation of the heater and bentonite buffer into the test pit. Bentonite buffer and backfill materials are based on the Japanese Kunigel V1 bentonite. For the buffer, Kunigel V1 bentonite is mixed with sand and emplaced at a dry density of 1.6 g/cm^3, whereas for the backfill, rock debris is mixed in, for an emplacement dry

density of 1.4 g/cm^2. The experimental area was then isolated by a concrete plug and the heater was finally turned on January 15, 2015. Sensors have been installed in buffer, backfill, and rock to monitor temperature, stress, strain, pore pressure, humidity, displacement, pH, resistivity, electric potential, and seismic velocity.

Figure 4-15 shows some early time measurements of heater surface temperature as well as pore pressure at the bottom of the test pit (within the sand layer). During the construction and installation of the buffer, backfill and plug, water was pumped out of the test pit. The pump was turned off on December 22, 2014 i.e. 24 days before the heater was turned on. Figure 4-15a shows that the water pressure increases due to inflow from the rock and reaches a steady value about 60 kPa after 15 to 20 days.

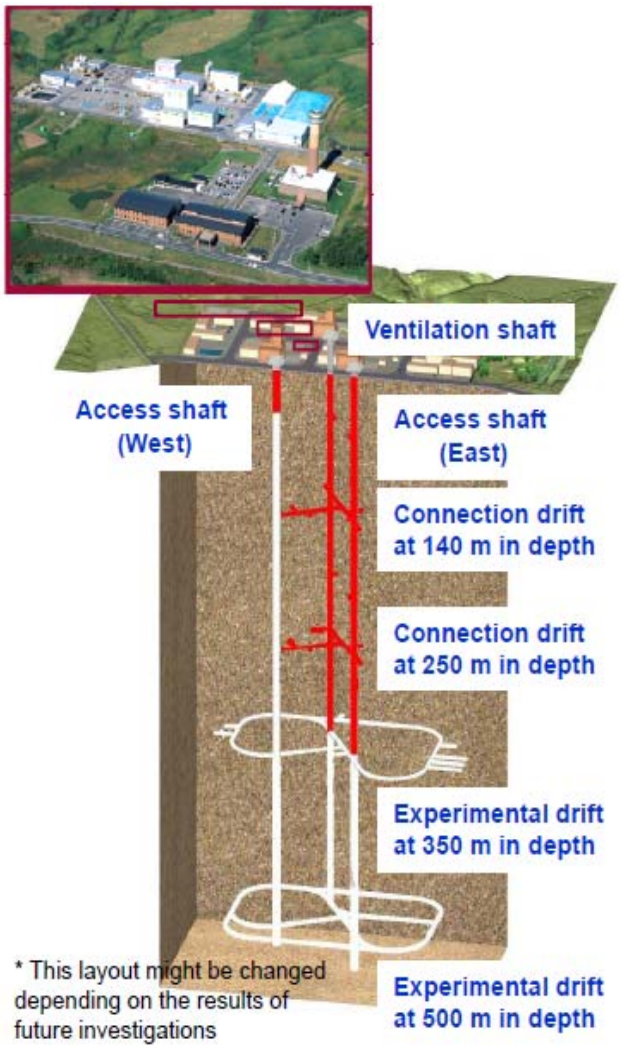

Figure 4-13. Layout of the Horonobe URL in Hokkaido, Japan.

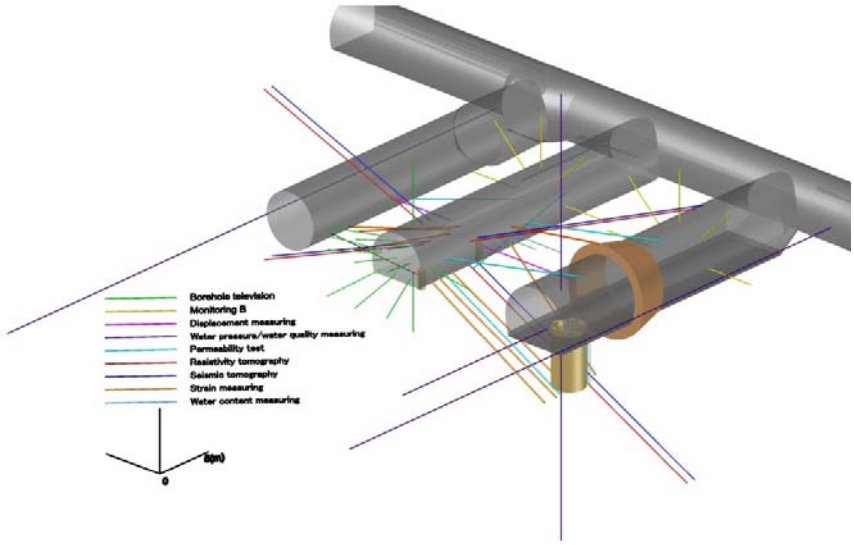

(a)

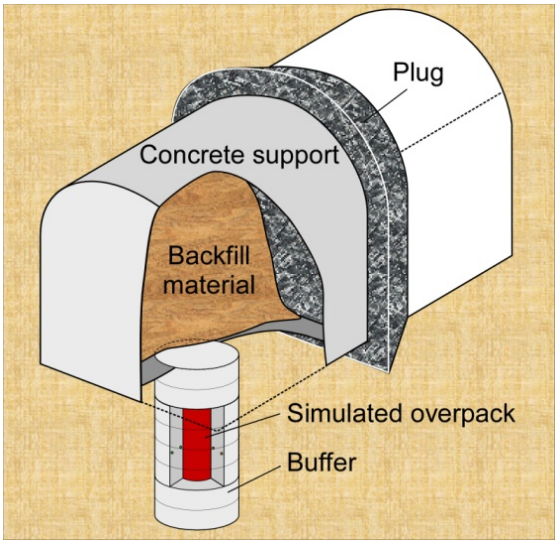

(b)

Figure 4-14. General description of the EBS experiment at the Horonobe URL Project in Japan.

Table 4-2. Details on the sequence of construction and installation of the Horonobe EBS experiment

Sequence of the Horonobe EBS Experiment	
Excavation of the experimental gallery	Oct 29 – Dec 6, 2013
Opening of the test pit	Feb 3 – 8, 2014
Emplacement of the buffer	Aug 18 – Sept 6, 2014
Emplacement of the backfill	Sep 8 – Oct 3, 2014
Plugging	Oct 9 – 27, 2014
Stop pumping up water from pit	Dec 22, 2014 at 14:00

Start of heating	Jan 15, 2015 at 14:20

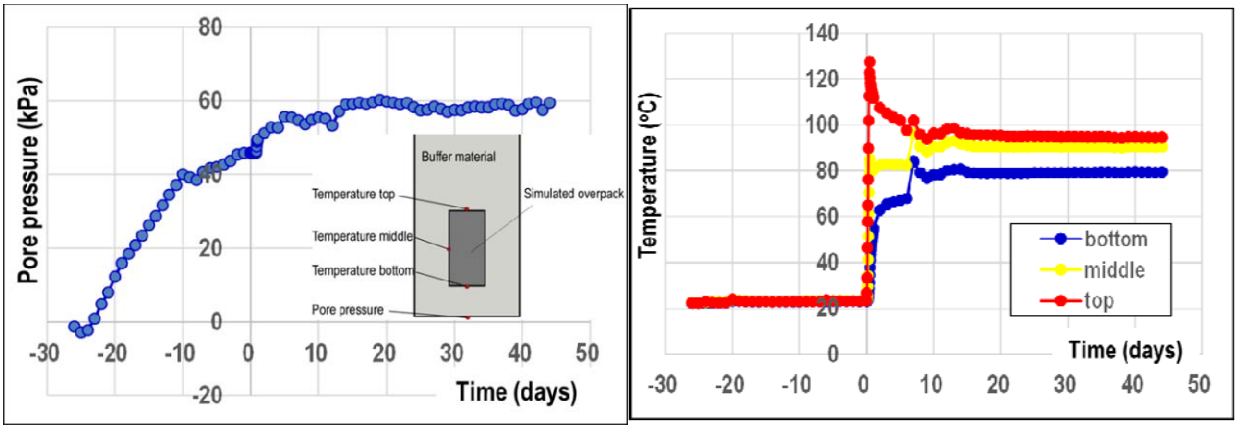

(a) (b)

Figure 4-15. Early time monitored fluid pressure in the test pit and temperature evolution at the heater surface that will help to define boundary conditions in the interpretive modeling of the Horonobe EBS experiment.

4.3.1 DECOVALEX modeling tasks and status related to Horonobe EBS experiment

The DECOVALEX Task B2 related to the Horonobe EBS experiment is divided into the following steps;

- Step 1 (1D benchmark test with comparison of numerical models)
- Step 2 (Prediction analysis)
- Step 3 (Calibration analysis)

The 1D benchmark test (Step 1) was defined with exact properties and boundary conditions given by the JAEA. The benchmark test was conducted for the teams to familiarize themselves with the problem and for precise comparison of computer codes before going into the more complex full-scale case. Thereafter, in Step 2, a model of the real experimental design should be constructed and a first predictive analysis was to be performed for several years from the start of the heating. The heating started on January 15, 2015, and JAEA will eventually provide the monitored data for the first six months of heating to the research teams. The research teams should then calibrate their models against this first 6 months of field data and then carry out coupled numerical analysis for long-term predictions (100–1,000 years) using the test conditions of the EBS experiment.

JAEA provides reports from the investigations at the Horonobe URL for input parameters related to the mudstone host rock and buffer material properties for the Kunigel V1 bentonite from the previous H12 project, whereas properties for the backfill are being investigated along with this project.

DECOVALEX-2015 Task B2 started in May 2013 with Step 1, which has been completed. In the FY14 milestone report entitled “Investigation of Coupled Processes and Impact of High

Temperature Limits in Argillite Rock" (Zheng et al., 2014), we presented the final results of the Step 1 benchmarking with comparison to the results of other DECOVALEX-2015 teams. In this report we present Step 2 model predictions of the full scale EBS experiment with comparison of the results to other DECOVALEX-2015 modeling teams. In DECOVALEX-2015, five research teams are participating in the modeling of the Horonobe EBS experiment with the models listed in Table 4-3. Some of the models listed in Table 4-3 have been extensively applied in previous DEOCOVALEX project phases, whereas some are new and being developed.

Table 4-3. DECOVALEX research teams and numerical simulators in modeling Horonobe EBS experiment

Research Team	Numerical Simulator	Brief Description of Numerical Simulator
DOE U.S. Department of Energy's Research Team: Lawrence Berkeley National Laboratory (LBNL)	TOUGH-FLAC	TOUGH-FLAC is a simulator for analysis of coupled THM processes under multiphase fluid flow conditions being developed at the LBNL (Rutqvist et al., 2002). The simulator is based on linking of the existing computer codes TOUGH2 and FLAC3D, and has been extended for modeling of coupled THM and THMC processes associated with nuclear waste disposal with backfilled emplacement tunnels in clay formations (Rutqvist et al., 2014).
	ROCMAS	ROCMAS is a finite element program for analysis of coupled THM processes in porous and fractured rock developed at LBNL (Rutqvist et al., 2001a). It can model unsaturated media with single-phase liquid flow and vapor diffusion in a static gas phase The code has been extensively applied in earlier phases of the DECOVALEX project for THM analysis in bentonite-rock systems (Rutqvist et al., 2001b; 2005).
BGR Bundesanstalt für Geowissenschaften und Rohstoffe's Research Team: University of Tübingen	GeoSys/ Rockflow	GeoSys/Rockflow is based on object-oriented programming (Kolditz et al., 2003). It was first applied in previous DECOVALEX phases for analysis of thermal-hydrological and thermal-mechanical processes and has been extended to THM (Wang et al., 2006). For the present study, an unsaturated single-phase liquid flow and vapor diffusion is considered.
CAS Chinese Academy of Sciences' Research Team	EPCA3D	The EPCA code (Elasto-Plastic Cellular Automata) uses the concept of cellular automata inspired by the self-organizing theory in biology. This code has been successfully used to simulate the failure process of heterogeneous rocks with and without consideration of hydro-mechanical coupling (Feng et al., 2006; Pan et al., 2008).
JAEA Japan Atomic Energy Agency's Research Team, including Hazama Cooperation	THAMES	THAMES is a finite element program for analyzing coupled THM processes in porous and fractured rock developed at the Kyoto University (Ohnishi and Kobayashi, 1996). The code has been extended to unsaturated media with single-phase liquid flow and vapor diffusion in a static gas phase (Chijimatsu et al., 2005).
KAERI Korean Atomic Energy Research Institute	FLAC/ FLAC3D/ Tough2	Simulation tools being developed along with the DECOVALEX-2015 project based on FLAC and FLAC3D linked with TOUGH2.

4.3.2 TOUGH-FLAC Model prediction of the full scale Horonobe EBS experiment

We made a 3-D model and a prediction of the THM responses at the Horonobe EBS experiment. The model is half symmetric, including half of the tunnel and half of the deposition hole (Figure 4-16). It contains all relevant materials, including mudstone rock, buffer, backfill, a sand layer at the rock/buffer interface, concrete lining and plug. In this model prediction, we use the properties of the buffer and rock developed associated with the 1D benchmark calculation (Table 4-4). Additional properties for the backfill, sand layers, concrete lining and plug were provided by the JAEA to DECOVALEX -2015 modeling teams. The intrinsic permeability of gas flow in the bentonite is orders of magnitude higher than the intrinsic permeability for liquid flow and this is simulated in TOUGH2 using a high value of the Klinkenberg parameter (see Section 4.1 and Equation (4-1)).

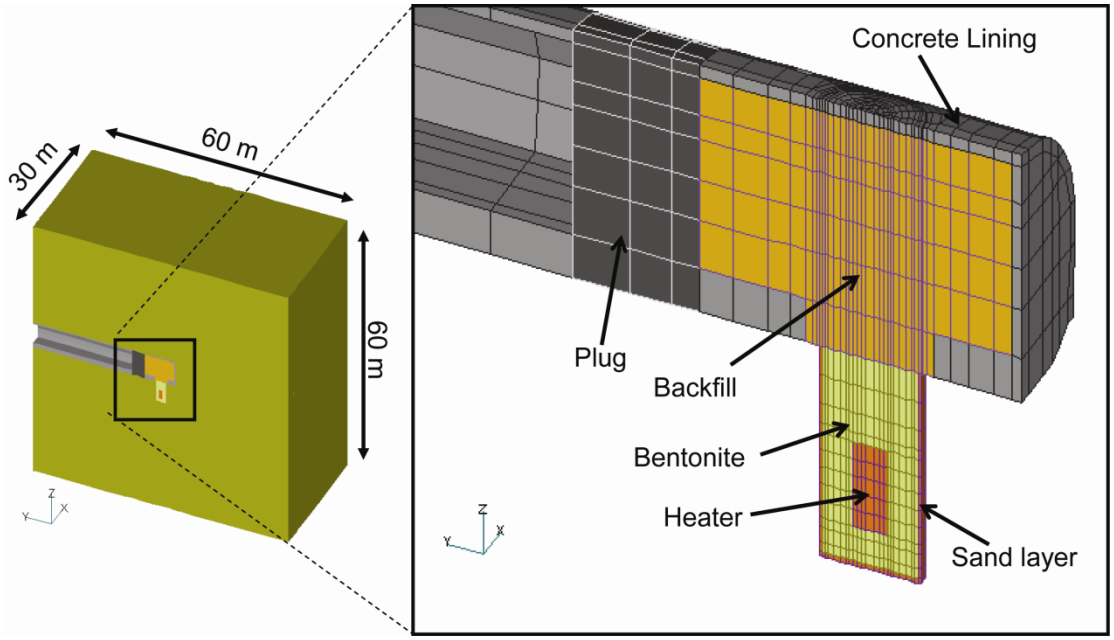

Figure 4-16. TOUGH-FLAC 3-D numerical grid of the Horonobe EBS experiment.

Table 4-4. Material parameters for modeling Horonobe EBS experiment.

Parameter	Symbol	Overpack	Buffer	Backfill	Rock
Grain density (kg/m^3)	ρ_g	10,000.	2680.	2680.	2454.
Porosity	ϕ	0.403	0.403	0.460	0.4482
Permeability (m^2)	K	5 x 10^{-51}	4 x 10^{-20}	1.5 x 10^{-19}	1.33 x 10^{-15}
Thermal conductivity (saturated) (W/mºC)	λ_{wet}	20	1.986	1.250	1.231
Specific heat (solids) (J/kg°C)	C	10,000	341	341	626
Thermal conductivity (desaturated) (W/mºC)	λ_{dry}	20	0.444	0.444	0.579
Water relative permeability parameters using power function $k_{rw}(S_w) = \left(\frac{S_w - S_r}{S_m - S_r}\right)^A$	A	1.3	1.3	1.3	NA
	S_r	0	0	0	NA
	S_m	1	1	1	NA
Water relative permeability parameters using van-Genuchten equations $k_{rw}(S_w) = \left(\frac{S_w - S_r}{S_m - S_r}\right)^{1/2}\left[1 - \left\{1 - \left(\frac{S_w - S_r}{S_m - S_r}\right)^{1/m}\right\}^m\right]^2$	M	NA	NA	NA	0.503
	S_r	NA	NA	NA	0
	S_m	NA	NA	NA	1
Capillary pressure parameters using van-Genuchten equation $\psi(S_w) = 1/\alpha\left\{\left(\frac{S_w - S_r}{S_m - S_r}\right)^{-1/m} - 1\right\}^{1-m}$	α (m^{-1})	8 x 10^{-3}	8 x 10^{-3}	8 x 10^{-3}	9.928 x 10^{-3}
	m	0.375	0.375	0.375	0.503
	S_r	0	0	0	0
	S_m	1	1	1	1
Vapor diffusion coefficients (m^2/s)	D_v	3.5 x 10^{-6}	3.5 x 10^{-6}	3.5 x 10^{-6}	3.5 x 10^{-6}
Young's modulus E, (MPa)	E	200.000	37	3	1820.0
Poisson's ratio (-)	ν	0.3	0.3	0.4	0.21
Linear thermal expansion coefficient (C^{-1})	C^{-1}	1 x 10^{-6}	1 x 10^{-6}	1 x 10^{-6}	1.33 x 10^{-5}
Moisture swelling coefficient, β_{sw}	β_{sw}	0	0.0108	0.0108	0

We simulated the experiment in 3 steps:

1) Excavations are open for 3 months.

2) Excavations are filled with backfill and the heater, buffer and plug are all installed for 6 months.

3) Then heating starts.

In this model prediction, we simulated heating for about 2 years. The results of temperature and saturation evolution for points located in the buffer and near-field rock are shown in Figures 4-17 and 4-18. When keeping the heater temperature constant at 100°C, the simulation shows that the temperature at the buffer-rock interface (P3, P4 in Figure 4-17) increases to about 60°C after 2 years. The liquid saturation in the buffer increases slowly by water infiltration from the surrounding rock (Figure 4-18). Also, a slight desaturation was predicted in the sand layer during the first 200 days. The liquid saturation at the inner part of the buffer decreases due to evaporation and vapor flow transport (P1 in Figure 4-18). Figure 4-19 presents results of displacements relative to an anchor at the rock wall. The calculated results in Figures 4-17 through 4-19 are sensible and show that we are able to use this full 3-D TOUGH-FLAC model of the Horonobe EBS experiment for making a model prediction of the THM responses during the heating.

The results of the model predictions provided by all the DECOVALEX-2015 modeling teams, have been compared. Figure 4-20 and 4-21 shows example of comparison related to the evolution of temperature and liquid saturation in the bentonite buffer. The results are quite

consistent and in good agreement between the modeling teams, though some outliers can be observed. The next step is to complete Step 3, which is the calibration analysis using measured data to be provided by the JAEA.

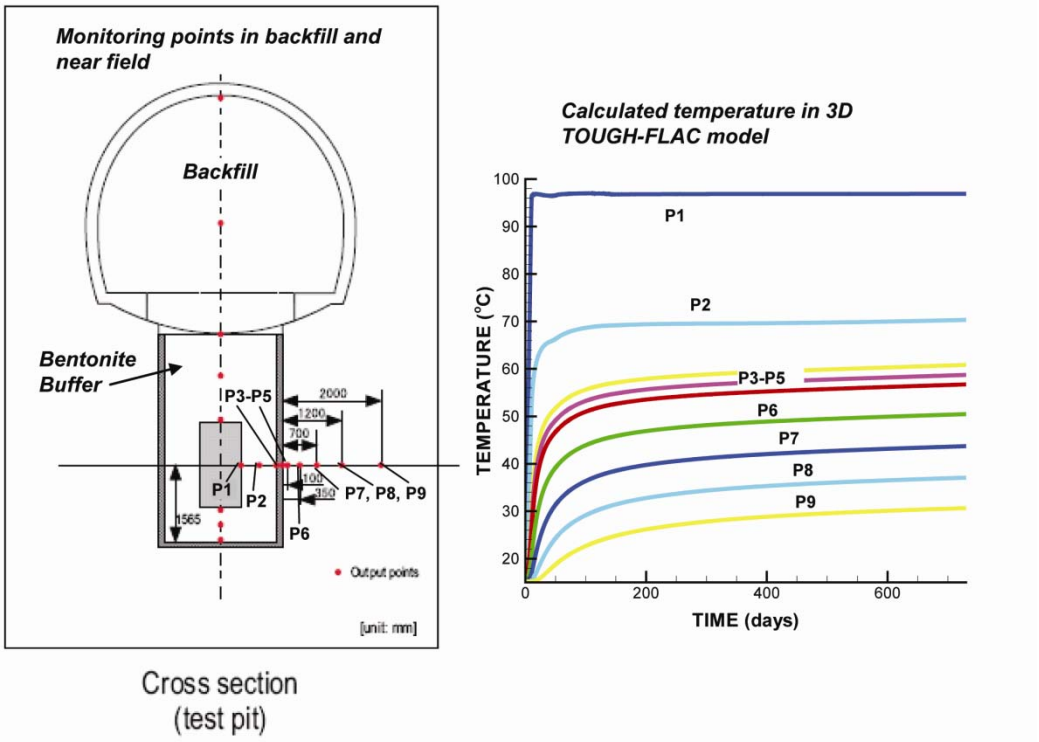

Figure 4-17. TOUGH-FLAC simulation results of temperature in the buffer and rock.

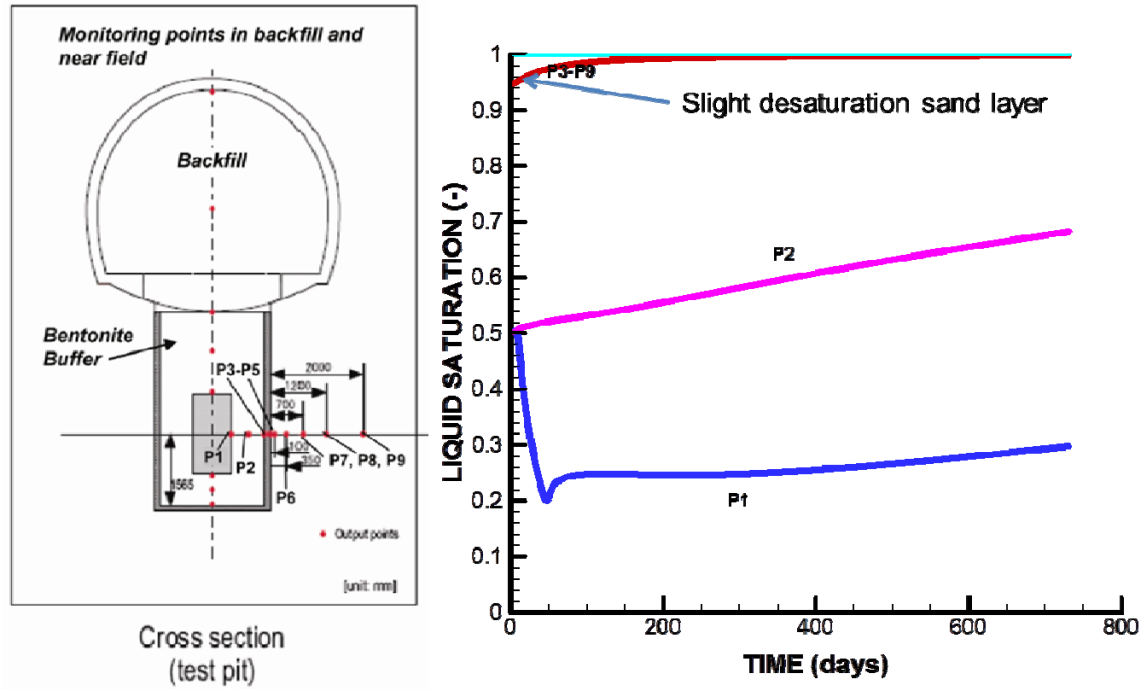

Figure 4-18. TOUGH-FLAC simulation results of liquid saturation in the buffer, sand layer and rock.

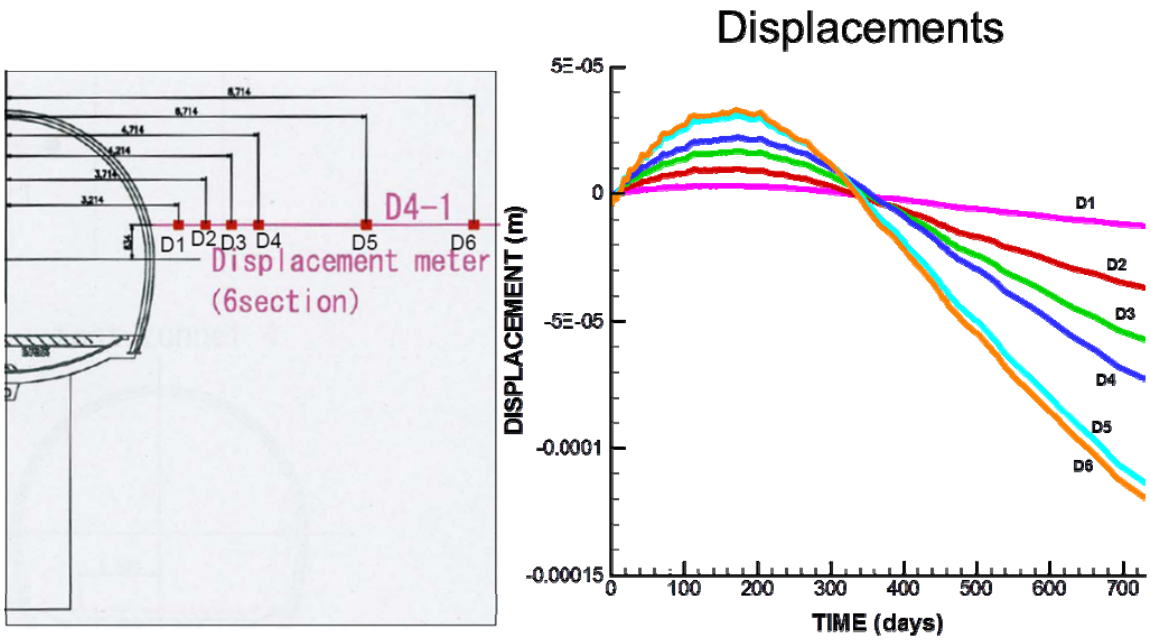

Figure 4-19. TOUGH-FLAC simulation results of extensometer displacements in the rock.

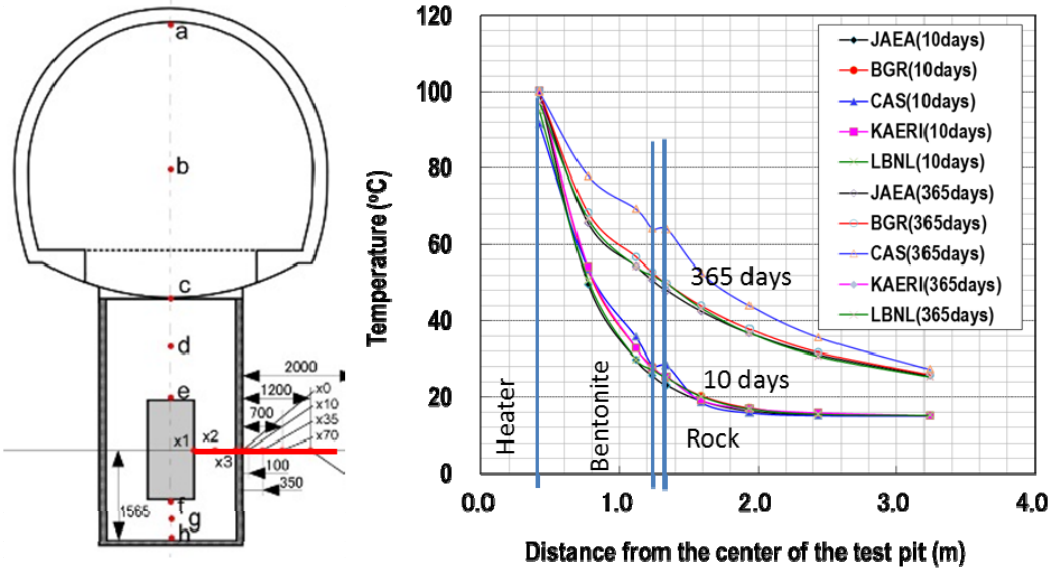

Figure 4-20. Comparison of simulated temperature profiles at 10 and 365 days among the DECOVALEX modeling teams.

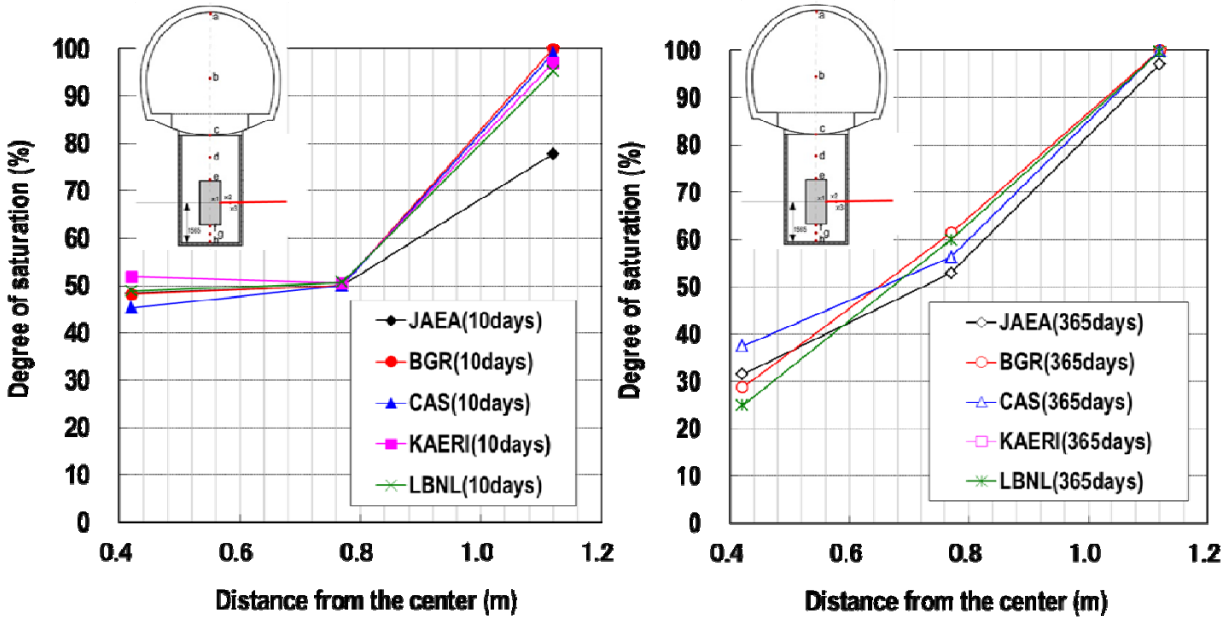

Figure 4-21. Comparison of simulated saturation profiles at 10 and 365 days among the DECOVALEX modeling teams.

4.4 FE Experiment at the Mont Terri Site (Mont Terri Project)

In this section, we present the current status of the FE Experiment and modeling. The current status of the Mont Terri FE experiment is that all the heaters, bentonite buffer and instrumentation have been installed, the tunnel has been plugged, and the final heater was turned on February 15, 2015 (Figure 4-22). The modeling activities during this year have been focused on the prediction of the temperature evolution as part of the experimental field test design. In the final design, a staged heating approach was employed in which the three heaters were turned on in stages, to monitor and validate the models for predicting the temperature in the buffer. Moreover, we are actively working on defining the material properties for the granular bentonite and bentonite blocks that were emplaced in the experimental tunnel.

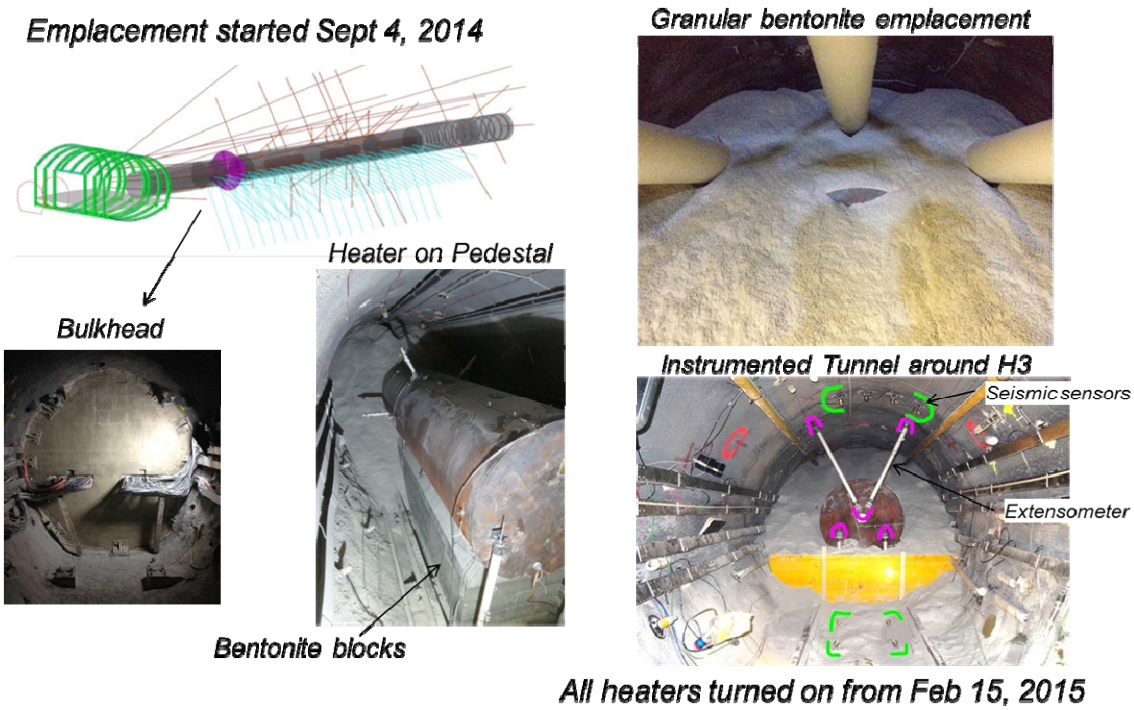

Figure 4-22. Images from the construction and installation of heaters, bentonite buffer and plugs from NAGRA daily reports by Herwig Müller, NAGRA.

As mentioned, the Mont Terri FE Experiment will be one of the largest and longest-duration heater tests worldwide, with focus on both the EBS components and the host-rock behavior. The FE experiment is conducted in a side tunnel at Mont Terri, excavated along the claystone bedding planes for this purpose, extending 50 m in length and about 2.8 m in diameter (Figure 4-23). Heating from emplaced waste will be simulated by three heat-producing canisters of 1500 W maximum power. The temperature is expected to exceed 100°C, with a target temperature 125 to 135°C at the inner parts of the buffer. A sophisticated monitoring program is planned, including dense pre-instrumentation of the site for *in situ* characterization, dense instrumentation of the bentonite buffer and host rock, and extensive geophysical monitoring (seismic and electric tomography).

The experiment will provide data useful for the validation of THM coupling effects regarding the processes in the host rock, while correctly accounting for (and examining) the conditions in the emplacement tunnel (temperature, saturation, and swelling pressure). Due to the 1:1 scale of the experiment, it will be possible to achieve realistic temperature, saturation, and stress gradients. It will also be possible to test backfilling technology with granular bentonite, as well as lining technology with shotcrete, anchors, and steel ribs. Processes examined in the test cover many aspects of repository evolution, such as creation and desaturation of the EDZ during tunnel excavation and operation (including ventilation for about one year), as well as reconsolidation of

the EDZ, resaturation, thermal stresses, and thermal pore-pressure increase after backfilling and heating (heating and monitoring period > 10 years).

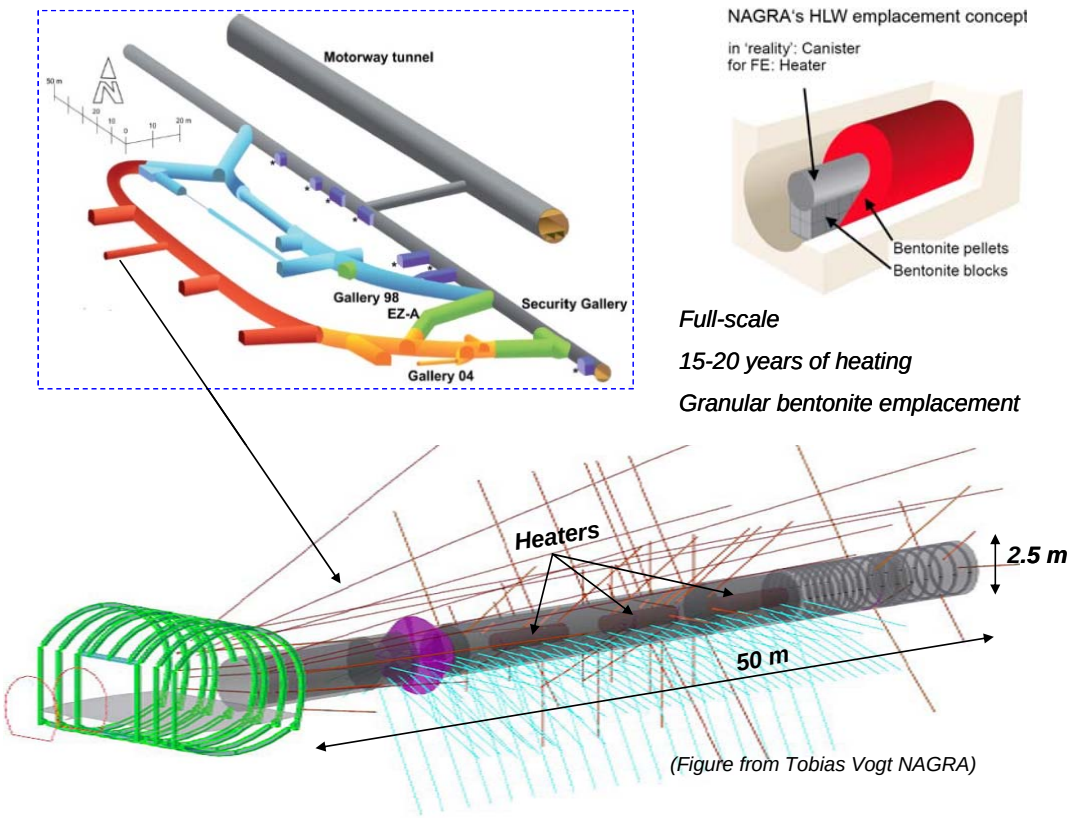

Figure 4-23. Plan view of experiment setup and borehole layout.

In 2011, a niche in front of the FE tunnel was constructed, followed by a first phase of instrumentation of the rock mass surrounding the tunnel, using boreholes from the niche. The FE tunnel was then excavated by road-header in 2012; this was followed by another phase of instrumentation. The tunnel was open for a 1-year ventilation period. This was followed by the emplacement of the heaters, bentonite buffer, and a concrete plug, after which the heating was gradually turned on during the fall of 2014. The heating is then expected to go on for at least 15 years, with continuous monitoring of THM processes in both the bentonite buffer and surrounding rock.

4.4.1 FE-E experiment modeling tasks

DOE is one of the experimental partners for the FE heater experiment, and LBNL is one of the modeling teams. In addition to LBNL, six other modeling teams are currently involved in the Mont Terri FE experiment from Germany (2 teams), U.K., Spain, Switzerland, and Canada.

The THM modeling program includes three types of computations:

1) Scoping calculations

2) Bench Marking

3) Predictive computations

The scoping calculations include brainstorming on potential ongoing processes, evaluating their significance and parameter range, comparing simulation results and input parameters derived by each team, and lessons learned (parameter range, importance, expected response). The benchmarking uses well-defined geometry problems with exact parameter values given to the teams, focusing on process modeling with precise comparison of codes. In the predictive calculations, likely parameters values and the as-built information of the experiment will be frozen.

Each modeling team develops its conceptual models and material properties using available literature (papers and reports) on lab experiments and previous Mont Terri *in situ* tests, etc. Moreover, this is complemented with a restricted benchmark test for code comparison, in which properties and model geometry are set by NAGRA. In the FY13 UFD milestone report titled "Report on International Collaboration Involving the FE Heater and HG-A Tests at Mont Terri (Houseworth et al., 2013), we presented results on the scoping calculations and the benchmarking which was completed in April 2014. We also made a first full THM 3-D simulation of the FE heater test, including the BBM model for calculating the mechanical responses. These were scoping and preliminary predictions with the material properties available at the time, though in some cases including a different kind of bentonite.

In the following, we present the current LBNL model of the Mont Terri FE experiment, including numerical grid and thermal and hydraulic material properties. Finally, we present some simulation results related to the thermal evolution for different heat power schemes. This includes a staged heating during the first few months of the experiment, perhaps using only one of the three heaters. The staged heating schedule will be conducted to enable an early model calibration of the *in situ* thermal properties that can then be used to make a more reliable prediction of the peak temperature, once the full thermal power is applied. This will be done to ensure that the temperature will not be so high as to damage the monitoring system.

4.4.2 TOUGH-FLAC model prediction of the Mont Terri FE Experiment

For the modeling of the FE experiment, we have developed a conceptual model and modeling approach that was presented previous milestone report (Houseworth et al., 2013; Zheng et al., 2014). The host rock is modeled using TOUGH-FLAC with anisotropic properties considering bedding planes of the Opalinus Clay. The bedding planes across the FE tunnel are inclined, as can be seen in Figure 4-24. To accurately model anisotropic thermal and hydrological behavior, we created an inclined TOUGH2 mesh. Anisotropic mechanical material behavior is simulated using the FLAC3D ubiquitous joint model, with initial properties of those derived from the excavation design analysis of the experimental tunnels. In the ubiquitous joint model weak planes are assumed along the bedding planes of the Opalinus Clay in which the shear strength properties are different along bedding versus across bedding. The mechanical model used for the Opalinus Clay was presented in Houseworth et al. (2013), but is not used in this study of peak temperature. For the bentonite, we started with the BBM model as applied by the CINEMAT and UPC (Garitte and Gens, 2012), and derived specific input material parameters for the MX-80

bentonite pellets that will be used as the emplaced bentonite buffer around the heaters. With this modeling approach, we are able to simulate THM processes in both, the bentonite and host rock, as well as their interactions.

Figure 4-24. View of FE tunnel face from the FE niche showing beddings dipping 45° (Vietor, 2012).

Figure 4-25 presents the 3-D TOUGH-FLAC numerical grid of the FE experiment. This model grid includes all vital material components for the modeling of the FE experiment, including layered Opalinus Clay host rock; excavation disturbed zone, tunnel, three heaters, bentonite buffer, concrete liner, and concrete plug. The initial conditions for the model simulation are 2 MPa pore-fluid pressure and 15°C temperature for the host rock. The 2 MPa pore pressure is not under hydrostatic conditions, and the process is affected by the existing tunnel system at the site. In our simulations, we first run a simulation with an open tunnel at atmospheric pressure for 1 year, creating a pressure drop and hydraulic gradient around the tunnel. Thereafter, we assume instantaneous emplacement of the heater and buffer, and start our heating simulation.

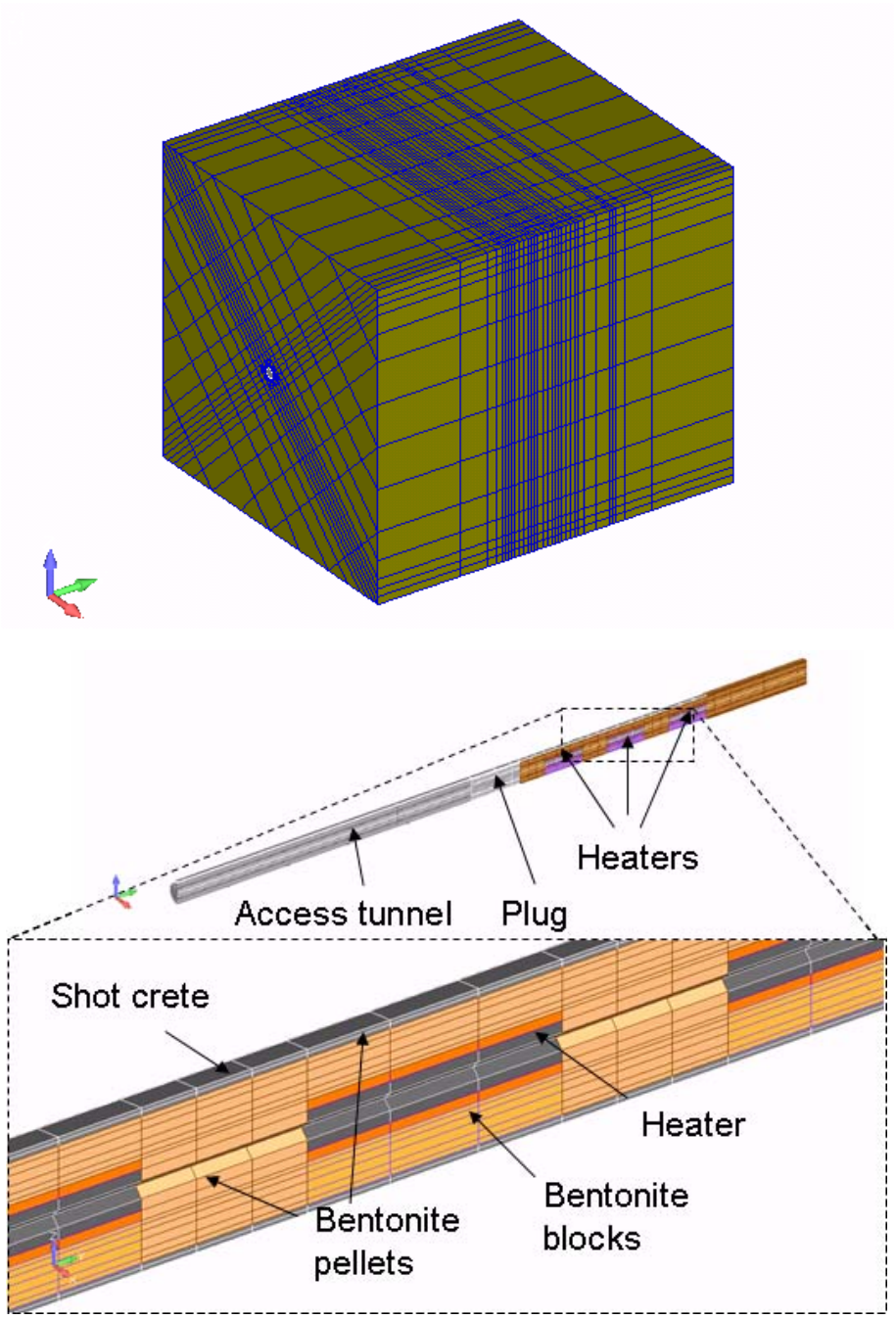

Figure 4-25. TOUGH-FLAC 3-D numerical grid of the FE experiment.

The thermal and hydraulic material properties for modeling the FE experiment are given in Table 4-5. These include properties defined by NAGRA and used for the 1-D benchmarking exercise and reported in FY2013 milestone report "Report on International Collaboration Involving the FE Heater and HG-A Tests at Mont Terri" (Houseworth et al., 2013), and is considered the current best estimate of the properties. The intrinsic permeability of gas flow in the bentonite is orders of magnitude higher than the intrinsic permeability for liquid flow and this is simulated in TOUGH2 using a high value of the Klinkenberg parameter (see Section 4.1 and Equation (4-1)).

In this simulation of temperature and moisture evolution we did not invoke the mechanical part, tough a preliminary simulation using the BBM model was presented in Houseworth et al. (2013).

Table 4-5. Parameters for the Opalinus and Bentonite clay used in the modeling of the FE experiment.

Parameters	Symbol	Opalinus Clay	Bentonite	Concrete (shotcrete and plug)	Unit
Grain density	ρ_g	2.7×10^3	2.7×10^3	2.7×10^3	kg/m^3
Porosity	$\emptyset$	0.15	0.46	0.15	-
Intrinsic permeability	k	5.0×10^{-20}	2.0×10^{-21}	3.5×10^{-21}	m^2
Liquid relative permeability using power law $k_{rw}(S_w)=\left(\frac{S_w-S_r}{S_m-S_r}\right)^A$	A	-	5	-	-
Liquid relative permeability using van-Genuchten model $k_{rw}(S_w)=\left(\frac{S_w-S_r}{S_m-S_r}\right)^{1/2}\left[1-\left\{1-\left(\frac{S_w-S_r}{S_m-S_r}\right)^{1/m}\right\}^m\right]^2$	m	0.52	-	0.52	-
Capillary curve using van-Genuchten model $\psi(S_w)=P0\left\{\left(\frac{S_w-S_r}{S_m-S_r}\right)^{-1/m}-1\right\}^{1-m}$	P_0	1.09×10^7	1.00×10^7	1.09×10^7	Pa
	m	0.29	0.4	0.29	-
	S_{ls}	1.0	1.0	1.0	-
	S_{lr}	0.01	0.0	0.01	-
Thermal conductivity (wet)	λ_{sat}	1.7	1.0	1.7	W/m-K
Thermal conductivity (dry)	λ_{dry}	1.06	0.3	1.06	W/m-K
Grain specific heat	C	800	950	800	J/kg-K

The simulation of the heating is conducted with the initial saturation in the bentonite equal to 20%. Although the bentonite pellets when emplaced will be very dry, with a saturation of a few percent, experience and monitoring in the Mont Terri HE-E experiment shows that moisture is quickly taken up by the pellets from the surrounding humid air. This means that an initial saturation of 20% is realistic. In our modeling, we assign an initial capillary pressure, corresponding to theinitial saturation of 20% (Figure 4-26).

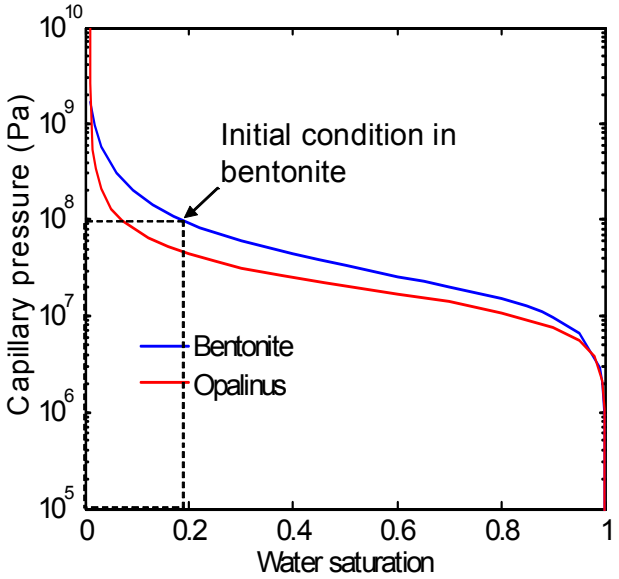

Figure 4-26. Capillary curves for Bentonite and Opalinus clays.

Figure 4-27 shows our prediction of temperature and saturation evolution considering a staged heating only in the heater that is emplaced first, i.e., the one placed farthest into the tunnel. Figure 4-27 includes the temperature and saturation evolution at all three heaters, although heating is turned on only at one heater. We can conclude that during the first 100 days, the temperature and saturation evolution is identical at heaters that are turned on (solid lines). That is, the temperature and saturation evolution at one heater is not affected by the heating, temperature, saturation at the other two heaters. Figure 4-27 also shows the difference in temperature and saturation evolution between heaters that are turned on or off. At heaters that are turned off, there is no drying near the heater (red dashed line) and there is some slow infiltration from the rock, causing a slow increase in saturation (blue dashed line). The results indicate that for the heating design it is possible to first turn on only one heater with the staged heating test to calibrate the THM models. It might be possible to turn on the heater emplaced first and make this initial heating test before the entire test tunnel is completely backfilled. In the experiment, the temperature should not exceed 150°C, because this could be damaging for some of the monitoring sensors.

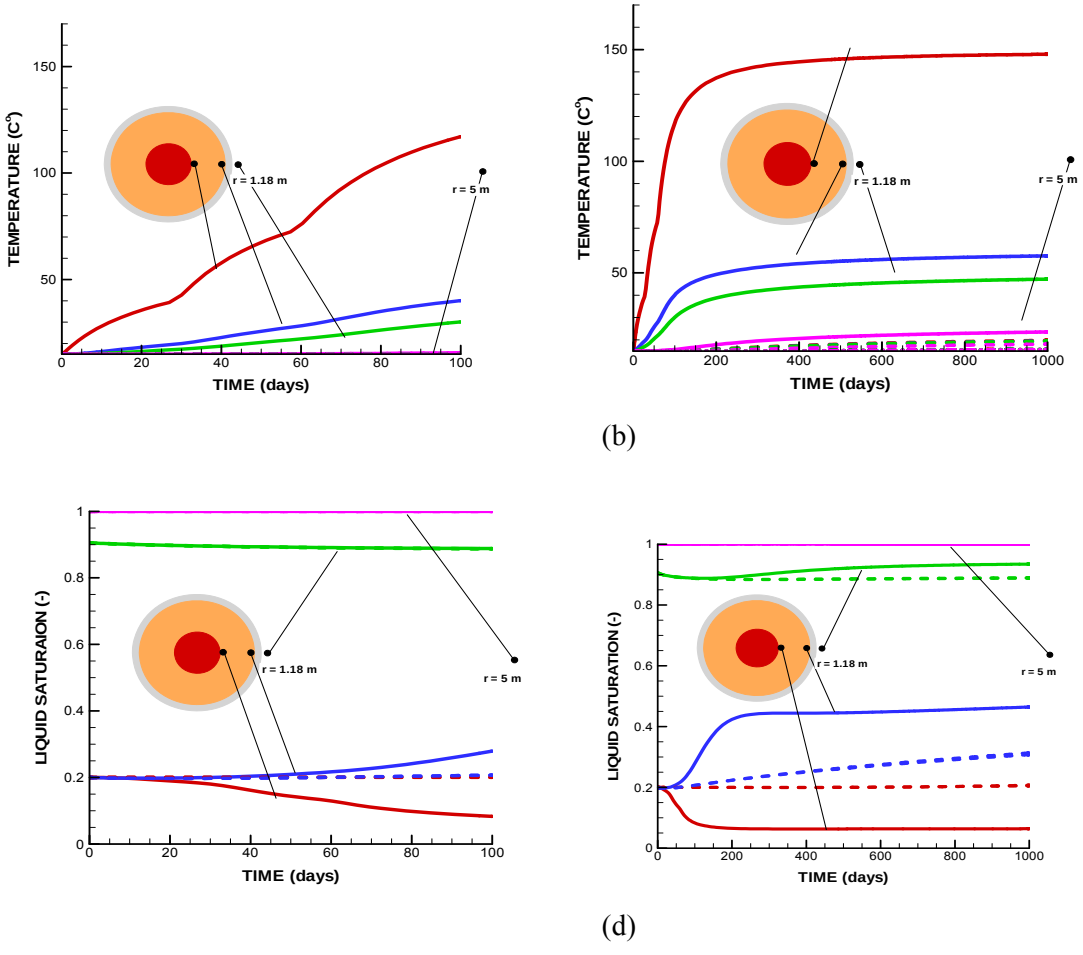

Figure 4-27. Model prediction of (a, b) temperature and (c, d) liquid saturation for staged power in first emplaced heater. The results in (a) and (b) and (c) and (d) are the same but using different

range on the time axis to highlight the early time behavior (a) and (c) of the first 100 days and longer term response (b) and (d) up to 1000 days. Solid lines refer to evolution at the heater that is turned on, whereas dashed lines refers to evolution at heater that are turned off.

4.5 Status of THM Modeling of Heater Experiments and Plans

UFD and LBNL greatly benefit from participating in these international activities for developing expertise and testing advanced models for coupled THM processes. LBNL is leveraging previous experience and existing models (e.g. TOUGH-FLAC) that are extended to meet technical requirements for being able to predict the long-term THM and THMC evolution of a multibarrier nuclear waste repository system, involving backfilled emplacement tunnels in argillite host formations. While the work in previous years has been focused on model development and testing, in FY2015 work has been focused on modeling of the large scale in situ heater experiments involving both bentonite and rock, the Mont Terri HE-E, Horonobe EBS, and Mont Terri FE experiments. Modeling these require large 3-D models, involving all relevant components, such as simulated waste package, bentonite buffer, and host rock, as well as their interactions. Modeling the real system at full scale is the ultimate test of the numerical models developed in this project.

The main accomplishment in FY2015 is that we have been able to successfully conduct model predictions of the THM responses at all these three experiments using state-of-the-art constitutive models for bentonite and host rocks. Some comparison to measured data has been conducted in the case of the Mont Terri HE-E experiment. The heating has just started in 2015 for the Horonobe EBS experiment and the Mont Terri FE experiment, and comparison between measured and predicted responses can be started once the data is provided to the modeling teams.

For the remainder of FY2015 we plan to complete interpretive modeling of the Mont Terri HE-E experiment and Horonobe EBS experiment as part of the DECOVALEX-2015 project, which is due to end at the end of year 2015. The last DECOVALEX-2015 workshop will be help in October 2015. Related to the Mont Terri FE experiment, LBNL will participate in a joint journal paper with the Swiss nuclear waste organization NAGRA and other organization in a Mont Terri 20-years anniversary, scientific paper for the Swiss Journal of Geosciences. This will include work done by FE experiment modeling teams, including code benchmarking and design modeling predictions.

Our work for FY2016 will be first to complete and document work related to DECOVALEX-2015 and at the same time initiate work related to DECOVALEX-2019. It is very likely that the Mont Terri FE experiment will be part of DECOVALEX-2019; it will be an upscaling from the half-scale HE-E experiment to the full scale FE experiment. We also propose that our work on coupled THM modeling be focused on 1) improving and gaining experiences in applying the dual-structure model for granular bentonite and 2) implementing and applying damage models for the evolution of the excavation damaged zone in host rocks.

We have previously shown the importance of considering the dual-structure behavior of bentonite clay associated with the permeability and long-term resaturation behavior. This is at the forefront of research on bentonite behavior and currently only a few codes, including TOUGH-FLAC are capable of modeling such behavior using a constitutive model similar to the Barcelona Expansive Model (BExM). However, there is still a lack of experimental data and experience to use such a complex model with confidence. Moreover, the highly non-linear

behavior and the way it is implemented into TOUGH-FLAC make it, at the moment, computationally demanding. One of the main Tasks for FY2016 will be the improvement of the BExM in TOUGH-FLAC and to gain experience in applying it efficiently, including gaining confidence in the determination of input parameters. The inclusion of the FE heater experiment into DECOVALEX-2019 will be helpful for international collaboration on this, including collaboration with the University of Catalonia, which is the only other group in the world that has implemented BExM into a numerical simulator.

The implementation and application of a damage model for the evolution of the excavation disturbed zone will be an important addition to the current model for calculating the evolution of permeability along with damage as well as sealing and healing. Different approach can be tested, including to build upon previous work on the Two-Part Hooke's Model (TPHM), as well as other continuum damage models considering fracture evolution implicitly. Such a model can be benchmarked against discrete fracture modeling of damage-zone fractures using TOUGH-RBSN. The goal is to build a pragmatic continuum model that can be validated against field experiments such as sealing experiments conducted in underground research laboratories.

Finally, we note that by participating in these international activities we are making significant progress toward achieving UFD goals to fill data needs and confirm advanced modeling approaches (by 2015), and to have a robust modeling and experimental basis for evaluation of multiple disposal system options (by 2020).

References

Alonso EE, Gens A, Josa A (1990) A constitutive model for partially saturated soils. Geotechnique. 40: 405-430.

Chijimatsu M, Nguyen TS, Jing L, de Jonge J, Kohlmeier M, Millard A, Rejeb A, Rutqvist J, Souley M, Sugita Y (2005) Numerical study of the THM effects on the near-field safety of a hypothetical nuclear waste repository – BMT1 of the DECOVALEX III project. Part 1: Conceptualization and characterization of the problems and summary of results. Int. J Rock Mech & Min Sci 42:720–730.

Garitte B. and Gens A. (2012) TH and THM Scoping computations for the definition of an optimal instrumentation layout in the Full-scale Emplacement (FE) experiment NAGRA NIB 10-34, March 2012.

Gaus I, Wieczorek K, Schuster K, Garitte B, Senger R, Vasconcelos R and Mayor JC(2014) EBS behaviour immediately after repository closure in a clay host rock: HE-E experiment (Mont Terri URL). Geological Society, London, Special Publications, first published March 7, 2014; doi 10.1144/SP400.11

Gens, A, Alonso, E. A framework for the behaviour of unsaturated expansive clays. Can. Geotech. J. 29, 1013–1032 (1992).

Gens A, Sánchez, M Sheng, D (2006) On constitutive modelling of unsaturated soils. Acta Geotechnica. 1, 137-147

Gens, A., Sánchez, M., Guimaraes, L.D.N., Alonso, E.E., Lloret, A., Olivella, S., Villar, M.V., Huertas, F. (2009) A full-scale in situ heating test for high-level nuclear waste disposal: observations, analysis and interpretation. Geotechnique 59, 377–399.

Feng Xia-Ting, Pan Peng-zhi, Zhou Hui (2006) Simulation of rock microfracturing process under uniaxial compression using elasto-plastic cellular automata. Int J Rock Mech & Min Sci 43: 1091–1108.

Houseworth J., Rutqvist J., Asahina D., Chen F., Vilarrasa V., Liu H.H., Birkholzer J. Report on International Collaboration Involving the FE Heater and HG-A Tests at Mont Terri. Prepared for U.S. Department of Energy, Used Fuel Disposition Campaign, FCRD-UFD-2014-000002, Lawrence Berkeley National Laboratory (2013).

Itasca, FLAC3D V5.0, Fast Lagrangian Analysis of Continua in 3 Dimensions, User's Guide. Itasca Consulting Group, Minneapolis, Minnesota (2011).

Kristensson O, Åkesson M (2008) Mechanical modeling of MX-80 – Quick tools for BBM parameter analysis. Phys Chem Earth, Parts A/B/C. 33, Supplement 1: S508-S515.

Liu H.H., Houseworth J., Rutqvist J., Zheng L., Asahina D., Li L., Vilarrasa V., Chen F., Nakagawa S., Finsterle S., Doughty C., Kneafsey T., Birkholzer J. Report on THMC Modeling of the Near Field Evolution of a Generic Clay Repository: Model Validation and Demonstration. Prepared for U.S. Department of Energy, Used Fuel Disposition Campaign, FCRD-UFD-2013-000244, Lawrence Berkeley National Laboratory (2013).

Pan Peng-zhi, Feng Xia-Ting, Huang Xiao-Hua, Cui Qiang, Zhou Hui (2008) Study of coupled THMC processes in crystalline rock in the EDZ using an ECPA code. Environmental Geology.

Pruess, K., Oldenburg, C.M., Moridis, G. (2011) TOUGH2 User's Guide, Version 2.1, LBNL-43134(revised), Lawrence Berkeley National Laboratory, Berkeley, California.

Rutqvist, J., Börgesson, L., Chijimatsu, M., Kobayashi, A., Nguyen, T.S., Jing, L., Noorishad, J., Tsang, C.-F. (2001a) Thermohydromechanics of partially saturated geological media –

Governing equations and formulation of four finite element models. Int. J. Rock Mech. & Min. Sci. 38, 105-127.

Rutqvist J., Börgesson L., Chijimatsu M., Nguyen T. S., Jing L., Noorishad J., Tsang C.-F. (2001b) Coupled Thermo-hydro-mechanical Analysis of a Heater Test in Fractured Rock and Bentonite at Kamaishi Mine – Comparison of Field Results to Predictions of Four Finite Element Codes. Int. J. Rock Mech. & Min. Sci. 38, 129-142.

Rutqvist, J., Wu, Y.-S., Tsang, C.-F. and Bodvarsson, G. (2002). A modeling approach for analysis of coupled multiphase fluid flow, heat transfer and deformation in fractured porous rock. International Journal of Rock Mechanics & Mining Sciences, 39, 429-442.

Rutqvist J., Chijimatsu M., Jing L., De Jonge J., Kohlmeier M., Millard A., Nguyen T.S., Rejeb A., Souley M., Sugita Y. and Tsang C.F. Numerical study of the THM effects on the near-field safety of a hypothetical nuclear waste repository – BMT1 of the DECOVALEX III project. Part 3: Effects of THM coupling in fractured rock Int. J. Rock Mech. & Min. Sci, 42, 745-755 (2005).

Rutqvist J., Barr D., Birkholzer J.T., Fujisaki K., Kolditz O., Liu Q.-S., Fujita T., Wang W. and Zhang C.-Y. A comparative simulation study of coupled THM processes and their effect on fractured rock permeability around nuclear waste repositories. Environ Geol, 57, 1347–1360 (2009)

Rutqvist J. Status of the TOUGH-FLAC simulator and recent applications related to coupled fluid flow and crustal deformations. Computers & Geosciences, 37, 739–750 (2011).

Rutqvist, J., Ijiri, Y. and Yamamoto, H. (2011). Implementation of the Barcelona Basic Model into TOUGH-FLAC for simulations of the geomechanical behavior of unsaturated soils. Computers & Geosciences, 37, 751-762.

Rutqvist J., Davis J., Zheng L., Vilarrasa V., Houseworth J., Birkholzer J. Investigation of Coupled THMC Processes and Reactive Transport: FY14 Progress. Prepared for U.S. Department of Energy, Used Fuel Disposition, FCRD-UFD-2014-000497, Lawrence Berkeley National Laboratory, LBNL-6720E (2014a).

Rutqvist J., Zheng L., Chen F, Liu H.-H, and Birkholzer J. Modeling of Coupled Thermo-Hydro-Mechanical Processes with Links to Geochemistry Associated with Bentonite-Backfilled Repository Tunnels in Clay Formations. Rock Mechanics and Rock Engineering, 47, 167–186 (2014b).

Sánchez, M., Gens, A., Guimarães, L. do N., Olivella, S. A double structure generalized plasticity model for expansive materials. Int. J. Numer. Anal. Meth. Geomech., 29, 751–787 (2005).

Vietor T. (2012).Mont Terri Project - FE Experiment Modelling Kick-off Meeting. February 9, 2012, Mont Terri, Switzerland. NAGRA Technical Discussion TD-217Wang W, Xie M, Nowak T, Kunz H, Shao H, Kolditz O (2006) Modeling THM coupled problem of Task D of the DECOVALEX project. Proc. GEOPROC2006 International symposium: 2nd International Conference on Coupled Thermo-hydro-mechanical-chemical processes in Geosystems and Engineering, HoHai University, Nanjing, China, May 22-25, 2006, 226–232, HoHai University.

Zheng L., Rutqvist J., Steefel C., Kim K., Chen F., Vilarrasa V., Nakagawa S., Houseworth J., and Birkholzer J. Investigation of Coupled Processes and Impact of High Temperature Limits in Argillite Rock Prepared for U.S. Department of Energy, Used Fuel Disposition, FCRD-UFD-2014-000493, Lawrence Berkeley National Laboratory, LBNL-6719E (2014).

5. DISCRETE FRACTURE NETWORK (DFN) APPROACH FOR THM DAMAGE MODELING IN ARGILLACEOUS ROCK

Mechanical and hydrological interactions in porous geologic media are fundamental and universal mechanisms that deform the geologic structure and control the behavior of water and other fluids in its pores (Neuzil, 2003). Geotectonic phenomena produce deformations and strains that tend to alter fluid pressure. Resulting pressure perturbations can be dramatic, and many cases of so-called "anomalous" pressure generation appear to have occurred in this manner. Conversely, the effects of fluid pressure on mechanical behavior are also profound. Pore fluids control deformation of porous media by bearing loads, and consequently geologic structures deform and fail largely in response to effective stress (i.e. skeleton stress or grain-to-grain stress).

In argillaceous rocks, fractures are typical mechanical features of particular importance to determine hydrological properties. While the clay-rich formations usually exhibit low permeability, under certain conditions there may be fractures which increase the permeability. Fracturing has been often observed as a result of fluid overpressure. Due to the low permeability of argillaceous rocks, fluids can only be transmitted very slowly. Consequently, the rock systems are not in pressure equilibrium (Gonçalvès et al., 2004), and the overpressure conditions can trigger hydraulic fracturing if the effective stress resulting from fluid pressure exceeds the rock tensile strength (Cosgrove, 2001). This fluid-driven fracturing process is relevant to many geoengineering applications. For example, hydraulic fracturing and stimulation of fracture networks are utilized by the energy industry (e.g., shale gas extraction, enhanced geothermal systems, etc.) to increase permeability of geological formations. From the opposite perspective, related to underground CO_2 sequestration, fracturing of the repository rock could be detrimental for geo-environmental issues due to increasing the risk of contaminant leakage (Bossart et al., 2004; Chiaramonte et al., 2008). Fluid-driven fracturing needs to be considered as a tightly coupled hydro-mechanical process if it is to be accurately modeled. Especially in the presence of multiple fractures (e.g., propagating fractures and pre-existing natural fractures), modeling the fracturing process can be very challenging because of the complex interactions between propagating fractures and natural fractures (e.g., Fu et al., 2013).

This report covers an overview of the TOUGH-RBSN code for coupled THM processes in Sections 5.1 and 5.2. The simulation code combines TOUGH2 with the rigid-body-spring network (RBSN) model, which enables a discrete representation of individual fractures and fracture networks in rock formations. The discrete fracture network (DFN) approach is facilitated in the Voronoi discretization via a fully automated modeling procedure. In Section 5.3, the numerical program is verified through a single fluid-driven fracture simulation, and hydraulic fracturing simulations within complex fracture networks are conducted to demonstrate the modeling capabilities for coupled hydro-mechanical processes. Subsequently, some numerical problems with the current modeling scheme are presented to recognize the necessity for a new dynamic modeling approach. Section 5.4 documents the development phase of the new dynamic simulation code based on the lattice modeling approach (i.e., RBSN) based upon kinematics of particles.

5.1 RBSN for Mechanical Damage Modeling of Geomaterials

5.1.1 Voronoi discretization

Voronoi discretization is an effective approach to partition a computational domain into a set of spatial regions or cells. Each Voronoi cell is associated with an individual nodal point, which can be either prescribed or randomly generated. Discretization process is basically carried out in three steps: nodal point generation, Delaunay tessellation, and Voronoi tessellation (Figure 5-1).

In the first step, a set of nodal points are positioned regularly or irregularly inside the domain (Figure 5-1a). For random point generation, the points are sequentially generated with a minimum allowable distance l_{min} between neighboring points, which defines the desired nodal density to fill in the domain so that the grid size can be controlled. Furthermore, gradient grid geometry is attainable using a user-specified spatial correlation function for l_{min}. The random point generation involves choosing an arbitrary trial point within the domain by a pseudo-random number generator. If the trial point does not violate the l_{min} constraint, it is secured to be a member of the final nodal point set; otherwise, it is discarded and a new trial point is randomly selected. This process continues until either a specified total number of nodal points has been obtained or the domain is saturated with points. Practically, it is assumed that the domain becomes saturated when no more trial points are secured after a certain large number of trials. Nodal points also can be predefined at a specific position from input if necessary for assignment of boundary conditions.

The second step provides the Delaunay tessellation in which a collection of tetrahedra connect the nodal points (Figure 5-1b). The Delaunay tessellation is constructed using the concept of a super-tetrahedron (Sloan, 1987; Taniguchi et al., 2002). The circumsphere of each tetrahedron is the smallest sphere that circumscribes the corresponding four nodal points. The Delaunay tessellation is defined by the disjoint tetrahedra that do not include any other nodal point inside their circumspheres. In general, a randomly distributed point set corresponds to a unique Delaunay tessellation, in which no two coincidental circumspheres exist. The resulting Delaunay tessellation represents the unstructured grid of lattice elements. Each tetrahedral edge connects two adjacent nodes, by which the nodal connectivity of the lattice element is defined.

Following the Delaunay tessellation, the dual Voronoi tessellation is constructed with convex polyhedra called Voronoi cells (Figure 5-1c). The Voronoi diagram is also uniquely determined by the given set of nodal points, where each nodal point corresponds to exactly one Voronoi cell. The Voronoi cell for a nodal point is a territory in which the locations are closer to the corresponding point than any other points. Locations on a cell boundary are equally close to the neighboring nodal point for which the Voronoi cell shares that boundary (i.e., common Voronoi cell boundary). Consequently, the domain is collectively filled with the disjoint Voronoi cells through the recursive discretization process for all the nodal points. Also, the Voronoi diagram has a unique geometric correspondence with the Delaunay tessellation (Okabe et al. 2000). These geometric characteristics are used for the RBSN element formulation, which will be discussed in the next subsection.

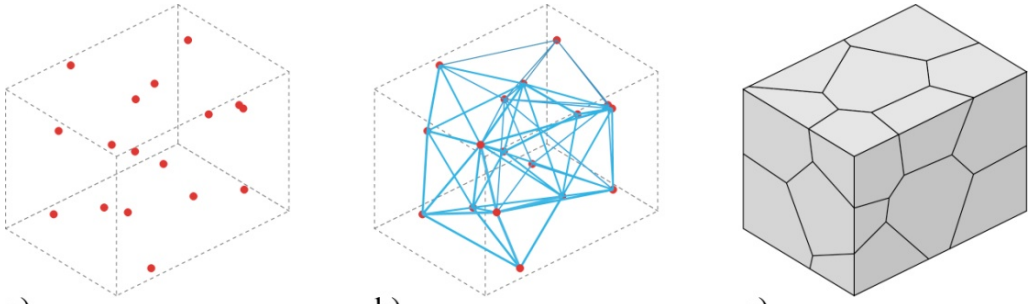

Figure 5-1. Discretization process: a) nodal point generation; b) Delaunay tessellation; and c) Voronoi tessellation.

5.1.2 Model formulation

The geometry of a RBSN is defined by the dual Delaunay tessellation of the nodal points. A basic unit of the lattice element that connects arbitrary nodes *i* and *j* consists of: 1) a zero-size spring set that is located at position *C* (the centroid of the common Voronoi cell boundary); and 2) rigid arm constraints that link the spring sets and the nodal degrees of freedom (Figure 5-2b). Each node has six degrees of freedom for the case of 3-D modeling. The spring set is formed from three axial springs and three rotational springs as shown in Figure 5-2c (the rotational springs have been intentionally omitted for clear illustration).

Note that the Voronoi cell is basically considered to be rigid in the sense that it maintains its original shape during the process of loading and material deformation (assumption of small strain). The flexibility of the motion is lumped into the spring sets; therefore, the separation and interpenetration of the cells are permitted.

The spring coefficients are scaled in proportion to the distance between the element length h_{ij}, and the area of the Voronoi cell boundary A_{ij}:

$$k_s = k_t = \alpha_1 k_n = \alpha_1 \alpha_2 E \frac{A_{ij}}{h_{ij}}, k_{\phi n} = E \frac{J_p}{h_{ij}}, k_{\phi s} = E \frac{I_{ss}}{h_{ij}}, k_{\phi t} = E \frac{I_{tt}}{h_{ij}} \quad (5\text{-}1)$$

in which E is the elastic modulus, J_p, I_{ss}, and I_{tt} are the polar and two principal moments of inertia of the Voronoi cell boundary with respect to the centroid, respectively. By adjusting α_1 and α_2 in accordance with experimental results, macroscopic modeling of both elastic constants (E and Poisson ratio, ν) is possible. For the special case of $\alpha_1 = \alpha_2 = 1$, the Voronoi scaling of the spring coefficients enables the model to be elastically homogeneous under uniform modes of straining, albeit with zero effective Poisson ratio (Bolander and Saito, 1998; Asahina et al., 2011).

The relationship between the generalized spring displacement, **d** (6×1 column vector), and the generalized nodal displacements in local coordinates, $\mathbf{u}_e$ (12×1 column vector), can be expressed by

$$\mathbf{d} = \mathbf{B}\mathbf{u}_e \quad (5\text{-}2)$$

where **B** is a 6×12 geometric transformation matrix:

$$\mathbf{B} = \begin{bmatrix} -\mathbf{I} & \mathbf{B}_{12} & \mathbf{I} & \mathbf{B}_{14} \\ \mathbf{0} & -\mathbf{I} & \mathbf{0} & \mathbf{I} \end{bmatrix} \tag{5-3}$$

Submatrices $\mathbf{B}_{12}$ and $\mathbf{B}_{14}$ are defined by

$$\mathbf{B}_{12} = \begin{bmatrix} 0 & -z_C & y_C \\ z_C & 0 & -h/2 \\ -y_C & h/2 & 0 \end{bmatrix} \text{ and } \mathbf{B}_{14} = \begin{bmatrix} 0 & z_C & -y_C \\ -z_C & 0 & -h/2 \\ y_C & -h/2 & 0 \end{bmatrix} \tag{5-4}$$

where y_C and z_C are the distances between the centroid C and the intersection of the y- and z-axes and the Voronoi cell boundary, respectively (Figure 5-2b). The element stiffness matrix, $\mathbf{K}_e$, can be obtained by

$$\mathbf{K}_e = \mathbf{B}^T\mathbf{D}\mathbf{B} \tag{5-5}$$

The local spring stiffness matrix **D** is filled with the spring coefficients from Equation (5-1):

$$\mathbf{D} = \text{diag}[k_s, k_t, k_n, k_{\phi n}, k_{\phi s}, k_{\phi t}] \tag{5-6}$$

The system matrix **K** is assembled for all the lattice elements and nodal displacements **u** are computed by solving the system equations:

$$\mathbf{K}\mathbf{u} = \boldsymbol{\phi} \tag{5-7}$$

where $\boldsymbol{\phi}$ is the global vector of nodal forces. At the stage of constructing the system stiffness matrix, which is usually sparse, a skyline matrix storage form is used to economize the use of computer memory. Then, the system equations are solved by the Crout elimination scheme.

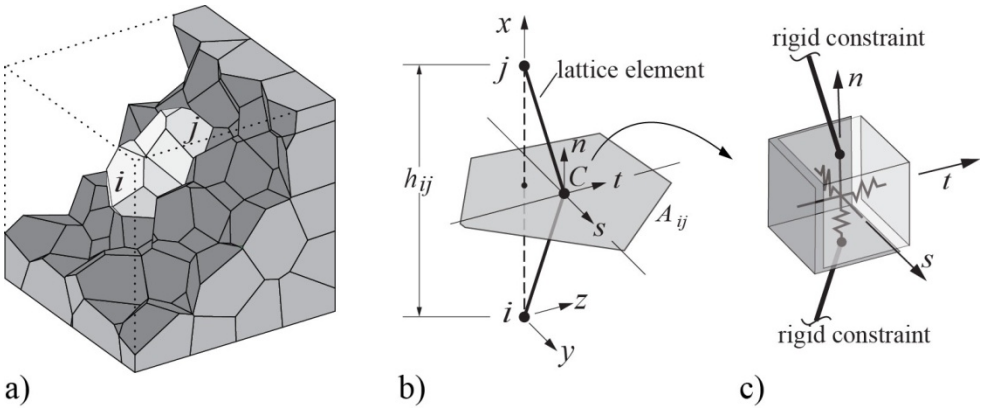

Figure 5-2. Typical RBSN element *ij*: a) within a Voronoi grid; b) isolated from the network; and c) a zero-size spring set located at centroid *C* of Voronoi cell boundary area A_{ij}.

5.1.3 Evaluation of criticality of element stress state

The RBSN model provides a discrete representation of fracture by damaging/breaking the local springs. For the damaged spring set, the local stiffness matrix is

$$\mathbf{D}' = (1 - \omega)\mathbf{D} \tag{5-8}$$

where ω is a scalar damage index with a range from 0 (undamaged) to 1 (completely damaged). In the modeling of brittle fracturing, which is applied to the cases presented in this report, ω is either 0 or 1. Fracture may initiate within a lattice element when the stress state exceeds the given material strength. To determine the criticality of the stress state, a stress ratio is calculated for each lattice element:

$$R_f = \sigma_e / \hat{\sigma} \tag{5-9}$$

where σ_e is the element stress state and $\hat{\sigma}$ is the critical stress defined by fracture criteria. During iterative calculations, only one element, with the most critical stress state (i.e., the largest $R_f \geq 1$), is allowed to break per iteration, and the fracture event entails a reduction of spring stiffnesses and a release of the associated elemental forces. To date, three types of fracture modeling in the RBSN have been used to evaluate the criticality of stress state with different fracture criteria, which will be presented and reviewed herein.

Resultant stress measures

The RBSN models have been applied to simulate fracture process predominantly subjected to tensile loading (Berton and Bolander, 2006). In general, the global loading direction is mostly skewed to the local element axes; therefore, all the normal and tangential components of spring forces are activated in the direction of the element axes. Nodal displacements produce forces F_n, F_s, and F_t in the respective axial springs, and the resultant vector of the spring forces with a measure of $F_R = (F_n^2 + F_s^2 + F_t^2)^{0.5}$ is used to obtain a stress state:

$$\sigma_R = F_R / A_{ij}^P \tag{5-10}$$

where A_{ij}^P is the projected area of A_{ij} on a plane perpendicular to the direction of the resultant force. σ_R serves as σ_e in Equation (5-9), whereas $\hat{\sigma}$ varies according to a tensile softening relation. The tension/compression condition is determined by the direction of the normal spring force.

This uniaxial, vectorial stress approach is energy-conserving and mesh-insensitive for predominantly tensile stress fields. For example, Thomure et al. (2001) demonstrated the model objectivity with respect to size and geometry of the lattice network. A random mesh provides uniform, controllable energy consumption which gives practically the same result as a straight line discretization of the crack trajectory. However, complications arise when such uniaxial notions of stress are applied to modeling cases of multiaxial stress.

Maximum principal stress from tensorial stress state

Asahina et al. (2011) have used the stress tensor to determine the failure of RBSN elements. The calculation of stress tensor at a Voronoi cell node is possible by considering the equilibrium conditions of the spring forces. Sets of the spring forces are applied at the boundaries surrounding a Voronoi cell (Figure 5-3a), and nodal force components F_{nn}, F_{ns}, and F_{nt} can be calculated for an arbitrary section passing through the Voronoi cell node with its corresponding local *n-s-t* coordinates, which satisfy the equilibrium condition with all the forces acting on the remaining cell boundaries (Figure 5-3b). Moment contributions to equilibrium are not considered here. By dividing these force components by the cut-face area, the corresponding stress components σ_n, σ_s, and σ_t can be obtained. By repeating this process for three mutually

perpendicular sections, the full stress tensor is obtained (Figure 5-3c). Details are given elsewhere (Yip et al., 2005).

From the stress tensors at two neighboring nodes, the stress tensor of the inter-element is calculated according to

$$\bar{\boldsymbol{\sigma}} = (\boldsymbol{\sigma}_i + \boldsymbol{\sigma}_j)/2 \tag{5-11}$$

where $\boldsymbol{\sigma}_i$ and $\boldsymbol{\sigma}_j$ are the stress tensors at the neighboring nodes i and j, respectively. The maximum principal tensile stress of $\bar{\boldsymbol{\sigma}}$ serves as σ_e in Equation (5-9). In this way, fracture under multiaxial stress conditions can be simulated. However, this approach does not readily account for the possibility of softening behavior since the ambiguity still exists for calculation of the nodal stress tensor from the damaged spring forces.

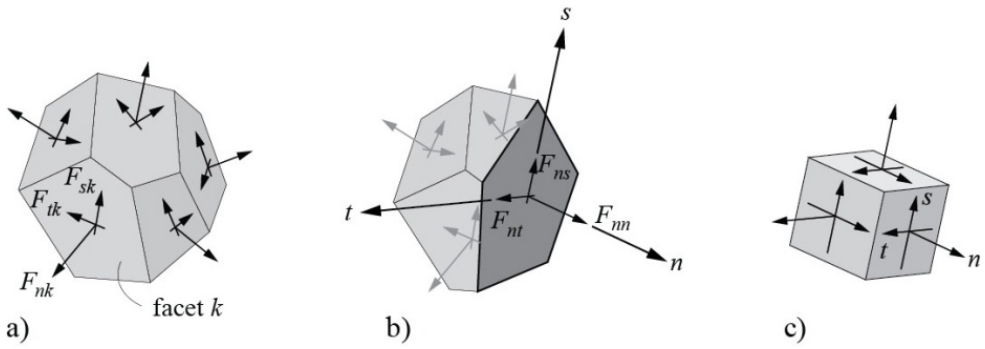

Figure 5-3. Stress tensor at a Voronoi cell node: a) components of spring force local coordinates; b) a set of nodal forces satisfying the equilibrium; and c) complete stress tensor at Voronoi cell node (Adapted from Yip et al., 2005).

Stress components with Mohr-Coulomb surface

Strength properties of each element are determined as critical stress components on a Mohr-Coulomb surface. Figure 5-4 shows the fracture surface with a tension cut-off, where the envelop is defined by three parameters: the angle of internal friction ψ (surface inclination with respect to σ_n-axis); cohesive strength c (surface intersection with the shear axes); and the tensile strength f_n. Measures of stress $P(\sigma_n, \sigma_s, \sigma_t)$ are derived by averaging the axial spring forces F_n, F_s, and F_t over the cell boundary area A_{ij}. The criticality of the stress state is assessed as $R_f = \overline{OP}/\overline{OP_O}$, where P_O is the point at which $\overline{OP}$ intersects the fracture surface. At the present stage of model development, there is no option to gradually damage the springs (e.g., with softening behavior) for fracturing. However, other studies have indicated the possibility of modeling damage process by shrinking the Mohr-Coulomb surface (Shen and Shen, 2002; Kim and Lim, 2011). This fracture modeling approach will be utilized for the simulations in Section 5.3.

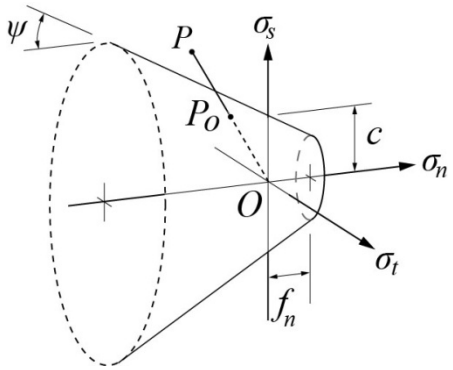

Figure 5-4. Mohr-Coulomb fracture surface with tension cut-off.

5.2 Hydro-Mechanical Modeling Using TOUGH-RBSN

5.2.1 Linkage between TOUGH2 and RBSN

TOUGH2 is a general-purpose simulator for flow and mass transfer in porous and fractured media (Pruess et al., 2011), which has an applicability to diverse modeling problems by adopting various equation-of-state (EOS) modules. Simulations presented in this paper use the EOS1 module for single-phase flow problems with isothermal conditions. The modeling approach is based on the integral finite difference method (IFDM), thus possesses the advantage of being compatible with regular or irregular gridding in any number of spatial dimensions. It also allows for flexibility of fracture representation, in which fractures and fracture networks form in response to the hydro-mechanical forces and conditions (Zhang et al., 2004; Rutqvist et al., 2013).

For modeling of coupled hydro-mechanical processes, the TOUGH2 simulator is linked with the RBSN approach. The general coupling procedure of TOUGH-RBSN is basically similar to that of the TOUGH-FLAC software (Rutqvist et al., 2002), but the coupling modules are substantially modified for the DFN approach. Figure 5-5 shows a schematic flow diagram of the coupling procedure between TOUGH2 and RBSN, which are linked through external modules that handle two-way coupling of the relevant quantities at each time step.

First, the TOUGH2 to RBSN link, shown on the left side of Figure 5-5, supplies pressure and degree of saturation to update the mechanical quantities. From the pore pressure P, the effective (grain-to-grain) stress $\sigma_n{}'$, applied to the lattice element, is calculated using Biot's theory (Biot and Willis, 1957):

$$\sigma_n{}' = \sigma_n + \alpha_p P \tag{5-12}$$

where σ_n is the total normal stress obtained from overall loading, including external loads; α_p is Biot's effective stress parameter. Note that tensile stress is taken to be positive. By averaging the nodal pressure, Equation (5-12) can be modified to calculate the effective stress applied to a lattice element *ij* in incremental form:

$$\Delta\sigma' = \Delta\sigma + \alpha_p(\Delta P_i + \Delta P_j)/2 \tag{5-13}$$

where ΔP_i and ΔP_j are the pressures increments measured at nodes *i* and *j*.

It is assumed that the saturation change induces the strain increment in the element *ij* as follows:

$$\Delta\varepsilon_s = \alpha_s(\Delta S_i + \Delta S_j)/2 \tag{5-14}$$

where ε_s is shrinkage/swelling strain; and α_s is the hydraulic shrinkage coefficient. If an expansible matrix material is subjected to constant stress conditions in an elastic region, the effective stress can be affected by the swelling/ shrinking strain as

$$\Delta\sigma' = \Delta\varepsilon_s E \tag{5-15}$$

Thereafter, the RBSN to TOUGH2 link, shown on the right side of Figure 5-5, supplies the effective stress and the strain calculated at the lattice element to update the hydrological properties of the corresponding Voronoi cells *i* and *j* in the TOUGH2 model. Porosity, permeability, and capillary pressure are generally related with the effective stress and strain values (Rutqvist and Tsang, 2002).

If fracturing occurs at the element *ij* (i.e., $\omega \neq 0$), the associated fracture node and additional connections are activated in the TOUGH2 model. The permeability of an individual fracture can be defined by the fracture aperture *b* (Bear, 1972; Bear et al., 1993), however, herein the fracture is simply assumed to have a constant permeability very high relative to that of the rock matrix.

The TOUGH-RBSN simulator has several advantages that stem from the availability of sharing the same grid geometry based on the Voronoi discretization. This simplifies coupling of nodal quantities and data exchange between the two numerical models. Also, discrete fractures for hydrological behavior can be more easily introduced in the grid and directly related to mechanical damage. The modeling scheme for the DFN approach in the unstructured grid geometry is described in the next subsection.

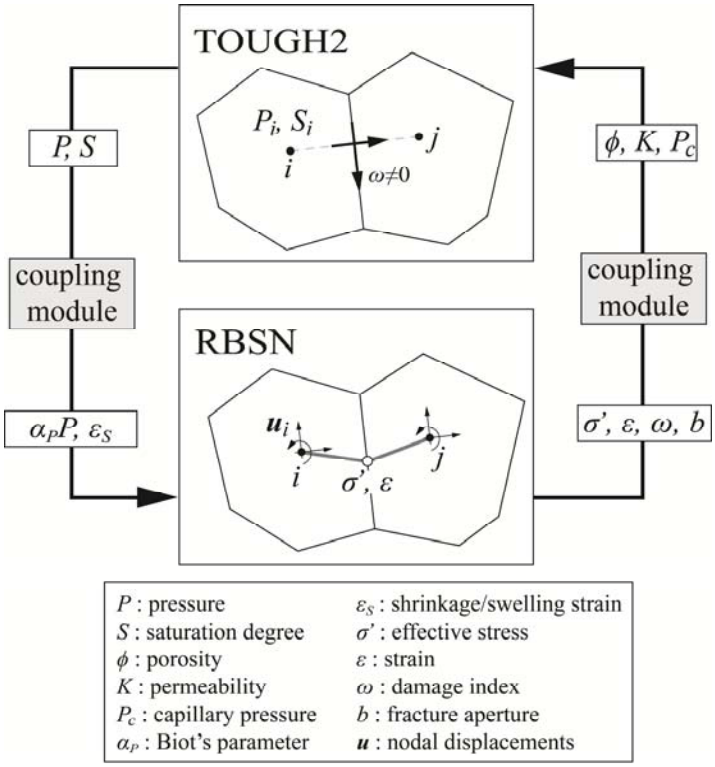

Figure 5-5. Flow diagram of the coupling procedure between TOUGH2 and RBSN (adapted from Asahina et al., 2014).

5.2.2 Representation of discrete fractures in rock formations

Fractures within geological systems may facilitate storage and flow of fluids and contribute to discontinuous mechanical responses. Such fractures and discontinuities are explicitly modeled as discrete features within the Voronoi grid.

The Voronoi grid represents the matrix component of geomaterial structures, and pre-existing or newly generated fractures are placed on the Voronoi cell boundaries. Descriptors of fractures (e.g., orientation, length, curvature) can be obtained by field mapping, computer-generated statistical representations, or the simulation outcomes of mechanical models. An example of the discretization procedure in 2-D modeling involving a straight fracture path is as follows:

i. Generate a Voronoi unstructured grid for the spatial domain.
ii. Overlay the reference fracture path onto the grid.
iii. Test all connections of natural neighboring nodes to check if they cross the fracture path. For example, compare connections *ij* and *jk* in Figure 5-6.
iv. The collection of the Voronoi cell boundaries corresponding to the nodal connections that cross the reference fracture (such as *ij*) forms discretized fractures.

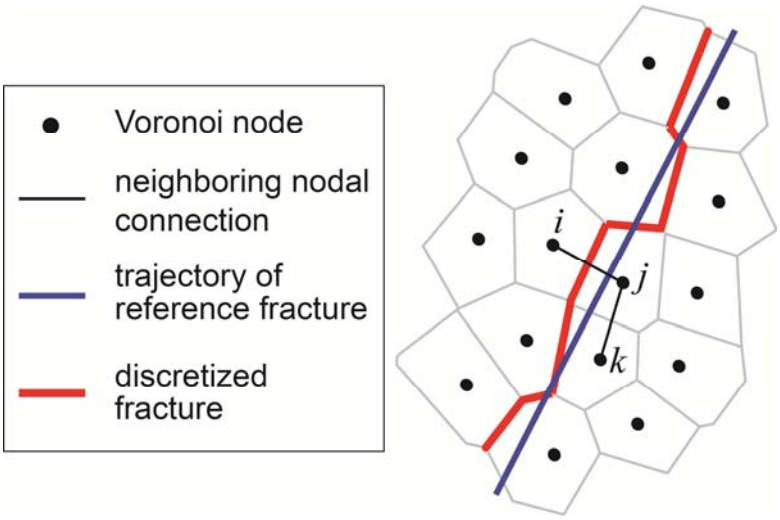

Figure 5-6. Fracture mapping and discretization within an unstructured Voronoi grid.

By repeating the above process for multiple fractures, a network of discrete fractures can be generated. This fracture discretization process is completely automated and can be easily extended to more complicated geometries in 3-D modeling. The grid size should be carefully chosen to obtain a sufficiently accurate representation of the reference fracture. With a finer grid, the discretized fractures correspond more closely to the reference path, but the computational effort may be increased.

In TOUGH2 simulations using a basic Voronoi grid, flow and mass transfer are enacted only through the connections of the neighboring matrix nodes (called matrix-matrix connections in Figure 5-7a). However, if fracturing occurs within the matrix, substantial flow may arise through the fracture apertures. For the DFN approach, dynamic formation of such flow channels is implemented by introducing fracture nodes and the associated connections within the Voronoi grid. As shown in Figure 5-7b, a fracture node is inserted on the Voronoi cell boundary where the matrix-matrix connection crosses. The original matrix-matrix connection is divided into two matrix-fracture (and vice versa) connections by the newly inserted fracture node. In addition, the connections between the fracture nodes are established to activate flow channels in discrete fractures. Hydrological properties of the discrete fractures are related to the grid geometry and the local fracture aperture. Fracture geometries can be either assigned as a pre-existing fracture property or computed by the mechanical-damage analysis of the RBSN model.

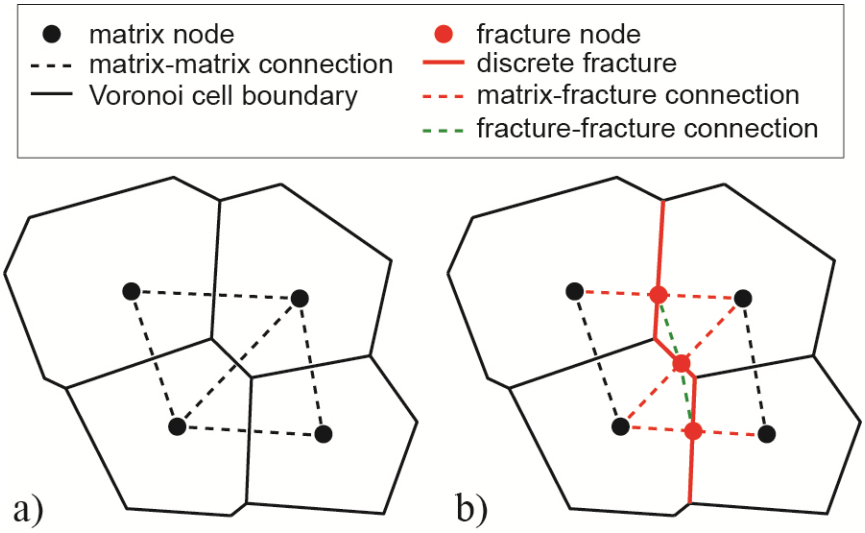

Figure 5-7. Adjustment of nodal connections for flow modeling with discrete fractures: a) original matrix nodes and connections; and b) insertion of fracture nodes and connections.

5.3 Fluid-Driven Fracture Simulations

5.3.1 Model verification

Fracture initiation and propagation incurred by the pressurized fluid are simulated to verify the TOUGH-RBSN simulator. A 2-D rectangular domain with dimensions of 100×120 m is prepared, in which an unstructured Voronoi grid is generated with graded nodal density for computational efficiency (Figure 5-8a). A reference line is prescribed in the middle of the domain such that a single, straight fracturing path results. Symmetric boundary conditions are applied through a slipping (roller) configuration on the left side boundary. The point of fluid injection is located on this boundary at the end of the reference line.

The fracture geometry from the simulation result is compared to the analytical solutions for fracture opening versus length relationship. Classic 2-D fracture models, such as the Khristianovic-Geertsma-de Klerk (KGD) model (Khristianovic and Zheltov, 1955; and Geertsma and de Klerk, 1969) and the Perkins-Kern-Nordgren Model (PKN) model (Perkins and Kern, 1961; and Nordgren, 1972), have considered that the cross section of the fracture would be an elliptical shape based on the linear elastic fracture mechanics theory and the assumption of uniform fluid pressure along the fracture length.

The aperture width of the resulting fracture is measured by the generalized displacement of the fractured lattice element, and the fracture profiles are plotted at times 10, 15, and 20 sec. in duration of fluid injection (Figure 5-8b). As the hydraulically driven fracture gets wider and longer with time, the fracture profiles retain elliptic shapes, which are analytically drawn with the fracture length and the wellbore aperture chosen as the principal radii of ellipses.

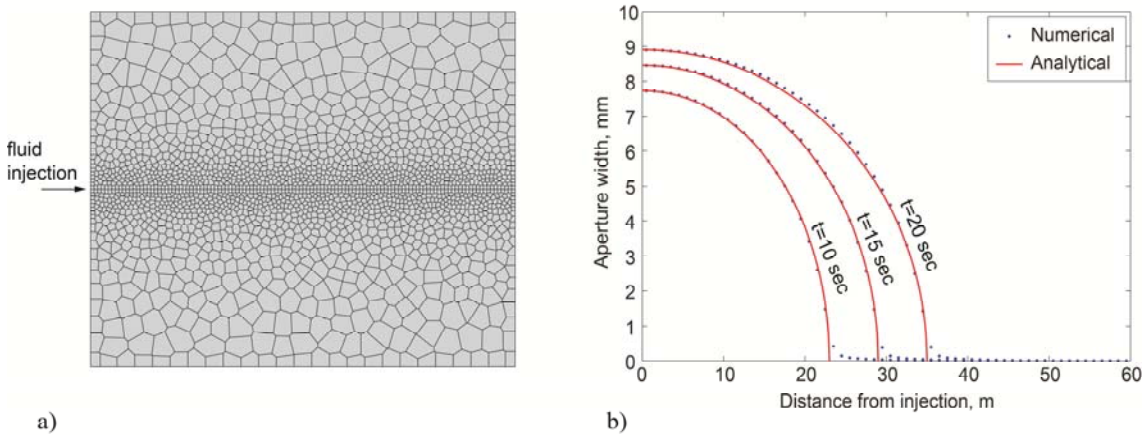

Figure 5-8. Hydraulic fracturing simulation of a single fracture: a) 2-D model set up; and b) comparison between the numerical model and the analytical approximation in terms of fracture aperture profiles.

5.3.2 Hydraulic fracturing within discrete fracture networks

The purpose of this study is to demonstrate the current TOUGH-RBSN modeling capabilities extended to hydraulic fracturing simulations through the prediction of actual laboratory experimental behavior. In the experiments, pre-existing fracture networks are designed and fabricated within soda-lime glass blocks by generating thermally induced micro-cracks with the 3-D laser-engraving technique. The fracture network pattern is made up of clouds of these micro-cracks and its geometric topology is obtained for numerical modeling (Figure 5-9a). In the numerical model, the discrete fractures are replicated using the scheme presented in Section 5.2.2. In Figures 5-9b and c, two cases of fracture modeling with different mesh density show a similarity of the fracture pattern.

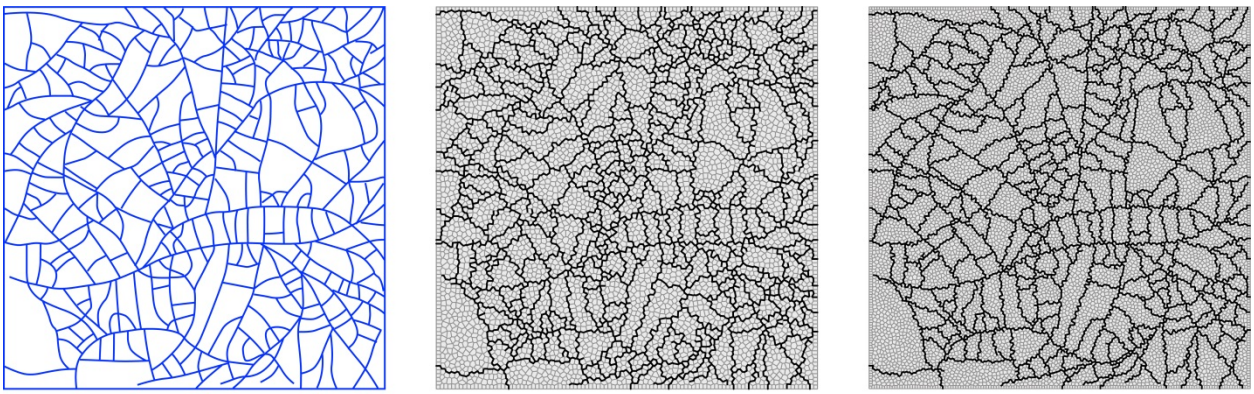

Figure 5-9. Modeling of discrete fracture networks: a) geometric topology of fracture networks; and mapping of the fracture pattern onto unstructured Voronoi grids with different mesh density: approximately b) 5000 and c) 10000 Voronoi cells, respectively.

For simplicity, the matrix (soda-lime glass) is assumed to be impermeable and non-porous. An 88.9 mm square domain is discretized for modeling. Mechanical properties of the matrix are as follows: Young's modulus E =73.8 GPa, tensile strength f_t =30 MPa. Parameters for the Mohr-Coulomb fracture criterion are cohesive strength c =22.5 MPa and internal friction angle ψ =45°. In the experiment, overall strength of the pre-existing fractures can be varied by modifying the micro-crack density. Since the strength of these fractures have not been determined at this point, for the numerical modeling, it is assumed that pre-fractured elements have Young's modulus and tensile strength reduced from those of the intact glass by 50%.

Hydrological properties of the pre-existing fractures are set as those of the intact glass unless the fractures are activated by subsequent hydro-mechanical responses. Once a new fracture occurs or a pre-existing fracture is activated, the mechanical resistance is removed and the permeability and the porosity are increased (e.g., a permeability of 1 darcy and a porosity of 0.8) for the fractured element while compressibility remains at zero. The borehole is assigned a permeability of 1 darcy, porosity of 1, and zero compressibility.

Because the glass is prone to brittle fracturing, the injection needs to be performed very carefully to capture the fracture propagation. As a suggestion, this simulation is conducted with injecting water into a borehole at the center of the domain. The injection rate is chosen to be 2×10^{-7} kg/s per unit millimeter. Anisotropic confining stresses of 7.24 MPa and 4.83 MPa (in the vertical and horizontal directions, respectively) are applied at the boundary edges.

Figure 5-10a presents the deformed shape at a final stage of hydraulic fracturing (t =1.25 sec), in which the nodal displacements are exaggerated (50 times) for better visibility. The fluid pressure triggers fracturing process and induces fracture opening throughout the activated fractures. Figure 5-10b illustrates the fracture propagation (in red) overlaid on the pre-existing fracture network (in blue). Two dominant fractures are shown stretching from the borehole in the direction sub-parallel to the maximum confining stress, and the details of the fracturing paths show a preference for forming along pre-existing fractures.

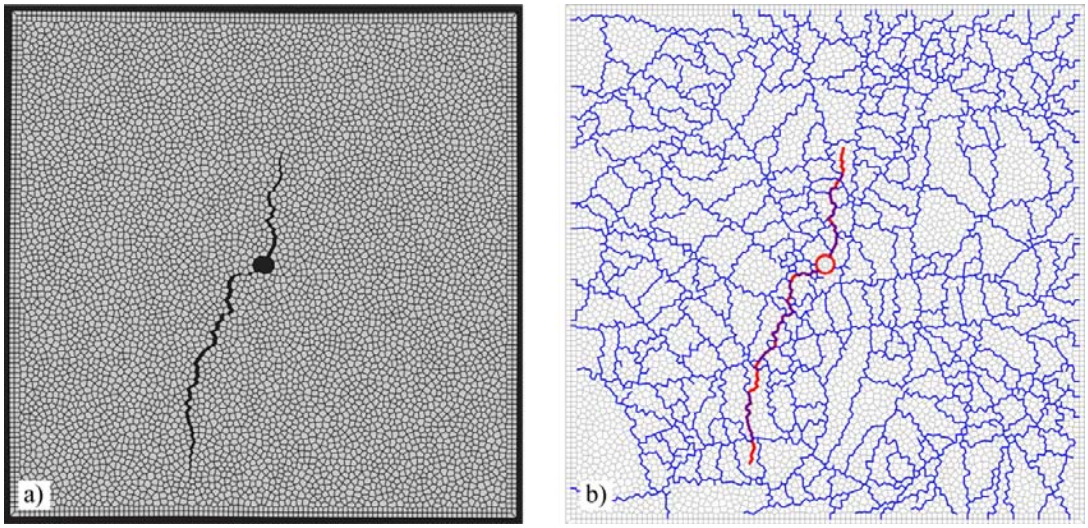

Figure 5-10. Simulation results at a final stage of hydraulic fracturing: a) deformed shape; and b) fracture propagation paths overlaid on the pre-existing fracture network.

Figure 5-11 arranges snapshots of pressure distributions, captured at the point of fracture initiation, at the intermediate stages of fracture propagation, based on the length of the fracture, and at the final stage of the simulation. Up until fracture initiation, the pressure at the borehole increases due to the fluid injection (Figure 5-11a). During hydraulic fracture propagation the fluid is directly transferred from the borehole into newly created volume along the fracture paths, so the fluid pressure at the borehole decreases with the advance of fractures (Figures 5-11b through d). Figure 5-11d shows the pressure distribution at the final stage, in which the region with higher pressure clearly indicates the hydraulic fracture paths illustrated in Figure 5-10b.

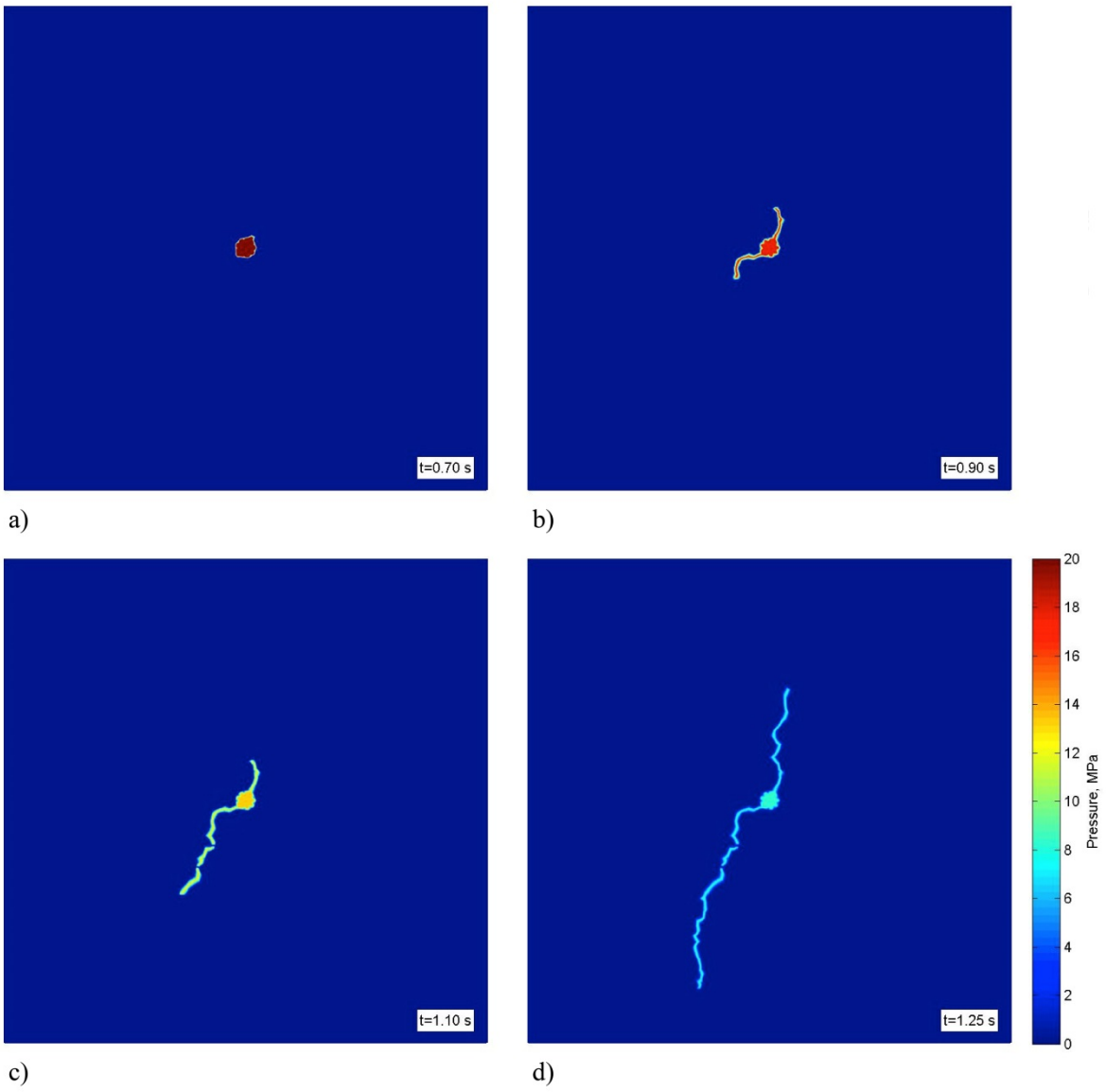

Figure 5-11. Pressure distributions captured at: a) at the point of fracture initiation; b) at the early stage; c) at the latter stage; and d) at the final stage of fracture propagation.

Next, a sensitivity analysis for fracture formation was conducted by varying the storage coefficient as an independent variable. For accurate modeling of the system response, it is crucial to represent the specific storage of the injection device correctly (including the storage resulting from the compliance of the borehole) as well as the storage created by the opening of hydraulic fractures. The storage coefficient is apparently related to the compressibility of the model domain. Two cases of the compressibility parameters for the borehole blocks are considered: zero and 4.6×10^{-9} Pa^{-1}. Note that all the other conditions and parameters, including the injection rate, are identical in the simulations.

Figure 5-12 compares the pressure evolutions at the borehole for the two cases. As depicted by the blue curve, zero compressibility allows gradual fracture propagation from the borehole with intermittent pressure release at the borehole. In contrast, the red curve for the higher compressibility case leads to a longer period for pressure development up to the triggering pressure. The delayed fracture initiation results in greater strain energy stored in the system, thus rapid fracture develops with a subsequent instantaneous pressure drop after fracture initiation. This analysis suggests that a stiff injection system with a low storage coefficient is desirable for producing stable propagation of hydraulic fractures.

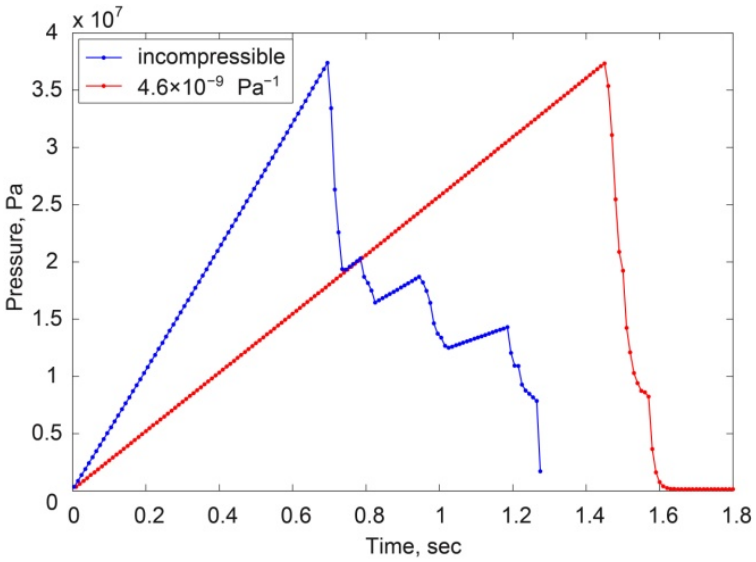

Figure 5-12. Evolutions of injected fluid pressure for different compressibility coefficients of the borehole region.

5.3.3 Observations of problems with the current modeling scheme

This study demonstrates the modeling capacities of the TOUGH-RBSN simulator for coupled hydro-mechanical processes. The mechanical effect of the excessive pressure produced by fluid injection (i.e., hydraulic fracturing) and the preferential flow features through the newly generated fracture path are realistically represented. However, the simulator inherently has shortcomings due to the equilibrium-based calculations generated by the RBSN model. While the main coupling procedure is driven by TOUGH which computes hydrological behavior with

the passage of time, the RBSN model does not have the terms of time in its governing equations (i.e., static simulations).

For nonlinear calculations with fracturing processes, damaging/breaking the elements are iterated to retain the convergence to the equilibrium-state of the system, in which the LHS and RHS of Equation (5-7) are balanced. However, especially when fracture propagation reaches the domain boundary, the system keeps trying to make fracturing at irrelevant elements in absurd places since no more elements at the boundary can be fractured. In that respect, the simulation results sometimes lead to unreal fracture behavior or the system becomes unstable and the numerical solution fails to converge.

This type of behavior has been found in the above simulation example. Figure 5-13 shows fractured elements at two consecutive time steps (t =1.25 sec and 1.26 sec). The fracture paths in Figure 5-10b are redrawn in Figure 5-13a for comparison. As can be seen in Figure 5-13b, after the main fracture paths reach the boundaries, trivial fractures are generated over the boundaries to break up the domain. These numerical artifacts may be reduced by choosing smaller time increment, but that cannot be guaranteed.

To resolve this problem, a new dynamic simulation framework has been being developed based on the RBSN. Equations of motion are solved at each time step for mechanical behavior, so the time variables are retained in the two-way coupling procedure. Details of the methodology are presented in the next section.

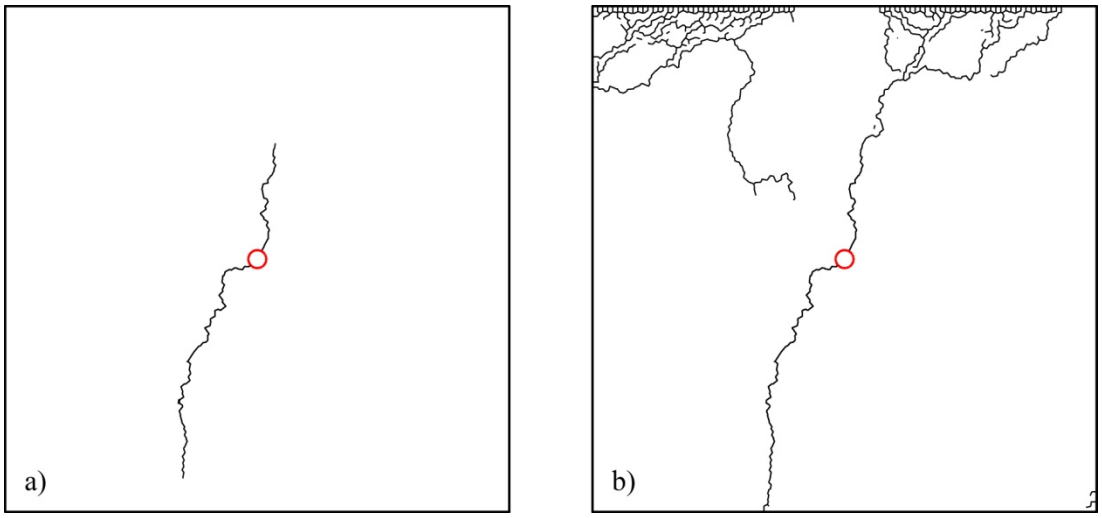

Figure 5-13. Abnormal break-up of the domain due to numerical instability: a) final time step as a meaningful result; and b) abrupt fracture generation at the next time step.

5.4 Development of Dynamic Simulation Code

5.4.1 Equation of motion and time stepping method

In dynamic modeling of mechanical behavior, the motion of the system is governed by a differential equation of the displacements of the Voronoi nodes. The nodal displacements,

velocities, and accelerations are calculated by a time-stepping method for integrating the equation of motion. The governing equation is constructed based on Newton's second law of motion.

Figure 5-14 shows a free-body diagram of a Voronoi cell subjected to external load applied at the node and local internal forces generated at the spring sets. Let us consider the external load vector $\mathbf{p}(p_X, p_Y, p_Z, \tau_X, \tau_Y, \tau_z)$ in the global *X-Y-Z* coordinates and a local internal force vector $\mathbf{f}_k(f_{nk}, f_{sk}, f_{tk}, m_{nk}, m_{sk}, m_{tk})$ for a Voronoi facet *k*. Both the external and internal force sets have six components (three translations and three rotations), in the figure the rotational components (i.e., m_{nk}, m_{sk}, m_{tk}) of the spring forces are omitted for visibility. With coordinate transformations, the local internal force vectors for *n* facets are assembled into a global internal force vector:

$$\mathbf{f} = \sum_{k=1}^{n} \mathbf{\Gamma}_k{}^T \mathbf{f}_k \tag{5-16}$$

where $\mathbf{\Gamma}_k$ is a 6×6 matrix for coordinate transformation from global *X-Y-Z* to local *n-s-t* for individual Voronoi facet *k*.

The governing equation for nodal displacements and rotations varying with time can be constructed as

$$\mathbf{M\ddot{u}} + \mathbf{f} = \mathbf{p}(t) \tag{5-17}$$

where $\mathbf{\ddot{u}}$ is a second derivative of displacement vector (i.e., acceleration) **M** is the inertia matrix containing mass and moment of inertia tensor of the Voronoi cell. For numerical modeling, Equation (5-17) is discretized in the time domain.

$$\mathbf{M\ddot{u}}_n + \mathbf{f}_n = \mathbf{p}_n \tag{5-18}$$

The time scale is divided into a series of time steps by uniform duration Δt and a discrete time instant $t_n = n\Delta t$, denoted as time *n*.

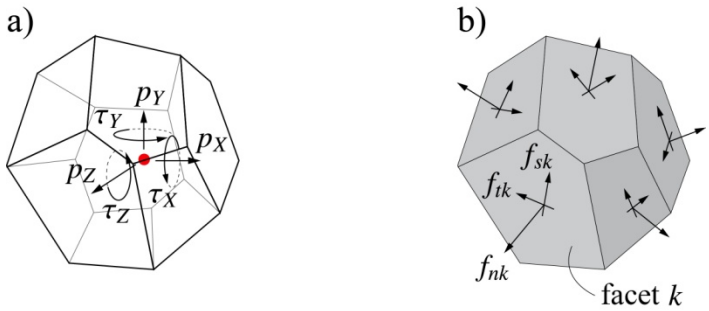

Figure 5-14. Free-body diagram of a Voronoi cell: a) with external nodal forces; and b) with internal spring forces.

Time stepping-methods enable the evaluation of the response that satisfies Equation (5-17) at time n +1:

$$\mathbf{M}\ddot{\mathbf{u}}_{n+1} + \mathbf{f}_{n+1} = \mathbf{p}_{n+1} \tag{5-19}$$

When applied successfully with n = 0, 1, 2, 3, … the numerical time-stepping procedure gives the desired response at all time n +1. In this study, an explicit time integration scheme, the velocity Verlet algorithm, is used to conduct time-stepping procedure.

From the known kinematic information up to time n, the unknown displacement at time n +1 can be calculated as

$$\mathbf{u}_{n+1} = \mathbf{u}_n + \dot{\mathbf{u}}_n \Delta t + \frac{\ddot{\mathbf{u}}_n}{2} \Delta t^2 \tag{5-20}$$

Then, the internal force $\mathbf{f}_{n+1}$ is explicitly evaluated as a function of nodal displacement $\mathbf{u}_{n+1}$. By manipulating Equation (5-19), the acceleration $\ddot{\mathbf{u}}_{n+1}$ is derived from the unbalanced internal and external forces:

$$\ddot{\mathbf{u}}_{n+1} = \mathbf{M}^{-1}[\mathbf{p}_{n+1} - \mathbf{f}_{n+1}] \tag{5-21}$$

Finally, the unknown velocity $\dot{\mathbf{u}}_{n+1}$ is calculated as

$$\dot{\mathbf{u}}_{n+1} = \dot{\mathbf{u}}_n + \frac{\ddot{\mathbf{u}}_{n+1} + \ddot{\mathbf{u}}_n}{2} \Delta t \tag{5-22}$$

This second-order time integration scheme is known to be more accurate than single-step integration schemes such as the Euler method, and therefore commonly used in the molecular dynamics and particle dynamics simulations (Amini et al., 1987; Martys and Mountain, 1999; Kim et al., 2008). Also, unlike the static analysis program of the RBSN approach, the solution procedure using an explicit time integration scheme is simple and does not require building the whole system matrix equation. In that regard, the program code is expected to be easily parallelized for large-scale computations.

5.4.2 Suppression of boundary artifacts

The dynamic RBSN method offers more flexibility with boundary conditions than the current equilibrium model for geomechanical and fracture damage modeling. Boundary effects are important to control because earth models almost always must use artificial boundaries in numerical models for systems that are effectively unbounded. One method to control these effects is to implement damping (or frictional) effects of movement near the boundary. This tends to reduce reflections of disturbances from the boundaries, which is needed if the boundaries are artificial. The following analysis provides an example of how damped boundary masses in a mass-spring system can suppress reflections from boundaries.

Mass-spring system

As shown in Figure 5-15, a one-dimensional mass-spring system with rigid boundaries consists of N masses and $N + 1$ springs. This is the simplest mechanical analogue available to investigate the effects of boundary conditions on mechanical disturbances. Each mass is characterized by m

and each spring has an associated spring constant, k. Each spring has a neutral (no force) length of ℓ. The spring force on mass n connected on each side to a springs n and $n+1$.

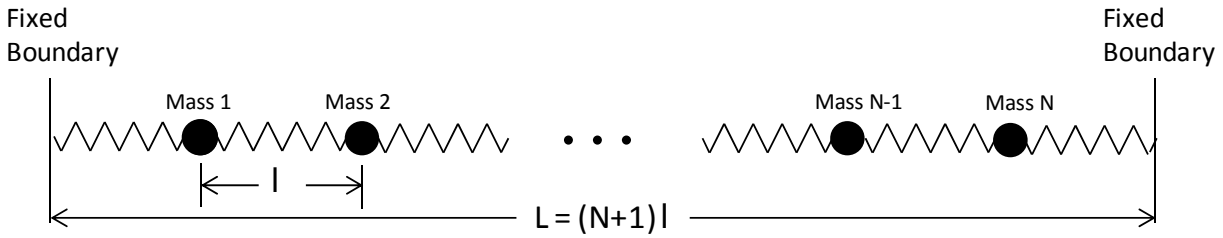

Figure 5-15. Conceptual drawing of mass-spring system.

The time-dependent positions of each mass is given by $x_n(t)$.

$$F_n = -k(x_n - x_{n-1} - \ell) + k(x_{n+1} - x_n - \ell) \tag{5-23}$$

An additional resistive damping (or frictional) force acts on each mass and is proportional to the negative of the velocity of the mass with a coefficient r_n. Therefore,

$$m\frac{d^2x_n(t)}{dt^2} = -r_n\frac{dx_n(t)}{dt} - k(x_n(t) - x_{n-1}(t) - \ell) + k(x_{n+1}(t) - x_n(t) - \ell) \tag{5-24}$$

This may be written as the following pair of first-order differential equations by letting

$$\frac{dx_n(t)}{dt} = y_n(t) \tag{5-25}$$

$$\frac{dy_n(t)}{dt} = -\frac{r_n}{m}y_n(t) - \frac{k}{m}(x_n(t) - x_{n-1}(t) - \ell) + \frac{k}{m}(x_{n+1}(t) - x_n(t) - \ell) \tag{5-26}$$

with $x_0 = 0$ and $x_{N+1} = L$ being the fixed endpoints of the first and last spring. For $n = 2$ to $n = N - 1$ these may be written as

$$\frac{dx_n(t)}{dt} = y_n(t) \tag{5-27}$$

$$\frac{dy_n(t)}{dt} = -\frac{r_n}{m}y_n(t) - \frac{2k}{m}x_n(t) + \frac{k}{m}x_{n-1}(t) + \frac{k}{m}x_{n+1}(t) \tag{5-28}$$

For $n = 1$,

$$\frac{dx_1(t)}{dt} = y_1(t) \tag{5-29}$$

$$\frac{dy_1(t)}{dt} = -\frac{r}{m}y_1(t) - \frac{2k}{m}x_1(t) + \frac{k}{m}x_2(t) \tag{5-30}$$

and for $n = N$,

$$\frac{dx_N(t)}{dt} = y_N(t) \tag{5-31}$$

$$\frac{dy_N(t)}{dt} = -\frac{r}{m}y_N(t) - \frac{2k}{m}x_N(t) + \frac{k}{m}x_{N-1}(t) + \frac{kL}{m} \tag{5-32}$$

In non-dimensional form for $n = 2$ to $N - 1$,

$$\frac{dx_{dn}(\tau)}{d\tau} = y_{dn}(\tau) \tag{5-33}$$

$$\frac{dy_{dn}(\tau)}{d\tau} = -2x_{dn}(\tau) + x_{dn-1}(\tau) + x_{dn+1}(\tau) \tag{5-34}$$

For $n = 1$,

$$\frac{dx_{d1}(\tau)}{d\tau} = y_{d1}(\tau) \tag{5-35}$$

$$\frac{dy_{d1}(\tau)}{d\tau} = -r_d y_{d1}(\tau) - 2x_{d1}(\tau) + x_{d2}(\tau) \tag{5-36}$$

and for $n = N$,

$$\frac{dx_{dN}(\tau)}{d\tau} = y_{dN}(\tau) \tag{5-37}$$

$$\frac{dy_{dN}(\tau)}{d\tau} = -r_d y_{dN}(\tau) - 2x_{dN}(\tau) + x_{dN-1}(\tau) + 1 \tag{5-38}$$

The dimensionless variables are defined as:

$$\tau = \sqrt{\frac{k}{m}}t \tag{5-39}$$

$$r_d = \frac{r}{\sqrt{km}} \tag{5-40}$$

$$x_{dn}(\tau) = \frac{x_n(t)}{L} \tag{5-41}$$

$$y_{dn}(\tau) = \sqrt{\frac{m}{k}}\frac{y_n(\tau)}{L}. \tag{5-42}$$

Computed Example

Equations (5-33) through (5-38) are solved using explicit time integration with a constant dimensionless time step of 0.001. A disturbance is introduced through the initial condition in which mass 1 is displaced 0.04 dimensionless distance units towards mass 2 relative to its neutral position. All other masses are initialized at their neutral positions. After mass 1 returns to a

position close to its neutral position (at a dimensionless time of 1.121), its damping coefficient is changed from 0 to 0.01 (strong damping) such that the initial disturbance is a simple pulse. For the damped case, the dimensionless damping coefficients are incremented by 0.0001 starting from a value of 0.0001 for mass 11 up to a value of 0.001 for mass 20. Using a set of ever-increasing damping coefficients over the 10 masses closest to the far boundary was found to do a better job at reducing reflected disturbances from the far boundary than the use of a single highly damped mass next to the far boundary.

Solving for a system of 20 masses and 21 springs gives the results in Figure 5-16. Figure 5-16a shows the reflected disturbance that propagates away from the far boundary ($x_d = 1$). The reflected disturbance is a boundary artifact if the model boundary is not a physical boundary but an artificial numerical model boundary. Figure 5-16b shows the elimination of the reflected disturbance for the case in which damping is used for masses 11 through 20. Damping has little effect on the initial disturbance propagating through the undamped masses (masses 2 through 10). This is shown by superimposing the two cases in Figure 5-17. The responses for masses 2 through 10 diverge only at later times when the reflected wave moves through the undamped system (red lines in Figure 5-17). The comparison also shows the effects of damping for masses 11 through 20 on the propagation of the initial disturbance.

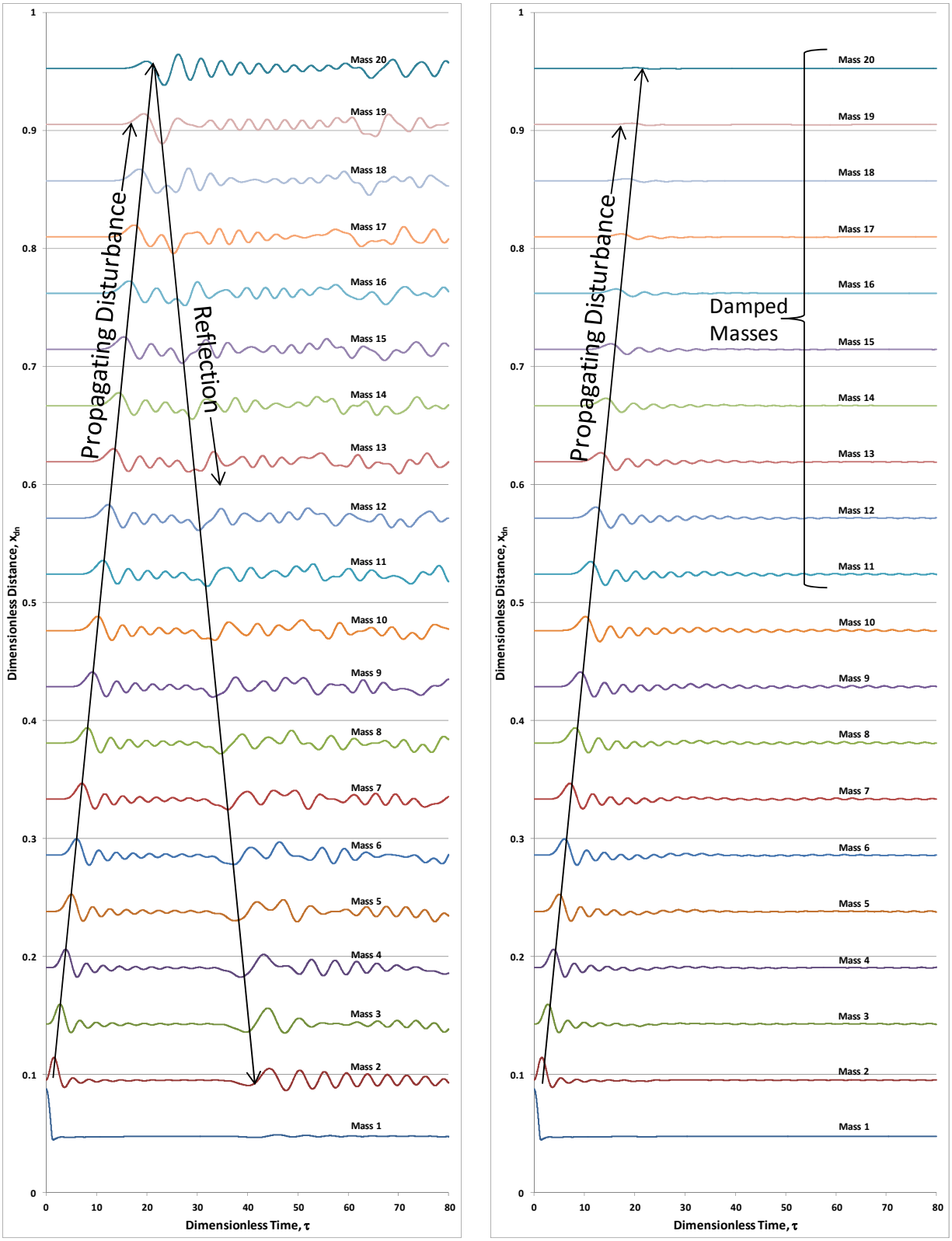

Figure 5-16. Propagation of a disturbance in the mass-spring system: a) no damping except for mass 1; and b) damping for masses 11 through 20 and mass 1.

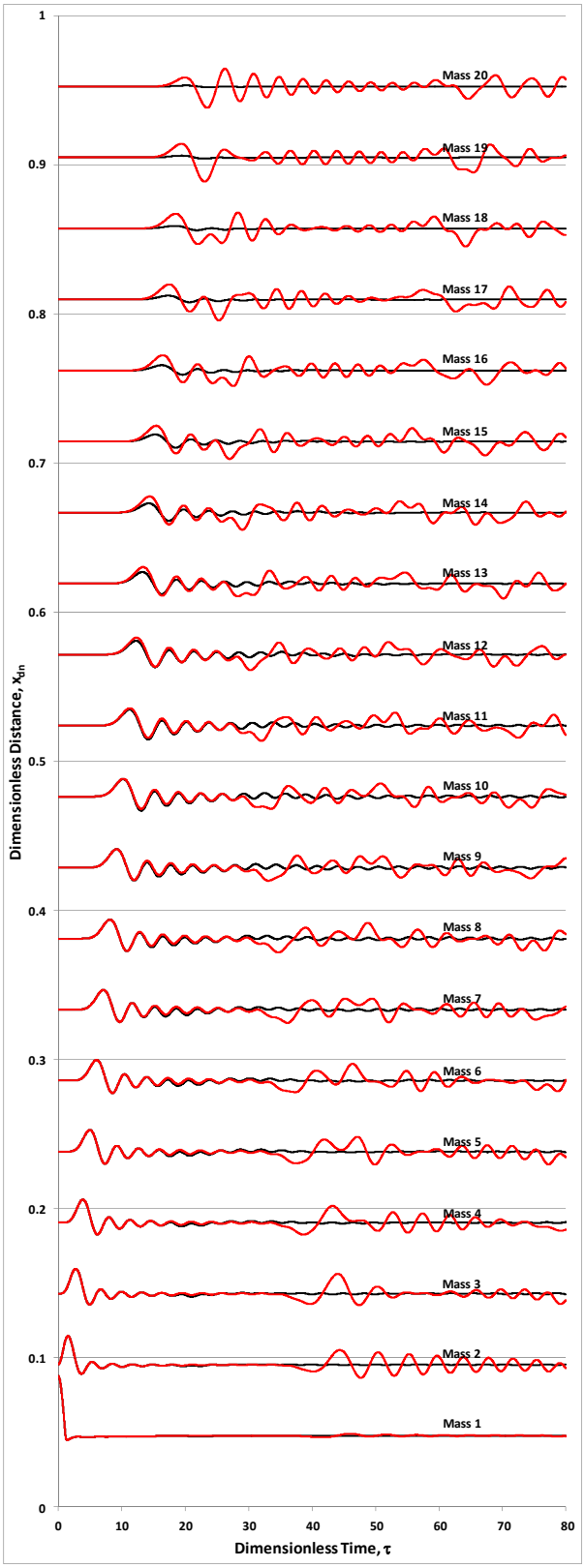

Figure 5-17. Comparison of damping with no damping of masses 11 through 20. Black lines for damped case, red lines for undamped case (except mass 1 which is damped in both cases).

5.5 Conclusions

In this study, an effective coupling between the TOUGH2 and the RBSN approach has been implemented and applied to hydraulic fracturing simulations. The simulator provides a discrete representation of hydrological (flow and mass transfer through fracture networks) and mechanical (fracture initiation and propagation) responses within geomaterials using the DFN approach within unstructured Voronoi grids.

The numerical program is verified through a simulation of a single fluid-driven fracture, in which the elliptical fracture aperture profiles are in close agreement with the analytical solution based upon the linear elastic fracture mechanics theory. Subsequently, predictive simulations including a sensitivity study of the effect of injection system compliance are conducted for hydraulic fracturing within complex pre-existing fracture networks. The simulation results demonstrate relevant modeling capabilities of TOUGH-RBSN, and the sensitivity analysis provides insights for controlling hydraulic fracture propagation. In addition, an inherent shortcoming of the current RBSN approach due to the equilibrium-based calculations is observed, where abrupt and unstable fractures break up the computational domain at near-final stage of the simulation.

As a part of efforts to resolve the problems with the current RBSN approach, we have initiated development of a new dynamic simulation framework. In the new methodology, the terms of time exist in the governing equation and the force unbalance is naturally allowed, so that the numerical instability found in the static modeling approach can be prevented. Nodal kinematic information (displacements, velocities, and accelerations) is calculated through the explicit time integration scheme, by which the code implementation with parallelization can be easily realized. Finally, a specific boundary configuration with damping is discussed for reduction of the effects of artificial boundary conditions. An example calculation with a mass-spring model proves that the propagation of a disturbed displacement is absorbed by damped masses at the boundary.

5.6 Future Work

A modeling program using the DFN approach for coupled THM processes has been developed and verified through fluid-driven fracture simulations. While the simulation results demonstrate the relevant modeling capabilities of TOUGH-RBSN for tightly coupled hydro-mechanical behavior, unphysical features exist due to the equilibrium-based calculations of the RBSN models within the current THM coupling procedure. To resolve the numerical artifacts, we have set to develop a new dynamic simulation framework for RBSN. A summary of the accomplishments so far is as follows:

- The basic methodology to compute the elemental forces (i.e., force-displacement relationship) is based on the existing RBSN approach.
- The equations of motion of Voronoi cells are solved to get the nodal accelerations, which are integrated through a time-stepping procedure (e.g., velocity Verlet algorithm) to derive the nodal velocities and displacements.
- Boundary effects due to the wave reflection can be suppressed using layered damped masses over the boundary.

Recommended work for FY16 includes:

- Regarding the RBSN to TOUGH2 coupling module, hydrological properties (e.g., permeability) of an individual fracture will be defined on the basis of the fracture aperture in order to conduct rather quantitative simulations.
- Also, in the Mohr-Coulomb fracture criterion, gradual damage by shrinking the fracture surface will be implemented for more realistic energy-based fracture processes.
- The dynamic simulation framework uses explicit time integration schemes without building the whole system matrix and its inverse, so the program code is expected to be easily parallelized for large-scale computations.
- Verifications of the dynamic simulation framework will be provided through simple geomechanics examples.

References

Amini, M., Eastwood, J.W., and Hockney, R.W. (1987) Time integration in particle models, *Computer Physics Communications,* 44, 83–93.

Asahina, D., Houseworth, J.E., Birkholzer, J.T., Rutqvist, J., and Bolander, J.E. (2014) Hydro-mechanical model for wetting/drying and fracture development in geomaterials, *Computers & Geosciences*, 65, 13–23.

Asahina, D., Landis, E.N., and Bolander, J.E. (2011). Modeling of phase interfaces during pre-critical crack growth in concrete. *Cement & Concrete Composites*, 33, 966–977.

Bear, J. (1972) *Dynamics of Fluids in Porous Media*, Elsevier, New York, New York.

Bear, J., Tsang, C.-F., and de Marsily, G. (1993) *Flow and Contaminant Transport in Fractured Rock*, Academic Press, San Diego, Calif.

Berton S. and Bolander, J.E. (2006) Crack band model of fracture in irregular lattices, *Computer Methods in Applied Mechanics and Engineering*, 195, 7172–7181.

Biot, M.A. and Willis, D.G. (1957) The elastic coefficients of the theory of consolidation, *Journal of Applied Mechanics*, 24, 594–601.

Bolander, J.E. and Saito, S. (1998) Fracture analyses using spring networks with random geometry, *Eng. Fract. Mech.*, 61, 569–91.

Bossart, P., Meier, P.M., Moeri, A., Trick, T., and Mayor, J.-C. (2004) Structural and hydrogeological characterisation of the excavation-disturbed zone in the Opalinus Clay (Mont Terri Project, Switzerland), *Applied Clay Science*, 26, 429–448.

Chiaramonte, L., Zoback, M.D., Friedmann, J., and Stamp, V. (2008) Seal integrity and feasibility of CO_2 sequestration in the Teapot Dome EOR pilot: geomechanical site characterization, *Environ. Geol.*, 54, 1667–1675.

Cosgrove, J.W. (2001) Hydraulic Fracturing during the Formation and Deformation of a Basin: A Factor in the Dewatering of Low-Permeability Sediments, *AAPG Bulletin*, 85(4), 737–748.

Fu, P., Johnson, S.M., and Carrigan, C.R. (2013) An explicitly coupled hydro-geomechanical model for simulating hydraulic fracturing in arbitrary discrete fracture networks*, Int. J. Numer. Anal. Meth. Geomech.*, 37, 2278–2300.

Geertsma J. and de Klerk, F. (1969) A rapid method of predicting width and extent of hydraulically induced fractures, *Journal of Petroleum Technology*, 21, 1571–1581.

Gonçalvès, J., Violette, S., and Wendling, J. (2004) Analytical and Numerical Solutions for Alternative Overpressuring Processes: Application to the Callovo-Oxfordian Sedimentary Sequence in the Paris Basin, France, *Journal of Geophysical Research*, 109, 14.

Khristianovic, S.A. and Zheltov, Y.P. (1955) Formation of vertical fractures by means of highly viscous liquid, *Proceedings of the Fourth World Petroleum Congress, Rome*, 579–586.

Kim, K., Lim J., Kim J., and Lim, Y.M. (2008) Simulation of material failure behavior under different loading rates using molecular dynamics, *Structural Engineering and Mechanics,* 30(2), 177–190.

Kim, K. and Lim, Y.M. (2011) Simulation of rate dependent fracture in concrete using an irregular lattice model, *Cement & Concrete Composites,* 33, 949–955.

Martys, N.S., and Mountain, R.D. (1999) Velocity Verlet algorithm for dissipative particle-dynamics-based models of suspensions, *Physical Review E,* 59(3), 3733–3736.

Neuzil, C.E. (2003) Hydromechanical coupling in geologic processes, *Hydrogeology Journal*, 11, 41–83.

Nordgren, R.P. (1972) Propagation of a vertical hydraulic fracture, *Society of Petroleum Engineers Journal*, 12, 306–314.

Okabe, A., Boots, B., Sugihara, K., and Chiu, S.N. (2000) *Spatial Tessellations: Concepts and Applications of Voronoi Diagrams*, 2nd ed., Wiley, NYC, 696 pages.

Perkins, T.K. and Kern, L.R. (1961) Widths of hydraulic fractures, *Journal of Petroleum Technology*, 13, 937–949.

Pruess, K., Oldenburg, C., and Moridis, G. (2011) *TOUGH2 User's Guide, Version 2*, Report LBNL-43134 (Revised), Lawrence Berkeley National Laboratory, Berkeley, Calif.

Rutqvist, J., Leung, C., Hoch, A., Wang, Y., and Wang, Z. (2013) Linked multicontinuum and crack tensor approach for modeling of coupled geomechanics, fluid flow and transport in fractured rock, *J. Rock Mech. Geotech. Eng.*, 5, 18–31.

Rutqvist, J. and Tsang, C.-F. (2002) A study of caprock hydromechanical changes associated with CO_2-injection into a brine formation, *Environmental Geology*, 42, 296–305.

Rutqvist, J., Wu, Y.-S., Tsang, C.-F., and Bodvarsson, G. (2002) A modeling approach for analysis of coupled multiphase fluid flow, heat transfer and deformation in fractured porous rock, *International Journal of Rock Mechanics & Mining Sciences*, 39, 429–442.

Shen, X. and Shen, G. (2002) A fracture-energy-based elasto-softening-plastic constitutive model for joints of geomaterials, *Applied Mathematics and Mechanics*, 23(9), 1097–1104.

Sloan, S.W. (1987) A fast algorithm for constructing Delaunay triangulations in the plan, *Advances in Engineering Software*, 9(1), 34–55.

Taniguchi, T., Yamashita, Y., and Moriwaki, K. (2002) Generation of arbitrary 3-dimensional domain from nodes on its surface, *8th Conference on Numerical Grid Generation*, Hawaii, USA.

Thomure, J.L., Bolander, J.E., and Kunieda, M. (2001) Reducing mesh bias on fracture within rigid-body-spring networks, *Journal of Structural Mechanics and Earthquake Engineering*, 18(2), 95–103.

Yip, M., Mohle, J., and Bolander, J. (2005) Automated modeling of three-dimensional structural components using irregular lattices, *Computer-Aided Civil and Infrastructure Engineering*, 20, 393–407.

Zhang, K., Wu, Y.S., Bodvarsson, G.S., and Liu, H.H. (2004) Flow focusing in unsaturated fracture networks: a numerical investigation, *Vadose Zone Journal*, 3, 624–633.

6. SUMMARY

(1) Investigation of the Impacts of High Temperature Limits with THMC modeling (Chapter 2)

This chapter documents progress on simulations to analyze the impact of strongly elevated temperature on the bentonite backfill and near-field clay host rock in a geologic repository for radioactive waste. One of the major achievements in FY15 is the implementation of a time-step management scheme in the TOUGHREACT-FLAC3D simulator to reduce the simulation time, which enables us to extend the simulations from 1,000 years to 100,000 years. The simulator was also revised to include chemical-mechanical coupling for clay formations. Specific findings are as follows:

- Results for 100,000-year simulations have found some degree of illitization in the EBS bentonite and NS clay formation and that illitization is enhanced under higher temperature. Other major chemical alterations include the dissolution of K-feldspar and calcite, the precipitation of quartz, chlorite, and kaolinite. The most important chemical factors for illitization are the concentration of K and dissolution rate of K-feldspar.
- Model results reveal that for the "high T" scenario, illitization is stabilized after about 2,000 years in bentonite near the waste package, but continues in bentonite near the EBS-NS interface. For the "low T' scenario, illitization is nearly stabilized after 2,000 years for the entire volume of EBS bentonite.
- In contrast to the previous 1,000-year simulations in Liu et al., (2013) and Zheng et al., (2014), the simulation results at 100,000 years show that bentonite near the EBS-NS interface undergo more illitization than that near the waste package for the "high T' scenarios.
- The dissolution rate of K-feldspar, which was thought to be critical for illitization as revealed by the 1,000-years simulations, is not as important as the amount of K-feldspar available for longer time periods.
- The simulations conducted in FY15 also reveal that the dissolution of calcite delays illitization by around 30-50 years for the case of Kunigel-VI and FEBEX bentonite if Ca-smectite is the major smectite phase in the bentonite. Although this effect is short-lived and not important as far as long term illitization is concerned, calcite dissolution might explain why illitization was not observed in some laboratory and field experiments.
- The effect of chemical changes on swelling stress as a result of smectite dissolution in bentonite was analyzed for a time period of 100,000 years. The results show more significant reductions in swelling stresses, ranging from 3% to 53%, than previously revealed by the 1,000-year simulations. Greater reductions in swelling stress were found at higher temperatures for Kunigel-VI bentonite compared with FEBEX bentonite.
- Chemical effects were incorporated in the mechanical model for the clay formation and the effect of chemical change in clay formation on the total stress was evaluated. Chemical change leads to about a 2.6% decrease in stress near the EBS-NS interface and about 0.7% in the far field. In general, chemical change does not have significant impact on the stress in the clay formation.

In the remaining months of FY15 and FY16 the following activities are proposed:

- A more rigorous approach to link chemistry to mechanics is needed for more accurate calculations than the current extended linear elastic swelling model. More comprehensive

links between chemistry and mechanics, taking advantage of the framework provided by a dual-structure model, was implemented in TOUGHREACT-FLAC (Rutqvist et al., 2014), and could be used to simulate the chemical-mechanical coupling for EBS bentonite in the future.

- In the current model, the canister serves only as a heat source; chemical changes on the surface of the canister are neglected for simplification. Further model analysis is needed to consider chemical changes in the canister, specifically the release of Fe^{+2}, which might enhance the dissolution of smectite by forming chlorite.
- Current models show significant precipitation of silicate minerals during illitization, which could result in the cementation of bentonite and subsequently lead to change in the mechanical properties of bentonite. While the current model can quantify the formation of silicate minerals, the change of mechanical properties as result of cementation needs to be quantified. This requires a mechanical-chemical coupling scheme for cementation to be incorporated and tested in the next version of the simulator.

(2) Developing THMC models for FEBEX-DP (Chapter 3)

The key findings from current modeling work are as follows:

- Adjusting key hydrological parameters such as permeability of bentonite and granite may lead to the good fit of measured relative humidity at given location, but cannot explain relative humidity across the entire bentonite barrier. Mechanical change (especially swelling) has to be considered.
- Including Non-Darcian flow into the TH model leads to a significant underestimation of the relative humidity data in the entire bentonite barrier (even in bentonite near the bentonite/granite interface). The reason could be that the calibration of relative permeability (and retention curve) already encompasses the nonlinear relationship between gradient and flux for bentonite, which would obviate the consideration of Non-Darcian flow in the model. Non-Darcian flow under unsaturated conditions still needs more study.
- In comparison with the chemical data obtained after the dismantling of heater 1 in 2002, the THC model captures the general trend of the concentration profiles of major cations and anions. However, the model overestimate the concentration level in bentonite near the bentonite/granite interface; this effect will be reduced when mechanical change is included in the model, i.e. with THMC models.
- The preliminary prediction of the chemical change after the dismantling of heater 2 shows that concentration levels of aqueous species will continue going down in bentonite near the heater; calcite dissolves and dolomite forms, and illite precipitates in bentonite near the bentonite/granite interface, accompanied by the dissolution of smectite at the same place.

In the remaining months of FY15 and FY16, the following activities are recommended:

- The mechanical processes will be added to the current THC model. Once coupled THMC model is developed, mechanical-hydrological coupling will be calibrated against measured stress, dry density, water content and relative humidity data.

- The chemical model will be further refined. Once the concentration profile of chloride can be nicely matched by the THMC model, predictions will be made for other chemical species and mineral phases.
- Once the corrosion of the steel liner is analyzed, chemical changes of steel will be included in the chemical model to evaluate the interaction of steel and bentonite.

Ultimately, after the THMC models for FEBEX *in situ* test are fully validated with data, they will used to explore THMC change in the long run under higher temperature.

(3) THM modeling: FE heater test and DECOVALEX (Chapter 4)

While the work in previous years has been focused on model development and testing, in FY2015 work has been focused on modeling of the large scale in situ heater experiments involving both bentonite and rock,the Mont Terri HE-E, Horonobe EBS, and Mont Terri FE experiments. The main accomplishment in FY2015 is that we have been able to successfully conduct model predictions of the THM responses at all three of these experiments using state-of-the-art constitutive models for bentonite and host rocks. Some comparison to measured data has been conducted in the case of the Mont Terri HE-E experiment.

The heating has just started in 2015 for the Horonobe EBS experiment and the Mont Terri FE experiment, and comparison between measured and predicted responses can be started once the data is provided to the modeling teams. In the remaining months of FY15 and FY16 the following activities are recommended:

- For the remainder of FY2015 we plan to complete interpretive modeling of the Mont Terri HE-E experiment and Horonobe EBS experiment as part of the DECOVALEX-2015 project, which is due to end at the end of year 2015. Related to the Mont Terri FE experiment, LBNL will participate in a joint journal paper with the Swiss nuclear waste organization NAGRA and other organizations in a Mont Terri 20-year anniversary, scientific paper for the Swiss Journal of Geosciences. This will include work done by FE experiment modeling teams, including code benchmarking and design modeling predictions.
- Our work for FY2016 will be first to complete and document work related to DECOVALEX-2015 and at the same time initiate work related to DECOVALEX-2019. It is very likely that the Mont Terri FE experiment will be part of DECOVALEX-2019; it will be an upscaling from the half-scale HE-E experiment to the full scale FE experiment. We also propose that our work on coupled THM modeling be focused on 1) improving and gaining experience in applying the dual-structure model for granular bentonite and 2) implementating and applying damage models for the evolution of the excavation damaged zone in host rocks.
- One of the main Tasks for FY2016 will be the improvement of the BExM in TOUGH-FLAC and to gain experience in applying it efficiently, including gaining confidence in the determination of input parameters. The inclusion of the FE heater experiment into DECOVALEX-2019 will be helpful for international collaboration on this, including collaboration with the University of Catalonia, which is the only other group in the world that has implemented BExM into a numerical simulator.

- The implementation and application of a damage model for the evolution of the excavation disturbed zone will be an important addition to the current model for calculating the evolution of permeability along with damage as well as sealing and healing. Different approaches can be tested, building upon previous work on the Two-Part Hooke's Model (TPHM), as well as other continuum damage models considering fracture evolution implicitly. Such a model can be benchmarked against discrete fracture modeling of damage-zone fractures using TOUGH-RBSN. The goal is to build a pragmatic continuum model that can be validated against field experiments such as sealing experiments conducted in underground research laboratories.
- These activities will allow significant progress to be made toward achieving UFD goals to fill data needs and confirm advanced modeling approaches (by 2015), and to have a robust modeling and experimental basis for evaluation of multiple disposal system options (by 2020).

(4) Discrete Fracture Network (DFN) Approach for THM Damage Modeling in Argillaceous Rock (Chapter 5)

In this study, an effective coupling between the TOUGH2 and the RBSN approach has been implemented and applied to hydraulic fracturing simulations. The simulator provides a discrete representation of hydrological (flow and mass transfer through fracture networks) and mechanical (fracture initiation and propagation) responses within geomaterials using the DFN approach within unstructured Voronoi grids. The numerical program is verified through a simulation of a single fluid-driven fracture which is found to be in close agreement with an analytical solution. The model has also been used for predictive simulations of hydraulic fracturing within complex pre-existing fracture networks. The simulation results demonstrate relevant modeling capabilities of TOUGH-RBSN, and the sensitivity analysis provides insights for controlling hydraulic fracture propagation.

While the simulation results demonstrate the relevant modeling capabilities of TOUGH-RBSN for tightly coupled hydro-mechanical behavior, unphysical features exist due to the equilibrium-based calculations of the RBSN models within the current THM coupling procedure. To resolve the numerical artifacts, we have initiated development of a new dynamic simulation framework for RBSN. A summary of the accomplishments so far is as follows:

- The basic methodology to compute the elemental forces (i.e., force-displacement relationship) is based on the existing RBSN approach.
- The equations of motion of Voronoi cells are solved to get the nodal accelerations, which are integrated through a time-stepping procedure (e.g., velocity Verlet algorithm) to derive the nodal velocities and displacements.
- Boundary effects due to the wave reflection can be suppressed using layered damped masses over the boundary.

In the remaining months of FY15 and FY16 the following activities are recommended:

- Regarding the RBSN to TOUGH2 coupling module, hydrological properties (e.g., permeability) of an individual fracture will be defined on the basis of the fracture aperture in order to conduct quantitative simulations.

- Also, in the Mohr-Coulomb fracture criterion, gradual damage by shrinking the fracture surface will be implemented for more realistic energy-based fracture processes.
- The dynamic simulation framework uses explicit time integration schemes without building the whole system matrix and its inverse, so the program code is expected to be easily parallelized for large-scale computations.
- Verifications of the dynamic simulation framework will be provided through simple geomechanics examples.

7. ACKNOWLEDGMENT

Funding for this work was provided by the Used Fuel Disposition Campaign, Office of Nuclear Energy, of the U.S. Department of Energy under Contract Number DE-AC02-05CH11231 with Lawrence Berkeley National Laboratory.